Smart Material Systems for Robotics and Sensing in Healthcare

Zur Erlangung des akademischen Grades eines

Doktors der Ingenieurwissenschaften

von der KIT-Fakultät für Informatik
des Karlsruher Instituts für Technologie (KIT)

genehmigte

Dissertation

von

Nikola Fischer

Tag der mündlichen Prüfung: 01.07.2024

1. Referentin: Prof. Franziska Mathis-Ullrich
2. Referent: Prof. Michael Beigl

Karlsruhe Institute of Technology

Smart Material Systems for Robotics and Sensing in Healthcare

Nikola Fischer M.Sc.

At the KIT Department of Informatics:

Institute for Anthropomatics and Robotics (IAR)
Health Robotics and Automation (HERA)

Institute of Telematics (TM)
Chair of Pervasive Computing Systems

First reviewer:	Prof. Dr. sc. Franziska Mathis-Ullrich
Second reviewer:	Prof. Dr.-Ing. Michael Beigl

1st June 2020 – 1st July 2024

Acknowledgment

I extend my sincere appreciation for the culmination of my dissertation journey, spanning a transformative period of four years. This endeavor has been marked by significant milestones and invaluable contributions that have profoundly influenced its trajectory and outcomes.

The foundation of this dissertation rests upon the bedrock of twelve publications, including eight as the first author, accompanied by three conference contributions. These achievements stand as testaments to the collaborative efforts and dedication poured into this work. I extend my gratitude to the Klaus Tschira Stiftung and the Carl-Zeiss-Stiftung for their funding, without which this dissertation would not have been possible.

Throughout this scholarly odyssey, my role transcended the boundaries of research to encompass mentorship and teaching. Guiding over 25 students, comprising master's and bachelor's candidates as well as research assistants, has been a privilege and a source of profound fulfillment. The dynamic interchange of ideas and the intellectual curiosity exhibited by my students have enriched my own research endeavors immeasurably.

I am indebted to my esteemed supervisors, Prof. Franziska Mathis-Ullrich and Prof. Michael Beigl, for their unwavering guidance, steadfast support, and enduring confidence in my scholarly pursuits. Their mentorship has been instrumental in shaping my academic and professional trajectory.

To my esteemed colleagues, both past and present, from diverse academic institutions and disciplinary backgrounds, I extend heartfelt appreciation for your camaraderie, collaborative spirit, and shared commitment to scholarly excellence. Together, we navigated the rigors of scientific inquiry, fostering an environment of collective learning and growth. Acknowledgment is also due to my collaborators in clinical settings, underscoring the indispensable role of interdisciplinary collaboration and effective communication in advancing scholarly endeavors.

To my cherished family and friends, your unwavering support, encouragement, and unwavering belief in my abilities have served as pillars of strength throughout this arduous journey. In particular, I am profoundly grateful to my parents and my sisters for their unwavering faith and steadfast reassurance.

In special remembrance of my grandmother, whose aspirations to pursue her passion as a teacher were thwarted by the constraints of life. Although she passed away shortly after the commencement of this academic pursuit, her guiding presence has remained ever since.

With the deepest gratitude, Nikola

Abstract

Smart Material Systems for Robotics and Sensing in Healthcare

The research field of robotics and sensing in healthcare has been advancing towards more enhanced and integrated systems. This involves a focus on technology moving towards smaller size, higher performance, increasing functionality, and reduced energy demand, all concurrently. The growing importance of smaller and lighter systems for minimally invasive procedures and for wearable assistive exoskeletons is becoming evident. All these applications rely on both structural and functional integrity to adhere to stringent safety standards for deployment inside and outside the body, while simultaneously minimizing spatial and weight requirements. Thereby, compliance and flexibility are considered important aspects for the development of surgical equipment and wearables in the domain of healthcare technology. This consequently holds also true for the fundamental components that provide actuation and sensing.

Smart materials, often referred to as such due to their ability to undergo deterministic property changes in response to external stimuli, hold significant promise for augmenting conventional system designs in healthcare technology. These materials offer the most compact actuation and/or sensing capabilities alongside their structural integrity, as the materials themselves become functional, making additional actuation and sensing components obsolete. This makes them well-suited to meet the demanding requirements of this field. Confronted with the vast variety of different smart materials, a critical investigation must be undertaken to determine the potential of these materials for addressing significant technical challenges in the field.

This dissertation advances the forefront of healthcare technology by exploring smart material systems based on shape memory alloys, ferromagnetic materials, and piezoresistive polymers for robotic and sensing applications in the realms of minimally invasive surgery and assistive exoskeletons. By leveraging the availability, scalability, and economic potential of these selected smart materials, this research aims to enhance key technical aspects of robotic and sensor systems in healthcare, such as compliance, flexibility, miniaturization, and practicability. This is compared to conventional actuators, sensors, and materials. The findings are intended to be easily transferable and adaptable by other researchers and professionals, facilitating broader adoption and implementation without requiring specialized technical infrastructure. As a method, multiple smart material systems were designed based on each of the mentioned materials. This involved the use of material-inherent actuation, material-based sensing, or a combination of both.

As the main contribution of this dissertation, five smart material systems are presented comprising three robotic systems incorporating shape memory alloys and two sensor systems, deploying ferromagnetic and piezoresistive materials. The contribution comprises

a novel self-assembling continuum robotic system measuring $15.4\,\mathrm{mm}$ in diameter, featuring a superelastic shape memory alloy backbone, enabling omnidirectional bending motion and extending up to $240\,\mathrm{mm}$, e.g., for gastroendoscopy. Leveraging the superelasticity enhances the robots' flexibility, dexterity, and workspace range while minimizing size and weight [1].
Furthermore, an even more compact flexible instrument in comparison to continuum robots was developed for laparoscopy, utilizing the immediate shape memory effect, and enabling complex shape changes with miniaturized actuation setups and a frame package size of less than $1\,\mathrm{cm}^3$ [2,3]. This shape memory alloy also features inherent self-sensing abilities, with its electric resistance correlating to shape and load. A data-driven model allows then for shape prediction without imaging support. It accurately estimates the instrument's bending deflection, resulting in mean errors of less than $3.6\,\mathrm{mm}$ [4].
In addition to self-sensing shape memory alloys, surgical instruments, such as for endovascular interventions, can be further improved by integrating ferromagnetic materials. These enhanced instruments can then be tracked with Euclidean distance errors of below $1.31\,\mathrm{mm}$ by a novel, compliant wearable array of Hall sensors, estimating its own bending shape with absolute errors of below $8.33°$ prior to the medical procedure. Hence, despite the added effort for shape estimation, overall tracking can be improved, minimizing spatial footprint compared to conventional imaging methods [5].
Beyond the augmentation of surgical instruments, smart materials such as piezoresistive polymers can also be utilized to improve surgical training platforms as cost-effective force sensors. These sensors can be integrated into additively manufactured training phantoms of the human vascular system, offering patient and patholgyspecific training scenarios [6,7].
Physical rehabilitation and daily assistance, which are essential and growing fields of healthcare, are further prime fields of application for smart materials. The physical interface of a robotic exoskeleton was successfully enhanced through the use of compliant actuator-sensor units featuring a shape memory alloy. Demonstrating a controllable actuation up to $62\,\mathrm{N}$ with effective force offsets of $13.7\,\mathrm{N}$ using less than $10\,\mathrm{W}$, these smart material units are able to replace conventional bulky cuff actuation methods of assistive robotic exoskeletons [8].

Based on these demonstrations of integrating smart material hardware, valuable practical advice was gleaned regarding system design, material selection, material processing, and material integration. This encompasses a thorough discussion of both the enhancements and limitations encountered when deploying smart materials.

In summary, this dissertation demonstrates that material systems from the three studied material groups – shape memory alloys, ferromagnetic materials, and piezoresistive polymers – can surpass traditional methods of actuation and sensing, particularly in terms of compliance, flexibility, and space requirements. The presented material systems and their components can thus serve as useful building blocks for future applications in robotics and sensing in medical technology. While technical feasibility and experimental evaluations have been demonstrated, the complex and resource-intensive development towards fully operational medical devices remains a challenging task for future research in the field of robotics and sensing in healthcare.

Keywords: *Medical robotics, continuum robotics, flexible instruments, exoskeletons, shape memory alloys, piezoresistive polymers, ferromagetic sensing, smart phantoms*

Zusammenfassung

Intelligente Materialsysteme für Robotik und Sensorik in der Medizintechnik

Das Forschungsfeld der Robotik und Sensorik in der Medizintechnik richtet den Blick zunehmend auf fortschrittliche, integrierte Systeme. Hierbei steht vor allem die Entwicklung hin zu leistungsfähigeren und hochfunktionalen Systemkomponenten im Vordergrund, welche gleichzeitig einen geringen Platz- und Energiebedarf aufweisen. Insbesondere wird die Bedeutung kleinerer und leichterer Systeme für minimalinvasive, chirurgisch Eingriffe und bei mobilen Exoskeletten deutlich. Die konkreten Anwendungen sind sowohl auf strukturelle als auch auf funktionelle Integrität angewiesen, um strenge Sicherheitsstandards für den Einsatz innerhalb und außerhalb des menschlichen Körpers einzuhalten, während gleichzeitig Raum- und Gewichtsanforderungen minimiert werden sollen. Daher gelten Nachgiebigkeit und Flexibilität als wichtige Aspekte für die Entwicklung von chirurgischen und tragbaren Geräten im Bereich der Medizintechnik. Dies gilt auch für die grundlegenden Komponenten der Aktuierung und Sensorik.

Sogenannte Intelligente Materialien reagieren auf externe Stimuli mit deterministischen Eigenschaftsveränderungen. Ausgewählte Intelligente Materialien verfügen daher neben ihrer strukturgebenden Funktionalität auch über die Fähigkeit, auf einen bestimmten Stimulus mit einer Formveränderung (Aktuierung) oder der Variation einer physikalischen Eigenschaft, wie z. B. dem elektrischen Widerstand (Sensorik), zu reagieren. Durch diese kompakte Kombination und Integration der Funktionen direkt in das Material selbst bieten Intelligente Materialien ein erhebliches Potenzial, um herkömmliche Systemdesigns in der Medizintechnik zu verbessern. Angesichts der großen Vielfalt verschiedener Intelligenter Materialien ist es jedoch erforderlich, kritisch zu untersuchen, in welchem Ausmaß ausgewählte Intelligente Materialien dazu beitragen können, die genannten technischen Herausforderungen in der Medizintechnik anzugehen.

Die vorliegende Dissertation untersucht daher Intelligente Materialsysteme auf Basis von Formgedächtnislegierungen, ferromagnetischen Materialien und piezoresistive Polymere für robotische und sensorische Anwendungen im Bereich der minimalinvasiven Chirurgie und der assistiven Exoskelette. Die Arbeit leistet damit einen grundlegenden Beitrag zur Erforschung der Nützlichkeit, Skalierbarkeit und des wirtschaftlichen Potenzials dieser ausgewählten Intelligenten Materialien. Dabei werden konkrete Ansätze vorgestellt, wie die technischen Eigenschaften der Nachgiebigkeit, Flexibilität, Miniaturisierung und Praktikabilität, im Vergleich zu herkömmlichen Aktuatoren, Sensoren und Materialien in Roboter- und Sensorsystemen verbessert werden können. Die Forschungsergebnisse sollen für Dritte ohne eine besondere technische Infrastruktur leicht übertragbar und anpassbar sein, um eine niedrigschwellige Implementierung zu ermöglichen.

Als Methode wurden mehrere Intelligente Materialsysteme auf Basis von jeweils einem der genannten Materialien konzipiert. Dabei wurden die materialinhärente Aktuier-

barkeit, die materialgebundene Sensorik, oder eine Kombination von beiden angewendet. Die Systeme wurden anschließend aufgebaut und ihre technischen Eigenschaften im Versuch experimentell evaluiert, um ihren Nutzen für den Einsatz in der Medizintechnik zu eruieren.

Als Beitrag dieser Dissertation zur medizintechnischen Forschung werden fünf Intelligente Materialsysteme vorgestellt, darunter drei Robotersysteme mit Formgedächtnislegierungen und zwei Sensorsysteme, welche ferromagnetische und piezoresistive Materialien einsetzen. Der Beitrag umfasst ein neuartiges, sich-selbst-zusammensetzendes System eines Kontinuumroboters mit einem Durchmesser von $15{,}4\,\mathrm{mm}$. Wegen seines superelastischen Rückgrats aus Formgedächtnislegierung ermöglicht es eine omnidirektionale Biegebewegung bei einer Ausfahrlänge von bis zu $240\,\mathrm{mm}$, z. B. für den Einsatz in der Gastroendoskopie. Die Nutzung der Superelastizität erhöht die Flexibilität, Beweglichkeit und den maximalen Arbeitsbereich des Roboters und minimiert gleichzeitig die Größe und das Gewicht [1].
Darüber hinaus wurde im Vergleich zu herkömmlichen Kontinuumsrobotern ein noch kompakteres, flexibles Instrument für die Laparoskopie entwickelt, das den Formgedächtniseffekt unmittelbar einsetzt. Dadurch konnten mit einem miniaturisierten Aktuierungsaufbau von weniger als $1\,\mathrm{cm}^3$ komplexe Formänderungen erzeugt werden [2, 3]. Die verwendete Formgedächtnislegierung verfügt auch über eine materialinhärente Sensoreigenschaft, wobei ihr elektrischer Widerstand mit der Formveränderung und Belastung korreliert. So konnte ein datengetriebenes Modell generiert werden, das die Schätzung der Form ohne weitere Unterstützung einer Bildgebung mit durchschnittlichen Fehlern von weniger als $3{,}6\,\mathrm{mm}$ ermöglichte [4].
Neben dem Einsatz der materialinhärenten Sensoreigenschaft von Formgedächtnislegierungen können chirurgische Instrumente, z. B. für endovaskuläre Eingriffe, auch mithilfe integrierter ferromagnetischer Materialien weiterentwickelt werden. Diese ferromagnetisch modifizierten Instrumente und ihre Bewegung im Körper können dann von einem neuartigen, tragbaren Hall-Sensorfeld erfasst werden, das seine eigene Biegeform mit absoluten Fehlern von unter $8{,}33°$ vor dem medizinischen Eingriff schätzen kann. Das Sensorfeld ermöglicht anschließend während des Eingriffs eine Instrumentenverfolgung mit euklidischen Distanzfehlern von unter $1{,}31\,\mathrm{mm}$. Es kann für die Instrumentenverfolgung trotz des zusätzlichen Aufwands für die Formschätzung insgesamt eine höhere Genauigkeit erreicht werden, wobei der Platzbedarf für das Sensorsystem im Vergleich zu herkömmlichen Bildgebungsmethoden minimiert wird [5].
Über die Anwendung in chirurgischen Instrumenten hinaus können Intelligente Materialien wie piezoresistive Polymere auch als flexible und kostengünstige Kraftsensoren in additiv hergestellten, chirurgischen Trainingsphantomen eingesetzt werden. Die Trainingsphantome, z. B. des menschlichen Gefäßsystems, können durch die integrierte Sensorik nützliche patienten- und pathologiespezifische Trainingsszenarien abbilden [6, 7].
Ein weiteres Anwendungsfeld für Intelligente Materialien in der Medizin ist die physische Rehabilitation und die Bewegungsunterstützung der Patienten nach einer Operation. Es war möglich, die physische Schnittstelle eines robotischen Exoskeletts mit nachgiebigen Aktuator-Sensor-Einheiten auszustatten, die auch eine Formgedächtnislegierung einsetzen. Diese Materialsysteme zeigen eine kontrollierbare Aktuierung von bis zu $62\,\mathrm{N}$ mit effektiven Kraftdifferenzen von $13{,}7\,\mathrm{N}$ bei einem Verbrauch von weniger als $10\,\mathrm{W}$. Sie können damit zukünftig größere und schwerere konventionelle Aktuationsmethoden von physischen Schnittstellen von assistiven robotischen Exoskeletten ersetzen [8].

Durch die verschiedenen gezeigten Arten der Hardwareintegration konnten fundierte, praxisrelevante Empfehlungen zu Systemdesigns, sowie der Auswahl, der Verarbeitung und der Implementierung von Intelligenten Materialien formuliert werden. Diese Dissertation umfasst dabei auch eine umfangreiche Diskussion sowohl der Verbesserungen als auch der Limitationen, die bei der Verwendung der ausgewählten Intelligenter Materialien beobachtet werden konnten.

Zusammenfassend zeigt diese Dissertation, dass Materialsysteme aus den drei untersuchten Materialgruppen der Formgedächtnislegierungen, ferromagnetischen Materialien und piezoresistiven Polymeren konventionelle Methoden der Aktuierung und Sensorik übertreffen können. Dies gilt insbesondere in Bezug auf Nachgiebigkeit, Flexibilität und Platzanforderung. Die vorgestellten Materialsysteme und ihre Komponenten können damit als nützliche Bausteine für zukünftige Anwendungen in der Robotik und Sensorik in der Medizintechnik dienen. Während die technische Machbarkeit und eine experimentelle Evaluation demonstriert wurden, bleibt die komplexe und ressourcenintensive Entwicklung hin zu real einsetzbaren medizinischen Geräten eine herausfordernde Aufgabe zukünftiger Forschung im Feld der Medizintechnik.

Stichwörter: *Medizinrobotik, Kontinuumsrobotik, flexible Instrumente, Exoskelette, Formgedächtnislegierungen, piezoresistive Polymere, ferromagnetische Sensorik, intelligente Phantome*

Contents

Abstract vii

Zusammenfassung ix

I. Introduction 1

1. Motivation 3
- 1.1. Problem Statement 3
- 1.2. Research Question and Thesis 5
- 1.3. Scientific Contribution 6

2. Healthcare Robotics 9
- 2.1. Medical Background 9
  - 2.1.1. Abdominal Surgery: Laparoscopy 9
  - 2.1.2. Gastroendoscopy 10
  - 2.1.3. Endovascular Surgery 10
  - 2.1.4. Limitations of Minimally Invasive Procedures 10
- 2.2. Robotic Types for Healthcare 11
  - 2.2.1. Articulated Robots 12
  - 2.2.2. Continuum Robots 13
  - 2.2.3. Assistive Exoskeletons 14

3. Smart Materials 17
- 3.1. Shape Memory Alloys 18
  - 3.1.1. Shape Memory Effect 18
  - 3.1.2. Self-Sensing of Shape Memory Alloys 21
  - 3.1.3. Shape Memory Alloy Compositions in Medicine 23
- 3.2. Magnetic Materials 24
  - 3.2.1. Electromagnetic Fundamentals: Maxwell Equations 24
  - 3.2.2. Magnetic Field Quantities 25
  - 3.2.3. Magnetic Hysteresis 26
  - 3.2.4. Modeling Magnetic Fields: Coulombian Approach 27
  - 3.2.5. Hall Effect 29
- 3.3. Piezoresistive Polymers 30
  - 3.3.1. Carbon-Impregnated Composite Polymers 30
  - 3.3.2. Application of Piezoresistive Polymers 31

II. Smart Material Systems for Minimally Invasive Surgery 33

4. Self-Assembling Continuum Robots with Shape Memory Alloys 35
4.1. Tendon-Driven Continuum Robots 35
4.2. Design of an Extendable Continuum Robot 37
    4.2.1. Self-Assembly: Extension and Retraction Mechanism 37
    4.2.2. Control and User Interface 39
4.3. Experimental Evaluation 40
    4.3.1. Self-Assembly Performance 40
    4.3.2. Bending Performance 41
4.4. Towards Extendable Surgical Robots 44

5. Shaping Surgical Instruments with Shape Memory Alloys 47
5.1. Shape Memory Alloy – Actuation 47
    5.1.1. Flexible Instruments with Shape Memory Alloys 47
    5.1.2. Design of a Novel Flexible Instrument 48
    5.1.3. Experimental Evaluation of the Actuation 50
    5.1.4. Application Example: An Active Laryngoscopic Blade 53
5.2. Shape Memory Alloy – Sensing 55
    5.2.1. Self-Sensing in Shape Memory Alloys 55
    5.2.2. Shape Sensing of Flexible Instruments 56
    5.2.3. Modeling Self-Sensing Characteristics 58
    5.2.4. Experimental Evaluation of Actuation and Sensing 60
5.3. Towards Actuated Self-Sensing Instruments 65

6. A Compliant Sensor Arrays for Passive Magnetic Instrument Tracking 67
6.1. Tracking Instruments with the Human Body 67
6.2. Design of a Compliant Magnetic Sensor Array 69
    6.2.1. Sensor Hardware 69
    6.2.2. Magnetic Model 70
    6.2.3. Tracking Approach 70
    6.2.4. Bending Shape Estimation 70
    6.2.5. Path Tracking of a Magnetic Target 71
6.3. Experimental Evaluation of the Sensor Array 71
    6.3.1. Experimental Setup 71
    6.3.2. Experimental Procedure 72
    6.3.3. Bending Shape Estimation Accuracy 73
    6.3.4. Tracking Accuracy with Estimated Bending Angle 74
6.4. Towards Compliant Self-Sensing in Real-Time 75

7. Sensorized Training Platforms for Endovascular Surgery 77
7.1. Training Platforms for Endovascular Surgery 77
7.2. Design of a Sensorized Training Platform 79
    7.2.1. Phantom Fabrication 80
    7.2.2. Impact Force Sensing 81
    7.2.3. Data Processing 81
7.3. Experimental Evaluation of the Platform 81
    7.3.1. Experience and Expertise 83
    7.3.2. Learning Curve 85

7.3.3. Participant Questionnaire 87
7.4. Towards Sensorized Training Platforms with Real-Time Feedback 87

III. Smart Materials Systems for Assistive Robotics 89

8. Compliant Actuator-Sensor Units for Active Exoskeleton Interfaces 91
8.1. Light-Weight Assistive Exoskeletons 91
8.2. Design of a Compliant Actuator-Sensor Unit 93
8.2.1. Force Range Specification 93
8.2.2. Use Case Definition 94
8.2.3. Shape Memory Alloy Actuation 95
8.2.4. Capacitive Force Sensing 96
8.3. Experimental Evaluation of the Compliant Actuator-Sensor Unit 97
8.3.1. Characterization of the Shape Memory Alloy Actuator 98
8.3.2. Characterization of the Capacitive Sensor 100
8.3.3. On-Body Testing 101
8.4. Towards Integrated Exoskeleton Interfaces 102

IV. Smart Material Systems for Healthcare Applications 103

9. Critical Discussion 105
9.1. Challenges and Limitations of SMAs 106
9.1.1. Material Processing 106
9.1.2. Shape Setting of Shape Memory Alloys 108
9.1.3. Material Integration and Configuration 109
9.1.4. Stimulus and Material Response 110
9.1.5. Hazards 113
9.2. Best-Practice for Shape Memory Alloys 115
9.3. Towards SMA-Driven Healthcare Robotics 116

10. Overall Conclusion 117

V. Appendix 121

AI Utilization Statement 123

Acronyms 125

List of Variables 132

List of Tables 133

List of Figures 135

Bibliography 143

Part I.

Introduction

1. Motivation

In the ever-evolving landscape of global healthcare, the imperative for a patient-centered approach has become increasingly pronounced. The confluence of demographic shifts, technological advancements and geopolitical complexities has accentuated the need for healthcare solutions that transcend traditional boundaries. A critical challenge lies in the simultaneous surge in global population, compounded by the inevitable aging of societies [9, 10], leading to an increased amount of absolute cases of age-associated co-morbidities such as cardiovascular diseases [11] and cancer [12, 13], that require surgical treatment. This burgeoning demand for healthcare is further exacerbated by disparities in access, particularly in remote rural regions, less developed or disadvantaged areas [14] and even in conflict-ridden war zones.

1.1. Problem Statement

Amidst this growing demand, the number of clinicians [15] and caregivers [16] has not witnessed a proportionate increase. Paradoxically, the field of medicine is experiencing a trend towards deeper specialization, with an expanding array of medical disciplines and sub-specialties. This specialization, while contributing to advancements in diagnosis and treatment, may be one reason for a persistent shortage of medical professionals across all specialties. The perpetual challenge lies in delivering patient-centered care when resources are strained and medical expertise is spread thin.

Recognizing this multifaceted dilemma, a possible solution lies in harnessing technical innovation to bolster the efficiency, efficacy, and safety of healthcare delivery. As a potential panacea, imaging modalities such as computed axial tomography (CAT)[1] and magnetic resonance imaging (MRI), as well as robotics in healthcare emerge as a promising avenue to alleviate the strain on clinicians, empowering them to navigate the complex web of challenges with dexterity. By integrating robotic technologies into healthcare workflows, the augmentation of medical professionals' capabilities is aimed for, offering a scalable and adaptable solution to the global healthcare crisis. This shift towards a technologically supported healthcare paradigm holds the potential to enhance the patient experience while addressing the perpetual shortage of medical expertise across diverse settings, from the far reaches of remote regions to the uncharted frontiers of space.

The research field of healthcare robotics has been advancing towards more enhanced and integrated systems. This involves a focus on actuation and sensor technology moving towards smaller size, higher performance, increasing functionality, and reduced energy demand, all concurrently.

---

[1] CAT and computed tomography (CT) are often used as interchangeable terms.

Technological Advancements in Minimally Invasive Surgery

In particular, the growing importance of smaller and lighter robotic systems becomes evident for minimally invasive procedures. A notable benefit of minimally invasive surgery (MIS) lies in its reduced invasiveness, resulting in smaller incisions and subsequently lowering the risk of complications such as infections and bleeding. This translates to diminished pain and discomfort for patients, ultimately contributing to a swifter recovery and minimizing the extent of scarring [17]. Surgical robotic systems depend on structural and functional integrity to meet their high safety standards for incorporeal deployment. Thus, compliance and flexibility are regarded as pivotal aspects in the development of adaptable and pliable systems. This principle also holds true for the fundamental robotic components of actuation and sensing. However, traditional components such as electric motors and rigid force sensors can only partially meet these requirements, imposing limitations on scalability and miniaturization, particularly in the context of densely populated operating rooms filled with essential equipment.

Assistive Exoskeletons in Rehabilitating Mobility

In the realm of healthcare, the journey towards recovery extends far beyond the confines of the operating room. From surgical interventions to post-operative care, patients often require comprehensive measures to facilitate rehabilitation and restore independence. Traditionally, rehabilitation following surgery or injury has relied heavily on conventional approaches such as physiotherapy. These interventions are designed to facilitate recovery, improve mobility and restore functionality. However, for individuals facing significant challenges such as partial paraplegia or other mobility impairments, conventional methods may not always suffice. Furthermore, there is a constant shortage of trained (medical) workers that are required for the labor-intensive tasks of rehabilitation and daily assistance [18, 19]. Many individuals depend on devices of assistance such as simple crutches, walkers, or wheelchairs to navigate daily life and manage tasks independently. Despite their utility, these devices typically come with limitations and can hinder full participation in various activities. Assistive exoskeletons are robotic devices designed to augment human motion capabilities and provide assistance to individuals with mobility impairments. They offer a novel approach to rehabilitation. These wearable devices cater to a diverse range of users, including individuals recovering from surgery (e.g., spinal cord injury rehabilitation [20], stroke rehabilitation [21]), those with permanent disabilities [22, 23], the elderly [24, 25] and even healthy individuals working in physically demanding environments [26]. By bridging the gap between conventional rehabilitation methods and assistive devices, exoskeletons empower individuals to regain independence, improve quality of life and participate more fully in society.

Similar to the realm of MIS, exoskeletons and their mechanical components also rely on structural and functional integrity to adhere to high safety standards for on-body deployment. Therefore, compliance and flexibility are considered crucial aspects in the development of adaptable and wearable exoskeletons. This principle extends to the fundamental robotic components of actuation and sensing. As with MIS, traditional components like electric motors and rigid force sensors can only partially fulfill these requirements, imposing limitations on scalability and miniaturization, especially in contexts with limited available space and load-bearing constraints.

1.2. Research Question and Thesis

Various so-called smart materials appear promising to provide actuation and sensing capabilities to address multiple of the aforementioned challenges for both MIS and assistive exoskeletons. Confronted with the vast potential of smart materials, it must be critically assessed, to what extent smart materials can contribute to the technical challenges in healthcare technology. This may include use cases, in which smart materials enhance or even replace conventional actuation and sensing systems. While in other cases, smart materials must be discarded as alternatives due to fabrication and implementation challenges (e.g., material handling, stimuli powering, and control), as well as critical limitations (e.g., load, workspace, hazardous heat transfer, and biocompatibility). Crucial aspects of smart material deployment thus comprise the matching of material (-combinations) and suitable medical applications, where the advantages of a material outweigh the disadvantages, the efforts, and risks associated with their implementation. Therefore, this dissertation addresses the following research question:

How can smart materials be applied for robotic and sensing applications in healthcare?

This generalized research question however requires further specifications regarding the selection of smart material groups, the targeted application in the realm of healthcare robotics, as well as the technical improvement aspects in focus.

Research Focus

For this dissertation, the emphasis is placed on utilizing **smart materials**, including shape memory alloys (SMAs), ferromagnetic materials, and piezoresistive polymers. This material selection is based on their availability, scalability, and potential for economic integration. This ensures that the findings and insights of this research endeavor can be easily transferred and adapted by other researchers and professionals without requiring specialized technical infrastructure.

Furthermore, this dissertation is centered on robotic and sensing **applications** in healthcare. This particularly includes the domain of MIS, with a specific focus on laparoscopy, gastroendoscopy, and endovascular interventions. The scope is extended further to the physical recovery of patients, more specifically, the deployment of smart materials within assistive exoskeletons.

Thereby, this research focuses on leveraging the aforementioned smart materials to enhance specific **technical aspects** of robotic and sensor systems in healthcare. Key areas of focus include improving compliance, flexibility, miniaturization, and practicability compared to conventional actuators, -sensors, and -materials.

This leads to the thesis of this dissertation:

Shape memory alloys, ferromagnetic materials, and piezoresistive polymers can be applied in the realms of minimally invasive surgery and exoskeletons to improve compliance, flexibility, miniaturization, and practicability of robotic and sensing systems in healthcare.

1.3. Scientific Contribution

This dissertation delves into smart material systems, comprising three robotic systems utilizing shape memory alloys, alongside one sensor system each for ferromagnetic and piezoresistive materials (Figure 1.1). The presented smart material systems and their pre-work have been published in various, internationally renowned scientific journals, including:

- *IEEE Robotics and Automation Letters*,
- *IEEE Sensors Letters*,
- *International Journal of Computer Assisted Radiology and Surgery*,
- *Current Directions in Biomedical Engineering*,
- *at-Automatisierungstechnik*,

and presented at conferences such as:

- *IEEE-RAS International Conference on Humanoid Robots (Humanoids)*,
- *Computer Assisted Radiology and Surgery (CARS) Congress*,
- *German Society for Computer and Robot-Assisted Surgery (CURAC) Congress*.

Method of Exploration

Employing a methodical approach, all systems were meticulously crafted around the actuation and sensing capabilities of the designated materials. Through rigorous experimentation, their performance was evaluated to ascertain their applicability within the realm of healthcare robotics. A detailed description of each specific applied method is given in the respective Chapters 4–8 of this dissertation.

Contributions for the Research Community

The essential findings of this explorative dissertation shall provide the following contributions for the research community:

- **Proof-of-concept**: Feasibility examples of smart material hardware integration.
- **Practical advice** on system design, material selection, -processing, and -integration.
- **Enhancements and limitation** of deploying the selected smart materials.
- **Building blocks** of smart material actuator and sensor systems.

These contributions can offer tangible insights into the integration of smart materials, presenting a foundation for further advancements in the field of robotics and sensing in healthcare, and paving the way for future innovation and applications.

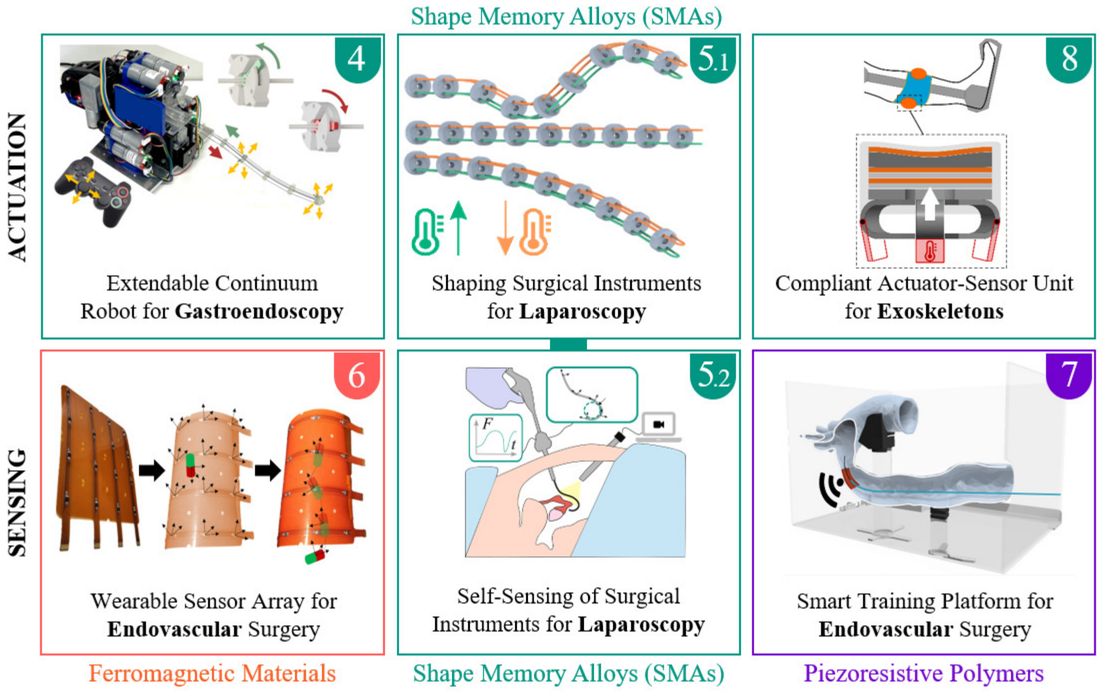
Shape Memory Alloys (SMAs)
ACTUATION
4
Extendable Continuum Robot for **Gastroendoscopy**
5.1
Shaping Surgical Instruments for **Laparoscopy**
8
Compliant Actuator-Sensor Unit for **Exoskeletons**
SENSING
6
Wearable Sensor Array for **Endovascular** Surgery
5.2
F
t
Self-Sensing of Surgical Instruments for **Laparoscopy**
7
Smart Training Platform for **Endovascular** Surgery
Ferromagnetic Materials
Shape Memory Alloys (SMAs)
Piezoresistive Polymers

Figure 1.1.: Visual abstract of this dissertation, delineating the organizational structure of this document by the sequential order of chapters through numerical labels. The contributions include three robotic systems deploying SMA-based actuation (top row), as well as three material-based sensor systems utilizing ferromagnetic materials, shape memory alloys, and piezoresistive materials (bottom row). Adapted from [1–8], 🅭🅯 4.0. and © IEEE 2023.

Organizational Structure of this Dissertation

This dissertation illuminates various application possibilities for smart materials, with a horizontal emphasis. After the motivation in Part I, the basic concepts of healthcare robotics and smart materials are introduced, including required fundamentals of smart materials in general and the material groups of SMAs, ferromagnetic materials and piezoresistive polymers, which are particularly relevant to this work. In Part II, the scientific contributions of smart material systems in the field of MIS are presented. This includes a self-assembling continuum robotic system with a superelastic SMA backbone (Chapter 4, [1]) In contrast, a more simplified and miniaturized design has been developed for hand-held applications: a flexible, SMA-driven surgical instrument (Chapter 5), capable of changing its shape [2, 3] and to inherently sense deformation through self-sensing [4]. Beyond the self-sensing of SMAs, surgical instruments can be further enhanced with ferromagnetic materials. By means of self-sensing magnetic sensor arrays, these instruments can then be intraoperatively tracked inside the human body (Chapter 6, [5]). In addition to enhancing surgical instruments, the integration of smart materials, such as in piezoresistive polymer sensors, can also augment clinical training platforms to detect force impacts (Chapter 7, [6, 7]). In healthcare, the path to recovery extends beyond surgical procedures. Many patients can benefit from exoskeleton technology during their physical recovery and for daily assistance. Hence, Part III addresses the on-body utilization of SMA actuation within the compliant physical interfaces of assistive lightweight exoskeletons (Chapter 8, [8]). This dissertation closes with Part IV and a critical discussion of the presented smart materials in the context of healthcare robotics, followed by an overall conclusion.

2. Healthcare Robotics

Healthcare can be broadly defined as the entity of services and systems that aims for maintaining, promoting and restoring people's health in a preventive, acute, or permanent manner. Thereby, medical professionals rely on a large variety of instruments and technical devices for both, diagnosis and therapeutic purposes. Robotic systems, formerly designed to improve efficiency and precision in industrial production lines, were soon to be found useful tools also in the context of healthcare[1]. In particular in MIS, where complex operating scenarios afford manual dexterity by the clinicians, these qualities show an interesting potential if carefully deployed.

This chapter introduces basic surgical concepts and the benefits of utilizing specialized robotic systems alongside conventional medical instruments.

2.1. Medical Background

In the operating room, non-invasive techniques and MIS emerge as promising alternatives to conventional open surgery, offering reduced infection risks and shorter post-operative recovery times in medical facilities [27]. Moreover, an improved cosmetic outcome is expected due to smaller scars. These benefits are realized through the utilization of specialized instruments during surgery, which can be inserted into the patient's body via natural orifices [28] (e.g., mouth, anus) or a limited number of small incisions.

In the following, the minimally invasive approaches are briefly introduced for the medical use cases addressed in this dissertation.

2.1.1. Abdominal Surgery: Laparoscopy

Laparoscopy, is a medical procedure that allows the exploration, manipulation, or repair of organs within the abdominal cavity by means of long rigid instruments which introduced through trocars into the human body. It offers a minimally invasive alternative to laparotomy, a traditional open surgical procedure involving a larger incision in the abdominal wall. This intricate surgical discipline spans a broad spectrum of procedures, encompassing gastrointestinal surgeries, liver and pancreas interventions, as well as abdominal wall reconstructions, among others. Through a meticulously performed incision, surgeons achieve entry into the abdominal cavity, enabling precise visualization and treatment of internal organs. Abdominal surgery may be necessitated by various conditions such as tumors, infections, trauma, or functional abnormalities. Further procedures include biopsies, tissue removal, organ repair, and even complex surgeries such as hysterectomy or gastric bypass. [17, 29]

---

[1] The term "medical robotics" typically refers to a surgical context. In order to extend this context towards assistive exoskeletons, the more general term "healthcare robotics" is used throughout this dissertation.

2.1.2. Gastroendoscopy

Gastroendoscopy is a minimally invasive diagnostic and therapeutic procedure within the realm of gastroenterology, primarily employed for the examination and treatment of the upper gastrointestinal (GI) tract. This technique usually requires the insertion of a flexible endoscope, a slender and illuminated tube equipped with a camera and light source, through natural body openings, typically the mouth. The endoscope is advanced through the esophagus, stomach, and duodenum, allowing real-time visualization of the mucosal lining. Gastroendoscopy serves various purposes, including the detection and biopsy of abnormalities such as ulcers, tumors, or inflammation, as well as the removal of polyps. Additionally, therapeutic interventions, such as dilation of strictures or control of bleeding, can be performed during the procedure. [30]

2.1.3. Endovascular Surgery

Endovascular surgery, a minimally invasive therapeutic technique in vascular surgery, employs catheters, guidewires, and imaging modalities to diagnose and manage vascular conditions. This technique is typically applied to pathologies affecting blood vessels, particularly arteries and veins. Unlike traditional open surgical procedures, endovascular interventions are conducted through small incisions or percutaneous access points, often in the groin or wrist, to introduce catheters into the vascular system. The catheters are then advanced under fluoroscopic guidance to the target site, where various endovascular devices, such as stents, balloons, or coils, may be deployed to address conditions such as aneurysms, stenoses, or thrombotic occlusions. [31]

2.1.4. Limitations of Minimally Invasive Procedures

Besides aforementioned benefits, MIS is not without drawbacks. For both, rigid and flexible instrumentation, the general difficulties of impaired vision [32] (e.g., limited depth perception) and the instrument handling from a remote position remain. More specifically, they include the loss of wrist articulation, diminished tactile sensation [33], and suboptimal tool ergonomics, challenging the clinicians' dexterity. Especially for laparoscopy (i.e., keyhole surgery), increased tremors and reduced accuracy may be observed, particularly during the initial stages of the learning curve of novice clinicians [34]. In this context, the so-called fulcrum effect plays a crucial role. In laparoscopic surgery, a trocar is typically placed into small incisions within the abdominal wall, creating a safe and stable access point for the instrument to be inserted into the body cavity. The fulcrum effect refers to the mechanical phenomenon where the surgical instruments are inserted through those small incisions while the abdominal wall serves as a pivot point (fulcrum). This effect creates a challenging situation for clinicians, where movements of the instrument handles outside the body result in reinforced opposite movements at the instrument tips inside the body, complicating the surgeon's manipulation and coordination [35,36].

Despite these drawbacks, continuous advancements strive to overcome limitations and elevate the overall effectiveness of minimally invasive surgical techniques across diverse surgical fields. Particularly, the promising potential of robotic innovation stands out as a key contributor to such progress [37].

2.2. Robotic Types for Healthcare

A robot is an electromechanical device designed to perform tasks autonomously or semi-autonomously, typically characterized by a capacity for programmed or teleoperated operation. Rooted in the interdisciplinary field of robotics, these machines are equipped with sensors, actuators, and a computational system, enabling them to perceive their environment, process information, and execute predefined actions. The design and functionality of robots vary widely, ranging from industrial robots employed in manufacturing processes to advanced robots engineered for intricate interactions in research, medical, or service applications. Advances in artificial intelligence, machine learning, and sensor technologies have propelled the evolution of robots, allowing for increased adaptability, learning capabilities, and enhanced human-robot collaboration. For further comprehensive insights beyond this brief introduction, refer also to [38].

Robotic technology in surgery offers a myriad of advantages that significantly enhance the overall surgical experience for clinicians. One compelling aspect is the potential for remote control, allowing surgeons to operate non-sterile and maintain an ergonomically ideal posture during extended hours in the operating room. This alleviates physical strain and enhances comfort, contributing to improved focus and performance. Additionally, robotic systems address the challenging issue of instrument handling by eliminating the need for clinicians to compensate for the fulcrum effect, as the robot assumes control of translation and rotation transmission. This not only makes the process more ergonomic for the clinician but also reduces cognitive demands. [39]

Moreover, the accuracy of robotic systems is noteworthy, as they can precisely hold and move end-effectors (i.e., instruments) to specific locations with exceptional precision. Tremor compensation further refines the precision, ensuring stable and controlled movements. The system's ability to automatically limit the safe handling area adds an extra layer of safety, preventing unintended movements and enhancing overall procedural safety. Furthermore, robots can take over assistive tasks, such as holding and manipulating the endoscope to allow for an optimized vision, or providing instruments and other equipment on demand. [40]

For this dissertation, robot types with special utility for healthcare applications are relevant. Therefore, the following section presents a selection of most relevant concepts, namely articulated robots, continuum robots, and assistive exoskeletons in further detail (Figure 2.1).

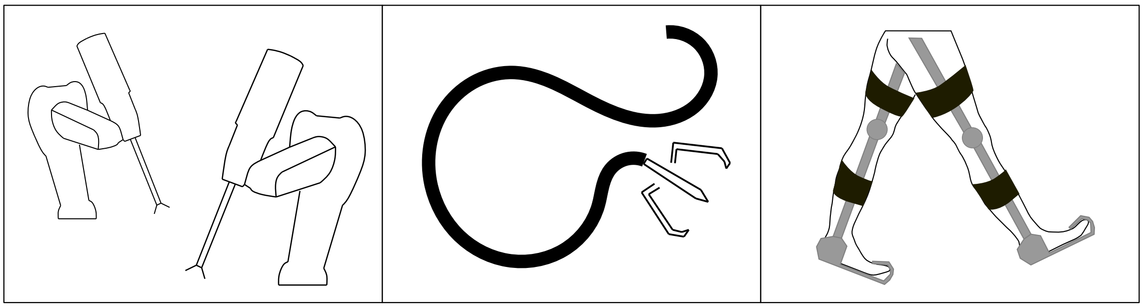

Figure 2.1.: Schematic of selected robotic types for healthcare: articulated robots (left), continuum robots (middle), and exoskeletons (right).

2.2.1. Articulated Robots

An articulated robot is a type of robotic manipulator designed with a series of interconnected segments (links) joined by rotary joints, resembling the structure of a human arm. The multiple joints provide the robot with a wide range of motion and flexibility, allowing it to articulate and move in various directions. The quantity of joints sets the degrees-of-freedom (DOF), which impacts the robot's range of motion and manipulability. At the end of the articulated robot's arm is the end-effector, a tool, or device specialized for specific applications.

These robots originally derive from industrial automation. Thus, they are widely used in industries like manufacturing (e.g., welding), assembly, and material handling due to their adaptability and ability to perform precise and complex tasks. Programming an articulated robot involves specifying the desired positions and movements of each joint to achieve the desired end-effector motion. This makes them suitable for tasks that demand high dexterity and adaptability, particularly in environments where reaching around obstacles or working in confined spaces is required. For further comprehensive insights beyond this brief introduction, refer also to [38].

Those characteristics of dexterous manipulation within confined spaces can be highly useful in the surgical context, forming the realm of surgical robotics. Relevant robotic end-effectors in the operating room can be for example surgical (e.g., grasper, retractor, electrocautery device), diagnostic (e.g., biopsy needles, swabs), and imaging related (e.g., endoscopic cameras).

Multiple articulated robotic arms can create a surgical robotic system, manipulating multiple surgical instruments and endoscopes within the body cavity for a robotic-assisted surgery. The most prevalent procedures through robotic surgery are primarily conducted in general surgery (e.g., cholecystectomy), urology (e.g., prostatectomy), and gynecology (e.g., hysterectomy) [41–43]. Yet, robotic surgery is increasingly being used in further specialties. Examples are found in orthopedics (e.g., knee-, hip replacements [44]; joint reconstruction, spine surgery [45]), otorhinolaryngology (e.g., transoral tumor resection [46, 47]), and even neurosurgery [48] (e.g., intracranial biopsies [49]).

Commercial robotic systems, deploying articulated robots for surgical interventions, include Da Vinci Robotic Surgical System (Intuitive Surgical, USA), VERSIUS Surgical System (CMR Surgical, UK), Hugo Surgical System (Medtronic, UK), and Bitrack Robotic Platform (ROB Surgical Systems, Spain).

Aforementioned systems offer a leader-follower control approach. The clinician (i.e., leader) can comfortably utilize a non-sterile, ergonomically optimized, and remote user interface (UI), featuring input modalities such as handles and pedals, while monitoring the site of operation in high-resolution stereo vision. Those inputs are then used to generate manipulation tasks of the end-effector of the surgical robotic system (i.e., follower), preventing the cognitive load of coping with the fulcrum effect. Remote in this context describes the spatial separation of the clinician from the operating table and the patient. The UI is often located within the operating room. Yet, it can be located elsewhere to perform or assist on a remote surgery through teleoperation. This possibility makes these systems appealing for deployment in far remote clinics, combat zones (military) [50], or even on space stations (aerospace) [51], where no clinician is on-site, but a surgical intervention is urgently required.

However, most of these robotic systems are not able to perform surgical tasks autonomously [52]. Yet, robotic-assisted surgery improves the patient outcome compared to conventional or open surgery [53, 54], including a reduced morbidity and mortality [55]. Furthermore, they are limited by the lack of haptic feedback. The haptic sensation of a clinician's hand when working with the various types of human tissue gives useful information, which is omitted by the robotic system in between patient and clinician. This information includes texture, density, elasticity, temperature, and any abnormalities or irregularities in the tissue. Clinicians rely on these tactile cues to make assessments during procedures, such as determining the presence of tumors, identifying healthy tissue margins, and assessing the overall condition of organs or structures being manipulated. This tactile information enhances the clinician's ability to make precise and informed decisions during surgery or other medical interventions [56]. While there are concepts of creating an artificial haptic feedback experience for the clinician using sensor on the instruments and actuators on the UI, the development of a realistic perception that can be effectively integrated into commercially available surgical robotic systems remains an ongoing challenge [57]. In addition, the end-effector instruments of articulated robots are usually long and rigid, and thus comparable to conventional laparoscopic instruments. Yet, the tip of the end-effector can feature the same DOF as the clinician's hand (e.g., Da Vinci Robotic Surgical System), allowing for a smooth translation of dexterous motions from the clinician's hands to the surgical tool tip. Still, the effective workspace within the body cavity remains restricted due to the rigid tools. Obstacles or delicate anatomical structures (e.g., in neurosurgery) often cannot be bypassed in straight trajectories, which makes more incisions necessary, weakening the advantages of the minimally invasive approach.

2.2.2. Continuum Robots

In order to overcome the drawbacks of rigid kinematic chains and tools, continuum structures and flexible instruments are becoming more popular in the field of surgical robotics. Continuum robots are snake-like, deformable manipulators with an infinite number of joints, enabling smooth bending and twisting motions [38]. However, their design and control pose challenges due to their hyper-redundant nature, where the number of DOF exceeds the count of individually controllable actuators [58]. Continuum robots contribute to expanding the user's scope and operational space, especially in challenging-to-access operation sites. This includes navigation within the human body, such as winding organs in the gastrointestinal tract, as well as in neurosurgery, where intricate paths must be taken to avoid critical structures [59].

More specifically, a flexible instrument can be characterized as a simplified continuum robot featuring a pliable or bendable component and less DOF (1–2 bending axes) than a continuum robot, frequently employed in medical procedures to navigate through confined spaces while minimizing tissue trauma. Although the flexibility of such an instrument does not necessarily imply continuous deformation, it caters to specialized applications like endoscopy and minimally invasive surgical tools. Notably, within the context of this dissertation, the concept of a flexible instrument leans towards a handheld device [60] rather than a remotely controlled robotic component. Handheld devices allow for direct haptic experience of the clinician. Therefore, such devices must be very compact and low-weight to be a real benefit to the user.

Commercially available continuum robot systems for surgery include the Monarch (Johnson & Johnson MedTech, USA) for bronchoscopy, and the Niobe Robotic Magnetic

Navigation System (Stereotaxis, USA) for endocardial catheter ablation and gastrointestinal capsule endoscopy.

Flexibility and Compliance

In the robotic field, both terms “flexible” and “compliant” refer to the mechanical characteristic of a robotic component or an entire robotic structure which can adapt their shape, e.g., when traversing within the human body. Thus, the risk of damaging anatomical structures is highly reduced by flexibility and compliance in comparison with rigid robotic components when interacting with human tissue [61]. To be precise in their distinction, flexible structures can be deformed and retain a new shape. In contrast, compliant structures elastically deform under external force and pressure. Upon removal of these external factors, compliant structures revert to their original shape. Both traits represent coveted attributes of smart material systems in the context of robotics and sensing in healthcare. Consequently, they serve as focal points throughout this dissertation.

Targeted Limitations of Continuum Robotic Systems

Common actuation methods for continuum robot devices encompass pneumatic, hydraulic, electromagnetic, and tendon drives [62]. Hence, they typically necessitate substantial actuation setups, such as fluid pumps and valves for pneumatic and hydraulic systems, or multiple electric motors for tendon manipulation. Consequently, achieving the desired downsizing of the robotic structure towards smaller diameters, greater lengths, and larger bending angles is constrained. Thus, for usage of controllable and flexible continuum robotic devices for MIS, these aspects of design and performance remain key [2]. Smart materials can play a major role in enhancing continuum robotic devices and optimizing their spatial footprint by introducing novel actuation strategies, deploying the robotic structures themselves, as presented in Chapter 4 and Chapter 5.

2.2.3. Assistive Exoskeletons

Exoskeletons are assistive wearable robotic systems. They are utilized to augment the performance of individuals with varying needs, including the injured, impaired, or those seeking to enhance their physical abilities. Exoskeletons can be categorized into two primary types: passive and active.

Passive exoskeletons provide mechanical assistance without the need for active, external power sources, relying on springs, dampers, or other mechanisms to support specific body parts. They store energy temporarily in order to reduce load and effort for the user. For the lower limbs, passive foot-leg exoskeletons assist the user, e.g., during normal gait cycles [63] and can help to avoid foot drops, keep the user from falling [64]. In contrast, for the upper limb, passive exoskeletons can support during over-head work [65]. Active exoskeletons, on the other hand, integrate powered actuators and sensors to dynamically enhance human performance, offering adjustable assistance tailored to the user’s movements and requirements. Many systems for rehabilitation of the lower-limbs are wired and therefore stationary, as they require a power source [66]. However, batteries are becoming increasingly powerful, enabling exoskeletons to be further developed for mobile applications, regardless of a cable. This improvement is in particular important for gait-assistive exoskeletons [67, 68].

Assistive exoskeletons can support various extents of the human body parts, ranging from hand exoskeletons, which assist in tasks requiring precise dexterity [69–71], up to full-body lightweight exoskeletons designed to support a range of wide motions while minimizing additional weight [72, 73]. Additionally, there are heavyweight exoskeletons capable of carrying the entire body, providing support for individuals with severe impairment (e.g., paraplegia) or for workers facing heavy-duty tasks [74, 75].

Targeted Limitations of Exoskeletons

The development of exoskeletons faces challenges, notably in securing sufficient mobile power supplies for extended wear and safely handling heavier loads. These hurdles often lead to increased weight and bulkiness, reducing practicability, especially for elderly or impaired users. Ensuring proper fit and alignment with the wearer's body is vital to prevent misalignment issues that may harm joints [76]. Addressing these challenges with smart materials promises to improve mobility and enhance quality of life for individuals with varied needs (Chapter 8).

Chapter Summary

In this Chapter 2, the fundamental principles of MIS were introduced, accompanied by a brief overview of the pertinent medical specialties covered in this dissertation: laparoscopy, gastroendoscopy, and endovascular surgery. Furthermore, the chapter outlined the key elements of healthcare robotics, including major robotic types such as articulated robots, continuum robots, and assistive exoskeletons. This discussion laid the necessary groundwork for comprehending the subsequent scientific contributions.

3. Smart Materials

Smart materials form a group of novel materials, which show deterministic and repeatable material responses (i.e., property changes) due to external stimuli. These materials are also referred to as stimuli-responsive, intelligent materials, active materials, and (multi-) functional materials [77].

Example stimuli include electric current, electric voltage, light, or heat that provoke significant material responses such as a macroscopic deformation and acting forces that can be deployed for robotic actuation. Unlike conventional actuation methods (e.g., electric motors, combustion engines, fluid pumps), the material itself becomes the actuator besides its purpose of structural-mechanical integrity. Conversely, one of the aforementioned external stimuli can also alter internal properties, such as the electric resistance. Smart materials with such a behavior could then be suitable for a multitude of sensor applications. Such extraordinary behavior allows potentially for further compliance, flexibility, miniaturization, and practicability beyond the known limits of conventional actuator and sensor components.

Important smart materials are found in various material groups such as metals, polymers, ceramics, biomaterials, and composites. Piezoelectric ceramics are some of the most popular and widely used smart materials. When their crystal lattice is mechanically deformed, an electronic potential is measured on its surface. Those ceramics are already fairly understood and thus widely commercially used as rigid actuators [78] or sensors [79]. Piezoelectric polymers demonstrate similar effects and potentials while providing a mechanically more flexible form [80]. Piezoresistive polymers, on the other hand, sense mechanical deformation in soft robotic applications as their electric resistance depends on the strain [81]. Further compliant materials are electroactive polymers that show mechanical bending deformation when electric voltage is applied [82], thus they are generally suitable for compact intrinsic actuation. Shape memory polymers exceed those capabilities by being able to memorize a specific, pre-set shape when heated after almost arbitrary mechanical deformation [83]. A similar temperature-induced behavior is known from SMAs where a phase change in the crystal lattice of the metal alloy leads to the phenomena of the shape memory effect and superelasticity [77]. Although already widely in use (and being deployed in some types of electric motors), magnetic materials can also be considered smart materials in a broader sense. Exposed to an external magnetic field as stimulus, magnetic materials will respond with some sort of realignment.

This overview has offered a concise and comprehensive overview of smart materials within the context of this dissertation. In the following sections, the fundamentals of SMAs, piezoresistive polymers, and magnetic materials are elaborated upon, as these materials are particularly pertinent to the applications discussed in this dissertation.

3.1. Shape Memory Alloys

SMAs are a class of thermo-responsive metallic materials that can exhibit a unique ability to return to a predetermined, original shape or form. This is referred to as the shape memory effect. This effect can be utilized in order to create superelastic medical devices, miniaturized structural machine elements, and material-driven actuators. Furthermore, some of these alloys exhibit a self-sensing capability alongside their shape memory.

This dissertation presents three different smart material systems based on SMAs which exploit the property of superelasticity (Chapter 4), shape memory actuation (Section 5.1, Chapter 8), and self-sensing (Section 5.2.1). Hence, this following Section 3.1 provides the required theoretical background for the reader, to fully understand the technical details of these presented smart material systems.

Crystal Structures of Metals and Alloys

The thermo-mechanical characteristics of metals and alloys depend on their crystalline structure. Different phases are created during the processing of the material that influence the material behavior. Two primary phases, high-temperature austenite (A) and low-temperature martensite (M), play a crucial role in the structural transformations of materials and thus for the shape memory effect. The parent austenite phase is characterized by a cubic structure. When martensite forms from austenite, its crystallographic structures vary based on composition or the addition of alloying elements (Figure 3.1). For instance, the introduction of alloying elements like copper (Cu) or lead (Pb) can induce a transformation in the martensite structure, changing it from monolithic to orthorhombic. Alternatively, it may lead to the formation of an intermediate R-phase with a rhombohedral structure, playing an important role for the self-sensing ability of the material [77].

This brief general introduction of the crystal structures of metals and alloys shall be sufficient to understand the following sections, where the major smart material properties of SMAs are introduced. For further comprehensive insights, refer also to [84].

3.1.1. Shape Memory Effect

The shape memory effect of SMAs occurs as the one-way shape memory effect, the two-way shape memory effect, and the phenomenon of superelasticity (i.e., pseudoelasticity).

One-Way Shape Memory Effect

Kumar and Lagoudas present a comprehensive introduction to the shape memory effect in [77]. Following the authors, the shape memory effect in a SMA manifests when the alloy undergoes deformation in the twinned martensite phase and is subsequently unloaded at a temperature below the austenite start temperature (A_s). Upon heating above the austenite finish temperature (A_f), the SMA reverts to its original shape by transforming back into the austenite phase. A thermo-mechanical loading scenario in a combined stress-strain-temperature space is depicted in Figure 3.1. The uniaxial stress σ due to an applied load is presented over the strain ε which corresponds to the change in length, normalized by the original length. The cycle begins with the austenite phase at an elevated temperature (A), followed by stress-free cooling (blue) below the martensite start temperature M_s and martensite finish temperature M_f, leading to the formation of twinned martensite (B). When the twinned martensite experiences an applied stress surpassing the start stress level σ_s, the reorientation process begins, causing certain favorably oriented martensite variants to grow at the expense of less favorable ones. A_s, A_f, M_s, and M_f are also referred to as transition temperature levels. The detwinning process concludes at a stress level σ_f, identified by the end of the plateau in the $\sigma - \varepsilon$ diagram. The material is then elastically unloaded (C to D), preserving the detwinned martensite state. Upon heating (red) without stress, the reverse transformation begins at temperature A_s (E) and completes at temperature A_f (F), where only the austenite phase exists. In detwinning without permanent plastic strain, the SMA returns to its original shape (A). The recovered strain from detwinned martensite to austenite, termed transformation strain $\varepsilon_{\text{trans}}$, enables the reinitation of self-accommodated twinned martensite variants during cooling. This cycle repeats the complete shape memory effect process. This is referred to as the one-way shape memory effect. The shape recovery occurs only during heating after the material has been detwinned due to an applied mechanical load (i.e., cold-formed). It is noteworthy, that SMAs exhibit a hysteresis [85] in their material response over temperature rise and fall (Figure 3.2). This nonlinear behavior is typical for SMAs and makes modeling and control challenging.

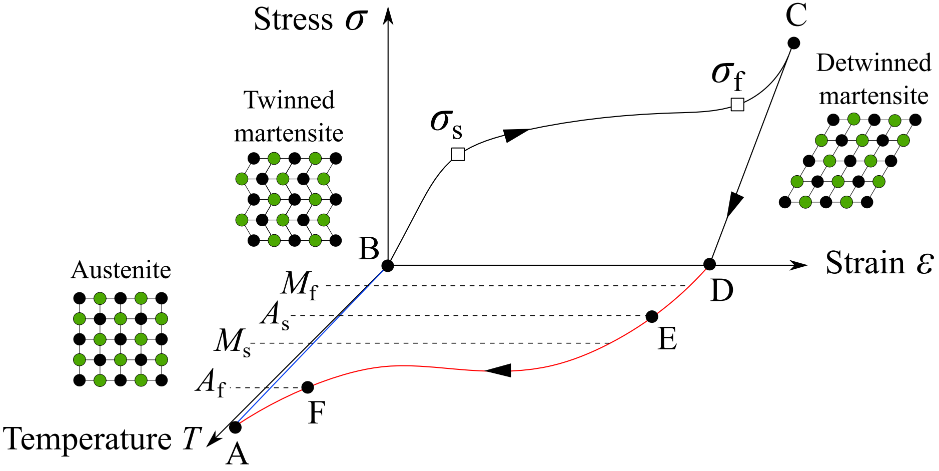

Figure 3.1.: A typical stress-strain-temperature behavior illustrating the shape memory effect for a typical SMA. The different crystalline structures of austenite and martensite are schematically indicated. Adapted from [77].

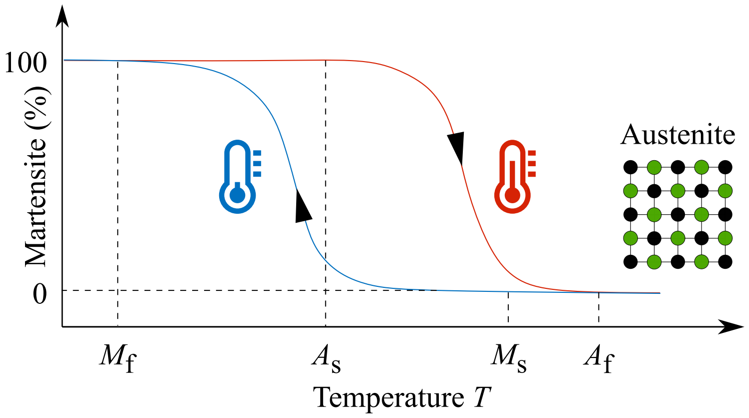

Figure 3.2.: Typical hysteresis response of SMA. The crystalline composition exhibits nonlinear changes with temperature.

Two-Way Shape Memory Effect

In addition to the one-way shape memory effect, also a two-way shape memory effect can be observed. This effect becomes apparent in an SMA material that has undergone repeated thermo-mechanical cycling along a loading path, also referred to as material training. In such a training, repeating cycles along a path over numerous cycles can induce changes in the microstructure, leading to macroscopically observable permanent alterations in the material's behavior. The changes are due to defects in the microstructure, which result in residual internal stress. This state facilitates the formation of preferred martensite variants when the SMA is cooled without external loads. As a consequence, it can be observed that the material will remember its austenite shape when heated and find back to the trained martensite shape autonomously and without applying external stress, i.e., cold forming [77]. It should be noted that any modification to the internal stress state, such as aging at high temperature or mechanical overload, can alter and compromise the two-way shape memory effect [86].

Figure 3.3 depicts a typical transformation cycle of a simple SMA wire with an original bent shape in the austenite, hot temperature phase (left). When cooling down, a phase change is observed from austenite towards twinned martensite but without a change of the bent shape (top). In the cold state, the SMA wire is plastically straightened by an external stress, leading to the creation of detwinned martensite (right). From there, increasing the temperature triggers the one-way shape memory effect, changing the phase back to austenite and bending the SMA wire back into its original shape. In contrast, after many thermo-mechanical training cycles, the two-way shape memory effect will perform the phase change without any external stress, cold-forming the bent shape into the straight shape by itself (pink).

For this dissertation, the two-way shape memory effect was not explicitly investigated or intentionally exploited. Yet, unintentional training effects were observed and are discussed in Chapter 5.

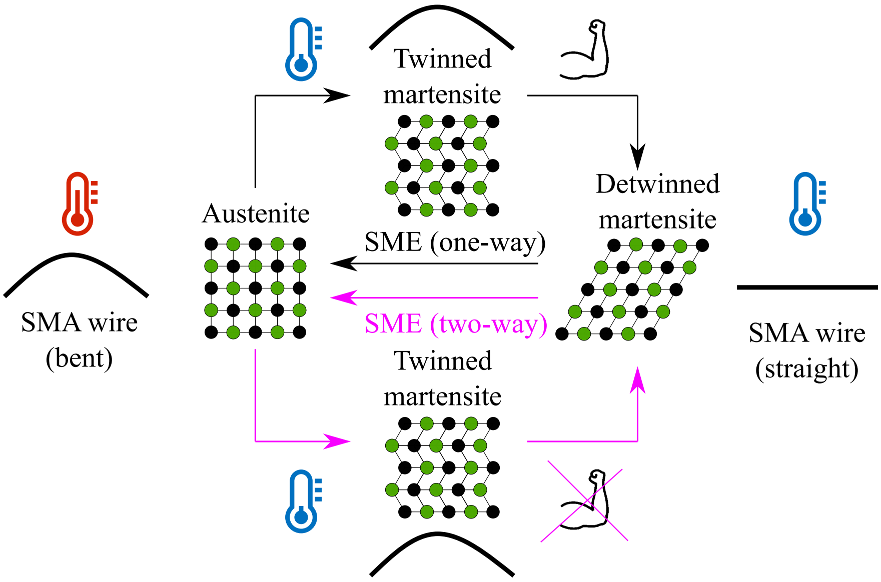

Figure 3.3.: Schematic of a typical transformation cycle of a simple SMA wire with an original bent shape in the austenite, hot temperature phase (left), and a targeted straight shape for the martensite phase (right). The one-way shape memory effect (SME) is indicated with black arrows, while the two-way shape memory effect is shown in pink. The two-way shape memory effect does not require external cold-forming.

Superelasticity

For load-induced deformations above the austenite finish temperature A_{f}, the effect of shape restoration is observed immediately after the load is taken away (Figure 3.4). For SMAs with austenite finish temperatures A_{f} below room temperature, this behavior might appear permanent and temperature-independent for the observer, since it does not require an additional heat stimulus that would increase the material temperature in addition to the object being exposed to an environment at standard room temperature ($\approx 20\,^{\circ}\mathrm{C}$). For the observer, this phenomenon may appear like an elastic behavior. Yet, the material response originates in the aforementioned crystalline phase shifts. Thus, this effect is also referred to as "pseudoelasticity" [87, 88]. Another common term is "superelasticity", since the extent of apparently elastic deformation exceeds the one of conventional metal or alloys. Consequently, this effect can be useful, where the mechanical characteristics of a metal are desired (e.g., hardness, durability) while the object should remain pseudoelastically deformable.

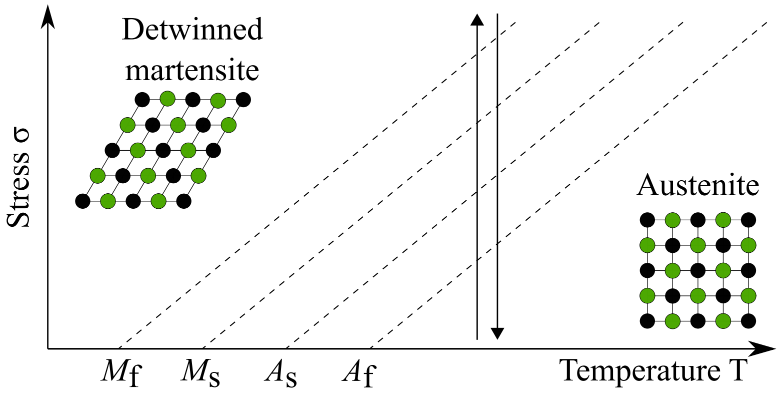

Figure 3.4.: Typical pseudoelastic behavior of a SMA when deformed under external stress above austenite finish temperature A_{f}. The material undergoes stress-induced phase changes at a constant temperature. Adapted from [77].

3.1.2. Self-Sensing of Shape Memory Alloys

In addition to shape memory actuation, SMAs also show potential to be used as sensors, either as sensor-actuator switches or as inherent strain sensors.

Sensor-Actuator Switch

In this sensor application, the SMA component is used as a temperature sensor for a preset temperature threshold (i.e., austenite finish temperature A_{f}). Once the outer temperature exceeds this threshold, the SMA component is actuated and deforms due to the shape memory effect (Section 3.1.1). Thus, the component acts like a switch, e.g., opening or closing valves in order to cool the medium down again. [89]

Inherent Strain and Shape Sensing

For certain SMAs, such as alloys based on nickel (Ni) and titanium (Ti), there exists a correlation between electric resistance R, temperature T, and strain ε in a conductive material where the voltage U is applied and the current I flows

$$R = \frac{U}{I}. \tag{3.1}$$

Following Lynch *et al.* in [90], the resistance is also dependent on the conducting material as in

$$R = \frac{\rho l}{A} \tag{3.2}$$

with the cross-sectional area A, and the length l. The correlation of dimensional change and resistance change can be written as in [91] as

$$\frac{\Delta R}{R_0} = (1 + 2\upsilon)\varepsilon + \frac{\Delta\rho}{\rho_0} \tag{3.3}$$

with the reference resistance R_0, the Poisson's ratio υ, the (thermo-responsive) strain $\varepsilon(T)$, the resistivity change $\Delta\rho$ in relation to a reference resistivity ρ_0. The variables can be written as resistance change

$$\Delta R = R - R_0 \tag{3.4}$$

and the resistivity change, respectively,

$$\Delta\rho = \rho - \rho_0. \tag{3.5}$$

Furthermore, the resistivity is temperature-dependent, stated in

$$\rho(T) = \rho_0 \left(1 + \alpha_T(T - T_0)\right) \tag{3.6}$$

where the temperature coefficient α_T, the temperature reference T_0 and the resistivity at the temperature reference ρ_0.

Due to the thermo-responsive nature of the shape memory effect, the strain ε (Equation 3.3), and the resistivity ρ (Equation 3.6) will both be influenced by a change in temperature T. However, this only holds true for an SMA object in one single crystalline phase. Yet, to describe an object undergoing phase changes in an actuation cycle, the shares of the different phases must be considered using

$$\rho = \rho_{\mathrm{A}}(1 - \xi_{\mathrm{M}} - \xi_{\mathrm{R}}) + \rho_{\mathrm{M}}\xi_{\mathrm{M}} + \rho_{\mathrm{R}}\xi_{\mathrm{R}} \tag{3.7}$$

with the crystalline fractions of martensite ξ_{M}, of the R-phase ξ_{R} and the resistivities of austenite phase ρ_{A}, martensite ρ_{M}, and the R-phase ρ_{R} , respectively. Lynch *et al.* further underline the influence of the applied stress σ to the material since it affects both the resulting strain (Equation 3.2), and the phase transformation temperatures and thus the distribution of crystalline fractions (Equation 3.7). As a consequence, the relationship between strain ε and electric resistance R is nonlinear, in contrast to the linearity of the single-phase material behavior [92].

Despite the nonlinearity of the self-sensing effect, SMAs have significant potential for simplified, integrated, scalable, and customized actuation and sensing in various robotic applications.

3.1.3. Shape Memory Alloy Compositions in Medicine

Various alloys exhibit a shape memory and are thus able to “recover large inelastic strains under relatively high stress levels” [93]. The characteristics of the shape memory (e.g., transition temperatures, hysteresis) are thereby influenced by the alloy components and their quantity, alongside with parameters of the fabrication process. For example, iron based alloys (e.g., FeNiCoTi, FeMnSi) are inexpensive and allow for relatively simple processing (i.e., formability, machinability). Copper-based alloys (e.g., Cu-Zn, Cu-Al) add high conductivity to the set of characteristics, making it more suitable for applications where the material is meant to conduct electric current or heat more efficiently, in comparison with iron materials. [77]

Superelastic Implants and Devices from NiTi

The integration of SMAs across diverse medical specialties has made significant advancements since the 1980s [94]. This progress is particularly notable in the field of endovascular surgery. This innovation primarily stemmed from the unique properties of SMAs, notably their superelasticity, which presents a significant advantage over traditional stainless steel alloy implants [95]. The superelasticity enables easier collapse and insertion of implants into a catheter, subsequently deployed in vascular branches as expandable implants (e.g., stents). Moreover, compared to polymer-based implants [96], SMAs exhibit improved mechanical properties, offering enhanced strength and durability. These attributes have led to their widespread acceptance in clinical practices.

Nickel-titanium-based alloys, specifically nickel-titanium (NiTi), stand out as the preferred shape memory material for (superelastic) medical applications due to their exceptional combination of properties. In comparison to aforementioned material groups in and outside the shape memory domain, NiTi demonstrates remarkable biocompatibility and corrosion resistance [97], making it well-suited for implantable medical devices (e.g., endovascular stents). Furthermore, it comes with a superelastic strain of up to 13% [98], useful for e.g., endovascular guide wires and retrieval devices. Besides, NiTi has been utilized in orthodontics to move and hold teeth in targeted positions [99].

Shape Memory Actuation of NiTi

The addition of copper to NiTi alloys has been explored for its advantageous effects, such as the reduction of pseudoelastic hysteresis and maximum strain in nickel-titanium-copper (NiTiCu). In contrast, TiNiCu containing 5% < Cu(at[1]%) < 10% is being particularly preferred for actuators [77].[2] SMAs in the form of NiTi-wires can yield a superior power-to-weight ratio compared to traditional electric motors. They offer a far simpler implementation compared to other smart materials like electroactive polymers and permit larger displacements than piezoceramics [100]. Within actuators, SMA wires can serve even as quasi-elastic components or dampers [101], leveraging their superelastic strain. Additionally, they facilitate linear motion and can generate repeatable strains of over 5% [77, 102] when heated through conduction or Joule heating. Yet, also more enhanced motion modalities such as complex shape changes are feasible. Although of high interest for the field of health care robotics, such have hardly been investigated so far.

---

[1] Abbreviation for atomic percentage (at).

[2] For this dissertation, ”SMA” is used synonymously for alloys containing mainly Ni and Ti.

3.2. Magnetic Materials

Magnetism is a fundamental force of nature that manifests in various phenomena such as attraction, repulsion, and the torque-induced reorientation of magnetic materials when exposed to magnetic fields. Magnetic fields derive from either electric currents or magnetic materials. Various types of magnetic materials exhibit distinct behaviors in response to an external magnetic field. These magnetic materials are: diamagnetic (repelling), paramagnetic (weakly attracted), and ferromagnetic materials (strongly attracted). [103]

Ferromagnetic materials are particularly interesting for the scope of this dissertation, since they react stronger when exposed to an external magnetic field than the aforementioned magnetic materials. Furthermore, ferromagnetic materials become permanently magnetized in an external magnetic field. More specifically, they retain a magnetic field even after the external field disappears and hence become the source of a magnetic field themselves (i.e., spontaneous magnetization).

Due to these properties, ferromagnetic materials can enhance surgical instruments, making them permanently magnetic. These instruments can then be tracked within the human body without conventional medical imaging technology (e.g., MRI, CT). Instead, sensor systems based on less complex, magnetically sensitive Hall sensors can detect and track the ferromagnetically augmented surgical instrument.

A smart material sensor system to track ferromagnetic surgical instruments was developed within this dissertation, as presented in Chapter 6. Hence, this following Section 3.2 provides the required theoretical background concerning magnetism, ferromagnetic materials, and Hall sensors.

3.2.1. Electromagnetic Fundamentals: Maxwell Equations

While magnetism might initially seem like an isolated physical phenomenon, it is intricately linked to electricity, forming what is known as electromagnetism. This relationship is elucidated by Maxwell's equations [104], which succinctly describe four fundamental mathematical formulas governing the behavior of electromagnetic fields and phenomena.

The Gauss's law for electricity describes the electric field (flux) $\boldsymbol{E}$ through a closed surface as proportional to the total electric charge, defined by the electric charge density ϱ and the permittivity in vacuum ϵ_0. It can be written as

$$\nabla \cdot \boldsymbol{E} = \frac{\varrho}{\epsilon_0}. \tag{3.8}$$

In contrast, the Gauss's law for magnetism states the absence of divergence of a magnetic field (flux density) $\boldsymbol{B}$, enforcing its field lines into closed loops and forbidding the existence of magnetic monopoles. It can be written in the form of

$$\nabla \cdot \boldsymbol{B} = 0. \tag{3.9}$$

The Faraday's law of electromagnetic induction correlates the rate of change of a time-varying magnetic field $\boldsymbol{B}$ with a corresponding curl of an electric field $\boldsymbol{E}$ in the form of

$$\nabla \times \boldsymbol{E} = -\frac{\partial \boldsymbol{B}}{\partial t}. \tag{3.10}$$

Finally, the Ampère's law with Maxwell's addition relates the curl of the magnetic field $\boldsymbol{B}$ to the sum of the electric current density $\boldsymbol{J}$ and the rate of change of the time-variant electric field $\boldsymbol{E}$. It can be written as

$$\nabla \times \boldsymbol{B} = \mu_0 \left(\boldsymbol{J} + \epsilon_0 \frac{\partial \boldsymbol{E}}{\partial t} \right) \tag{3.11}$$

where μ_0 is the vacuum permeability.

The latter two Maxwell Equations 3.10 and 3.11 clearly state that electric and magnetic fields condition each other. This understanding is important for the development and implementation of magnetic applications in the medical field, where other electromagnetic devices, such as surgical equipment (e.g., electrocauterization) and imaging devices (e.g., MRI), can cause strong electromagnetic interferences. For further comprehensive insights, refer also to [105].

3.2.2. Magnetic Field Quantities

This section focuses on magnetostatics as presented by Coey *et al.* in [103], addressing only magnetic fields created by static distributions of magnetic moments $\boldsymbol{m}$ and without time dependence.

In solid-state magnetism, the fundamental unit is the magnetic moment $\boldsymbol{m}$ (i.e., dipole moment), which arises from electron spins and orbital motions around nuclei. Although nuclei also possess spin, their magnetic moments are much smaller compared to electrons. Hence, they can be neglected in many scenarios. For ferromagnetic and paramagnetic materials, the magnetic dipoles rearrange according to external magnetic fields and reinforce them [106]. In contrast, diamagnetic materials do not exhibit permanent magnetic dipoles on an atomic level [107].

A local, steady, and homogenous mesoscopic average magnetization $\boldsymbol{M}_{\mathbf{mes}}$ can be defined as

$$\boldsymbol{M}_{\mathbf{mes}} = \frac{\mathrm{d}\boldsymbol{m}}{\mathrm{d}V} \tag{3.12}$$

with the time-averaged magnetic moment $\mathrm{d}\boldsymbol{m}$ and a mesoscopic volume $\mathrm{d}V$.

In order to obtain a macroscopically relevant quantity of magnetization $\boldsymbol{M}$, the average is calculated, using the mesoscopic average magnetization over all volume domains of a magnetic object. The magnetization $\boldsymbol{M}$ allows then the modeling of a ferromagnetic or paramagnetic object as an entity, which can be exposed to and magnetized by an auxiliary $\boldsymbol{H}$-field, and which becomes the source of a $\boldsymbol{B}$-field. Both the primary $\boldsymbol{B}$-field and the auxiliary $\boldsymbol{H}$-field are frequently referred to as "magnetic fields". The $\boldsymbol{B}$-field (i.e., magnetic flux density, magnetic induction) is measured in units of tesla (T), where $1\mathrm{T} = 1\mathrm{Wb\ m}^{-2}$. In contrast, the $\boldsymbol{H}$-field is also referred to as the magnetic field intensity, magnetic field strength, as well as the magnetizing and demagnetizing field, respectively. Its unit is $\mathrm{A\ m}^{-1}$.

In general, the $\boldsymbol{B}$-field and the auxiliary $\boldsymbol{H}$-field of a magnetic object can be correlated in vacuum, as

$$\boldsymbol{B} = \mu_0 \boldsymbol{H}. \tag{3.13}$$

Hence, both fields are almost identical in free space. When combined with a uniformly magnetized object causing an additional magnetic $\boldsymbol{M}$-field, the equation extends to

$$\boldsymbol{B} = \mu_0 (\boldsymbol{H} + \boldsymbol{M}). \tag{3.14}$$

Within the magnetic object, both the $\boldsymbol{B}$-field and the auxiliary $\boldsymbol{H}$-field can deviate strongly from each other and even point in opposite directions (e.g., in permanent magnets). It should be noted, that unlike the solenoidal $\boldsymbol{B}$-field ($\nabla \cdot \boldsymbol{B} = 0$), the $\boldsymbol{H}$-field is defined as conservative with sources and sinks ($\nabla \times \boldsymbol{H} = 0$).

3.2.3. Magnetic Hysteresis

The crucial practical characteristic of any ferromagnetic material lies in its nonlinear response of magnetization $\boldsymbol{M}$ to an external magnetic field $\boldsymbol{H}$, as rendered in its hysteresis. In essence, the retention of magnetization even in the absence of an external magnetic field enables the ferromagnetic material to act as a self-sustaining magnet, rendering it suitable for various technical applications.

Figure 3.5 presents a typical hysteresis loop starting from an initial demagnetized state ($M = 0$) and in the absence of any auxiliary field ($H = 0$). The application of an external magnetic field H then leads to an increase in magnetization, altering, and eventually eradicating the microstructure of ferromagnetic domains previously magnetized in different orientations. This process continues until reaching a saturation magnetization of M_{sat}. Upon removal of the applied magnetic field, a residual magnetization M_{r} remains in the material, also referred to as remanence. The coercivity H_{c} is indicated on the loop, representing the reverse field required to nullify the magnetization. [108]

The hysteresis loop offers valuable insights into the magnetic properties of ferromagnetic materials and their response to external fields. It allows classifying ferromagnetic materials into hard and soft materials. Hard materials, such as the rare-earth elements neodymium (Nd), samarium (Sm), and praseodymium (Pr), present a stronger resistance against demagnetization when exposed to a demagnetizing external magnetic field, correlating with a relatively high coercivity H_{c} [109]. These hard magnetic materials find applications in permanent magnets. In contrast, soft ferromagnetic materials, such as iron (Fe), cobalt (Co), and Ni, as well as various of their alloys, exhibit relatively lower coercivity H_{c}. Hence, they and are more easily magnetized and demagnetized, often used in electromagnetic devices and transformer cores [110].

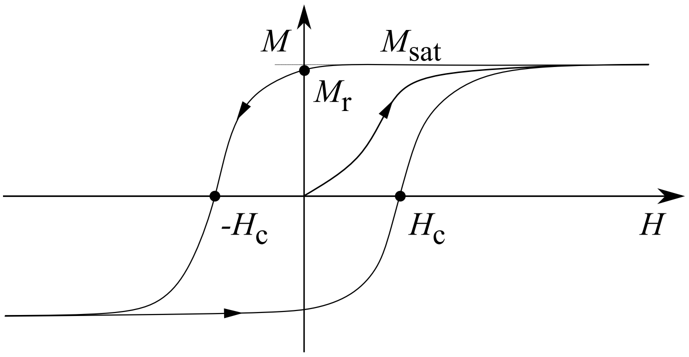

Figure 3.5.: Typical hysteresis loop of a ferromagnetic material. The ferromagnetic object is exposed to an external magnetic field $\boldsymbol{H}$ until it reaches saturation magnetization M_{sat}. Upon removal of the external field, the magnetization decreases but retains a residual magnetization M_{r}. H_{c} denotes the reverse field needed to cancel magnetization (coercivity). Adapted from [103].

3.2.4. Modeling Magnetic Fields: Coulombian Approach

Multiple ways are known, to calculate the magnetic fields deriving from a magnetized object. Following Coey *et al.* in [103], three major alternatives should be considered:

- **Dipole** approach for $\boldsymbol{B}$ with distribution of magnetization $\boldsymbol{M}$.
- **Ampèrian** approach for $\boldsymbol{B}$ with distribution of current density $\boldsymbol{j_{\mathrm{m}}}$.
- **Coulombian** approach for $\boldsymbol{H}$ with distribution of magnetic charge q_{m}.

While the dipole model is the simplest of the aforementioned approaches, and thus easy to efficiently implement, it is less accurate in proximity to and within the magnetic object compared to alternatives [111]. In contrast, the Ampèrian approach can calculate accurately the $\boldsymbol{B}$-field in the entire observed space. Yet, the Coulombian approach provides the same for the $\boldsymbol{H}$-field, but in a computationally more efficient regime [103]. It is therefore the chosen approach for this dissertation in Chapter 6, and described in the following in further detail as derived by Coey *et al.*

Coulombian Approach

Magnetic charges q_{m} are considered the magnetic analogy of electric charges. However, in contrast to their electric counterpart, magnetic charges are hypothetical monopoles, representing sources and sinks of the magnetic fields, and which have never been observed in nature. Hence, they are explicitly ruled out by Gauss's Law of magnetism for the $\boldsymbol{B}$-field (Equation 3.9). Yet, the concept of magnetic charges can be useful to model the $\boldsymbol{H}$-field in its surrounding. At a point P from the origin O and the position vector $\boldsymbol{p}$, the $\boldsymbol{H}$-field of a spherical magnetic charge q_{m} can be described with

$$\boldsymbol{H(p)} = \frac{q_{\mathrm{m}}\boldsymbol{p}}{4\pi p^3}. \tag{3.15}$$

When modeling a permanent magnet in a cylindrical shape, the magnetic charges are considered in the entire magnetic material. Figure 3.6 depicts a simplified magnet model of such a shape, utilizing the Coulombian approach. This is accounted for by utilizing the magnetic charge density ρ_{m} and integrating the term in Equation 3.15 in respect to $\boldsymbol{p}'$ as in

$$\boldsymbol{H(p)} = \frac{1}{4\pi}\int_V \frac{\rho_{\mathrm{m}}(\boldsymbol{p}-\boldsymbol{p}')}{\|\boldsymbol{p}-\boldsymbol{p}'\|^3}\mathrm{d}^3p'. \tag{3.16}$$

The magnetic charges and their field components are further subdivided into charge densities within the magnetic volume ρ_v and on the surface ρ_s, leading to

$$\boldsymbol{H(p)} = \frac{1}{4\pi}\left(\int_V \frac{\rho_\mathrm{v}(\boldsymbol{p}-\boldsymbol{p}')}{\|\boldsymbol{p}-\boldsymbol{p}'\|^3}\mathrm{d}^3p' + \int_S \frac{\rho_\mathrm{s}(\boldsymbol{p}-\boldsymbol{p}')}{\|\boldsymbol{p}-\boldsymbol{p}'\|^3}\,\mathrm{d}^2p'\right) \tag{3.17}$$

with

$$\rho_\mathrm{v} = -\nabla\cdot\boldsymbol{M} \tag{3.18}$$

and

$$\rho_\mathrm{s} = \boldsymbol{M}\cdot\boldsymbol{e}_\mathbf{n} \tag{3.19}$$

where $\boldsymbol{e}_\mathrm{n}$ is the unit normal vector defining the surface. This leads to

$$\boldsymbol{H(p)} = \frac{1}{4\pi}\left(-\int_V \frac{(\nabla'\cdot\boldsymbol{M})(\boldsymbol{p}-\boldsymbol{p}')}{\|\boldsymbol{p}-\boldsymbol{p}'\|^3}\mathrm{d}^3p' + \int_S \frac{\boldsymbol{M}\cdot\boldsymbol{e}_\mathbf{n}(\boldsymbol{p}-\boldsymbol{p}')}{\|\boldsymbol{p}-\boldsymbol{p}'\|^3}\,\mathrm{d}^2p'\right). \tag{3.20}$$

Assuming a uniform distribution of magnetization with $\nabla'\cdot\boldsymbol{M} = 0$, the volume component in Equation 3.20 diminishes, leaving only the surface components. The equation thus simplifies to

$$\boldsymbol{H(p)} = \frac{1}{4\pi}\int_S \frac{\boldsymbol{M}\cdot\boldsymbol{e}_\mathbf{n}(\boldsymbol{p}-\boldsymbol{p}')}{\|\boldsymbol{p}-\boldsymbol{p}'\|^3}\,\mathrm{d}^2p' \tag{3.21}$$

and allows calculating the $\boldsymbol{H}$-field distribution of a permanent magnet with a homogenous magnetization. This model of a permanent magnet and its magnetic field will be utilized in Chapter 6 in order to estimate the position of the real magnetic object (i.e., ferromagnetically augmented surgical instrument).

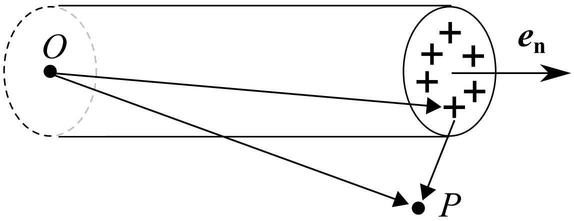

Figure 3.6.: Coulombian magnetic model to calculate $\boldsymbol{H(p)}$ at a point P from the origin O. The field derives from a magnetic charge q_m on the outer surface of the magnet, defined by $\boldsymbol{p'}$ and the surface defined by the unit normal vector $\boldsymbol{e}_\mathrm{n}$. Adapted from [103].

3.2.5. Hall Effect

Tracking a ferromagnetic object necessitates not only a magnetic model, but also the measurement of magnetic fields. Hall-effect sensors can be employed for this task.

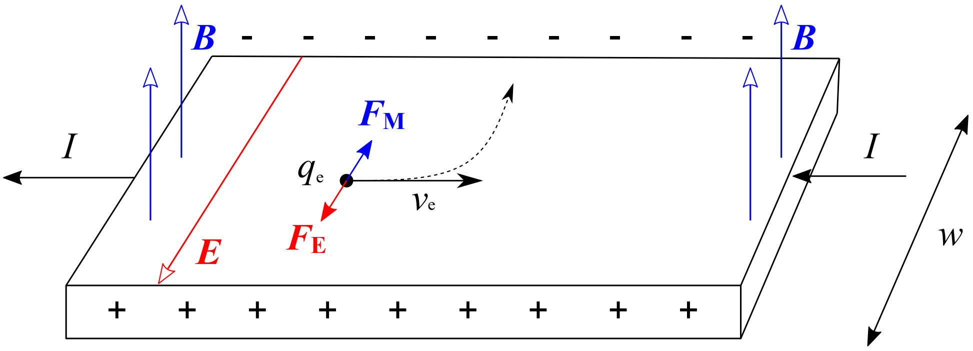

Figure 3.7.: Schematic of the Hall effect. Adapted from [112].

The Hall effect is a phenomenon observed when electric charge carriers, such as electrons q_e, flow with a current I through a (semi-) conductor of width w with a drifting velocity $\boldsymbol{v}_d$ under the influence of an applied magnetic field $\boldsymbol{B}$ (Figure 3.7). Within the magnetic field, the electrons are deflected by a magnetic force component [106]

$$\boldsymbol{F}_M = q_e(\boldsymbol{v}_d \times \boldsymbol{B}). \tag{3.22}$$

This causes an accumulation of charges on one side of the conductor, generating an electric field $\boldsymbol{E}$ perpendicular to both the magnetic field and the current flow, applying an electric force $\boldsymbol{F}_E$ on an electric charge carrier q_e such that

$$\boldsymbol{F}_E = q_e\boldsymbol{E}. \tag{3.23}$$

The sum of the electric and the magnetic force components is defined as the Lorentz force

$$\boldsymbol{F}_L = \boldsymbol{F}_E + \boldsymbol{F}_M \tag{3.24}$$

and can be written as

$$\boldsymbol{F}_L = q_e(\boldsymbol{E} + \boldsymbol{v}_d \times \boldsymbol{B}). \tag{3.25}$$

An equilibrium is reached when $\boldsymbol{F}_L = 0$, i.e., the electric force balances the magnetic force

$$\boldsymbol{F}_E = -\boldsymbol{F}_M \tag{3.26}$$

and leading to

$$\boldsymbol{E} = -\boldsymbol{v}_d \times \boldsymbol{B}. \tag{3.27}$$

In this state, the Hall voltage (i.e., Hall potential) can be measured between the conductor sides, analog to a parallel-plate capacitor with width w between its plates. This simplification can derive

$$U_H = w\boldsymbol{E} = -w(\boldsymbol{v}_d \times \boldsymbol{B}). \tag{3.28}$$

Due to $U_H \propto \|\boldsymbol{B}\|$, the magnitude of the $\boldsymbol{B}$-field can be calculated based on the measured Hall potential U_H.

In summary, utilizing a Hall-sensor system, in conjunction with a magnetic field model, effectively meets the needs for tracking a ferromagnetically enhanced surgical instrument within the human body, as presented in Chapter 6.

3.3. Piezoresistive Polymers

Piezoresistivity[3] in (semi-) conductors describes a change of their electric resistance due to an applied mechanical stress and deformation [91]. This effect can be used to form compact, compliant, and flexible smart material sensor systems, as presented in [6] and deployed in this dissertation in Chapter 7. This following Section 3.3 provides the required theoretical background.

Piezoresistive Sensing

Besides the temperature-related resistance changes due to dimensional deformation (Equation 3.3), and temperature-induced resistivity changes (Equation 3.6), as discussed in Section 3.1.2, piezoresistive materials exhibit an additional variability in their resistivity ρ_{pol} based on the applied stress as in

$$\frac{\Delta\rho_{\mathrm{pol}}}{\rho_{\mathrm{pol}}} = \pi_{\mathrm{t}}\sigma_{\mathrm{t}} + \pi_{\mathrm{l}}\sigma_{\mathrm{l}} \tag{3.29}$$

with the piezoresistive stress in transverse direction σ_{t} and longitudinal direction σ_{l}, as well as the piezoresistive coefficient π_{t} and π_{l}, respectively. Transverse stress and piezoresistive coefficient are characterized by the perpendicular orientation of mechanical stress and electric field, while longitudinal stress and piezoresistive coefficient are delineated by the parallel alignment of mechanical stress and electric field. [91]

Piezoresistive materials include silicon, diamond, silicon carbide, and carbon impregnated polymers. Since most polymeric materials are non-conductive, the polymer matrix is combined with a (semi-) conductive component as a filler (e.g., carbon black, graphene, carbon nanofiber, carbon nanotubes) turning them into a compliant composite material for flexible sensor application. [113]

3.3.1. Carbon-Impregnated Composite Polymers

Composite polymers with impregnated carbon are utilized to measure normal stress in “non-stiff” materials [114]. There exist the two major underlying effects for the piezoresistive behavior of these piezoresistive polymers, namely perlocation and quantum tunneling. [115]

Perlocation

In piezoresistive polymers, conductive filler particles are dispersed within a non-conductive polymer matrix. Percolation refers to the material transition from an insulating state to a conductive state as the concentration of conductive filler particles in the polymer matrix increases. At lower concentrations, the conductive particles may be isolated, and the material thus exhibits insulating behavior. However, when mechanical stress or deformation affects the particle arrangement, the concentration of these particles can increase over a critical threshold. As a result, the particles begin to form a connected or percolated network, which leads to a drastic change in the material’s electric conductivity, and allowing for the efficient movement of charge carriers. [116]

---

[3] Greek $\pi\iota\epsilon\zeta\omega$, meaning to press.

Quantum Tunneling

Quantum tunneling refers to a phenomenon where charge carriers (e.g., electrons) move through energy barriers by quantum mechanical processes. When pressure is applied to a piezoresistive polymer, it leads to a change in the distance between conductive particles or clusters within the material. This alteration in distance influences the probability of electrons tunneling through the energy barriers between these particles. As the distance changes due to mechanical deformation, the tunneling probability varies, resulting in changes in electric conductivity and, consequently, measurable changes in resistance. [116, 117]

3.3.2. Application of Piezoresistive Polymers

Piezoresistive polymers are used in many applications due to several aspects, that facilitates their utilization as pressure and deformation sensors. Those polymers are flexible and compliant, mechanically and chemically stable, and they can be processed into sheets and foils/films with variable thicknesses and in large dimensions at low-cost [117]. This makes it easy to customize sensor surfaces in a wide size range of sizes and patterns. By adding conductive electrodes (e.g., Cu, aluminum (Al)) to the piezoresistive polymer, and a relatively simple measurement circuit, the sensor system is complete. There is even the potential to include the measurement circuit in the fabrication process with an additive manufacturing approach [113]. However, piezoresistive polymers exhibit noticeable nonlinear effects such as hysteresis and creeping, which require adequate compensation in signal processing making use of nonlinear modeling [118].

A widely applied composite material is Velostat (i.e., Linqstat, 3M Company, USA) which is a polyethylene matrix with carbon black as conductive filler material. Despite exhibiting lower sensitivity in comparison to other piezoresistive materials designed for sensing on flexible surfaces, such as piezoresistive ink (Voltec Electrónica, Columbia), and ThruMode Matrix Array (Sensitronics, USA), Velostat provides the advantage of low hysteresis [119]. Furthermore, Fatema *et al.* could demonstrate in [120] a long-term (210 days) reliability of Velostat as sensor material for large surfaces, confirming a “settling effect” [116] of its nonlinear characteristics. Velostat and comparable piezoresistive polymers have been applied in the sensorization of gloves for finger-gesture recognition [121], tactile gloves [122], the creation of a foot controller for navigation in VR [123], the measurement of body pressures with a wearable device [117], and the analysis of sitting postures [124]. Hopkins *et al.* [125] explored Velostat and its performance characteristics in lower limb prostheses. They discovered that this affordable material is easy to integrate into the individual stump interface, while also noting inaccuracy as a drawback.

However, the diverse range of applications and the aforementioned advantages underscore the potential of piezoresistive polymer Velostat as a compliant and flexible sensor material for sensing healthcare applications in this dissertation.

Chapter Summary

This Chapter 3 described the fundamentals of the three key materials used in this dissertation: SMAs, ferromagnetic materials, and piezoresistive polymers. It laid the necessary theoretical groundwork for understanding the subsequent scientific contributions.

Part II.

Smart Material Systems for Minimally Invasive Surgery

4. Self-Assembling Continuum Robots with Shape Memory Alloys

The content of this Chapter 4 was published in the *IEEE Robotics and Automation Letters 2023* [1] © IEEE 2023. Headlines, wording, and layout were carefully modified to fit within this work.

4.1. Tendon-Driven Continuum Robots

Continuum robots are characterized by their flexible and deformable structures and offer unique advantages in diverse applications. They excel in navigating confined or irregular environments, including manufacturing and inspection tasks in aerospace and industry, as well as in search and rescue missions [126]. Their compliant nature enhances safety in human-robot interactions, and furthermore, improve minimally invasive medical procedures within the human body cavity by reducing risk of tissue damage [127]. Flexibility and compliance of continuum robots derive from the infinite DOF in their robotic structures [38]. Those robots are usually steered by a limited number of actuators, leading to a hyper-redundancy of the structure [58]. When composed of multiple segments, a continuum robot can be moved in a snake-like manner around obstacles and into hard-to-reach spaces, while still elastically conforming to its surroundings, thus protecting delicate adjoining compartments [62].

A tendon-driven continuum robot is a particular type, in which externally driven tendons are used to bend an elastic backbone, which provides mechanical integrity and stability of the robot. Therefore, the tendons are routed through multiple backbone-mounted spacer disks and connected to the end of the robot segments, thus allowing for segment-wise bending [128]. The length of the segments and the distance between two spacer disks (i.e., section length) influence the reachable workspace. Their variability allows for multiple workspace configurations. Moreover, the configuration of tendons and their routing path through the spacer disks are crucial for the resulting controllable DOF [129], e.g., pure bending or even complex twining due to helical tendon routing [130]. Yet, most tendon-driven systems come with a fixed length of segments and sections (static), and a preset tendon routing for the robotic structure. This restricts the preoperative procedure planning of the operators, and their options to adapt their strategy during a procedure.

Related Work

Wang *et al.* present a system with robotically supported insertion for turbine inspection in aerospace, featuring 10 controllable static segments (Ø $12.7\,\mathrm{mm}$) of a continuum robot with $715\,\mathrm{mm}$ length of the entire system mounted on a movable stage [131]. However, the associated space requirements and handling challenges of such systems with a fixed length in the operating room can jeopardize the surgical workflow, impairing movement space and potentially leading to higher costs for the treatment. Instead of being moved with their entire robotic system, tendon-driven continuum robots with robotic extendability hold the potential to both, reducing spatial footprint and improving robotic dexterity. Dong *et al.* present an extendability approach, where a $1256\,\mathrm{mm}$ long continuum robot with 12 segments is coiled on a motorized drum with an outer diameter of only $275\,\mathrm{mm}$, containing all 12 motors for antagonistic tendon actuation. This way, uncoiling the robot from the drum leads to a linear extension [132]. To increase the overall stiffness, tendons can be replaced by bendable rods, leading to a "multi-backbone" structure. Kang *et al.* investigated an interlacing multi-backbone structure (Ø $30\,\mathrm{mm}$), able to perform a follow-the-leader motion during extension [133]. A more complex approach by Liu *et al.* uses flexible rods in a parallel configuration with connected geared pinion-racks within the segments. Two linear drives at the proximal actuator unit are thus able to bend the entire robotic structure (Ø $25\,\mathrm{mm}$) or extend it by up to $32.2\,\%$. However, the mechanism does not allow multidimensional snake-like shapes and has a minimal length of $176\,\mathrm{mm}$ [134]. Kanada *et al.* also use gear and pinion, but claim "unlimited" extendability. Three motorized pinon shafts create a linear motion on flexible tubes with a helical outer groove, instead of tendons [135]. A diameter of $80\,\mathrm{mm}$ however makes a deployment in the medical field unlikely. In addition, the flexible tubes for extension must be provided from behind the actuation unit, leading to increased space demand. A similar work by Matsuura *et al.* demonstrates that a "flexible screw as a backbone" and motorized disks in combination with tendons allow multidimensional bending. Furthermore, their demonstrator can continuously vary the section and segment lengths along the backbone, leading to an extensive workspace variability. Yet, its diameter is larger than $100\,\mathrm{mm}$ and the aspects of a space demanding feed storage and electric wiring for the disks remain unsolved [136]. Amanov *et al.* also modified a tendon-driven robot and its backbone. They replaced the elastic backbone with three superelastic tubes from NiTi, stacked telescopically into each other. The outer diameter of the robotic structure is only $7\,\mathrm{mm}$, qualifying the system as an instrument for minimally invasive surgery. When extended, magnetic spacer disks align equidistantly over the robot's maximum length of $165\,\mathrm{mm}$, of which $80\,\mathrm{mm}$ are extendable [137].

Contribution

The aforementioned complex continuum robot systems use different approaches to extend and retract continuum robots of different diameter size. This often makes the actuation setups larger when compared to a conventional, non-extendable tendon-driven continuum robot. Especially, the rare variability of section and segment lengths comes at the cost of bulky robotic structures and actuation units. In contrast, to explore narrow and complex spaces, both, a smaller footprint and the ability to extend and retract with an extensive workspace variability would be beneficial. Hence, a novel system design is presented, where the robotic structure is assembled during the extension process continuously from inside the actuation unit up to preset maximum extension with variable segment and section lengths. This system allows combining dexterous, tendon-driven actuation of two segments with a large extendable length at a small robotic diameter. In regard to the research objective of this dissertation, the utilization of a **superelastic SMA** serves to augment conventional tendon actuation of the continuum robot. This enables compliance and a miniaturization of the required storage capacity within the actuation unit for the continuum structure before assembly.

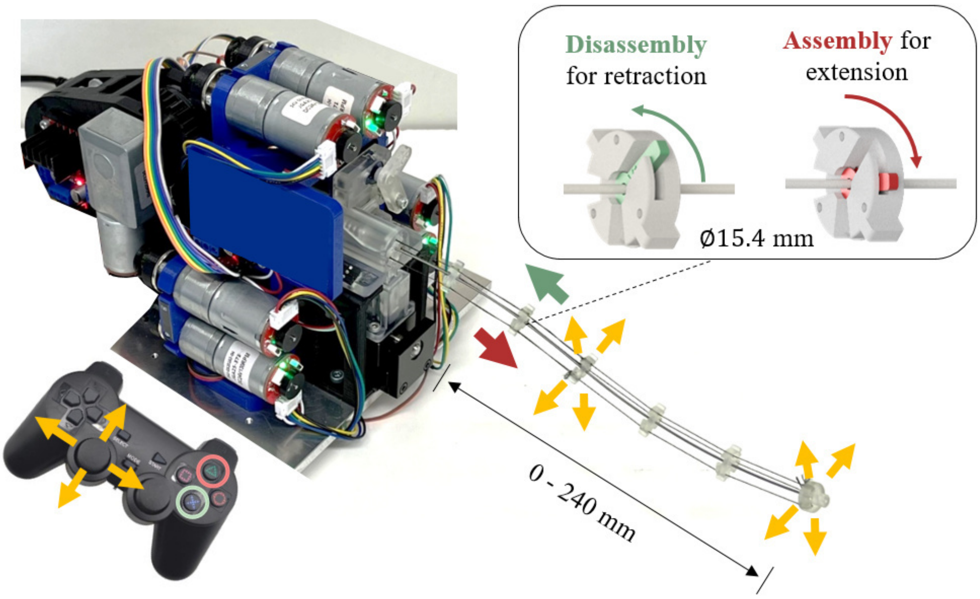

Figure 4.1.: The extendable tendon-driven continuum robot, featuring extension, retraction and omnidirectional bending of two segments. The robotic structure is assembled by clamping the disks onto the superelastic SMA backbone during the extension process and disassembled by loosening for retraction. [1] © IEEE 2023.

4.2. Design of an Extendable Continuum Robot

The complete robotic system is presented in Figure 4.1 and Figure 4.2a. It features the robotic structure and the actuation unit with storage and feeds for backbone and disks, as well as the assembly channel. The backbone is made from a durable, kink-resistant, and biocompatible SMA (NiTi, Ø $1\,\mathrm{mm}$). It plays a crucial role, enabling a compact storage of the disassembled components within the actuation unit. Structural parts were additively manufactured using fused deposition modelling (FDM) and stereolithography (SLA). Figure 4.2b shows the backbone and tendon routing inside the actuation unit. The design incorporates two fully extendable-retractable segments consisting of several disks along a backbone. Each segment's end disk is connected to three tendons, allowing omnidirectional bending of the extendable superelastic backbone. The end disk of the distal segment is permanently attached to the backbone, whereas the proximal end disk attaches to the backbone when required. Tendon actuation is implemented similar to [138]. The tendons are routed from the tendon motors (JGA25-371 DC $24\,\mathrm{V}$, 126 rpm, $0.41\,\mathrm{N\,m}$) via low-friction guiding edges through the disk storage and attached to the end disks. Dyneema Fiber (Ø $0.14\,\mathrm{mm}$) was chosen as tendon material due to its high stress resistance [137].

4.2.1. Self-Assembly: Extension and Retraction Mechanism

The continuum robot assembles itself during extension and disassembles during retraction. This is enabled through automatic attachment (clamping) and detachment (release) of the spacer disk or segment-end disk, respectively, on the extending backbone. Prior to the assembly process, the backbone is coiled and stored in the backbone storage drum, which prevents the backbone from unfavorable bending radii below $30\,\mathrm{mm}$. The backbone is fed with a motorized pulley (JGY25-371 DC $24\,\mathrm{V}$, 18 rpm, $1.18\,\mathrm{N\,m}$) and

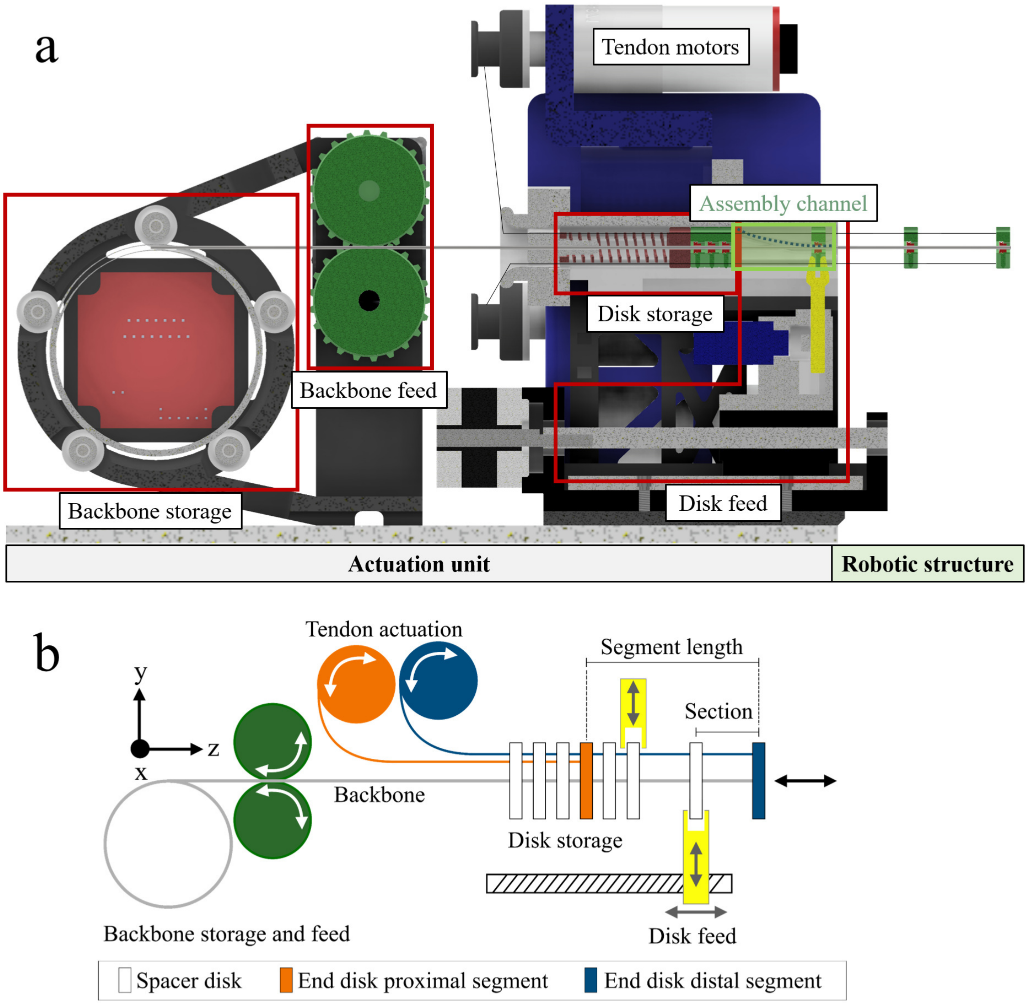
a
Tendon motors
Assembly channel
Backbone feed
Disk storage
Backbone storage
Disk feed
Actuation unit
Robotic structure
b
Tendon actuation
Segment length
Section
y
z
x
Backbone
Disk storage
Backbone storage and feed
Disk feed
▯ Spacer disk
🟧 End disk proximal segment
🟦 End disk distal segment

Figure 4.2.: The proposed robotic system including the actuation in cross-section with feed and storage for disks and backbone, (a) and a scheme of the superelastic SMA backbone and tendons routing through the entire disk storage for a two segment continuum robot (b). [1] © IEEE 2023.

routed through the disk storage. Here, all disks are loaded against a compression spring on one end and blocked by a motorized locking pin to the other. The assembly process is illustrated in Figure 4.3. Each disk (Ø $11.7\,\mathrm{mm}$, $4\,\mathrm{mm}$ thick) features two symmetrical keypin extrusions for rotation-free guidance of the disk in storage and assembly channel. The detachable bond between backbone and disk is realized with a force fit. Therefore, each disk forms a hub-lever compound (Figure 4.3a). The lever is clipped into the disk hub and can be rotated around the z-axis. Once rotated by 30° the central clamping mechanism is engaged. If a disk is to be attached to the backbone, it is released from the disk storage and grasped individually (Figure 4.3b) by a motorized gripper (Micro Servo SG90 $5\,\mathrm{V}$) and moved on a linear guide rail (NEMA11 stepper motor $24\,\mathrm{V}$) from the disk storage through the assembly channel, synchronously with the moving backbone. A sweeping groove in the inner walls of the assembly channel leads to a rotation of the lever when a disk is moved through the channel. Before the disk arrives at the channel outlet, the clamping is completed (Figure 4.3c). This process is repeated for each disk. During retraction, the process is reversed. The extension length can be selected in the continuous range between $0\,\mathrm{mm}$ and $240\,\mathrm{mm}$, in which the bending is feasible for any number of extended sections.

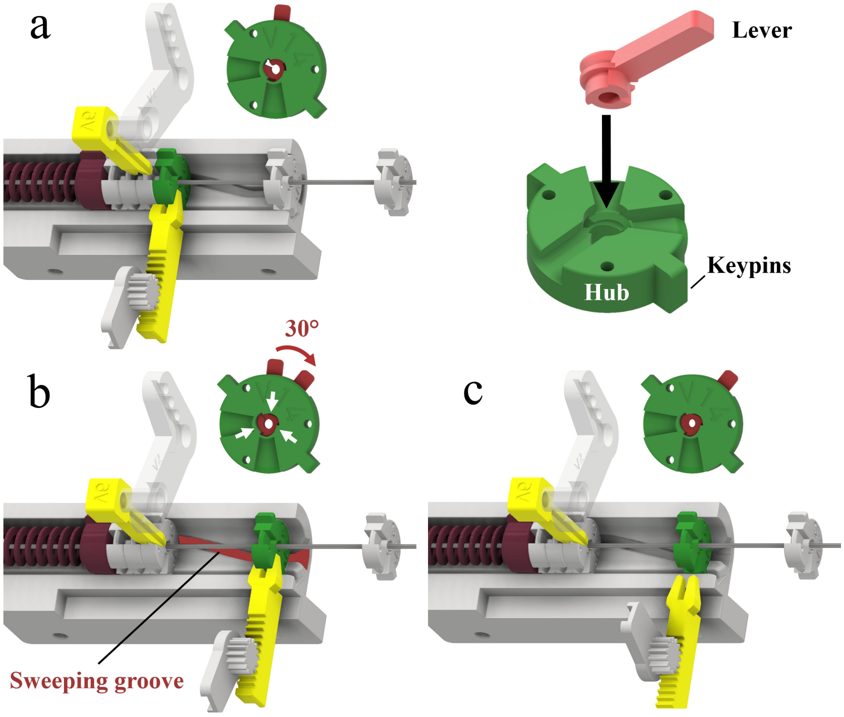

Figure 4.3.: Mechanism of the self-assembling procedure with disk hub and lever (a) without tendons. For extending the robot, a disk is released from the disk storage and pulled forward (b). Due to the sweeping groove in the channel wall, the lever is rotated during the forward movement, shrinking its inner diameter, and joining the disk with the backbone (c). The procedure is reversible, allowing also for retraction. Adapted from [1] © IEEE 2023.

4.2.2. Control and User Interface

To evaluate motions separately, two control modes are implemented of extension-retraction and the bending of the backbone through actuation of the tendons. A microcontroller (Arduino Mega 2560 Rev3) is used to control via pulse-width-modulation (PWM) the servo motors directly, while the direct current (DC) motors are controlled with L298N and the stepper motor with DRV8825 drivers. Incremental magnetic motor encoders allow monitoring the position of the motor shafts. Their readings are used as inputs to six proportional-integral-derivative (PID) controllers in order to achieve synchronous movement during extension and retraction between tendons, backbone, and disks. Deviation from synchronization could otherwise result in friction, jerking of the disks and excessive forces on material and actuators. The backbone position as well as the positions of the disks on the backbone can be computed based on the motor encoders' history. While this is sufficient for extraction, preliminary tests revealed that retraction appears less robust. Thus, the disks are not found at the expected position translated in encoder steps. It is assumed that minor slippage in the backbone feed and of the disk clamping mechanism as a reason. For compensation, an infrared proximity sensor (Joy-IT KY033LT) was added at the assembly channel outlet to detect passing disks during extension and retraction. For intuitive remote robot manipulation (i.e., with the human-in-the-loop) a wireless handheld controller was implemented. Extension and retraction of a section can be triggered via two different push buttons. The continuum structure then extends by a preset section length in order to move out one additional disk entirely. This process can be repeated until the robotic structure is extended to its maximum length of $240\,\mathrm{mm}$. The two thumb-sticks are used to bend the two segments individually at every extension stage (Figure 4.1).

4.3. Experimental Evaluation

The experimental evaluation of the extendable continuum robot included the self-assembly and the bending performance.

4.3.1. Self-Assembly Performance

To allow for multiple reliable extension and retraction cycles during a medical procedure, the disks must be repetitively positioned with high precision on the superelastic SMA backbone and thus provide a reliable section length. Furthermore, the functionality of the robotic bending depends on the ability to retain the clamped disks with a sufficiently high friction force at these positions on the backbone during tendon pulling.

Repeatability of Disk Positioning

To evaluate the precision of the repetitive disk positioning, five identical extension runs were programmed (sample size $n = 5$) with a preset section length of $31\,\mathrm{mm}$. The distance between the disks' centers were measured using a caliper.

Figure 4.4 shows the results, revealing mean errors $\bar{e}_{\text{disk}}$ of the disk positioning over all runs and sections of $0.39\,\mathrm{mm} \pm 0.83\,\mathrm{mm}$. Maximum errors of e_{disk} of up to $1.9\,\mathrm{mm}$ were measured, corresponding to less than $0.8\,\%$ of the maximum extension length. Yet, the maximum error appears small enough in this first proof of concept of the assembling mechanism to provide multiple reliable extension and retraction cycles. It is worth noticing that the absolute measured section length increases from proximal to distal end. In contrast, it remains below reference in between disk $1-2$ and $3-4$, and above reference between $5-6$. Presumably, this behavior is due to the friction between the backbone and the disks in the disk storage. When extending the first sections, the disk storage is filled and thus friction forces are larger compared to when the proximal sections are fed at last through an almost empty storage.

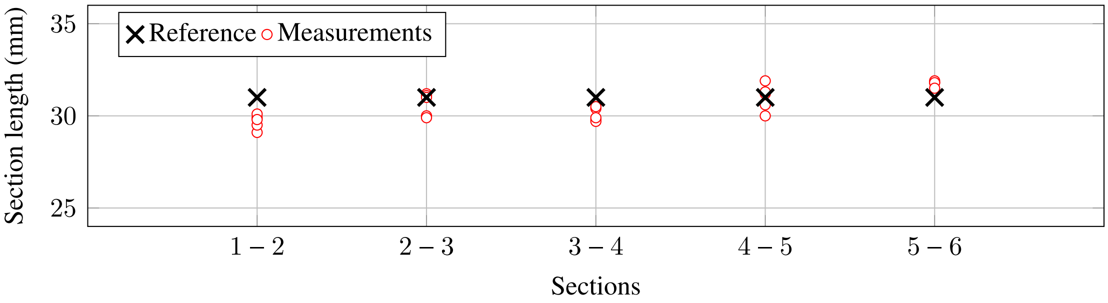

Figure 4.4.: Investigating the repeatability of disk positioning during the self-assembling procedure. For a reference section length of $31\,\mathrm{mm}$ all disks were assembled ($n = 5$). The measured section length revealed that the disk positioning error e_{disk} remains $< 1.9\,\mathrm{mm}$ ($0.8\,\%$ relative to maximum extension). Adapted from [1] © IEEE 2023.

Friction Forces of the Clamping Mechanism

The disk clamping mechanism is designed to maximize friction between disk and backbone during attachment for a reliable form-fit and minimize it when remaining detached in the disk storage for unhindered routing of the backbone. The static and sliding friction forces are therefore significant indicators of that bond and measured with a force gauge (PCE-DFG-N 10, PCE Instruments UK Ltd.). Here, tendon pulling of one released disk by bidirectional straight backbone routing ($n = 15$) was investigated (Figure 4.5a). For a clamped disk, a distinction was made between symmetrical (Figure 4.5b) and asymmetrical (Figure 4.5c) tendon forces ($n = 15$). A maximum (worst-case) static friction of $1.43\,\mathrm{N}$ (mean $0.89\,\mathrm{N}$) and sliding friction were measured, with a reduction of $53\,\%$ (mean $40\,\%$). Either moving direction caused similar friction amplitudes. In contrast, the backbone feed could apply more than $14\,\mathrm{N}$ on the backbone with a constant speed of $2\,\mathrm{mm\,s^{-1}}$ which would be sufficient to overcome the maximum friction caused by a disk storage filled with up to ten disks. For the case in which the tendons were (symmetrically) stressed while the backbone was pulled in the opposite direction, a minimum (worst-case) static friction (i.e., resistance force) of $2.35\,\mathrm{N}$ (mean $3.47\,\mathrm{N}$) was measured. The maximum theoretical tendon force ($82\,\mathrm{N}$) could exceed this minimum and potentially move the released disk relative to the backbone. While during the experiments the spacer disks remained unaffected, the end disk of the proximal segment occasionally shifted when two tendons were pulled simultaneously and the combined force thus exceeded the static friction level. In addition, a considerable creeping effect of the cured additively manufactured resin material of disks (Clear V4, Formlabs GmbH, Germany) and levers (Durable V2, Formlabs GmbH, Germany) was observed, resulting in reduced friction and, consequently, deterioration of the clamping mechanism over time. During omnidirectional bending of the robot, variations in stress on the individual tendons were observed in most scenarios, leading to an asymmetrical load on the end disk of each segment. In this study, the enhanced clamping effect of the disks was noted when subjected to an asymmetrical load, withstanding loads exceeding $20\,\mathrm{N}$ and causing material breakage rather than loosening of the disk. The hypothesis is that the clamping approach can withstand most bending loads, as asymmetrical scenarios constitute the majority of cases for omnidirectional bending motion.

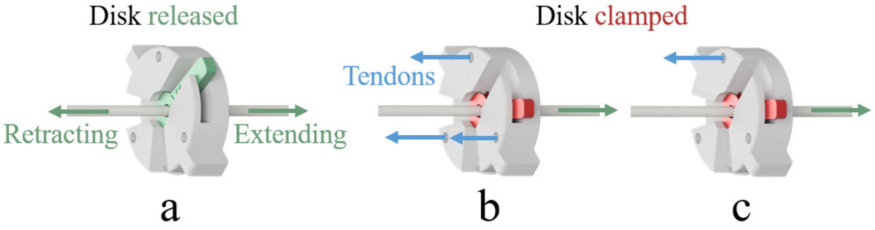

Figure 4.5.: Investigating friction forces on backbone routing through released (a) and clamped disks with symmetrical (b) and asymmetrical (c) load. [1] © IEEE 2023.

4.3.2. Bending Performance

The experimental evaluation of the bending performance included the investigation of the reachable workspace and the repeatability of the tip manipulation.

Workspace

Figure 4.6 shows the workspace of the extended robotic structure, with six extended disks and bending angles of 90° for each of the two segments. The section length can be varied between $15\,\mathrm{mm}$ (Figure 4.6a) and $40\,\mathrm{mm}$ (Figure 4.6b), resulting in maximum extension lengths (both segments) of 90 mm and 240 mm, respectively. The combination of extension and bending demonstrates a variable workspace volume, exceeding the workspace of non-extendable tendon-driven continuum robots.

Repeatability

To assess repeatability, the evaluation setup depicted in Figure 4.7 was employed. An electromagnetic spatial measurement system (Aurora, NDI Europe GmbH, Germany) tracked the pose of a sensor (Aurora 5DOF FlexTube, Ø 1 mm) attached to the robot's distal tip and suspended from above. The magnetic sensing supports a 500 mm×500 mm× 500 mm workspace with 40 Hz and an accuracy of 1.8 mm at a 95 % confidence interval (CI). To avoid parasitic interference from metal components, evaluation took place on a wooden platform and the actuation unit of the robot is removed as far as possible from the magnetic field generator. Further control units, power supplies and computers were not tolerated in a 3 m radius of the experiment.

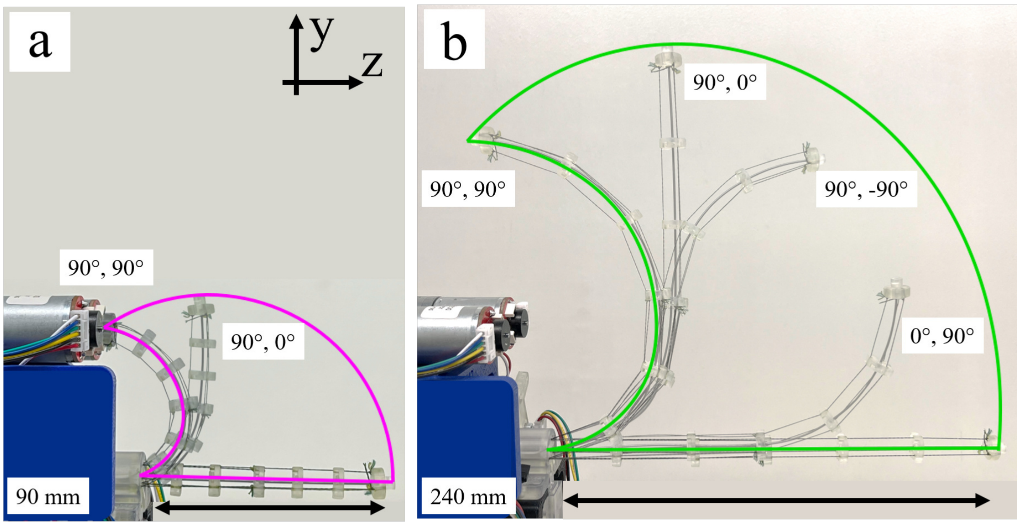

Figure 4.6.: Experimental workspace exploration using both segments with extended length of 90 mm (a) and 240 mm (b), demonstrating the usual dexterity from conventional tendon-driven continuum robots. The workspace volume increases with extension length. [1] © IEEE 2023.

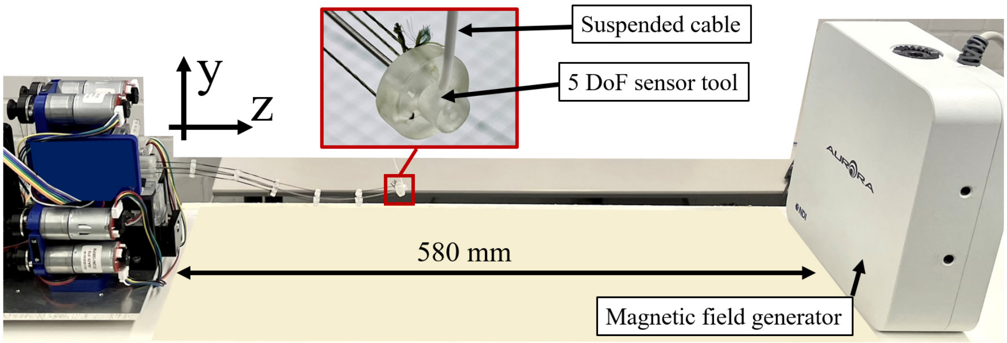

Figure 4.7.: Evaluation setup with a magnetic field generator to measure the sensor pose at the distal tip of the robotic structure. In order to minimize the influence of the sensor's weight, its connection cable is suspended from above the setup. [1] © IEEE 2023.

To examine the repeatability of the robot, ten representative configurations were defined (Figure 4.8). Configurations 1–3 required only bending of the distal segment (and its three tendon motors), while configurations 4–6 concerned bending of the proximal segment only. Eventually, 7–10 tested the bending of both segments combined. As initial straight configuration, an extension of $204\,\mathrm{mm}$ (section length $34\,\mathrm{mm}$) without bending was set. From the initial configuration, each configuration 1–10 was targeted ($n = 10$). To reduce the influence of vibration, the robot remained in the targeted configuration for $5\,\mathrm{s}$, before $n_p = 100$ samples of the position vector $\boldsymbol{p}$ were recorded ($\approx 2.5\,\mathrm{s}$) and the mean value $\bar{\boldsymbol{p}}$ was saved. The repeatability error for the bending e_{bend} was then defined as the Euclidean distance between this point $\bar{\boldsymbol{p}}$ and the reached position during one run.

The mean and maximum errors over all runs 1–10 for all ten configurations are shown in Figure 4.9. The repeatability errors range from $0.88\,\mathrm{mm}$ (mean) up to $7.31\,\mathrm{mm}$ (maximum) and median error of $2.39\,\mathrm{mm}$ which corresponds to $1.17\,\%$ of the robot's length. Configurations with only distal tip manipulation (1–3) show the smallest repeatability error while exclusive proximal manipulation (4–6) caused a larger error. As expected, the combination of both, distal and proximal bending, caused the highest mean and maximum error, except for configuration 9. Here, presumably the isolated proximal manipulation was outperformed, since the repeatability evaluation took only the distal tip into account. For isolated proximal manipulation, however, the tendon motors and motor-induced errors could just influence the proximal segment directly while the distal end can passively accumulate possible negative effects.

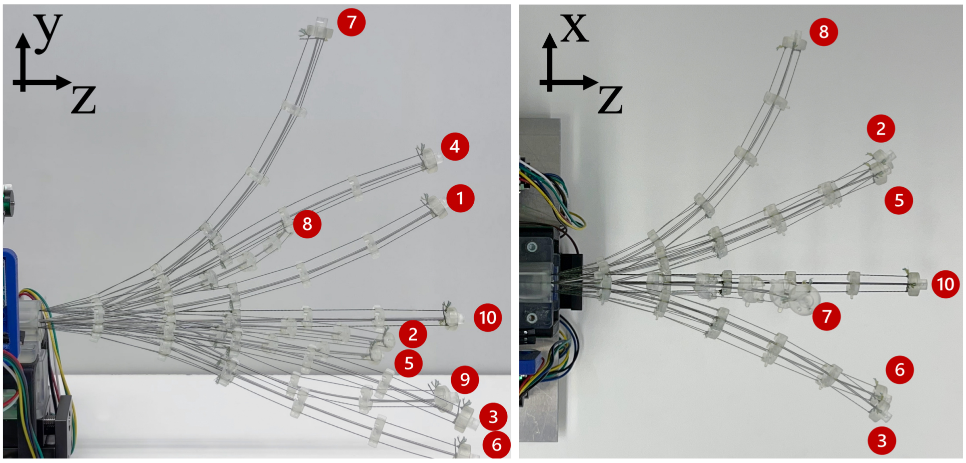

Figure 4.8.: Investigated configurations to determine repeatability performance of distal (1–3), proximal (4–6) and both segments combined (7–10). [1] © IEEE 2023.

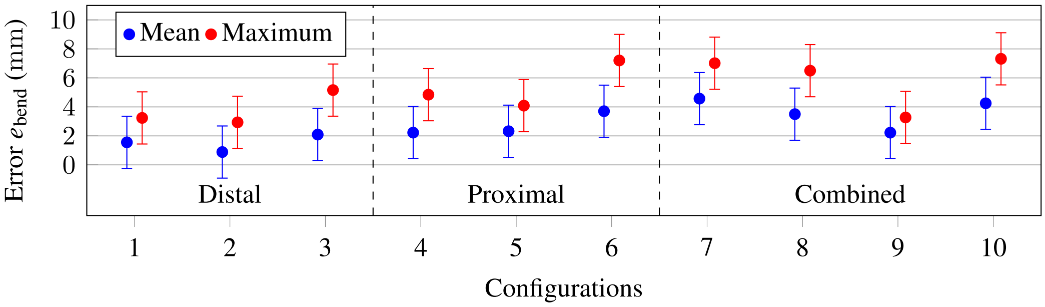

Figure 4.9.: Repeatability errors e_{bend} for the bending of configurations 1–10 for distal, proximal and both segments combined ($n = 10$). Error bars indicate the confidence interval (CI) of the measurement system. Adapted from [1] © IEEE 2023.

4.4. Towards Extendable Surgical Robots

The results demonstrate the feasibility of assembling a tendon-driven continuum robot during the extension process with sufficient precision, effectively varying the reachable workspace volume due to adjustable section and segment lengths. In addition to providing equidistant section lengths as required for constant curvature [129], varied section lengths could be beneficial for application scenarios, in which tight bending radii are required within the inner regions of a confined workspace. Short sections at the distal tip and long sections at the proximal end would then allow both, a large extension length and tight bending angles at the tip. This approach is only feasible due to the deployment of a superelastic SMA backbone and allows for a highly compact design of the robot ($240\,\mathrm{mm} \times 140\,\mathrm{mm} \times 145\,\mathrm{mm}$, $< 1.5\,\mathrm{kg}$) while the dexterity remains comparable to state-of-the-art tendon-driven continuum robots without extendability. In addition, extendable systems enhance the workspace size and variability depending on their extendable length. Figure 4.10 compares aforementioned extendable systems regarding extendable range and diameter size, in which the presented demonstrator proofs superior when considering maximum length.

The presented self-assembling approach is scalable within certain limits. For instance, an increased number of disks and actuated segments, allowing for an increased extendable length and more DOF at the cost of a moderately larger actuation unit for storage and actuators. Thus, a future iteration of the demonstrator could be able to extend even beyond the work by Dong *et al.* [132]. Yet, to hold more disks in storage, friction forces of the unlocked mechanism must be reduced without jeopardizing the clamping performance of the locked mechanism. The intention is to optimize the tribological characteristics by considering additional material combinations and exploring more complex locking mechanisms, which may involve a selective modification of the backbone surface and its associated friction. Furthermore, the aim is to undercut the robotic outer diameter size of $7\,\mathrm{mm}$ presented by Amanov *et al.* [137] by inverting the keypin extrusions on the disk design, ultimately striving for the largest extension and smallest diameter compared to related work.

It is noteworthy that, so far, only the extension and bending have been demonstrated in separate runs, with simultaneous manipulation in translation and bending remaining unconsidered, although it represents a promising control modality. It should also be noted that only a straight tendon-routing was implemented. However, the self-assembling of a helical tendon routing configuration as in [130] would also be feasible, if the backbone

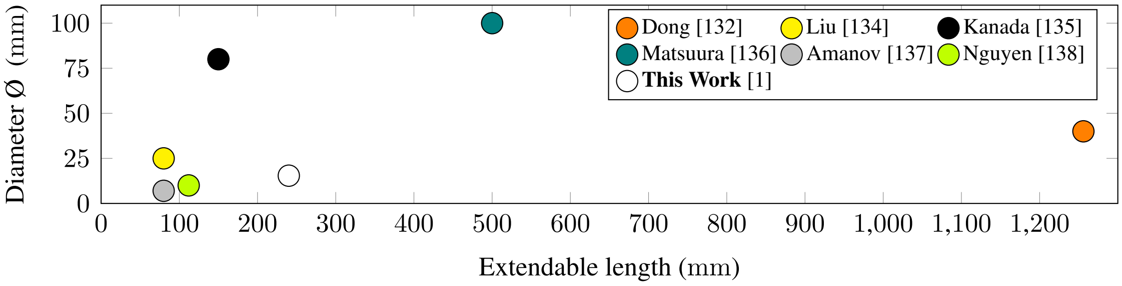

Figure 4.10.: Comparing extendable length and robotic outer diameter of this work to related work. High extendable length and small diameter size are desired. Wang *et al.* [131] are excluded since they move their entire actuation units instead of extending the robotic structure. Adapted from [1] © IEEE 2023.

can be axially rotated during runtime. Yet, the pulling of helical tendons would increase the demands on the locking mechanism additionally.

In envisioning future developments, the ultimate objective should be to establish a workflow that accommodates the variability inherent in segment and section lengths, along with diverse configurations of tendon routing, within the realms of task and path planning. This envisaged framework should not only recognize the aforementioned variabilities but also incorporate dynamic adjustability seamlessly during the execution phase.

Medical Application

Minimally invasive surgery can improve patients' healing during post-operative phases by reducing infection risk and hospitalization time compared to conventional open surgery as stated by Imaizumi *et al.* [27]. Consequently, continuum robots have been thoroughly investigated to enable sufficiently dexterous manipulation within the human body and without tissue damage [62,127]. Thus, a critical investigation and discussion of the potential for a medical application of the presented robotic design and its compact extendability feature are necessary.

In-Phantom-Validation

A preliminary experiment was conducted to test the dexterity (alternating extension and bending) of the demonstrator on a medical phantom for transoral endoscopy of the esophagus. In a conventional approach of this procedure (i.e., non-robotic), a flexible endoscope is inserted through the mouth, moved through the esophagus (up to $260\,\mathrm{mm}$ in length, $20\,\mathrm{mm} \times 30\,\mathrm{mm}$ [139]) to reach the stomach. On its path, it illuminates the human tissue and delivers visual images to the operator. This example procedure is chosen since it requires the clinician to move an instrument over a longer distance into the body cavity where it then should provide dexterous tip manipulation to steer camera, light source and tool to tissue areas of interest. A medical phantom was additively manufactured (Elastic 50A, Formlabs GmbH, Germany) as in [7] which includes a life-size esophagus and stomach of an adult human (Figure 4.11). In a clinical context, robotically assisted investigation of the esophagus may be performed with the human in the loop (i.e, teleoperated) or automatically to reach the stomach quickly and with minimal damage to human tissue. Here, the latter approach was employed to exclude the influence of a human operator and demonstrate the pure robotic performance. In this validation, the robot was manipulated

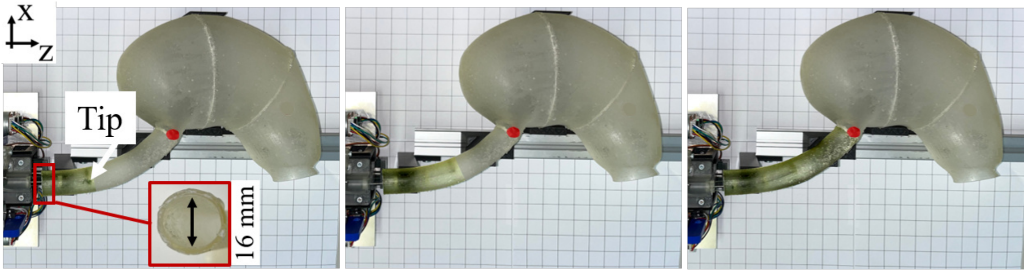

Figure 4.11.: Testing the continuum robot demonstrator in a medical phantom, mimicking a transoral endoscopy of the esophagus as a proof of concept. The entire extendable length was used to traverse the esophagus and reach the stomach (red marker). Tip additionally indicated due to partially translucent resin material. [1] © IEEE 2023.

iteratively along an interpolated path (consisting of six points) between the esophagus entry point and exit towards the stomach. Consequently, the robotic structure was properly extended into and retracted from the phantom, without decomposing or deforming the phantom walls.

Clinical Considerations

Towards future clinical application, the intention is to utilize one or multiple superelastic hollow backbones (e.g., $[\varnothing_{\text{out}}, \varnothing_{\text{in}}] = [1\,\mathrm{mm}, 0.8\,\mathrm{mm}]$) to facilitate access for small-scale surgical tools, endoscopic vision, and additional sensors. This is limited by the inner diameters of the backbones (*cf.* concentric tube robots [62]). Hygiene is a crucial aspect for surgical equipment to reduce the risk of infection. Future enhancements to the proposed extendable continuum robot must therefore account for sterility without jeopardizing the assembly process within the actuation unit and thus the variable extendability. For this design, a sterile extendable cover is required, attached only to the outlet of the actuation unit and to the distal end of the robotic structure. It should unfold alongside with the extending robot and collapse back to the outlet during retraction. However, unintended interaction between the cover and the robotic structure (e.g., sticking, flapping), and the hermetical sealing currently remain unsolved technical challenges.

Chapter Summary

In line with the contribution outlined in Section 4.1, this work introduced a novel self-assembling continuum robotic structure with a durable, kink-resistant, and biocompatible, superelastic SMA backbone. Only the utilization of this smart material enables an efficient storage of components within the actuation unit and minimizes the space demand for an effortless integration into a setup and workflow. The system design entails continuous assembly of the robotic structure during extension from inside the actuation unit up to a preset maximum extension, incorporating variable segment and section lengths. This innovative approach enables the combination of dexterous, tendon-driven actuation of two segments with a large extendable length at a small robotic diameter. Demonstrating state-of-the-art dexterity and workspace range, it has significant potential to enhance tendon-driven robotic systems for MIS.

5. Shaping Surgical Instruments with Shape Memory Alloys

This chapter focuses on the application of SMA materials as compact, integrated actuators in flexible surgical instruments, emphasizing their capability to deform in a controlled manner (Section 5.1) and sense their deformation without the need for additional sensor technology, i.e., self-sensing (Section 5.2). In contrast to conventional, teleoperated continuum robots, as discussed in the previous Chapter 4, flexible instruments are designed as hand-held devices. Therefore, flexible instruments require a less complex setup at the cost of limited available DOF compared to continuum robots.

5.1. Shape Memory Alloy – Actuation

The content of this Section 5.1 was published in *at-Automatisierungstechnik* [2]. Headlines, wording, and layout were carefully modified to fit within this work.

5.1.1. Flexible Instruments with Shape Memory Alloys

Smart materials such as SMA seem promising to contribute to the objectives of simplification and miniaturization of flexible instruments due to their ability to memorize an almost arbitrary shape when traversing a reversible crystal phase change from martensite to austenite caused by increasing temperature, referred to as the shape memory effect. If a task requires one particular target pose including a specific shape of the robotic structure, the SMA wires forming the robotic structure, can be prepared accordingly in advance (i.e., shape setting). They can reach that shape in a controlled manner during the actual task execution using simple electric power circuits with little space demand. This holds the potential of a beneficial trade-off between space demand and dexterity for particular medical applications.

Related Work

A widely used actuation principle for the more versatile continuum robot is the tendon drive, where tendons are pulled by at least one rotatory [140] or linear motor [141] per DOF for each segment. This principle was applied in the previous Chapter 4 and enhanced with a novel self-assembly approach of the robotic structure to minimize the space demand of the entire robotic system. Yet, despite the achieved miniaturization, the tendon-wise actuation requires still multiple actuators, eventually leading to bulky and complex overall hardware setups. To minimize space requirements further, tendons and their actuators could be replaced by SMA wires or spring coils, which create pulling forces by thermally induced material contraction. Despite the aforementioned large strains, SMA wires must come at great lengths to achieve sufficient bending. Besides those physical bending angle constraints, electronic connectors are required on each end of every SMA actuator [142], leading to a complex, error-prone electronic setup with increased initial load, which is additionally hard to integrate into a delicate device. To compensate for the bending constraint, Allen and Swensen [143] propose a hybrid of SMA and pneumatic actuation, reaching bending angles $> 180°$ at the cost of an additional setup for air pressure supply. In [144], SMA wires are deployed as "free-sliding" tendons within a polymeric substrate and allow for bending angles of up to $400°$. When combining multiple of such segments in a serial configuration by rigid links, a hyper-redundant robotic structure occurs, where multiple DOF can be actuated independently allowing for various complex robotic shapes, promising high dexterity and precise controlling of every segment pose [58]. When it comes to the interconnection between those segments, SMAs could be deployed in a straight configuration [145], within a pulley system, and in a purely antagonistic configuration, with an elastic joint or a hybrid combination [146]. When including the SMA's self-sensing ability, even closed-loop control regimes can be realized [147], e.g., for a three-dimensional (3D) manipulation of a needle tip in real-time. For further sensing modalities, Ren *et al.* [148] present a flat soft actuator from elastomer for variable stiffness applications, including embedded SMA and curvature sensors.

Contribution

Prior studies have predominantly focused on deploying one-dimensional (1D) strain variations of SMAs directly or in combination with a kinematic chain, leading to a multidimensional tip manipulation. However, exploration into the potential of SMAs to immediately perform more complex two-dimensional (2D) and 3D shape changes remains limited. In contrast to related work, the immediate utilization of the shape memory effect can overcome several challenges. These include extending the bending range without excessive longitudinal strains. It also reduces space requirements compared to conventional actuation approaches. Additionally, it simplifies the electric actuation setup drastically. Hence, this chapter delves into the potential of immediate shape-memory exploitation through the creation of a novel shape-changing actuator capable of executing controlled 2D bending and straightening motions for dexterous tasks during MIS. This is accomplished by deploying two **SMA actuation** wire loops with electrical contacts placed in proximity, each possessing different shape memories, alongside each other (Figure 5.1).

Regarding the research objective of this dissertation, the integration of a SMA not only replaces conventional actuation but also contributes to the objectives of flexibility, miniaturization, and practicability.

5.1.2. Design of a Novel Flexible Instrument

The novel instrument design consists of two SMA wire loops from NiTiCu forming a skeleton that provides individual actuation once heated above their austenite finish temperature $A_{\mathrm{f}} = 65\,°\mathrm{C}$. They are embedded in a monolithic flexible backbone and surround a central supply channel that connects proximal and distal ends of the instrument. The channel provides space for enhancements such as fiber optics or bendable needles. The instrument's proximal end allows for insertion of the aforementioned enhancements and to attach the contact electrodes for (controlled) power supply. Several spacer discs serve as wire guidance along the instrument to avoid short circuits. No further cable connection

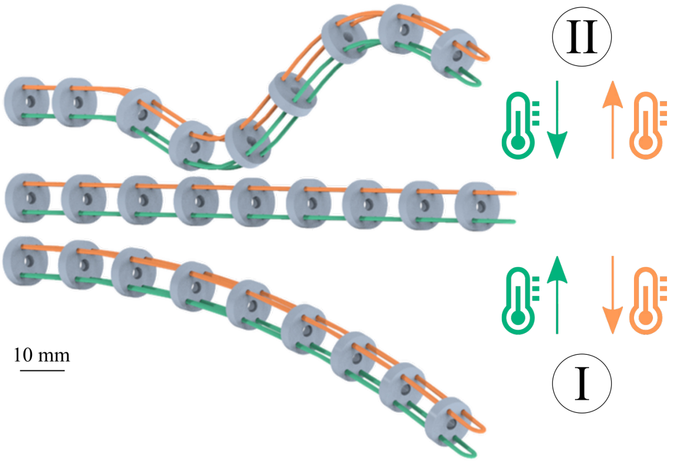

Figure 5.1.: Concept of the compact flexible actuator for minimally invasive instruments featuring two shape memory alloy (SMA) wire loops with preset shape memory for shape changing (orange), reset into straight shape (green) and central supply channel, e.g., for a gripping tool. The desired shapes are bent (I) and S-shape (II). [2] 🅭🅯 4.0.

is required for power or control actuation. For this work, two different instrument configurations were investigated and fabricated, as illustrated in Figure 5.1. Configuration (I) for a bending and (II) for an S-shape of the instrument. Both shape changes are independently obtained by an active-antagonist configuration, as described in [146]. Thus, each configuration features one SMA wire loop memorizing a shape change (bending or S-shape, respectively) referred to as shape loop (active). The other loop sets back the actuator to its initial straight shape, referred to as straight loop (antagonist). This design allows for a permanently retained pose of the distal tip without further heating if no external force is applied.

Fabrication and Assembly

The fabrication steps are presented in Figure 5.2. In step 1, segments of SMA wire with a diameter of $0.7\,\mathrm{mm}$ are cut with a length of $230\,\mathrm{mm}$ and cold-formed manually into a U-shape (loop) with a diameter of $3\,\mathrm{mm}$. To set the shape memory in step 2 for straight shape, bent shape and S-shape, heat treatment at $425\,^\circ\mathrm{C}$ for $30\,\mathrm{min}$ and subsequent quenching in water at room temperature is required for the loop segments [149,150]. Thereby, each loop segment must be clamped firmly in the desired shape and without torsion stress as it tries to restore its previous shape memory, i.e., the straight shape. Thus, holding racks are fabricated from Al, providing the desired curvature of the shapes to stabilize the loop segments during heat treatment. After heat treatment, all wire loops are cold-formed into straight shape at room temperature in step 3. In step 4, the flexible monolithic backbone with intermediate spacer disks and central supply channel is additively manufactured using a stereolithography printer with elastic resin (Formlabs GmbH, Germany). To allow for accurate evaluation, the flexible backbone model is extended for a mounting component at the proximal end and plane elements at each spacer disk for marker attachment. The wire loops are inserted into the printed backbone before its final curing. Thus, the fully cured backbone holds the SMA wires firmly throughout actuation.

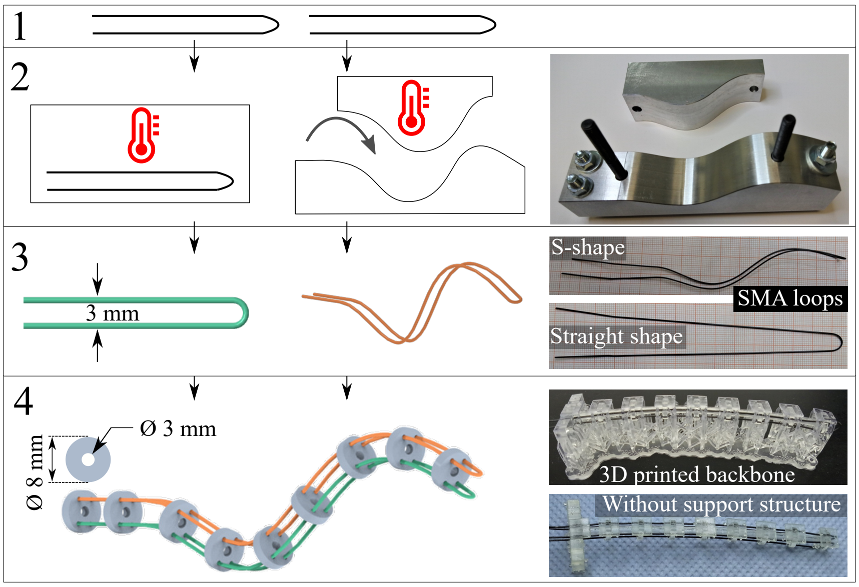

Figure 5.2.: Fabrication steps: Cold-forming wire loops (1), followed by heat treatment with customized racks from Al at $425\,^\circ\mathrm{C}$ (2). All wire loops are straightened by cold-forming (3) and inserted in the additively manufactured monolithic backbone, followed by the final curing of the instrument (4). [2] 🅭🅯 4.0.

5.1.3. Experimental Evaluation of the Actuation

The experimental setup for actuation and evaluation is presented in the following. The instrument was mounted at its proximal end in a horizontal position and connected to a laboratory power supply. Once electrified, Joule heating increased the temperature of the SMA wires, resulting in the wires memorizing their shape leading to an active shape change, and an antagonistic reset, respectively.

Visual Tracking and Instrument Shape

To control and evaluate the flexible instrument, shape estimation of its body is required. For visual tracking, a RealSense™ D435 camera (Intel Corporation, USA) observed the x-y-plane, tracking nine ArUco markers attached to the instrument body, as presented in Figures 5.4 a+c. A tracking algorithm was implemented in Python 3.9 and provided a tracking frequency of $30\,\mathrm{Hz}$. Thus, the positions of the geometrical marker center points provided time-depending shape information. Its performance was evaluated beforehand by tracking a stationary set of markers as utilized on the instrument over a time period of $90\,\mathrm{s}$, revealing a deviation of $\pm 0.35\,\mathrm{mm}$ and $\pm 0.05\,\mathrm{mm}$ in x and y, respectively. The pose for configuration I was represented by the distal end's bending. For simplicity, the two markers closest to the distal tip were used to define the instrument's orientation as the angle φ relative to the x-axis.

Control

To manipulate the flexible instrument, a PID controller was proposed in a closed-loop regime as shown in Figure 5.3 with the iteratively identified control parameters $K_\mathrm{P} = 50$, $K_\mathrm{I} = 0.5$ and $K_\mathrm{D} = 0.8$. The control variable was the bending angle φ of the distal tip. Further shape modeling parameters were not considered. For implementation, an ATmega328 (Arduino) microcontroller was deployed using two DC/DC-converters TSR-3

Series (Traco Electronic GmbH, Germany) that can perform each 3 A switching regulation via remote on/off input connected to the PWM outputs of the microcontroller at 10 Hz. The computed angle φ was transmitted from the Python script to the microcontroller via Serial Port.

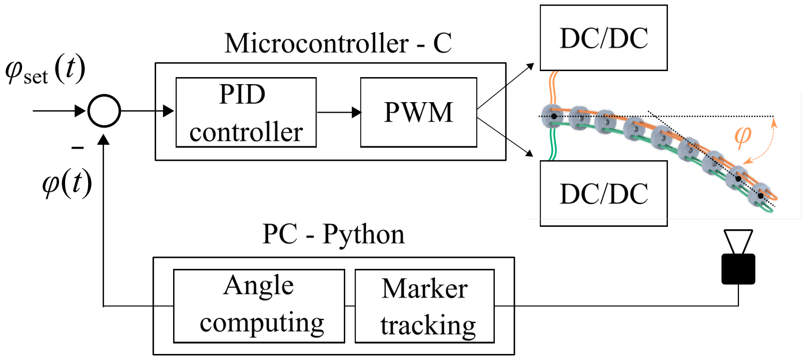

Figure 5.3.: Closed-loop control setup including marker tracking, angle computation (Python 3.9) and a PID-Controller running on a microcontroller. [2] 🅭🅯 4.0.

Evaluation Procedure

Each configuration was subjected to $n = 10$ experiment runs for workspace characterization, with cooling pauses of 180 s in between. In the case of configuration I, a control evaluation and a qualitative force validation were additionally conducted. To characterize the full workspace of the instrument, the shape loop was initially heated at current $I = 3$ A ($U_{\text{max}} = 2.6$ V) from initial straight shape and the displacement of all markers is monitored over 15 s. A (passive) cooling period of 30 s followed, during which the power supply was switched off. Then, the straight loop was heated for another 15 s. After a second cooling period of 30 s, the experiment was stopped. The cooling periods allowed for investigation of possible recoils in scenarios without power supply. Before the next experiment run started, the instrument was manually cold-formed to its initial straight shape. For force measurement, a spring scale (Micro-Line 20001 1 N, Pesola AG, Switzerland) was insulated at its interface and attached to the distal tip of the instrument (configuration I). Then, $I = 3$ A was applied, and the resulting force was measured. The control regime was demonstrated by following predefined setpoints from straight to bending shape, i.e., φ_{set} from 0° to 10° in iteration steps of 2°, each lasting for 15 s.

Results of the Experimental Evaluation

Figure 5.4a depicts the mean marker positions and Figure 5.4b the standard deviations at given times of the proposed instrument in configuration I. The maximum absolute displacement is 19.1 mm in y at the distal tip. During the cooling period, a recoil is visible, retaining an absolute displacement of the distal tip at $y < 12$ mm between $t = 15$ and 45 s. Heating the straight loop, in order to return the instrument to its initial shape, left the instrument with a remaining absolute displacement of $y > 5$ mm. Thereafter, another small recoil can be observed between $t = 60$ and 90 s.

Figure 5.4c shows configuration II in an actuated state. The planar S-shape exhibits an unintended torsion, visible on the basis of the last three markers at the distal tip. It is assumed that the SMA wire was slightly axially rotated at the distal part during assembly with the backbone, despite utmost caution. This would lead to a deviation from the strict planar shape change, and unintentionally demonstrating that the presented approach is not limited to planar shapes.

Figure 5.4d shows the workspace characterization results for configuration II. A maximum displacement of $y = 8.7\,\mathrm{mm}$ is observed close to the distal tip at $t = 60\,\mathrm{s}$. The antagonistic setback of the proximal instrument half is noticeable, while the distal half does not exhibit a significant shape deformation back to the straight shape. Presumably, the aforementioned torsion influenced the plane of bending for the distal instrument half, leading to an apparently restrictive setback in the x-y-plane. Furthermore, stronger recoils are measured as with configuration I. It should be noted that deflections in the initial poses ($t = 0\,\mathrm{s}$) are caused by manual resetting the instrument after each experiment run.

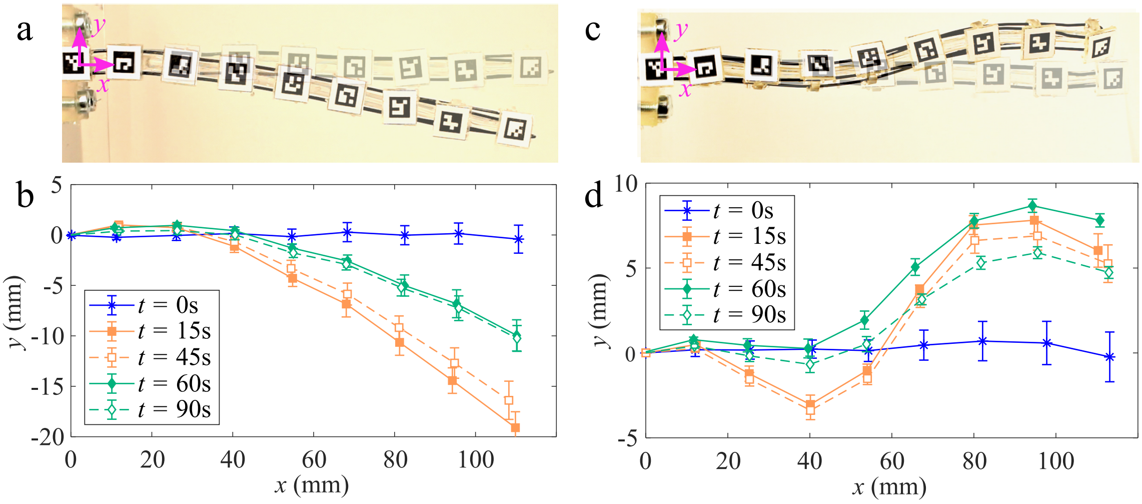

Figure 5.4.: Results of the workspace characterization for configuration I and II, showing initial pose (translucent) and maximum deflection (a+c). Shape was estimated using mean and standard deviation of marker positions at specific time steps over $n = 10$ experiment runs (b+d). The obtained shape change (orange) was reversed by the subsequent straightening (green). Dashed plots indicate the observed recoils after actuation has ended. [2] 🅭🅯 4.0.

In Figure 5.5a, the results of closed loop control of the instrument are presented. A steady-state error of $\varphi_{\mathrm{error}} < 2°$ is observed for larger setpoints. After reaching the maximum setpoint (at $10°$), angle control was lost at approximately $\varphi = 9°$. Figure 5.5b depicts an actuation with open-loop control for comparison, visualizing a much steeper bending characteristic and reaching a maximum bending angle within $15\,\mathrm{s}$. Furthermore, the force measurement revealed a maximum blocking force applied by the distal tip of $F = 90\,\mathrm{mN}$.

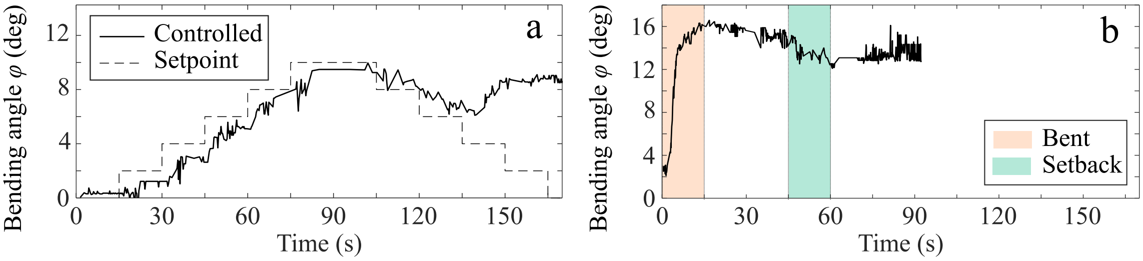

Figure 5.5.: Bending angle φ for configuration I controlled in closed-loop for setpoints φ_{set} (a). In contrast, bending angle φ for configuration I during characterization, with actuation phases for bending (orange) and setback (green) in open-loop control (b). [2] 🅭🅯 4.0.

Discussion

The workspace characterization reveals a repeatable deformation for both configurations. Although the deviation range appears usable for a handheld device, normally exposed to physiological tremor of the user, one single target shape presents an essential limitation in comparison with omnidirectional bending instruments and continuum robots, such as in [142]. In contrast, the presented approach does not require multiple individually supplied and actuated sections to transform into more complex shapes (e.g., S-shape), allowing for a smaller instrument diameter and a more compact actuation unit. For example, neglecting power supply (socket or battery) and microcontroller (which are required for all presented systems), the instrument only requires one DC/DC converter with a frame package size of $< 1\,\mathrm{cm}^3$ and two wire channels for one wire loop per desired shape. Yet in direct comparison to [142], the maximal workspace of the demonstrator is smaller, the antagonistic setback capability more restricted (especially for S-shape), and the response time slower. This is presumably due to the deployment of two SMA wire loops that reinforce and stiffen the flexible structure, thereby hindering the active wire loop mechanically, even when not actuated. This might be also the cause for the observed recoil. Furthermore, the method of passive cooling and the length of the cooling time in this work may not be optimal. Thus, a higher temperature in the shape loop could keep it from becoming fully inactive during the antagonistic setback. This hypothesis should be investigated by including temperature monitoring in future experimental setups. On the other hand, the increased stiffness of the instrument brings the advantage to avoid unintended displacement and deformation during insertion of additional instruments through the central supply channel (e.g., fiber endoscopes).

Regarding angle control, a notable path correction can be observed when comparing the angles obtained during closed-loop and open-loop control. A relatively small error φ_{error} of the bending angle for the increasing setpoint values demonstrates the effect of closed-loop SMA actuation. However, the loss of control after a longer period of actuation shows one major challenge of SMA-based robotics. When heating the wire loops over a longer period of time, they no longer leave the austenite phase but remain above the transformation temperature of $60\,^{\circ}\mathrm{C}$. Thus, the instrument stiffens and remains at its current position, where additional heating has little effect on the shape. Only a temperature change below the transformation temperature, unlocks the instrument. Hence, active cooling strategies should be considered for in-vivo use cases where multiple setpoints are targeted over a short period of time, causing heat accumulation. The transition temperature of the currently used material does not appear eligible for a surgical instrument yet, as it could damage the human tissue. Alloy compositions with an austenite finish temperature $A_{\mathrm{f}} \approx 40\,^{\circ}\mathrm{C}$ are more promising for future investigations into instrument design and fabrication. The maximum applicable force is measured to be relatively small but still in a relevant range for applications in ophthalmology (retraction, penetration) and vascular surgery (vascular clamping) [151].

5.1.4. Application Example: An Active Laryngoscopic Blade

Further medical applications can benefit from this approach, when the critical setback is not required for a procedure. As an example, a flexible laryngoscopic blade (single use) for an endotracheal emergency intubation was investigated in [3]. Endotracheal intubation is a medical procedure to secure a patient's airways, which can be challenging in emergency situations due to an individual's anatomy. Intubation blades can benefit from an adjustable design with shape memory alloys. The presented blade design, comes with two DOF, continuously transforming a straight into a curved blade, using NiTi wires with diameters of up to $2\,\mathrm{mm}$. The demonstrators thus reached mean angular deflections up to 16° without exceeding outer blade temperatures of $40\,^\circ\mathrm{C}$. Mean forces of almost $24\,\mathrm{N}$ were applicable. This experimental study emphasizes the potential to reduce the complexity of intubation procedures and increase the success rate, especially in time-critical emergency situations. This example underscores the practical applicability of this SMA-based actuation for flexible surgical instruments.

5.2. Shape Memory Alloy – Sensing

The content of this Section 5.2 was published in *at-Automatisierungstechnik* [4]. Headlines, wording, and layout were carefully modified to fit within this work.

5.2.1. Self-Sensing in Shape Memory Alloys

Despite the useful dexterity of a flexible instrument based on SMAs, their control within the human body remains challenging. The shape of the instrument within the body cavity depends on various influencing factors. Those factors are mainly the applied force at the external (proximal) end of the instrument, the mechanical property of the surrounding tissue, and the temperature of the SMA. Visual imaging devices (e.g., endoscopic cameras) that monitor the flexible instrument and the site of operation are thus crucial for clinicians to manipulate the instrument effectively. However, ideal imaging is not always provided during a medical procedure due to the lack of additional endoscopic devices, limited access into the confined space, or an impaired line of sight caused by body fluids and smoke.

For this reason, additional intraoperative information about the shape and the pose of the instrument's distal tip are highly beneficial to the operator. Due to the confined space in the cavity and the compactness of the delicate instruments themselves, attaching and operating additional sensor technology (e.g., resistance based flex sensors [152], fiber grading sensors [153]) is often hardly feasible. Instead, flexible instruments with inherent actuation such as SMAs could use the structural material for both, actuating and sensing (Figure 5.6). They not only provide intrinsic actuation once heated, but also present a variability of their electric resistance R in accordance with the change of their shape (i.e., self-sensing) [154].

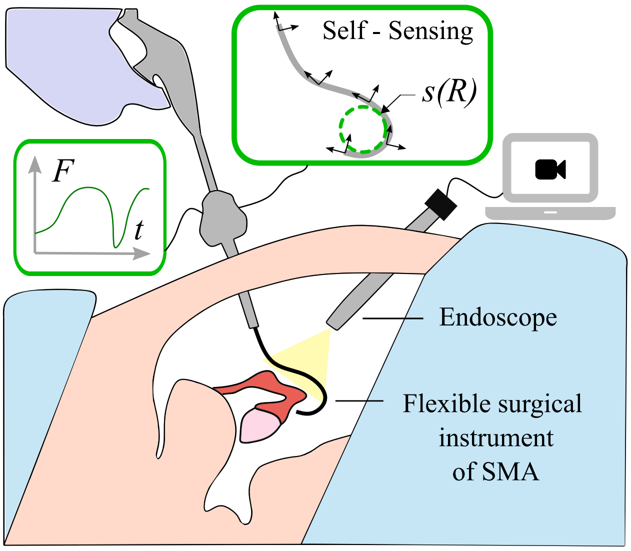

Figure 5.6.: Schematic of a minimally invasive surgery (MIS) with a flexible instrument made of a shape memory alloy (SMA). Augmenting the video endoscopy with information about deflection s and interaction forces $\boldsymbol{F}$. [4] ⓒⓘ 4.0.

Related Work

The change of the electric resistance R as an intrinsic property has been utilized in research in order to determine the strain of a NiTi alloy wire, e.g., Ikuta *et al.* [155] and Prechtl *et al.* [156]. Kaiser *et al.* have developed measurement and control electronics to use a microcontroller to heat a SMA using electric current and measure the electric resistance R [157], while Ma *et al.* implemented the control of a lengthening SMA wire using a neural network [158]. Furthermore, grasping applications driven by SMA wire actuators were investigated by Wang *et al.* who controlled the deformation of a flexible gripper to grasp deformable objects [145]. Since the electric resistance R changes as a function of the wire strain, a control based on self-sensing could be demonstrated. In addition, Lan *et al.* were able to control the position of the tip of a flexible micro-gripper [159]. They used a spring to elongate a SMA wire and forced it to contract by electric current (i.e., Joule heating). The authors followed the approach of length control further and investigated a data-driven approach using a polynomial model [160].

Contribution

Previous research has predominantly focused on estimating 1D strain variations of SMAs and has even demonstrated controlled actuation for defined loading conditions based on electric resistance. However, the potential of SMAs to immediately perform and estimate more complex 2D and 3D shape changes, has not been explored. Although, integrating compact **SMA-based actuation** and **self-sensing** at such a level could significantly enhance the design of minimally invasive surgical instruments, enabling them to access confined spaces more effectively. Therefore, this work presents the proof-of-concept of a polynomial modeling approach that correlates the electric resistance of a simplified SMA-based instrument with its shape, initially enabling 2D shape changes in novel smart minimally invasive instruments. Hence, this work introduces a proof-of-concept for a polynomial modeling approach that establishes a correlation between the electric resistance of a simplified SMA-based instrument and its shape, initially facilitating 2D shape alterations in novel smart minimally invasive instruments.

5.2.2. Shape Sensing of Flexible Instruments

A simplified instrument with inherent SMA actuation was fabricated and investigated in an experimental setup for multiple actuation cycles in different load-heat scenarios while recording various system parameters. Thus, a data-driven polynomial model could be designed which was able to estimate the instrument's shape (i.e., self-sensing).

As a simplified flexible instrument, a bending wire loop actuator was utilized as presented in Section 5.1, but without its antagonistic counterpart and the monolithic backbone (Figure 5.7a). The basic straightened (austenite) shape can be cold-formed (i.e., bent) under an external load. If the bent wire is then heated above the austenite finish temperature (here: $A_\mathrm{f} = 65\,^\circ\mathrm{C}$), the original straight austenite form is restored (Figure 5.7b). This effect of SMAs can be used to apply mechanical forces [161]. The aforementioned design allows to power the instrument at its proximal end, using Joule heating to increase the temperature of the wire, thus avoiding an interference of cable and connectors at the instrument's body.

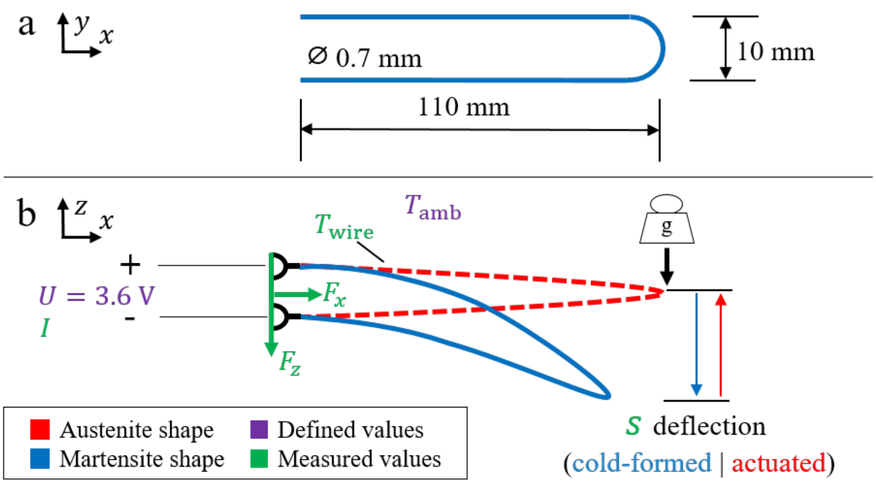
a
y
x
∅ 0.7 mm
10 mm
110 mm
b
z
x
T_{amb}
T_{wire}
g
+
$U = 3.6$ V
I
-
F_x
F_z
🟥 Austenite shape
🟦 Martensite shape
🟪 Defined values
🟩 Measured values
s deflection
(cold-formed | actuated)

Figure 5.7.: Simplified instrument design with a flat U-shaped wire from NiTiCu (a). Schematic of the shape changes between martensite (blue) and austenite states at $A_{\mathrm{f}} = 65\,°\mathrm{C}$ (red). Known parameters include power supply voltage U, ambient temperature T_{amb}, and load. Current I, force components F_x and F_z, deflection s, and wire temperature T_{wire} were measured during the experiments. [4] 🅭🅯 4.0.

Experimental Setup for Actuation and Sensing

The defined and measured values are schematically illustrated in Figure 5.7b. The electric resistance of the wire R depends on the applied voltage U at the proximal wire ends, and the electric current in the wire I, as stated in Equation 3.1. Further experimental parameters of interest include the wire surface temperature T_{wire}, the deflection s at the distal tip, as well as the applicable distal force $\boldsymbol{F}$.

The experimental setup is shown in Figure 5.8. The SMA actuator was mounted horizontally with its two proximal ends in a fixed clamp. In the unloaded state, the tip of the wire was aligned approximately at the horizontal level of the clamping. The actuator was powered via the clamped wire ends, and its temperature would increase due to Joule heating. This allowed to trigger a phase transformation from various cold-formed shapes back into the set horizontal austenite shape.

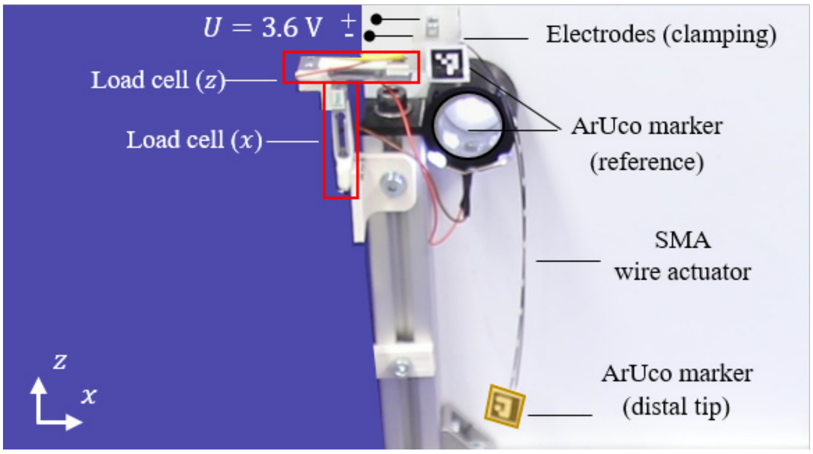
$U = 3.6$ V
+
-
Electrodes (clamping)
Load cell (z)
Load cell (x)
ArUco marker
(reference)
SMA
wire actuator
ArUco marker
(distal tip)
z
x

Figure 5.8.: Experimental setup for data acquisition of the SMA actuator. Two load cells (red) record reaction forces F_x and F_z at the clamping. Tracking ArUco markers at the clamping and the distal tip (yellow) allow measuring the deflection s. [4] 🅭🅯 4.0.

The electronics to power the wire and record the measurement data at the same time were controlled by a microcontroller (Arduino Uno Rev3 SMD). To measure the current I at a given voltage U, a measuring resistor (Isabellenhütte PBV R010, Germany) was used. Two operational amplifier circuits (Texas Instruments TLC 2272, USA) were implemented to amplify the voltage drops at the measuring resistor and the SMA wire. Then, R was calculated with Equation 3.1. The setup provided the resistance R of the SMA wire with a resolution of $1\,\mathrm{m\Omega}$ and an accuracy of $3\,\mathrm{m\Omega}$.

To measure the force components of $\boldsymbol{F} = [F_x, F_z]$ on the wire clamping, two load cells with measuring amplifier (Sparkfun Electronics TAL221, HX711, USA) were used. The signals were calculated and processed by the microcontroller and transmitted via Serial connection to a host computer. In the heating phase, $\boldsymbol{F}$ and R values were measured with a frequency of up to $385\,\mathrm{Hz}$, limited by the electronic evaluation system of the load cells. Data acquisition in the cooling phase was conducted with $1.75\,\mathrm{Hz}$ due to the fact that R could only be measured when current flows through the actuator. Consequently, the current rate had to be kept at a minimum during cooling phase to avoid additional unintended Joule heating.

A measurement script was developed (Python 3.9) to track the position of the wire tip with an ArUco marker and a visual camera (Intel Corporation RealSense™ D435, USA), as well as to compute and store the position data. Preliminary tests revealed a marker tracking position accuracy of $0.2\,\mathrm{mm}$. A thermal imaging camera (Teledyne FLIR LLC FLIR E60, USA) was used for contactless temperature monitoring of the wire surface T_{wire}. The ambient temperature T_{amb} was the constant room temperature ($22.5\,^{\circ}\mathrm{C}$) of the laboratory and was monitored with an additional sensor. The temperature fluctuation remained within a range of $2\,^{\circ}\mathrm{C}$.

To bend the actuator at ambient temperature, weights were attached to the actuator's distal tip. The load would pull the tip down in negative z direction. If the actuator was then powered, the shape memory effect opposed the shape change and lifted the weight. When the power was turned off and the temperature decreased, the wire again deformed by the gravitational force of the weight.

The generalized deflection s was utilized as a simplified measure of the bent shape of the wire (Figure 5.7 and Figure 5.9). In this work, s corresponds to z. It should be noted, that due to many past actuation cycles of the actuator ($n > 300$), a two-way shape memory effect was observed [162]. The bent shape in martensite phase had become part of the material's memory. Thus, the bent shape was obtained even in cases without any load. This way, a common starting point between $s = -138\,\mathrm{mm}$ (unloaded) and $s = -143\,\mathrm{mm}$ ($100\,\mathrm{g}$) was provided for both cases, with and without load.

5.2.3. Modeling Self-Sensing Characteristics

The modeling of the self-sensing characteristics of the SMA material includes the training data acquisition and the polynomial modeling.

Training Data Acquisition

Load cases were defined for data acquisition in order to subsequently fit a polynomial model. In a load case, a specific weight and heating period were defined. Weights were applied in the range from $0\,\mathrm{g}$ to $100\,\mathrm{g}$ in $10\,\mathrm{g}$ steps. Preliminary tests revealed a maximum

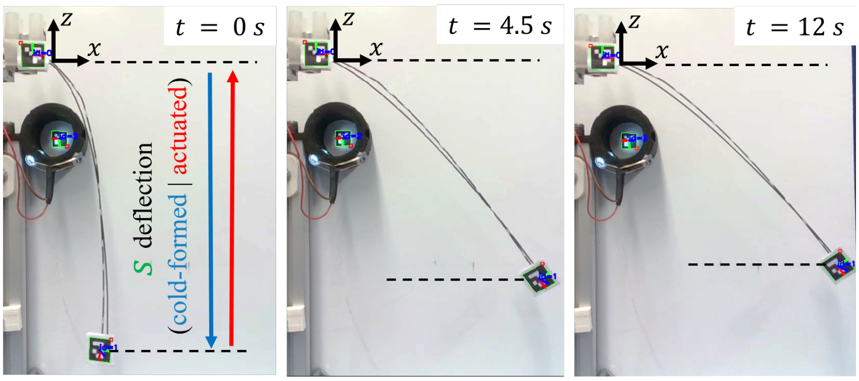

Figure 5.9.: Actuator bending shape at 0 s, 4.5 s and 12 s. A visible deflection of the distal tip over an actuation period of 0 s to 12 s can be observed. [4] 🅭🅯 4.0.

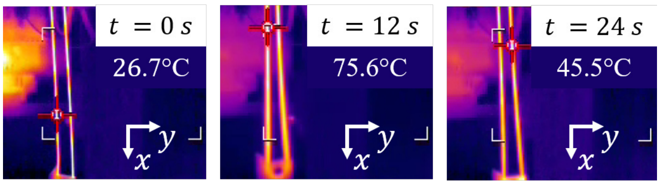

Figure 5.10.: Actuator surface temperature during an actuation cycle, captured with a thermal imaging camera. Heating period was set to 12 s, followed by a (passive) cooling phase for the remaining 228 s of data recording. Every trial started at $T_{\text{wire}} < 27\,^\circ\text{C}$. [4] 🅭🅯 4.0.

possible heating period of 12 s at 3.6 V, avoiding over-heating and damage to the setup. The heating period was set accordingly. Maximum temperatures on the actuator surface T_{wire} remained below $T_{\text{max}} = 80\,^\circ\text{C}$ during the investigations (Figure 5.10).

The experimental procedure of an actuation cycle started for each case with the loading of the actuator at ambient temperature T_{amb} (i.e., in martensite state). This lead to a deflection of the distal tip from the initial horizontal position. Then, a voltage of 3.6 V was applied by a laboratory power supply to reobtain the horizontal straight shape (Figure 5.9). Data were recorded for 240 s from the start of heating. This procedure was repeated twice without resetting the actuator load-free to the horizontal shape. The overall training data thus included 22 experimental training cycles, namely two trials for each of the eleven weights.

Polynomial Modeling

A polynomial approach was chosen for the shape estimation since it allows in a simple manner to represent a nonlinear relationship of the measurement in multiple dimensions. The model was developed in MATLAB 2021b and estimates the vertical deflection of the actuator tip $\hat{s}$ based on the measured input parameters of the resistance R, the vertical force at the clamping F_z, and the heating status, schematically shown in Figure 5.11.

The force data is required in addition to the resistance to cover medical use cases of arbitrary unknown interaction forces between instrument and tissue. Only F_z was considered as preliminary tests revealed it as the dominant force component for the investigated load cases. The general representation of the 2D-polynomials can be written as

$$\hat{s} = \sum_{i=0}^{N_R} \left(\sum_{j=0}^{N_F} (p_{ij} \cdot R^i \cdot F_z^j) \right) \tag{5.1}$$

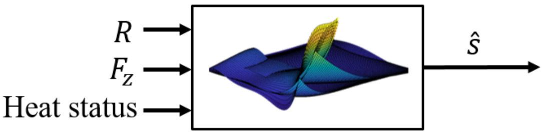

Figure 5.11.: Schematic of the polynomial model with the input variables of resistance R, force F_z, and heat status. The output is a deflection estimate $\hat{s}$. [4] 🅭🅯 4.0.

where i and j indicate the power of R and F_z with the coefficient p_{ij}. N_R and N_F indicate the highest degree of the polynomial in the dimension R and F_z, respectively. The polynomials were fitted to the data with the *RMSE* function minimizing the root-mean-square error Q_{RMS} defined as

$$Q_{\text{RMS}} = \sqrt{\frac{1}{N_{\text{data}}} \sum_{k=1}^{N_{\text{data}}} (\hat{s} - s)^2} \tag{5.2}$$

where $\hat{s}$ denotes the estimated value, s the actual measured value, and N_{data} is the number of measurement points during data acquisition. Since the relationship between R and s is characterized by a hysteresis depending on heating and cooling phases, the actuation cycle was subdivided. In contrast to Lan *et al.* [160], the hysteresis was not reduced to one single polynomial. Instead, four separate polynomials were fitted for the four different subsets, thus covering the hysteresis entirely (Figure 5.12). Each subset can be distinguished based on heating status (i.e., heating, cooling) and the resistance R (i.e., increasing, decreasing) and thus be modeled by a separate polynomial.

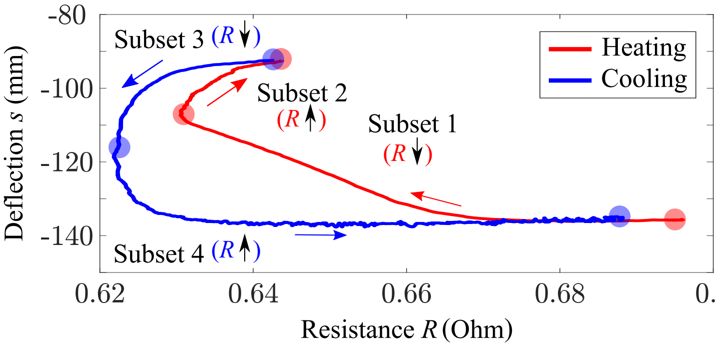

Figure 5.12.: Measured resistance R and deflection s for no load of a full actuation cycle of the actuator, including heating (red) and cooling phase (blue). Colored arrows indicate the chronicle order of subsets 1–4, subdividing the actuation cycle into four polynomial submodels, based on whether the resistance R increases or decreases. Semi-transparent circles denote the transitions between subsets. [4] 🅭🅯 4.0.

For real-time estimation, the model compares the actual measured resistance value to the last measured values. Based on the heating status and the behavior of the electric resistance, the model estimates the deflection within the corresponding section. The computed coefficients p_{ij} are listed in Table 5.1.

5.2.4. Experimental Evaluation of Actuation and Sensing

For the purpose of model evaluation, further experiments were conducted to test the model for three simplified application scenarios, as shown in Figure 5.13. Those included the actuation against no resistance i.e., $0\,\mathrm{g}$ load (Figure 5.13a), small resistance i.e., $20\,\mathrm{g}$ load (Figure 5.13b), and a blocking resistance occurring at 50% of maximum deflection (Figure 5.13c), which corresponds to $s \approx -116\,\mathrm{mm}$.

Table 5.1.: Coefficients for the 2D polynomial model. [4] 🅭🅯 4.0.

	Subset 1	**Subset 2**	**Subset 3**	**Subset 4**
Coefficients	$N_R = 4$	$N_R = 2$	$N_R = 3$	$N_R = 5$
p_{ij}	$N_F = 3$	$N_F = 4$	$N_F = 5$	$N_F = 4$
p_{00}	-3.298e+05	-3.907e+04	-1.86e+06	7.809e+06
p_{01}	-4.525e+04	7.412e+04	5.202e+06	-8.168e+05
p_{02}	8732	-3.771e+04	-3.158e+06	8.456e+04
p_{03}	-903.2	-9.15e+04	1.937e+04	-1.027e+04
p_{04}	-	-	7605	231.4
p_{05}	-	-	-636.9	-
p_{10}	2.048e+06	1.213e+05	8.762e+06	-5.79e+07
p_{11}	1.83e+05	-2.314e+05	-2.455e+07	4.761e+06
p_{12}	-2.311e+04	-50.25	1.488e+07	-3.535e+05
p_{13}	1284	-	-8.966e+04	3.009e+04
p_{14}	-	-	-8870	-271.7
p_{20}	-4.752e+06	-9.431e+04	-1.376e+07	1.716e+08
p_{21}	-2.467e+05	1.182e+05	3.861e+07	-1.041e+07
p_{22}	1.522e+04	-	-2.333e+07	4.9e+05
p_{23}	-	-	8.746e+04	-2.234e+04
p_{30}	4.883e+06	1.8e+05	7.202e+06	-2.543e+08
p_{31}	1.108e+05	115.4	-2.023e+07	1.013e+07
p_{32}	-	-	1.218e+07	-2.246e+05
p_{40}	-1.876e+06	-553.4	-	1.883e+08
p_{41}	-	-	-	-3.695e+06
p_{50}	-	-	-	-5.576e+07

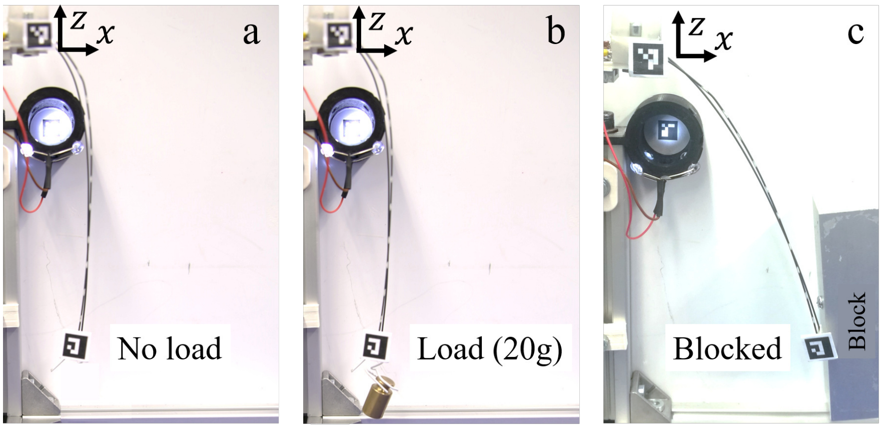

Figure 5.13.: Load-heat scenarios for model evaluation with no load (a), 20 g (b) weight, and blocked at 50% (c). [4] 🅭🅯 4.0.

In addition, the heating period for each scenario was varied. Besides the maximum heating period of 12 s representing a full actuation cycle, also shorter heating periods had to be considered. In medical use cases, flexible instruments might be actuated to transform into intermediate shapes between initial and maximum deflection. Therefore, the heating period of 4.5 s was also tested. In a third variation, a repetitive readjustment of the shape was simulated with a short heating period of 4.5 s, a 7.5 s cooling break, followed by another 6 s long heating period. Thus, for the evaluation, nine different load-heat scenarios were conducted with two experimental trials, each.

Figure 5.14 presents the quantitative evaluation procedure schematically. The estimated deflection $\hat{s}$ of the wire was subsequently calculated with the polynomial model using only the measured values of resistance R, the vertical force F_z, and the heat status as inputs. These estimated values were then compared to the recorded s_{eval} data. In Figure 5.15 the fitted 2D-polynomials are shown. The experimental training cycles for fitting the model included electric resistance R values from $0.62\,\Omega$ to $0.7\,\Omega$, loads from $0\,\text{g}$ to $100\,\text{g}$ and measured deflection values s from $-143\,\text{mm}$ to $-92\,\text{mm}$. Deflection estimations outside these ranges were not valid due to extrapolation errors with high-degree polynomials. Additionally, a comparison of measurement points of one evaluation trial without load is plotted.

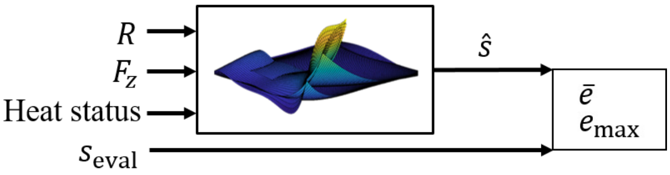

Figure 5.14.: Schematic of the evaluation of the polynomial model. Measured deflection data s_{eval} is collected for nine scenario-heating cases and compared to the estimated deflection of the model $\hat{s}$ to find the estimation error e. [4] 🅭🅯 4.0.

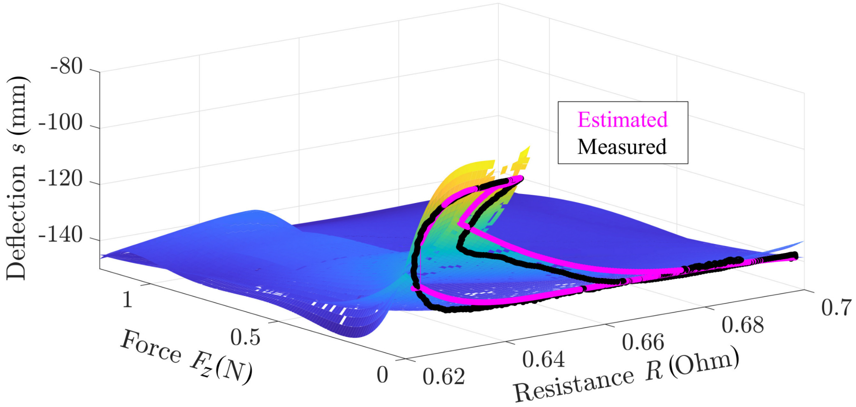

Figure 5.15.: 2D polynomial model for subsets 1–4 correlating resistance R and force F_z in order to find the deflection s. Comparing the model's estimation $\hat{s}$ and measured deflection s_{eval} for 12 s heating time and without load. [4] 🅭🅯 4.0.

The mean estimation error $\bar{e}_k$ over all measurement points k in N_{data} in one scenario is defined as

$$\bar{e}_k = \frac{1}{N_{\text{data}}} \sum_{k=1}^{N_{\text{data}}} \underbrace{(|s_{\text{eval}}| - |\hat{s}|)}_{e_k} \tag{5.3}$$

where the maximum error is $e_{\text{max}} = max(e_k)$. The mean estimation error $\bar{e}$ about all evaluation trials is

$$\bar{e} = \frac{1}{N_{\text{trial}}} \sum_{tr=1}^{N_{\text{trial}}} \bar{e}_k. \tag{5.4}$$

Results of the Model Evaluation

As mentioned in Section 5.2.3, the dataset to fit the model consists of 22 experimental cycles, two trials for eleven different weights. For the evaluation, new trials were carried out with nine different load-heat scenarios. Figure 5.16 shows the correlation of electric resistance R, as well as estimated deflection $\hat{s}$ and measured deflection s_{eval} for the nine load-heat scenarios, with Table 5.2 summarizing the mean estimation error $\bar{e}$ and maximum estimation error $e_{\max}$. Overall, $\bar{e}$ is found in a range of $0.17\,\mathrm{mm}$ to $3.61\,\mathrm{mm}$, and $e_{\max}$ in a range of $4.19\,\mathrm{mm}$ to $20.78\,\mathrm{mm}$, respectively. The load-heat scenario of $20\,\mathrm{g}$ for $4.5\,\mathrm{s}$ heating period obtained the smallest estimation error $\bar{e} = 1.23\,\mathrm{mm}$ and $e_{\max} = 4.19\,\mathrm{mm}$.

Figures 5.16 a-c present each a full actuation cycle, including subsets 1–4. For the unloaded case (Figure 5.16a), a deflection range of up to $44\,\mathrm{mm}$ was measured and estimated with a mean error of $\bar{e} = 0.21\,\mathrm{mm}$. The largest deviation occurred during the transition between subset 1 and 2 ($e_{\max} = 5.94\,\mathrm{mm}$). For the loaded case of $20\,\mathrm{g}$ (Figure 5.16b), the deflection was reduced to a range of approximately $20\,\mathrm{mm}$, while the mean estimation error increased to $0.88\,\mathrm{mm}$ and the maximum error decreased to $6.12\,\mathrm{mm}$ compared to no load. As presumed, the possible deflection decreases with increasing load. If the deflection is blocked entirely (Figure 5.16c), subsets 2 and 3 are forced on a similar deflection plateau. The estimation for those subsets is shifted towards larger absolute deflections, leading to a mean error $\bar{e} = 2.78\,\mathrm{mm}$ ($e_{\max} = 16.03\,\mathrm{mm}$). Similarly, high errors are observed with all blocking scenarios (Figures 5.16 f, i). It is hypothesized that the observed phenomenon and the associated high estimation errors are attributed to the force impact and direction upon the actuator's contact with the block, where the maximum force components measure $|F_x| = 0.1\,\mathrm{N}$ and $|F_z| = 0.04\,\mathrm{N}$. However, the model's training data only accounts for the z component, relevant in prior actuation cycles with given weights.

Table 5.2.: Results of the model evaluation. Absolute mean and maximum estimation errors for nine load-heat scenarios. Color-coded from the lowest error (green) to the highest error (red). [4] 🅭🅯 4.0.

		0 g	20 g	Blocked
12 s heating	$\bar{e}$	0.21 mm	0.88 mm	2.78 mm
	$e_{\max}$	5.94 mm	6.12 mm	16.03 mm
4.5 s heating	$\bar{e}$	3.61 mm	1.23 mm	1.97 mm
	$e_{\max}$	20.78 mm	4.19 mm	15.35 mm
4.5 s and 6 s heating	$\bar{e}$	0.33 mm	0.17 mm	2.03 mm
	$e_{\max}$	14.4 mm	9.33 mm	16.36 mm

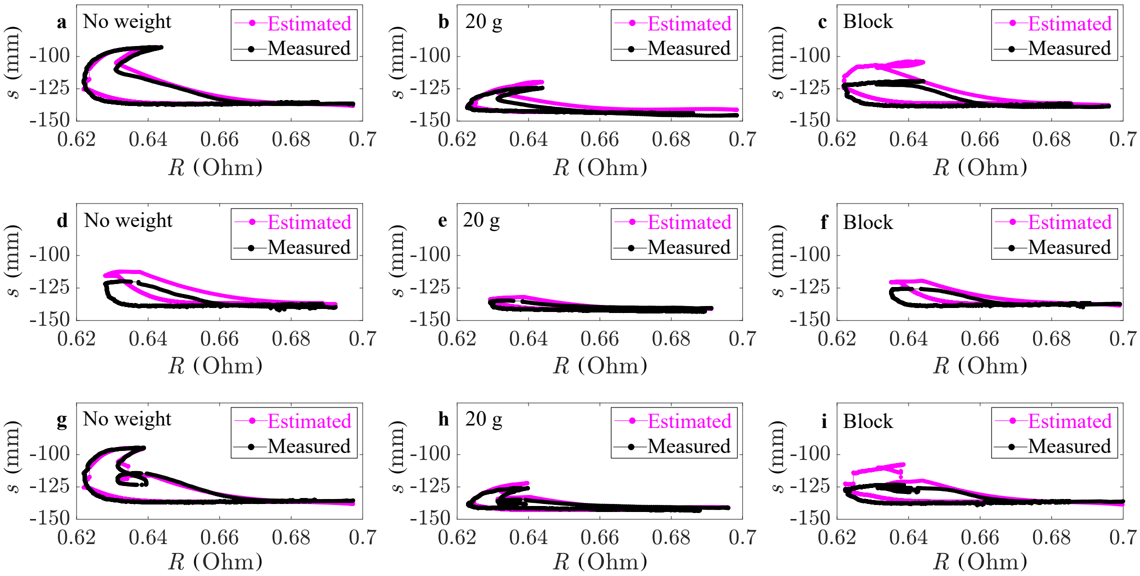

Figure 5.16.: Evaluation results of the polynomial model for nine exemplary load-heat scenarios. Comparing mean estimated deflection $\hat{s}$ to mean measured deflection s_{eval} for three different load cases and heating cases for 12 s (a–c), 4.5 s (d–f) and 4.5 s, and 6 s (g–i). [4] 🅭🅯 4.0.

Consequently, in this particular scenario, wherein F_x dominates, the model appears insufficient to accurately predict the deflection. This limitation should be addressed in future work.

Figures 5.16 d–f present each only partial actuation cycles with a limited heating period of $4.5\,\mathrm{s}$. Due to the shortened heating, the model does not estimate the deflection using subset 2 and 3. Figure 5.16d shows that the model estimates the deflection not as low as it was measured. This leads to the largest maximum estimation error $e_{\max}$ of $20.78\,\mathrm{mm}$. A similar behavior occurs in Figure 5.16f with block and limited heating period of $4.5\,\mathrm{s}$. In comparison, Figures 5.16 g–i display an extra loop between subset 2 and 3 where the intermediate cooling period interrupts the heating.

Discussion

The results of the experimental evaluation suggest that the presented model is able to predict deflections under certain boundary conditions, such as constant ambient temperature and defined load cases. Still, the model seems to be insufficient to estimate the deflection during shortened heating phases. It is hypothesized that this might be due to the lack of training data for such cases.

It is important to highlight that only one very simple wire geometry with a history of training cycles ($n > 300$) was investigated in this first proof-of-concept. SMA material is highly nonlinear [163] and its actuation behavior depends on its unique history of temperature and load. Therefore, the presented polynomial model in its current form might be capable to estimate the behavior of this one actuator. However, it may lack the ability to generalize, which refers to its capability to estimate the properties of another actuator with differing specifications (such as material composition, length, diameter) and operational history. The transfer to more complex, e.g., S-shaped actuator geometries, is also still pending. Moreover, the disadvantage of modeling with polynomials becomes apparent in the marginal ranges of the electric resistance and force values. If a measured value is processed that lies outside the fitting area of $0.62\,\Omega < R < 0.7\,\Omega$ and $0\,\mathrm{N} < F_z < 1.2\,\mathrm{N}$, respectively, the polynomials may tend towards $\pm\infty$ and estimate deflections accordingly.

In order to estimate the shape for unknown load cases, additional force sensors must be used. Adding another conventional sensor modality clearly weakens the efficiency of the self-sensing approach. Yet, in the context of hand-held instruments in MIS, cost-effective and compact multi-axial force sensors can be integrated easily in the handle design to enhance the instrument. It should be also noted that the observed maximum wire temperature of $T_{\mathrm{wire}} \approx 80\,^{\circ}\mathrm{C}$ is not suitable for an instrument outer surface in direct contact with human tissue. Thus, shape memory alloy compositions with lower austenite finish temperatures should be considered.

For future work, it is recommended to investigate multiple actuators for large-scale data acquisition and evaluation tests on new, unseen actuators. This would allow for a more comprehensive understanding of their behavior and performance. However, a major challenge is the problem of individual history of each actuator, which remains a limiting factor for efficient data acquisition and poses high demands on the shape-setting process. On the modeling, further nonlinear modeling approaches could be explored. By incorporating nonlinearities (e.g., Preisach modeling), the behavior and dynamics of the actuator could be estimated more accurately. Additionally, machine learning algorithms (e.g., reinforcement learning) could be employed to identify patterns in the behavior of the actuator and provide a more precise representation of its dynamics. Finally, the integration of these models into closed-loop control could lead to independence from visual support, at least for short periods of time.

5.3. Towards Actuated Self-Sensing Instruments

The given results in Section 5.1 demonstrate that multiple SMA wire loops can be combined in one actuator to create various bending motions and setbacks towards their initial pose with minimal space demand. Thus, the presented actuator proof-of-concept shows the potential as a space-effective alternative to shape a handheld surgical instrument, immediately utilizing the shape memory effect of SMA materials, for a certain target shape required to address known navigation challenges. However, the disadvantages of a limited workspace and the potential loss of control due to overheating may jeopardize the benefit of the actuator in the clinical environment. Therefore, it is crucial to identify those surgical procedures that can benefit even from small, anticipated shape changes and small applicable forces within a limited time window. A SMA-driven laryngoscopic blade for endotracheal intubation was discussed as a first example of such a suitable procedure, deploying an anticipated, one-way shape memory deformation. Future research shall address 3D-shape changes and design optimization regarding workspace enlargement, and enhanced temperature management to mitigate heat-related risks.

Furthermore, the approach of self-sensing, as presented in Section 5.2, has shown potential in facilitating non-visual tracking of intricate 2D shape changes in SMA-driven flexible instruments for medical applications. However, this work has shown that it is advisable to supplement this approach with additional force sensing capability to safely use it in procedures where interaction forces with human tissue are unknown. Augmenting information of flexible instruments with additional shape information during usage could then compensate for impaired visibility and make minimally invasive procedures safer in the future.

6. A Compliant Sensor Arrays for Passive Magnetic Instrument Tracking

The content of this Chapter 6 was published in the *IEEE Sensors Letters 2023* [5] © IEEE 2023. Headlines, wording, and layout were carefully modified to fit within this work.

6.1. Tracking Instruments with the Human Body

Minimally invasive interventions in medical fields, such as gastroendoscopy, laparoscopy, or endovascular surgery, present convincing alternatives to open surgeries since they promise faster recovery times and less post-operative complications [27, 164]. In the previous Chapters 4 and 5, innovative design methodologies for continuum robots and flexible instruments were explored. These approaches augment conventional instruments by providing additional DOF. However, as surgical instruments are inserted into the human body, the line-of-sight is lost. In the realm of endovascular surgery, intraoperative visual imaging, such as computed tomography angiography (CTA), can help and allows for minimally invasive endovascular navigation, usually at the cost of increased ionic radiation for patient and medical staff. As an improvement, instruments can be augmented with magnetic material and then tracked by magnetic field sensors, a harmless procedure for both, patients and staff. However, common bulky magnetic sensor systems in close body proximity can disturb the visibility and impede physical access for the medical experts, jeopardizing acceptance in the operation room.

Related Work

Wearable, compliant sensor systems for immediate attachment to the human body and with reduced spatial footprint can improve practical usability of magnetic tracking. The benefit of fixed attachment is substantial, as it eliminates unintended relative motion between the patient and the sensor system. Without it, constant monitoring and registration of the relative poses of the patient and sensor system would be necessary to maintain high tracking accuracy of the surgical instrument. This additional effort is exemplified when deploying a commercially available electromagnetic spatial measurement system (e.g., Aurora, NDI Europe GmbH), as utilized for evaluation purposes in Chapter 4. Furthermore, minimizing the distance between sensors and tracking target can lead to a better signal-to-noise-ratio, rendering sensing less prone to ambient electromagnetic disturbances [165] and thus decreasing the tracking error [166]. Moreover, the expected sensing error can simply be reduced by fusing the measurements from a larger number of sensors [167], e.g., arranged in multidimensional array configurations. Khalil *et al.* follow this approach by implementing a 1D line of Hall-effect sensors along a blood vessel in order to track a magnetic helical coil inside the vessel with a position error of $2.35\,\mathrm{mm} \pm 0.4\,\mathrm{mm}$. The coil is manipulated with externally rotating magnets and able to clear blood clots [168]. Son *et al.* present a rigid 2D planar sensor array featuring 8×8 Hall-effect sensors and a method to localize 5 DOF of an inserted capsule with a position error of $2.1\,\mathrm{mm} \pm 0.8\,\mathrm{mm}$ and angular error of $6.7° \pm 4.3°$ [169]. Furthermore, various groups investigate how to utilize 2D arrays to cover 3D volumes, such as Hu *et al.*, who surround a cuboid workspace with four 4×4 arrays using anisotropic magnetoresistive sensors, achieving an average position error of $1.8\,\mathrm{mm}$ and orientation error of $1.6°$ within the embraced volume [170]. To qualify such systems for medical usage, the sensor array can be mounted on a wearable harness, featuring additional permanent magnets directly on the human body, reducing errors induced by body movement from $30.1\,\mathrm{mm}$ to $3.8\,\mathrm{mm}$ [171]. In a comparable work, Fu *et al.* combine rigid sensor arrays with an inertial measurement unit (IMU) to account for the earth's magnetic field when a patient's pose changes during a procedure, leading to errors below $1.8\,\mathrm{mm}$ [172].

Maréchal *et al.* present a systematic design approach for sensor placement to monitor hand-held devices for ventriculostomy and conclude that optimized sensor placement can have a stronger impact than increasing purely the number of sensors [167]. The authors thus break with the convention of strictly ordered sensor alignment. However, a variable shape of multiple sensor units and thus unknown or insufficiently estimable sensor poses in space create an additional complex problem that must be solved prior to the actual tracking task. For an advanced sensor placement in the closest proximity to the body surface, Sun *et al.* present a compliant heterogeneous magnetic sensor system to localize a medical instrument during nasogastric intubation. The system features an additional resistance-based flex sensor to estimate its own bending and achieves localization errors below $2\,\mathrm{mm}$ [173]. The authors enhanced their approach by implementing several modules over the entire upper body to track the instrument on its entire path [174].

Contribution

In contrast to aforementioned related work, a wearable, compliant 2D sensor array is investigated, which is fabricated of a flexible printed circuit board (PCB) and 16 Hall-effect sensors, offering minimal, but effective mechanical constraints on the sensor array. The system is capable of estimating the bending angle of its own shape (i.e., self-sensing) without additional sensor modalities and sufficiently accurate to eventually track a **ferromagnetic** instrument inside the human body cavity. It is hypothesized that higher bending angles reduce the Euclidean distance error e_{array} of the tracking, since the distance between instrument and sensors decreases. As an unintended side effect, however, it is expected that higher bending angles can increase the bending estimation error $\hat{\lambda}_{\text{error}}$ in the same way. Therefore, these two effects are experimentally investigated in order to find, whether compliant sensor arrays can outperform rigid sensing systems.

In regard to the overall research question of this dissertation, the utilization of a ferromagnetic material enhances the surgical instrument so that it can be tracked with a compliant, compact, sensor system that can be easily worn by the patient during the operation. This work thus contributes to the overall research objective of this dissertation of achieving compliance, miniaturization, and practicability by means of a smart material.

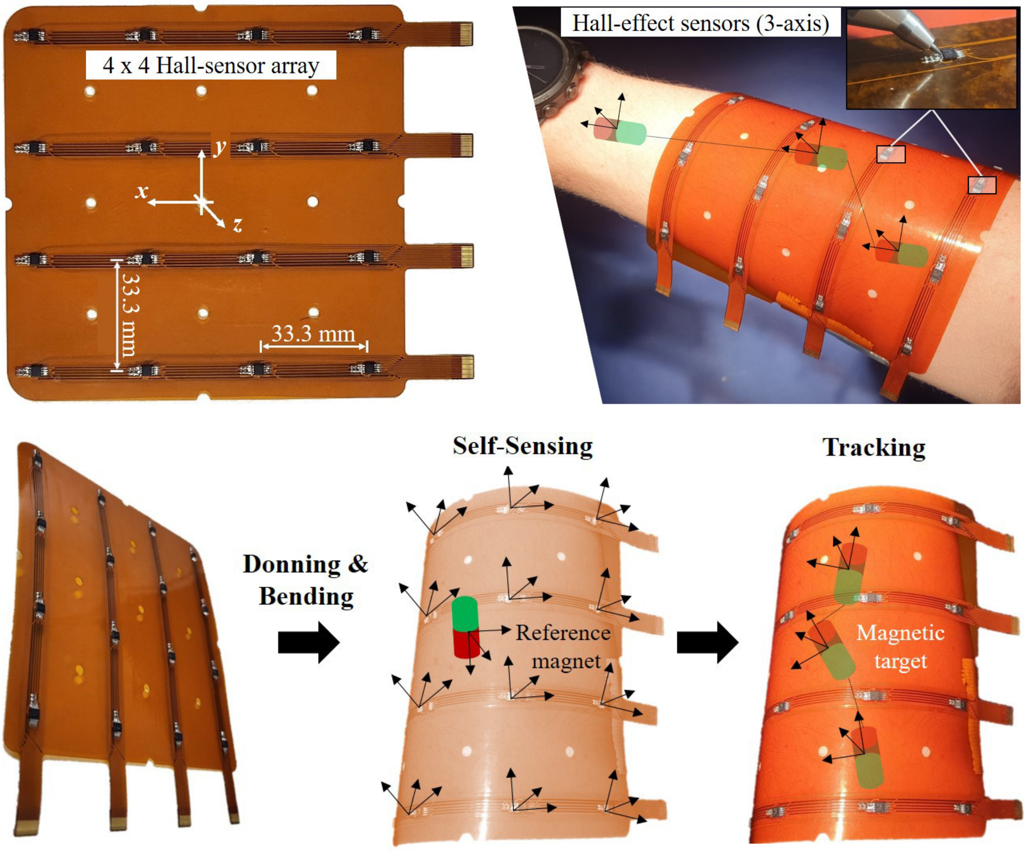

Figure 6.1.: Tracking a magnetic target (e.g., ferromagnetically enhanced surgical instrument) with a wearable compliant 4×4 Hall-effect array. Bottom: The sensor system is donned onto the human body and bent. A circular bending shape is determined through self-sensing, facilitated by a removable reference magnet. Then the magnetic target can be tracked within the body. Adapted from [5] © IEEE 2023.

6.2. Design of a Compliant Magnetic Sensor Array

To locate a magnetic target inside the human body, the sensor system can be attached to the body and bent to fit an arbitrary curved body surface, as shown in Figure 6.1. Subsequently, the system is calibrated in software for noise cancellation. Additionally, the sensor array shape is estimated to register the individual sensors' poses. Using this information, the magnetic target can be tracked. To simplify the calibration, the body shapes are approximated as cylindrical (i.e., legs, arms). In addition, only the position of a single magnetic target (e.g., instrument) is tracked.

6.2.1. Sensor Hardware

The sensor system consists of a customized compliant PCB. It was fabricated (Multi Leiterplatten GmbH, Germany) with $141\,\mathrm{mm}\times118\,\mathrm{mm}$ in size and a thickness of $161\,\mu\mathrm{m}$. The two-layered design of the conductive traces considers a preferred orientation to protect them from mechanical wear during shape variation. Preliminary tests with conductor grids embedded in silicone lead to broken cables when the array was deformed multiple times. This problem was solved by lamination of the PCB. The PCB carries a $100\,\mathrm{mm}\times100\,\mathrm{mm}$ array of 4×4 Hall-effect sensors (3-axis) TMAG5170A1 (Texas Instruments Inc., USA) with a linear magnetic range of $\pm25\,\mathrm{mT}$, leading to a full array sample rate $> 90\,\mathrm{Hz}$. Furthermore, this design allows subdividing the array into four individual sensor strips to investigate even more complex scenarios in future work, as recommended by Maréchal *et al.* in [167]. An interface of conventional PCBs connects the sensor array to a microcontroller (Arduino Mega, ATmega 2560) and via Serial connection to the host computer. To mimic a medical instrument with a magnetic tip, a neodymium magnet ($\varnothing 7.5\,\mathrm{mm}$ x $20\,\mathrm{mm}$) is chosen, magnetized axially along the axis of rotational symmetry.

6.2.2. Magnetic Model

The permanent magnet, described in Section 6.2.1, is numerically modeled to obtain the distribution of the magnetic flux density B and its gradient in a cylindrical coordinate system.

This is achieved by using the Coulombian approach, as introduced in Section 3.2.4, for a cylindrical workspace with the height $h_{\mathrm{ws}} = 400\,\mathrm{mm}$ and radius $r_{\mathrm{ws}} = 200\,\mathrm{mm}$, exploiting the rotational symmetry of the magnet's geometry. A remanence $M_{\mathrm{r}} = 1.44\,\mathrm{T}$ and a uniform magnetization over the magnet's volume are considered. For typical medical use cases, the magnetic target is either surrounded by air, water, or human tissue, thus the relative permeability of $\mu_{\mathrm{r}} = 1.0$ [175] is assumed. The discrete model is calculated with a resolution of $0.25\,\mathrm{mm}$ for both dimensions.

6.2.3. Tracking Approach

In order to detect a magnetic target $\boldsymbol{p} = [x, y, z]$ the least squares approach of the *scipy.optimized* package (Python 3.9.13) was implemented with the trusted region reflective method to minimize the cost

$$Q_{\mathrm{LS}}(\boldsymbol{p}) = \frac{1}{2} \sum_{u=0}^{15} \Phi \left(\left(\hat{\boldsymbol{B}}_u - \boldsymbol{B}_u(\boldsymbol{p}) \right)^2 \right) \tag{6.1}$$

where $\boldsymbol{B}_u$ is the measured magnetic flux density and $\hat{\boldsymbol{B}}_u$ is the estimated magnetic flux density based on the magnetic model for sensor u. Φ is a loss function to support reliable and fast convergence [176]. In this work, the L1-loss is defined as

$$\Phi(q) = 2(\sqrt{1+q} - 1) \tag{6.2}$$

with

$$q(\boldsymbol{p}) = \left(\hat{\boldsymbol{B}}_u - \boldsymbol{B}_u(\boldsymbol{p}) \right)^2 . \tag{6.3}$$

This approach can be deployed for both, the estimation of the bending shape and the actual position tracking.

6.2.4. Bending Shape Estimation

A cylindrical bending of the 2D-array is modeled in Figure 6.2. The overall bending can be described by the angle λ, where $\lambda/2$ corresponds to the angle between the flat, non-bent array and the tangential extension at the outer sensor. Assuming an ideal circular shape with constant radius r, array size, and sensor distances, the pose of each sensor can

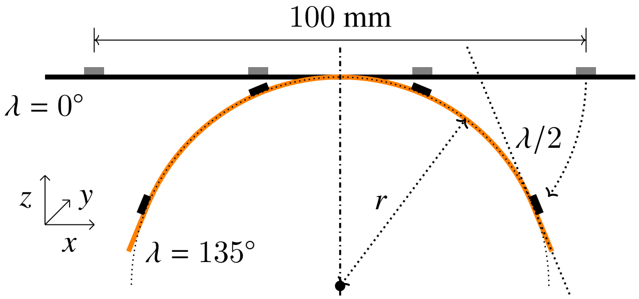

Figure 6.2.: Model of the array's circular bending shape, e.g., for $\lambda = 0°$ (yellow) and $\lambda = 135°$ (orange). [5] © IEEE 2023.

be computed. To estimate λ, a reference magnet (same type and size as the tracking target) is placed at a fixed, known position above the sensor array (Figure 6.3a). The algorithm starts by calculating a data set of all possible sensor poses along a circular shape for a preset list of λ-angles. Given the 16 magnet poses for any of the considered λ-angles, the pose of the reference magnet is estimated by the optimization described in Equation 6.1 using the modeled magnetic flux densities at these calculated sensor poses. The angle with the smallest deviation is determined as the estimated bending angle $\hat{\lambda}$.

6.2.5. Path Tracking of a Magnetic Target

With the given bending shape of the array, the actual tracking task can commence using measurements of all 16 sensors to detect the targeted magnet's position. The position of the numerical magnet model is obtained by minimizing the least squares error between the magnet model and the sensor values. At this optimized solution, the model's magnet position corresponds to the position of the target magnet.

6.3. Experimental Evaluation of the Sensor Array

The experimental evaluation of the compliant magnetic sensor array includes the experimental setup and procedure, as well as the accuracy results of the bending shape estimation (i.e., self-sensing) and the results of the tracking accuracy based on estimated bending angles.

6.3.1. Experimental Setup

Figure 6.3 shows the experimental evaluation setup. A parallel kinematic robot, i.e., Stewart platform (M-850, Physik Instrumente GmbH, Germany) was utilized to manipulate the tracking target with a minimum step length of $1\,\mu\text{m}$ and a unidirectional repeatability $< 1\,\mu\text{m}$. Furthermore, a coordinate measuring device (CMD) (FaroArm Platinum, FARO Europe GmbH, Germany) served to register the reference magnet above the array and the array itself including the sensor poses with the tracking target magnet and the Stewart platform. To maintain reliable bending with known bending angles, six customized evaluation frames for $\lambda = [0°, 45°, 90°, 135°, 180°, 225°]$ were additively manufactured (Stratasys F370, USA) with an accuracy of $\pm 0.2\,\text{mm}$ (Figure 6.4, left). Using

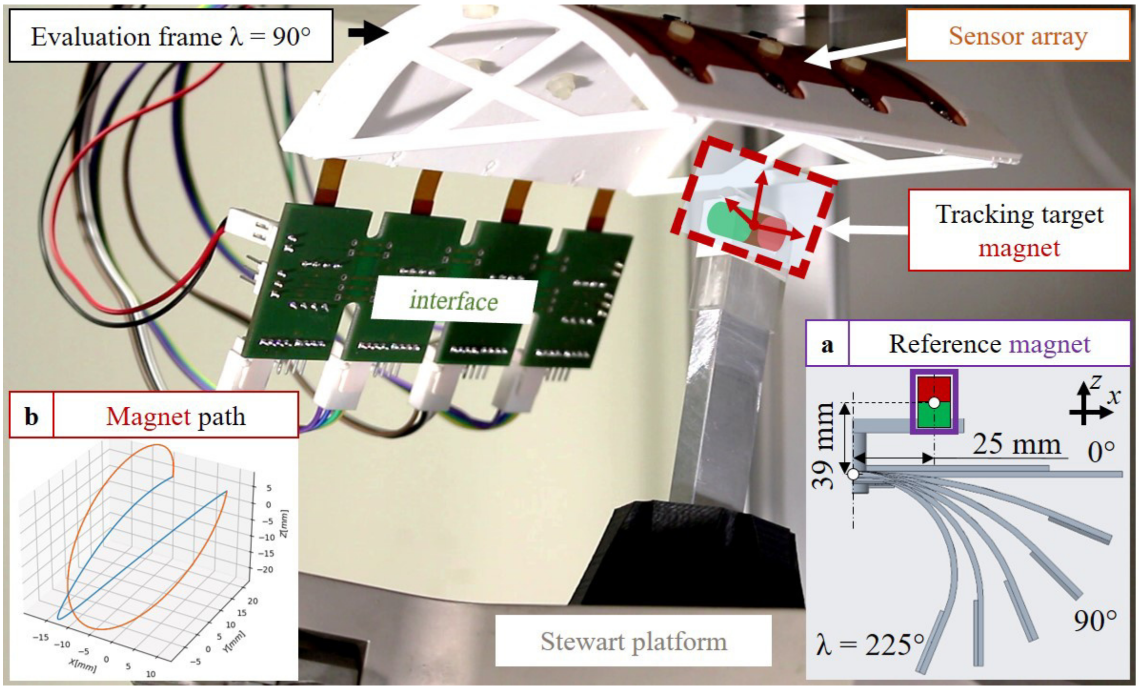

Figure 6.3.: Experimental evaluation setup. The sensor array was attached to an evaluation frame (here: 90°) and bending shape estimation was performed using a reference magnet (a, purple) which had been removed from the scene prior to tracking. The magnetic target (red) was then moved by a Stewart platform beneath the sensor array and its path (b) was tracked. [5] © IEEE 2023.

the CMD on the evaluation frames after printing, a deviation for λ_{cmd} of below 2° was measured (Figure 6.6, cp. λ_{cmd} and $\hat{\lambda}$).

6.3.2. Experimental Procedure

The Experimental procedure is subdivided into the bending shape estimation and the tracking accuracy.

Determining Bending Shape Estimation Accuracy

Initially, the sensor array was mounted on an evaluation frame. The reference magnet was then positioned at $[x, y, z] = [25\,\text{mm}, -25\,\text{mm}, 39\,\text{mm}]$ relative to the array center point, and aligned along the z-axis. Then, the algorithm for shape estimation was initiated. Three sets of 10^3 samples were recorded from the sensor array, encompassing all 16 sensors. The estimated λ was computed for each of the six evaluation frames, employing ten different random starting points for each frame.

Determining Tracking Accuracy with Estimated Bending Angle

Prior to the actual tracking task, the bending angle was estimated as in Section 6.3.2. Then, the target magnet was mounted on the Stewart platform and moved along a predefined path beneath the sensor array and evaluation frame (Figure 6.3b). The path consisted of a vertical elliptical helix to test positional accuracy. On this path, rotations around two axes were included. Two runs were conducted, each consisting of three subsequent cycles of the path for every evaluation frame. The sensor data were recorded and, together with the bending shape estimation, used as input for the tracking algorithm.

6.3.3. Bending Shape Estimation Accuracy

Figure 6.4 (right) graphs the bending shape estimation error $\hat{\lambda}_{\text{error}}$ for the six different evaluation frames. With increasing λ from $0°$ to $90°$, the absolute median error decreased. However, increasing the angle further increased the absolute median error and variability again. This trend of median error reversed, when the bending angle was higher than $180°$, while variability remained similarly high. This behavior could be caused by some Hall-effect sensors moving closer to the reference magnet and thus leading to higher accuracy. Interestingly, the algorithm showed the best performance for $90°$, which thereby outperformed the flat, non-bent sensor array (i.e., at $0°$), indicating that here, sensors seemed to obtain particular advantageous poses in the examined group. Furthermore, it should be noted, that angles between $0°$ and $90°$ were overestimated while angles $> 90°$ were underestimated. The overall average absolute error of medians was $8.33°$ (min. $2°$, max. $18°$) in comparison to reference λ as measured with the CMD. All median errors were in the range of ±20°.

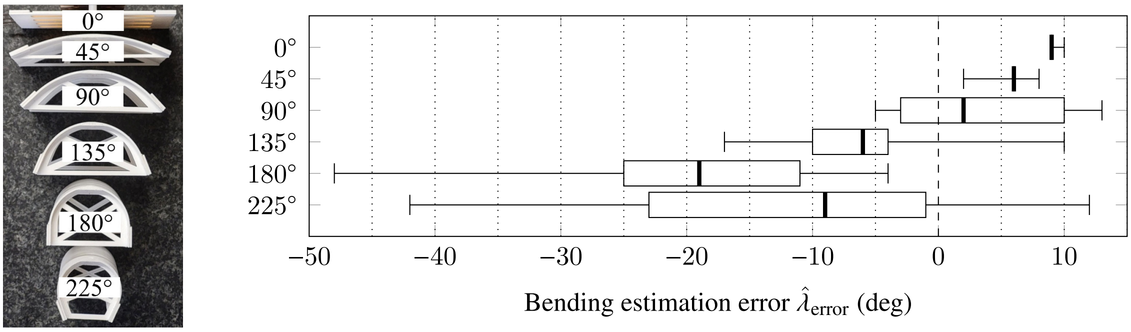

Figure 6.4.: Left: Evaluation frames for different bending angles λ to maintain known bending poses during evaluation. Right: Results of the estimated bending angle $\hat{\lambda}$ and the corresponding error $\hat{\lambda}_{\text{error}}$. [5] © IEEE 2023.

6.3.4. Tracking Accuracy with Estimated Bending Angle

Figures 6.5 (a+b) depict the tracking results for $\lambda = 0°$ after being estimated as $\hat{\lambda} = 9°$. The tracked path follows the robotic reference path closely with a small shift in $-z$, especially for $y = [-10\,\mathrm{mm}, 22\,\mathrm{mm}]$. The largest deviation is given for $y > 22\,\mathrm{mm}$ and increased noise appears for $z < -40\,\mathrm{mm}$. In contrast, Figures 6.5 (c+d) show the results for $\lambda = 225°$ (with $\hat{\lambda} = 216°$). Despite an estimation error of 9°, the robot path is followed with visibly less deviation and less noise than the flat array, indicating a tracking performance improvement for larger bending angles.

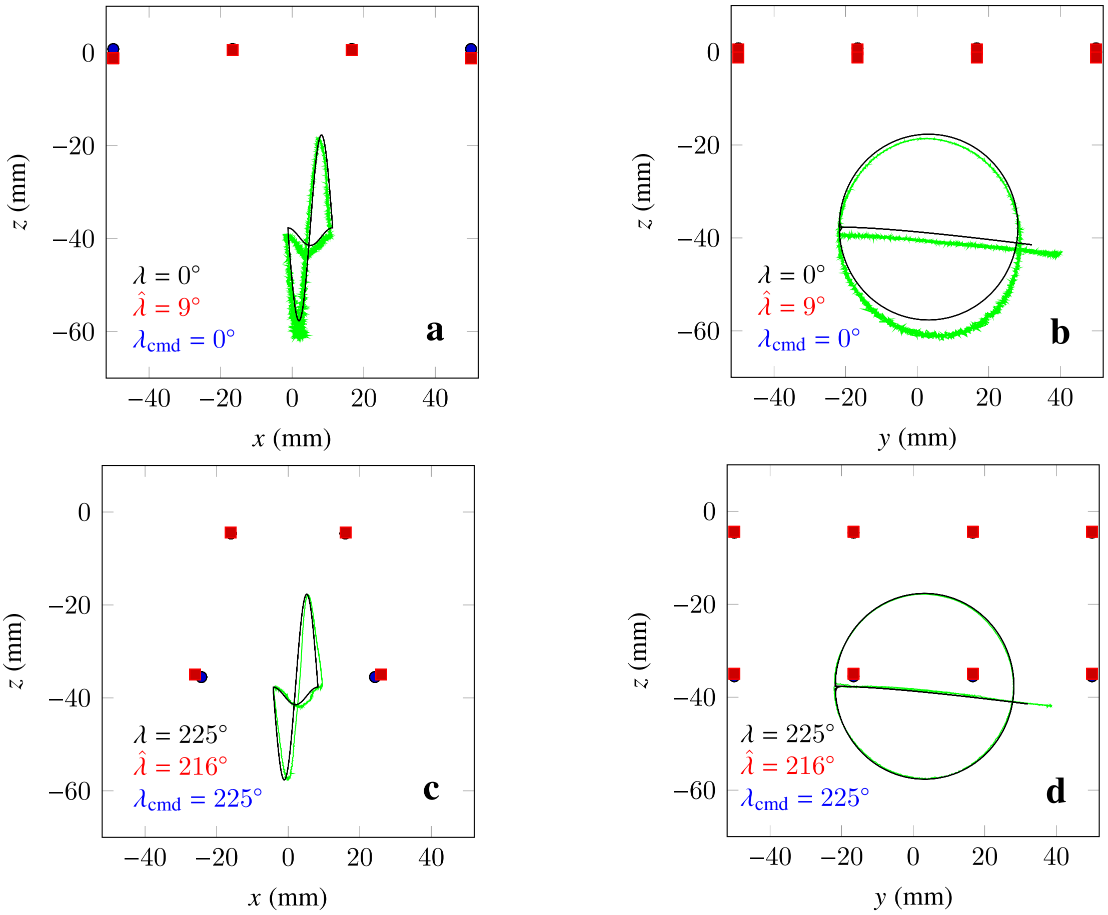

Figure 6.5.: Path deviation between target tracking (green) and robotic reference path (black) for the smallest and largest bending angles. Sensor locations measured with CMD are indicated by spheres (blue), estimated locations by squares (red). The tracking accuracy visibly improves when comparing the flat sensor array ($\lambda = 0°$) to the maximum bent array ($\lambda = 225°$). [5] © IEEE 2023.

This qualitative observation is strengthened by the quantitative analysis of the overall tracking performance (Figure 6.6, red). The median Euclidean distance error e_{array} decreases consistently from $3.38\,\mathrm{mm}$ for $\lambda = 0°$ to $1.31\,\mathrm{mm}$ for $\lambda = 225°$ with the largest variability found for $\lambda = 135°$ and $\lambda = 90°$. Remarkably, for $\lambda = 0°$ and $\lambda = 225°$, tracking based on $\hat{\lambda}$ seems to outperform the one based on λ_{cmd}, presumably due to the observed extensive variability of the bending estimation. Preliminary experiments to estimate the magnet's rotation result in unstable estimates, presumably due to non-convexity and nonlinearity of the problem. Estimation of rotation may thus be the scope of future work.

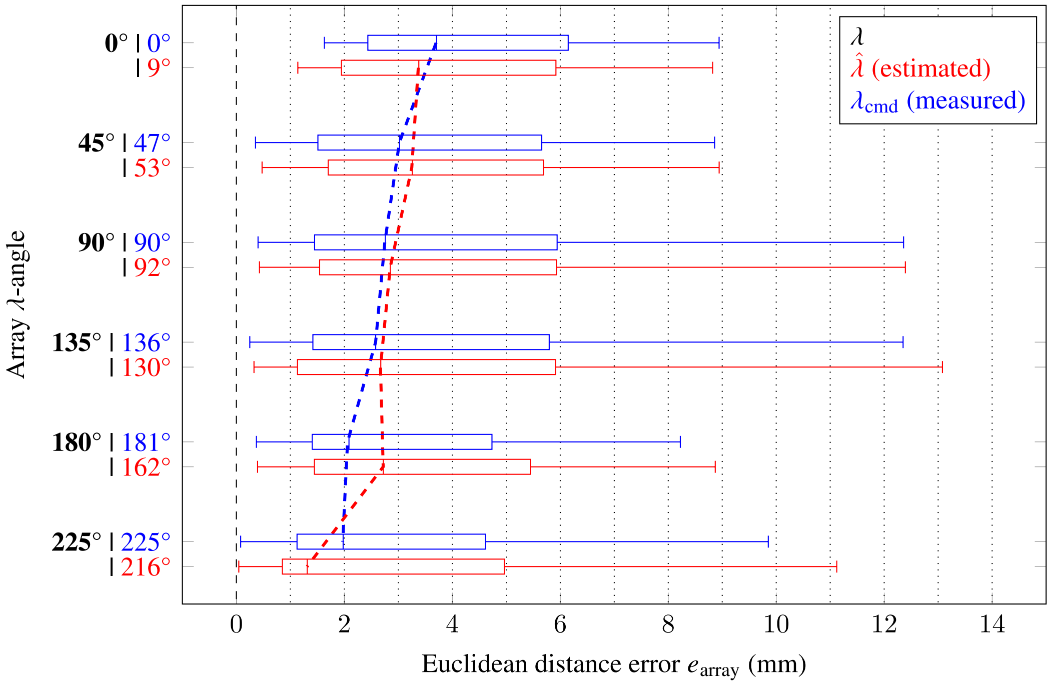

Figure 6.6.: Euclidean distance error e_{array} of target tracking with trend indication (dashed) for different bending angles λ, estimated bending angles $\hat{\lambda}$, and measured bending angles λ_{cmd}. The median Euclidean distance error decreases consistently from 3.38 mm for $\lambda = 0°$ to 1.31 mm for $\lambda = 225°$ [5] © IEEE 2023.

6.4. Towards Compliant Self-Sensing in Real-Time

As to be expected, deploying the error-prone bending shape estimation $\hat{\lambda}$ lead to a larger error than using the accurately determined bending angle λ_{cmd} in most cases. However, the magnitude of deviation for all investigated angles remained sufficiently small and similar to aforementioned related work. The results suggest that larger bending radii, and thus closer proximity between sensors and tracking target, compensate for the estimation error of the bending shape.

In conclusion, a highly compact, wearable, and compliant sensor array was developed for tracking the position of magnetic targets, such as ferromagnetically enhanced surgical instruments. The performance of the developed compliant sensor system is comparable to existing rigid and compliant approaches. The results demonstrate the potential of self-sensing using a single-sensor modality for small-size medical applications. This work thus contributes to the overall research objective of this dissertation of achieving compliance, miniaturization, and practicability by means of a smart material. Future work should address the modeling of error propagation, performance improvement using e.g., Kalman filter or graph optimization and the investigation of a machine learning approach, aiming for real-time capability.

7. Sensorized Training Platforms for Endovascular Surgery

The content of this Chapter 7 was published in the *International Journal of Computer Assisted Radiology and Surgery* [7]. Headlines, wording, and layout were carefully modified to fit within this work.

7.1. Training Platforms for Endovascular Surgery

Previous chapters explored the potential of inherent actuation and self-sensing by means of SMAs and the possibility of ferromagnetic instrument tracking for MIS. In particular, endovascular interventions, with their severe space restrictions when operating on and within delicate vessel branches, can benefit from such compliant smart material systems. Endovascular interventions aim for minimally invasive diagnostics and therapy, e.g., on patients with aneurysms, arterial occlusive disease or strokes.

Besides enhancing surgical instruments with additional robotic DOF, sensor modalities, and visualization, smart materials, such as piezoresistive polymer sensors, can also aid in the training of clinicians. The underlying reason for this is the necessity for adept insertion and precise maneuvering of various instruments (i.e., guidewires, catheters) through the vascular system of the patient. The objective is to reach the actual site of operation where stent placement, coil placement or thrombus removal take place. Challenges include the restricted visual and haptic feedback regarding the delicate manipulation of the instruments within the vascular system. Here, exerted force can easily damage the delicate vascular wall (*endothelium*) that may lead to dissection and consecutive dangerous perfusion impairment. While modern visual imaging techniques such as intraoperative CTA with contrast agent improve the visualization, there is no direct feedback provided regarding the interaction between instrument and human tissue.

Related Work

The instrument handling remains a difficult cognitive and dexterous task, requiring years of training. Clearly, teaching and training in a real operation scenario and on a living patient is indispensable. However, such trainee positions and training time are limited as well as patient pathologies and anatomies are limited to cases appearing in the hospital. Furthermore, beginners may introduce a higher risk of complications despite being supervised by an experienced mentor. Realistic procedure simulations can provide effective training outside the operating room and lead to efficiency improvement [177], as for example Kendrick *et al.* demonstrated for a thoracic endovascular aortic repair procedure [178]. A major complication includes damage to the vessel walls [179]. Thus, high impact forces from the instrument to the inner vessel walls must be avoided, and training simulations must consider this risk factor. Long before entering an operating room, trainees need to familiarize with instruments and techniques in a safe and radiation-free environment, ideally on a model featuring realistic anatomical patient-specific structures and instrument interaction.

Modern training platforms and simulators not only provide realistic haptics but also a feedback modality to relieve teachers from attending repetitive, time-consuming training sessions. Furthermore, such platforms provide qualitative and quantitative data to obtain comparative results and progress of training. Aggarwal *et al.* compare the training simulators Angio Mentor (Simbionix USA Corp, USA) and VIST (Mentics AB, Sweden), which measure collision and frictional forces during the intervention with real-time feedback [180]. Furthermore, the authors considered virtual reality (VR) enhanced systems as the CathLab VR (CAE Healthcare, Canada), which were demonstrated beneficial to training progress [181]. Another commercially available simulation platform is the CATHiS (CATHI GmbH, Germany), a highly compact and mobile system with strong focus on realistic simulation of visual imaging, force feedback and patient complications. In contrast to this black-box simulator, the Endovascular Evaluator EVE (BR Biomedical (P) Ltd., India) comes with silicone vessel models that mimic the arteries' elasticity and friction coefficients. However, high costs for purchase and maintenance [180, 182] of such systems exclude many young physicians from such a learning opportunity that potentially increase patients' safety and reduce teachers' obligations in this crucial part of training in endovascular surgery.

Besides commercially available solutions, several research groups investigate additively manufactured vessel phantoms and prove their benefit to facilitate surgical planning in endovascular interventions and other fields of application prior to the operation [183, 184]. Kaschwich *et al.* propose a simulator consisting of additively manufactured patient-specific phantom parts that are ultrasound capable for enhanced simulation scenarios [185]. To improve training, Payne *et al.* present a leader-follower system to insert and navigate a catheter, providing an intuitive controlling device, which can create a haptic feedback based on force gauges at the catheter's distal tip [186], rendering essential modification of the instrument. Chi *et al.* demonstrate a platform for online skill assessment featuring haptic guidance to learn by expert demonstration that also includes force feedback [187]. However, the handheld device interfacing the participant to the catheter may lead to an alienation instead of familiarization with a real instrument. Furthermore, Rafii-Tari *et al.* developed a simulation platform that measures impact forces by placing the entire phantom on a force-torque sensor and tracking catheter motion with rotary encoders [188]. While bearing the system on a sensor makes the platform more difficult to use, the encoders create an additional source of externally induced friction and resistance and thus influence the training unintentionally.

Contribution

The aforementioned systems are usually preset for one specific anatomy. However, training could strongly benefit from a modular system that can represent different anatomical parts for specific training episodes. Furthermore, the possibility to easily include patient-individual pathologies in the training phantoms would enable specific training and planning prior to an intervention. Most simulation platforms that include some force sensing modality address haptic feedback, but at the cost of additional modifications of the instruments and control devices that omit hands-on experience with the instruments.

Therefore, an authentic training platform is proposed, consisting of multiple independent modules with additively manufactured vessel phantom sections and integrated impact sensing based on piezoresistive polymer sensors for training of endovascular interventions providing feedback to the trainees (Figure 7.1). The platform concept allows for customization by creating phantom parts based on real patient CTA-data and mobile usage of single parts or the entire unit to skill labs or lecture halls.

This work thus contributes to the overall research objective of this dissertation of achieving flexibility, miniaturization, and practicability by means of an integrated **piezoresistive polymer sensor system**.

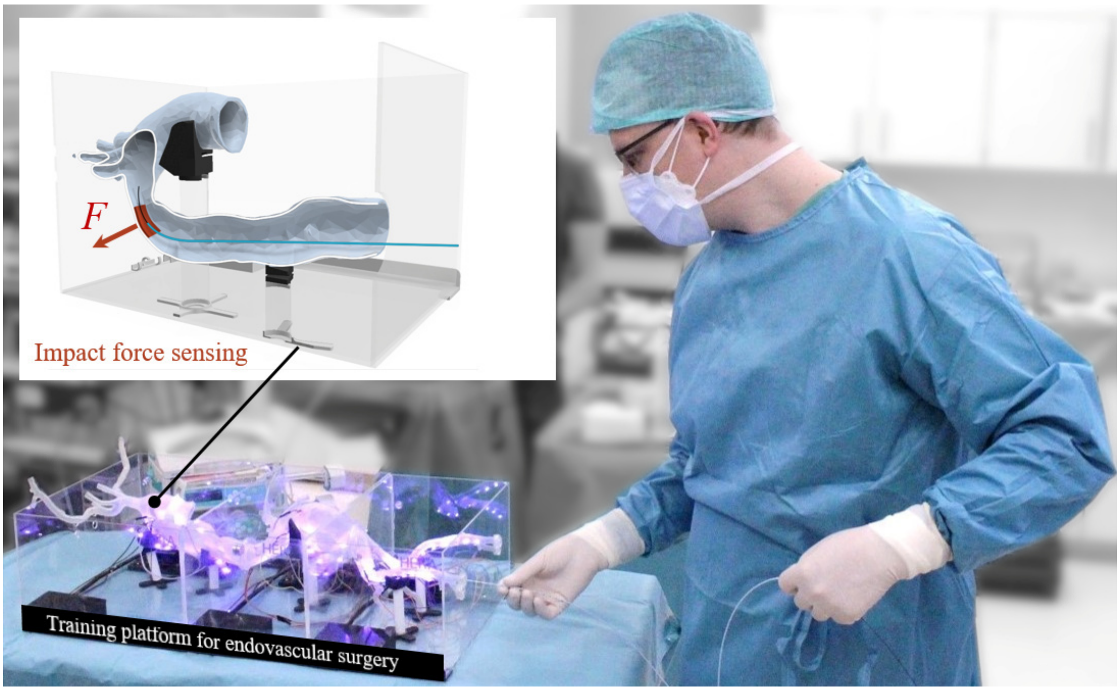

Figure 7.1.: The modular endovascular training platform during the experimental evaluation at Heidelberg University Hospital. Top-left: Schematic of a module box with an additively manufactured, patient-specific vessel phantom and an integrated impact force sensor made from piezoresistive polymers. Adapted from [7] 🅭🅯 4.0.

7.2. Design of a Sensorized Training Platform

The training platform is shown in Figure 7.2 and covers the complete aorta without organs (heart, lungs, liver, kidneys) from the supraaortic arch vessels downstream to the *A. poplitea*. It is subdivided into three modules of relevance, which can be operated individually or combined to create desired training scenarios. Following the classification according to Fillinger *et al.* [189], the platform includes aortic zones $0-5$ (top module), $6-9$ (middle module) and $10-11$ (bottom module). Each module features three piezoresistive sensors to measure impact forces on the vessel walls. Instruments can be inserted via the right *A. femoralis*.

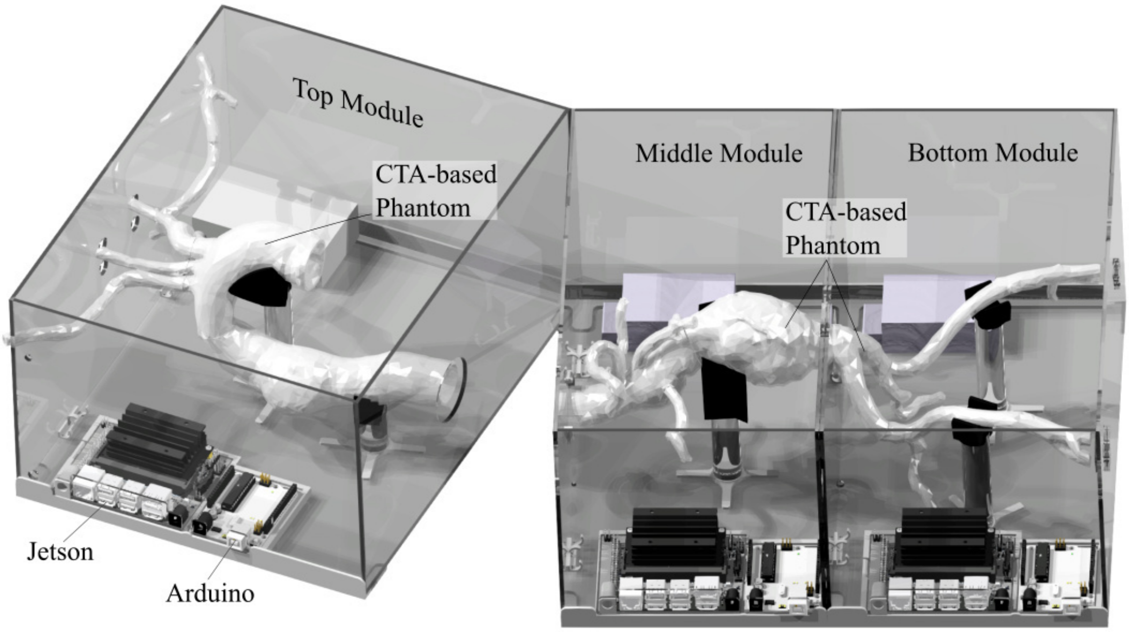

Figure 7.2.: Render of the three modules of the training platform in a computer-aided design (CAD) model. Each module comprises the respective section of the individualized vessel phantom, as well as hardware for sensing and processing. [7] 🅭🅯 4.0.

7.2.1. Phantom Fabrication

The vessel phantom is based on segmentation of anonymized CTA-data of a patient with an aneurysm of the abdominal aorta. The processing of the CTA-data and fabrication method allows for any patient data to be turned into an authentic and customized training phantom. From the CTA-data the aorta is segmented using The Medical Imaging Interaction Toolkit (MITK) as a single connected volume, exported as single raw shape and stored as *.stl file. Then, Blender is used to derive a model of the vessel wall with $1.5\,\mathrm{mm}$ thickness. Subsequently, this model is cut along the border of the boxes to obtain the respective models for each module box. These subsegments are then additively manufactured using a stereolithography printer (Form3, Formlabs GmbH, Germany) with a special resin that remains elastic after curing (Elastic 50A, Formlabs GmbH, Germany) to provide realistic haptics. The subsegments can be joined after curing, by manually applying liquid resin and curing it with a UV-flashlight. Thus, larger and more complex vessels can be fabricated. The cured resin is translucent and allows the participant to observe instruments within the phantom. Aiming at recreation of low friction between instrument and vessel wall, a preliminary experiment was conducted to select a low friction coating for the inner vessel walls. A catheter was extracted from a simplified phantom with a motorized setup while measuring forces. Out of three investigated coatings, a mineral spray oil (Komet, Fessmann & Hecker GmbH & Co.KG, Germany) provided minimal wall friction and was used to coat the inner vessel walls of the phantom. Due to the hydrophilic coating of many commercial catheters also a water-based coating was investigated. However, it was ruled out due to the risk of harming sensor electronics while not providing measurable benefits on friction. For the coating process, the phantom received a base coating by covering it in lubricant and letting excess oil drip off. During preparation of the studies, the coating was refreshed by applying small amounts to not form droplets or letting oil accumulate at the phantom's bottom.

7.2.2. Impact Force Sensing

The phantom vessel walls must remain elastic, but at the same time detect impact forces that would be harmful to real vessel tissue. Therefore, flexible compliant sensors are required for detection of impacts of the instrument tip. In addition, the buckling instrument might push against the vessel walls, e.g., when probing. Sensors made from piezoresistive polymers are well suited for this use case, as presented in [6]. These can be fabricated in almost arbitrary shapes, at low thickness of $< 400\,\mu\mathrm{m}$ and were initially demonstrated by Fischer *et al.* to measure impact forces of up to $1\,\mathrm{N}$ with $0.1\,\mathrm{N}$ resolution.

Here, such sensors are fabricated and placed at the circumference of the vessel phantom at selected locations on the inner vessel walls (Figure 7.3). In discussion between technical and medical experts, these locations were selected according to high-impact zones for a typical catheter trajectory. This included regions, where the catheter must take sharp turns to reach smaller vessels, the aortic bifurcation or at the aortic arch. The sensors must be attached on the inner vessel walls so that the sensor surface gets in direct contact to the instrument. Together with the elastic vessel wall, the sensor strip deforms at impact and provides an estimation of the impact force.

7.2.3. Data Processing

Each module box must show full functionality when operated stand-alone and in any anatomically meaningful combination with adjoining module boxes. While the box walls provide customized cuffs to interconnect them mechanically, also the sensor data acquisition and data processing must contribute to the modular concept. Therefore, each module box is equipped with a mini computer (NVIDIA Jetson Nano, Nvidia Corporation, USA) with Ubuntu 20.04 as operating system and Robot Operating System (ROS) noetic. Thus, each module box can be set up to acquire, process, distribute, and monitor its own sensor data as well as the data of all other adjoining module boxes in the network. Each module box also features an Arduino Uno (ATmega328-Microcontroller) to control and power the sensors and to feed the computed impact force data via serial connection to the minicomputer.

7.3. Experimental Evaluation of the Platform

To evaluate the training platform, a participant study was conducted at Heidelberg University Hospital. It was investigated whether the platform allows for differentiating between different levels of experience and expertise, as well as if young physicians could improve their skills in catheter and guidewire handling by training with it.

For the study, board-certified surgeons ($n_\mathrm{P} = 2$), surgical residents ($n_\mathrm{P} = 3$), medical students ($n_\mathrm{P} = 5$), and non-medical participants ($n_\mathrm{P} = 10$) tested the training platform in five runs each ($n_\mathrm{run} = 5$). Their performance was assessed by measuring mean runtime $\bar{t}_\mathrm{run}$, mean impact force $\bar{F}$, and calculating an impact-runtime score χ. The latter was defined as

$$\chi = \bar{t}_\mathrm{run} \cdot |\bar{F}| \tag{7.1}$$

where an unweighted product was chosen in order to obtain a participant-specific ordinal value to reflect performance including both metrics.

To analyze the influence of expertise on the performance on the training platform, the participants were subdivided into groups of medical experts, medical students, and non-medical participants. Five of the ten medical participants already had experience with the instruments on any other phantom (two participants) and on a patient (three participants). Three of the non-medical participants had already been familiar with the instruments and especially with the actual training platform. Then, the participants were regrouped according to their prior expertise with catheters and guidewires on phantoms and patients, respectively. Eventually, an analysis of variance (ANOVA) was conducted (MATLAB R2022a, Mathworks Inc., USA) to determine statistical significance in the differences of expertise and experience on performance.

Experimental Setup

Figure 7.3 shows the experimental setup with a total of three module boxes in operation. Each box was equipped with three force sensors (orange). To increase the visibility of the instruments for the participants, the phantom was illuminated with blue light from the bottom side in addition to the ambiance illumination of the experimental operating room. Furthermore, the defined starting point (femoral) and the end point (aortic arch) are illustrated. On the path in between, the instruments must pass through the module boxes from right to left, which corresponds to a realistic intervention. The utilized instruments were a guidewire (RADIFOCUS: M, 0.035” Flex L $3\,\mathrm{cm}$, $180\,\mathrm{cm}$ stiff type angled, Terumo Interventional Systems, Belgium) and a matching catheter (Accu-Vu Pigtail, 5F $1.8\,\mathrm{mm}\times 100\,\mathrm{cm}$, AngioDynamics, USA).

Experimental Procedure

Before the actual experiments, the twenty participants ($N_\mathrm{P} = 20$) were individually instructed about the experimental procedure and handling of the guidewire and catheter. The movement possibilities (DOF) and configurations were explained. In addition, reference was made to the objective of completing the parkour in the shortest possible time and with the lowest possible impact forces between instruments and phantom vessel walls. Prior to each run, the catheter was placed at the starting position (start) in the phantom. The experiment was started with an acoustic signal. The goal was to move the combination of guidewire and catheter to the exit of the aortic arch (target) and then remove the instruments completely from the phantom. The removal process was integrated into the procedure because impacts on the vessel wall causing eventual damage could also occur during removal. If an experimental run was not completed within $300\,\mathrm{s}$, participants were instructed to remove the instruments from the phantom immediately, regardless how far they had progressed. Preliminary tests revealed that runtimes were usually below $150\,\mathrm{s}$. With a safety margin of twice that duration, the goal was to capture the majority of the participants’ interaction with the phantom. The impact force at each sensor and its corresponding duration were measured for each run. The runs followed each other without breaks. After completion of all runs, the participants completed a questionnaire[1] in which they provided general information about their previous experience and suggestions for improvement. The board-certified surgeons, who had been familiar with endovascular surgery in their clinical routine, were asked additionally how realistic they considered the training platform and whether they would recommend it for surgical training.

---

[1] The questionnaire can be found online https://doi.org/10.1007/s11548-023-02935-w.

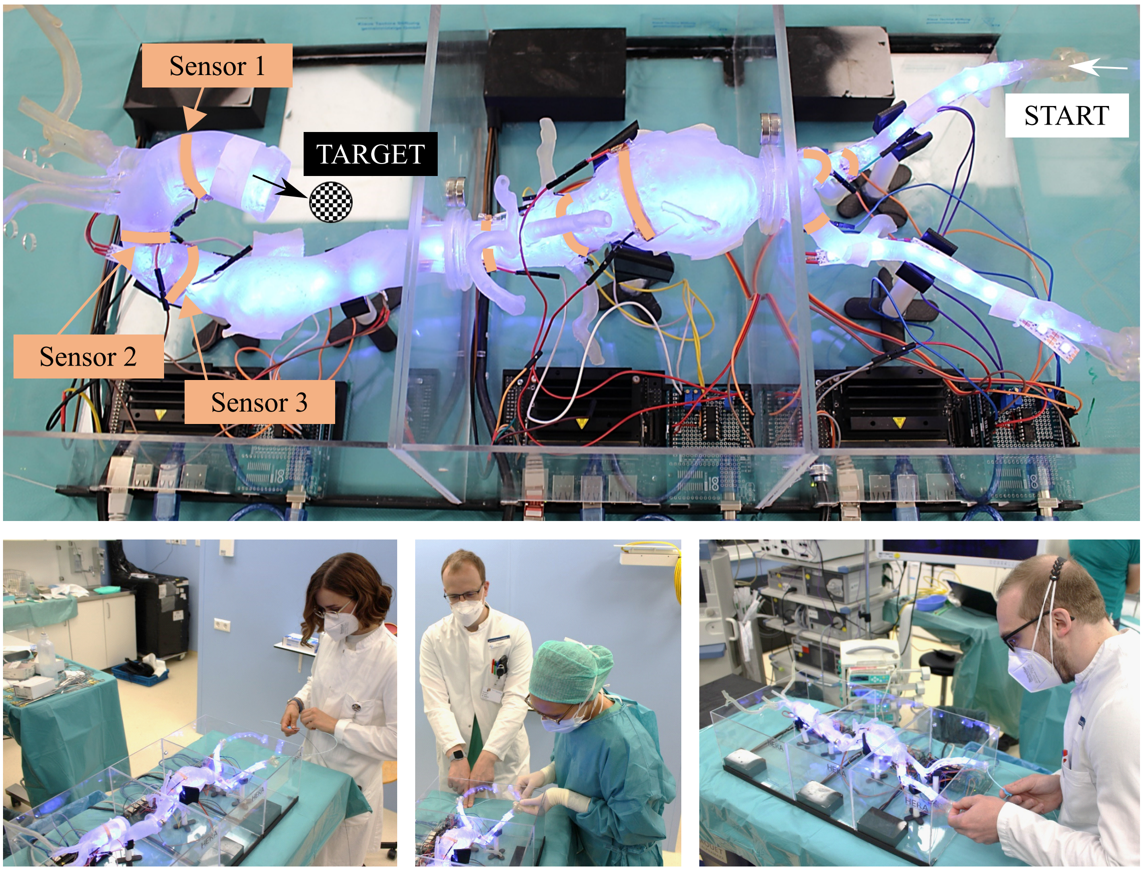

Figure 7.3.: The modular sensorized training platform as used for the participant study. Indicated positions of “START” and “TARGET” between a total of three module boxes, as well as the three sensor locations per box (orange). Bottom: Medical experts during the participant study. [7] 🅭🅯 4.0.

7.3.1. Experience and Expertise

Figure 7.4 shows the results of the evaluation with participants grouped according to their expertise (top row) and their expertise (bottom row), respectively.

When grouped following their expertise, medical participants required on average approximately one third of the mean runtime $\bar{t}_{\text{run}}$ of the non-medical group, $53.3\,\text{s} \pm 30.8\,\text{s}$ (experts) compared to $135.4\,\text{s} \pm 65.9\,\text{s}$ (non-medical), as seen in Figure 7.4a. Thereby, the medical students required a comparable duration as the medical experts. However, the latter achieved the lowest mean impact force $\bar{F}$ with $0.048\,\text{N} \pm 0.010\,\text{N}$ in contrast to $0.057\,\text{N} \pm 0.013\,\text{N}$ (students) and $0.062\,\text{N} \pm 0.007\,\text{N}$ (non-medical), as seen in Figure 7.4b. Consequently, the impact-runtime score χ was lowest with the medical experts ($2.33\,\text{N}\,\text{s} \pm 0.69\,\text{N}\,\text{s}$), closely followed by the medical students ($2.77\,\text{N}\,\text{s} \pm 1.65\,\text{N}\,\text{s}$). Non-medical participants obtained an impact-runtime score χ of $8.36\,\text{N}\,\text{s} \pm 4.41\,\text{N}\,\text{s}$ on average (Figure 7.4c). The group comparison based on the analysis of variance (Figure 7.5) reveals runtime (p-value $\leq 7.6 \cdot 10^{-5}$) and impact-runtime (p-value $\leq 9.4 \cdot 10^{-5}$) as valid factors for significant differentiation of medical and non-medical participants. In contrast, force impact can only be used to distinguish medical participants from the non-medical group. Thus, runtime seems to be the more meaningfully metric for identification of experience as well as expertise and as such more valuable as training feedback. However, the impact metric could become more relevant, when researching risk of vessel puncture in future work.

When grouped following their expertise, the medical experts with previous experience on patients required the least mean runtime $\bar{t}_{\text{run}}$ of $34.7\,\text{s} \pm 1.3\,\text{s}$ (Figure 7.4d) and applied the lowest mean impact force $\bar{F}$ of $0.05\,\text{N} \pm 0.005\,\text{N}$ (Figure 7.4e). This is in contrast to the comparison groups with only limited or no prior experience on phantoms. The data also show that the participants with previous experience on this particular training platform were not faster and worked with greater force than the experienced medical professionals. The advantage of real experience seems thus represented well by the impact-runtime score χ of the training platform.

Participants without previous experience performed similarly well as those who had already gained experience on other phantoms, since both groups achieved an impact-runtime score χ of $6.46\,\text{N\,s}$ with $\pm 4.77\,\text{N\,s}$ (none) and $\pm 7.01\,\text{N\,s}$ (any phantom), respectively (Figure 7.4f). This indicates that previous experience with other phantoms is not directly transferable to the training platform. However, the low number of participants in this group make statistical comparison difficult, as also indicated by the high standard deviation in this group with only two group members.

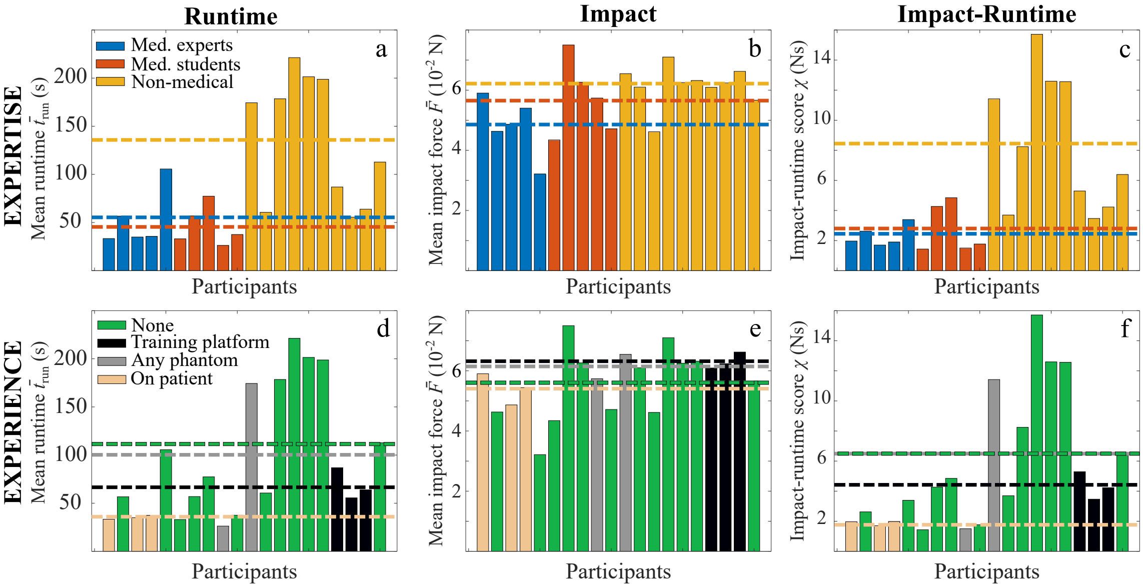

Figure 7.4.: Mean values over five runs and all sensors for runtime $\bar{t}_{\text{run}}$ (a, d), impact force $\bar{F}$ (b, e), and impact-runtime score χ (c, f) for each participant. Analysis of participant groups based on their expertise (top row) and experience (bottom row) with the mean values for each group (dashed line). [7] 🅭🅯 4.0.

Statistically, the combined score χ cannot be used for differentiation of participants with experience on a phantom or the training platform (p-value ≤ 0.67). A significant difference can only be shown for participants with experience on patient, compared to no experience (p-value $= 0.0095$), as seen in Figures 7.5 (d+f). The low impact-runtime score χ of the medical experts with experience on patients confirms the superiority of this expert group over all comparison groups. This correspondence is in agreement with the expected real distribution of experience and skills.

The grouping in this study by experience provides some further insights, but must be critically examined due to the potential inhomogeneity within the medical and non-medical group mentioned in Section 7.3. Furthermore, from the medical group, there was only one person from the specialty of (endo-)vascular surgery, while most medical experts were general and visceral surgeons. In addition, potentially controversial is the different number of members in the subgroups. Thus, twelve participants with no experience were

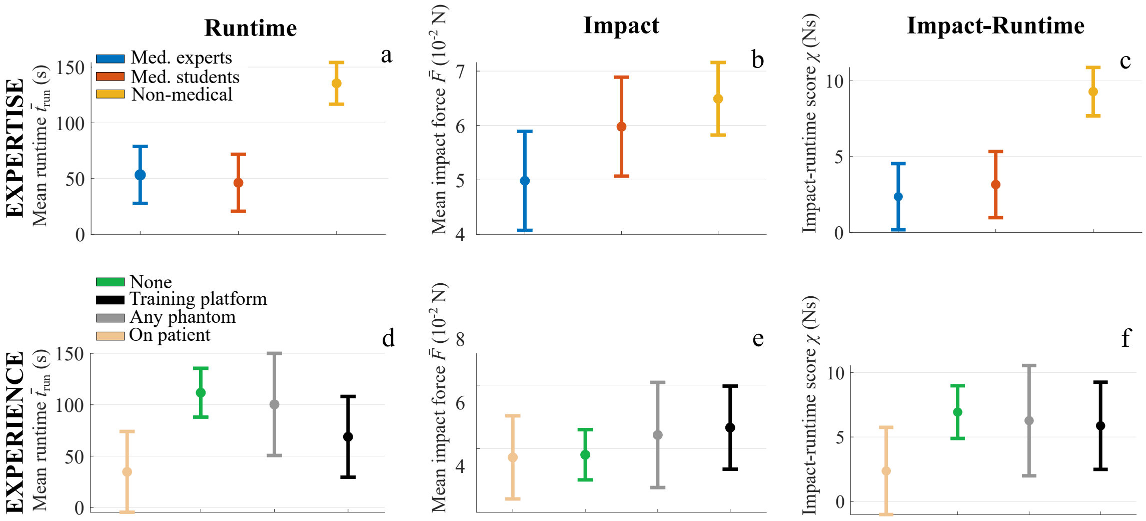

Figure 7.5.: Analysis of variance for the participant study. Displayed are estimated means and comparison intervals for runtime $\bar{t}_{\mathrm{run}}$ (a, d), impact force $\bar{F}$ (b, e), and impact-runtime score χ (c, f), for groups of expertise (top) and experience (bottom). [7] 🅭🅯 4.0.

compared to only two participants with previous experience on other phantoms. Due to the relatively small sample size, the statistical evaluation of the present study may not be representative for a larger population. Yet, it could be shown that the platform allows gathering of metrics which provide differentiation between professional participants based on experience and expertise. Thus, these metrics can provide valuable feedback for training and education.

7.3.2. Learning Curve

Figure 7.6 shows the runtime t_{run} of all participants for each of the five runs and the mean impact force $\bar{F}$ across all sensors (normalized to $0.2\,\mathrm{N}$) and visualized in color code. This allows examination of each participant's learning curve (i.e., runtime and impact) throughout the experiments, indicating the training effect. Most participants required longer runtimes initially and became faster towards the end of the experimental series. Except for participants P1, P12 and P20, each last run was the fastest run. Although participant P1 (a vascular surgeon with eight years of professional experience) started the first run with a low runtime and impact, their performance first improved in the second run and then declined towards the last runs. It can be assumed that they have already completed most of their learning curve long before the study.

Overall, it can be observed that the runtime varies considerably. For example, the total of terminations of runs due to exceeding maximum runtime of participants P5, P11, P14, P15 and P16 strongly differ to the fastest duration of only $7.1\,\mathrm{s}$ (P9). It can be concluded that the seven terminations out of a total of 100 runs confirm the functionality of the training platform and the feasibility of the task proposed in this study. All participants were able to conduct at least three complete runs successfully without exceeding the time limit of $300\,\mathrm{s}$.

Regarding impact, eleven out of the twenty participants showed an increased impact force on the vessel walls after five runs, while eight decreased their impact force level and one participant (P16) remained almost the same. During the tests, it was observed that the participants' self-confidence seemed to increase after each run. Whereas at the beginning there was still tentative trial and error out of careful consideration for the training platform,

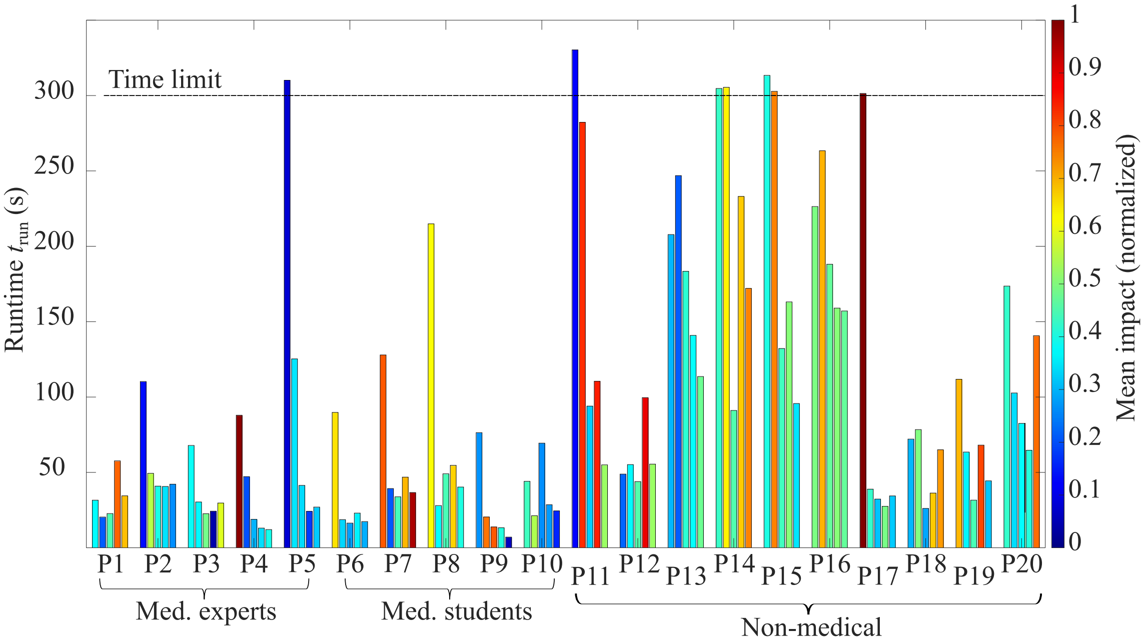

Figure 7.6.: Runtime of all medical participants (P1–P10) and non-medical participants (P11–P20) for all runs. Color-code indicates mean impact force $\bar{F}$ over all sensors, normalized for $0.2\,\text{N}$. [7] 🅭🅯 4.0.

it was quickly understood that it could withstand with its robust construction the stresses and that progress could be accelerated with greater effort, especially through dexterous repetitive rapid forward and backward movements. Also, many participants quickly found that the task set could be solved without pronounced configuration changes, as there was no need to probe steep vascular branches that would have required advanced skills with the catheter and guidewire. Such more complex tasks could be envisioned for future studies. This would be expected to result in even clearer distinction between experts and non-experts. Four medical (P1, P2, P5, and P7) and six non-medical (P11, P12, P13, P14, P18, and P20) participants did not improve impact forces, when comparing their first and the last run. This means that half of the participants were unable to reduce the impact force over five runs, independent of their background. A closer look at this group reveals that of a total of five medical students, four were able to improve, whereas among the medical experts, only one out of five was able to do so. Most medical experts already demonstrated a better performance from the beginning, compared to students and non-medical participants, which explains the lack of apparent improvement.

In summary, and with special regards to the target group of young physicians, all could reduce their runtime and 80% also the force impact from run $1-5$. Similar to the results from the analysis of expertise and experience, it can be seen, that impact readings do not display the same learning effect as seen for runtime. In this work, it still remains an open question how the sensory data can be translated to risk of vessel rupture. If such a metric is found, future studies with the presented phantom could look into increasing the learning effect with direct visual or auditory risk feedback.

7.3.3. Participant Questionnaire

The medical experts considered the advancement of the catheter inside the phantom to be moderately realistic compared to a real patient. On average, the experienced surgeons rated the resulting friction between instrument and phantom higher than in vivo. The experts agreed that retracting the catheter and the associated friction was realistic compared to the real patient. In the free-text statements, it was criticized that the individual modules of the platform were not attached to each other well enough so that the catheter could slide out between the modules during probing. Furthermore, the high friction of the system was criticized in general, as well as the insufficient monitoring of the instrument position within the phantom in particular sections. Interestingly, the sensing electrodes on the inner phantom walls, which create presumably the highest friction, were compared to atherosclerotic plaques, which can also cause increased friction in real patients. Overall, the training platform was well received by both, medical experts and non-medical participants. The participants consider the platform highly promising and useful for medical education. For further improvement, they recommend a participant interface with real-time feedback and quantitative measurement of the learning success.

7.4. Towards Sensorized Training Platforms with Real-Time Feedback

A training environment for hands-on training in endovascular surgery was investigated as an evaluation platform with realistic geometry and haptic experience, compatible with endovascular instruments such as catheters and guidewires. The presented method of manufacturing can be applied to create various patient-specific anatomies and pathologies of vessels and organs, featuring customized sensing capabilities throughout the elastic phantom structures.

The implementation of compliant and miniaturized impact force sensing represents a highly transferable and scalable approach, facilitated by the utilization of piezoresistive polymer embedded within the phantom structure, and thus, contributing to the overall research objective of this dissertation.

Furthermore, the conducted participant study showed in a first attempt, that the developed platform can enhance conventional radiation-free surgical skill training without endangering patients. However, the study's results are limited by the size and inhomogeneity of the participant cohort. Additionally, the manufacturing method, although transferrable to other patient's anatomies, was only demonstrated with one individual and the combination of all three modules. Moreover, piezoresistive impact measurement was not yet analyzed sufficiently to allow for inferring of risk for vessel rupture. The presented preliminary studies only evaluated the measurement of normal forces without regard for shear forces and friction.

Further developments should include the application of the manufacturing on other, even more delicate vessel systems such as in the brain, increasing sensor resolution and respond times towards real-time feedback ability, as well as camera imaging for better training.

Part III.

Smart Materials Systems for Assistive Robotics

8. Compliant Actuator-Sensor Units for Active Exoskeleton Interfaces

The content of this Chapter 8 was published at the *2023 IEEE-RAS 22nd International Conference on Humanoid Robots (Humanoids)* [8] © IEEE 2023. Headlines, wording, and layout were carefully modified to fit within this work.

8.1. Light-Weight Assistive Exoskeletons

In healthcare, the journey towards recovery extends beyond surgical intervention, as has been the focal point of this dissertation thus far. In contrast to surgery, physical recovery frequently entails prolonged durations and can significantly affect daily tasks for the remainder of a person's lifetime. However, conventional methods of rehabilitation (e.g., manual physiotherapy) may not suffice for individuals facing substantial mobility hurdles. Furthermore, a scarcity of adequately trained personnel for intensive rehabilitation tasks exacerbates the issue. While many rely on basic aids such as crutches, these can restrict autonomy, consequently compromising both quality of life and participation in society.

Robotic exoskeletons featuring smart materials can introduce a new paradigm in rehabilitation and assistance. Exoskeletons are wearable devices to enhance human body motion in force, speed, and accuracy. Passive exoskeletons already play a major role in rehabilitation [190] where they support the internal natural skeleton after injuries and operations and allow for patient-specific constraints of articulation to ensure a safe healing process. Active robotic exoskeletons further aim to compensate for permanent age- or injury related motion disabilities [66, 191]. In recent years, in particular light-weight compliant exoskeletons and exosuits are under investigation since they offer obvious advantages over rigid heavy systems, being more energy-efficient, less bulky, and more convenient and comfortable to wear [192, 193].

The integral physical connection between wearer and machine in human-robot interfaces of exoskeletons relies heavily on the strong and consistent attachment provided by fixation cuffs and straps. This ensures efficient transmission of force and torque during various motion modalities. Ensuring a tight fit, both at initiation and throughout use, is paramount. Any suboptimal fit or alignment at the outset, or dislodgement and potential misalignment during use, can lead to efficiency losses [194] and undermine the effectiveness of the robotic exoskeleton. Therefore, a tight and stable attachment of the exoskeleton to the human body is a critical requirement for optimal performance. Furthermore, improper attachment can cause displacement, resulting in harmful shear forces and friction. Conversely, sustained high pressure, similar to the effects of bedriddenness, can also cause damage [195]. Therefore, both excessive and inappropriate pressure can cause soft tissue deformation, swelling, and pressure injury [196], even leading to severe lesions and pressure ulcers [197].

Contribution

This work argues for an improved, actively controlled and self-readjusting interface with compliant sensors which monitor exoskeleton-user interaction forces for effective control. In addition, the sensors can gather valuable information, such as the muscle activity, to further analyze the functions of the other exoskeleton components. For these enhanced interfaces, compact and modular compliant actuator-sensor units (CASUs) are proposed (Figure 8.1). Each unit, equipped with a SMA actuator and a capacitive sensor, is capable of measuring interaction forces to maintain appropriate donning and holding forces, ensuring safe use and consistent force quantification.

Hence, this work contributes to the overall research objective of this dissertation of achieving compliance, miniaturization, and practicability by means of an integrated **SMA-based actuation system** within the physical exoskeleton-user interface.

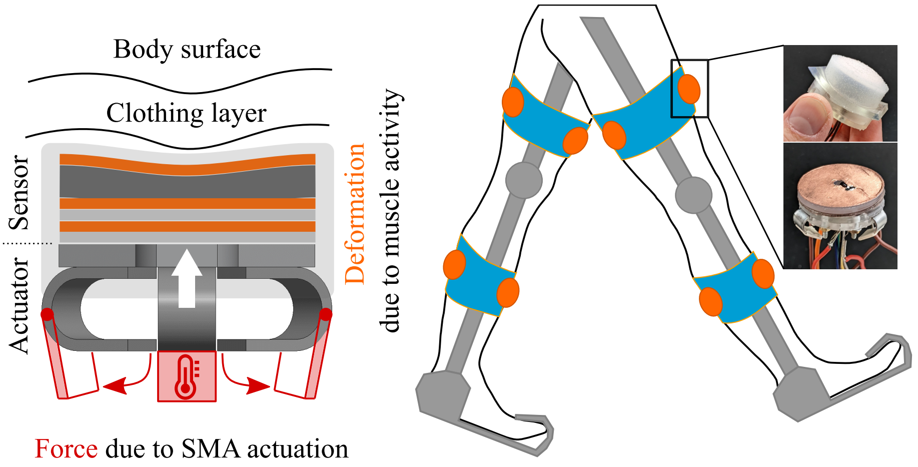

Figure 8.1.: The schematic (right) shows a lightweight robotic exoskeleton and its physical human-robot interfaces (blue) on the lower limbs. It incorporates the innovative Compliant Actuator-Sensor Units (left), which are positioned within specific cavities (orange). [8] © IEEE 2023.

Related Work – Shape Memory Alloy Actuation for On-Body Applications

A novel system is proposed that differs from soft robotic cuffs [194] by featuring a smaller footprint and compliant actuation using a SMA, contributing to state-of-the-art lightweight exoskeleton designs without the need for fluid-dynamic infrastructure. Unlike traditional motors, SMAs enable compliant actuator geometries suitable for wearable systems. This allows for a reduction in space, weight and complexity, especially in comparison with commonly used mechatronic and fluidic actuators.

While exoskeleton research often seeks to replace conventional actuation for motion support of the upper [198–200] and lower limbs [201, 202], there is limited literature addressing the challenges of interface and body contact. The use of SMAs has been suggested for compact haptic devices and active compression devices for the lower limb [203]. In this contribution, the thermo-mechanical shape memory effect is used within the exoskeleton interface itself, coupled with a soft sensor surface, to control optimal fit and interaction force sensing.

Related Work – Measuring Interaction Forces in Human-Robot Interfaces

Capturing exoskeleton-human interaction forces is crucial for secure, comfortable deployment [204] and enhanced user experience. Current methodologies explore various sensor technologies, from 3D force sensors and IMUs [205] to soft barometric sensors [206–208] for monitoring the lower limbs and classifying human motions. However, these sensors may be limited by rigidity, bulkiness, or error-proneness due to ambient pressure changes and spatial user motion [209].

Promising solutions include capacitive force sensors due to their design effectiveness and ease of manufacturing and integration into curved exoskeleton interfaces. Recent advancements, like partially additively manufactured multi-layer capacitive pressure sensors [210] or combining barometric sensors with electromyography (EMG) [211], show potential despite challenges due to the necessity of precise electrode positioning and inability to measure forces. However, once EMG sensors are involved, direct skin contact, precise positioning and slippage avoidance of the electrodes are essential, which makes such technology unpractical. Given the importance of force distribution and optimal sensor placement [212], the proposed method in this work utilizes a high-speed, high-accuracy, multi-layer low-profile capacitive force sensor with spatial resolution to capture normal forces when worn over clothing.

8.2. Design of a Compliant Actuator-Sensor Unit

The design of the CASU is dependent on the targeted force range and use case, both of which are presented in this section, followed by a presentation of the technical solutions involving SMA actuation and capacitive force sensing.

8.2.1. Force Range Specification

The operational force range of the CASU must respect physiological limits in order to prevent aforementioned skin injuries as well as musculoskeletal pain [213]. Low but permanent stress of $4.27\,\mathrm{kPa}$ can already lead to structural damage to the skin [214]. Considering the application, interaction forces up to $30\,\mathrm{N}$ on a lower-limb exoskeleton are expected, as reported in [197] for the REX Personal exoskeleton (Rex Bionics, New Zealand).

In this study, the goal is to specify the relevant force range for sensing and actuation when the CASU is attached to the lower limb, specifically to the thigh, without the inclusion of further components. To complement the aforementioned knowledge from literature regarding expected interaction forces, a male subject (age 29, $2\,\mathrm{m}$, $88\,\mathrm{kg}$) was equipped as test subject with a 3-axis force-torque sensor (FTS) (F6D-80e-60, ME-Meßsysteme GmbH, Hennigsdorf, Germany) on the right thigh on top of the subject's trousers (100% cotton, approx. $1\,\mathrm{mm}$ thickness). The subject was in a state of no muscle tension. For the exemplary movement scenarios of non-dynamic muscle contraction in a sitting position, without resulting leg motion (1), knee stretching and flexing (2), standing-up (3), and sitting-down (4) (see also Figure 8.11b), interaction forces between $5\,\mathrm{N}$ and $50\,\mathrm{N}$ were measured.

This corresponds to a pressure range of $0.07\,\mathrm{kPa}$ to $0.71\,\mathrm{kPa}$, assuming a circular contact surface with $30\,\mathrm{mm}$ in diameter, remaining below the aforementioned permanent stress limit of $4.27\,\mathrm{kPa}$. Hence, the focus was set on the interaction force range of $0\,\mathrm{N}$ to $50\,\mathrm{N}$.

It should be noted that, given the relatively slow response times of SMAs [215, 216], the objective was to optimize the initial donning and primarily compensate for unintended interface displacements during movements over extended wearing times. In contrast, responsive actuation during gait cycle was not intended.

8.2.2. Use Case Definition

Here, an example use case of the CASU is illustrated: The exoskeleton is donned in the morning. Each interface with multiple CASUs is attached to the user's limb and fastened manually by the user or an assistant with straps (i.e., donning). At least three CASUs per interface should lead to an effective self-centering configuration. The capacitive sensor of the CASU is thereby constantly measuring the interaction forces. It can provide helpful feedback to manually achieve a recommended donning force F_{don} as an initial force configuration; i.e., for the donning procedure. It is noteworthy that the CASU is only sensing and not actively applying any force in this situation. In contrast, in the course of the day, the exoskeleton interfaces are in an active state. In this state, a constant preset holding force F_{hold} is desired, with which the interface is pressed onto the limb. However, in a real scenario, the holding force is expected to decrease over time and spontaneously during various activities of daily life. Based on the measured interaction force, the CASU automatically compensates for a drop of F_{hold} without the user having to take any further action. It should be noted, that measured interaction forces above that setpoint are considered valuable sensor signals, containing information about the muscle activity, user intention or impacts from the environment onto the user.

In order to achieve a compact wearable unit for the described use case, the two subsystems of actuation and sensing are assembled and inserted into a cavity (Figure 8.2), which in future work will be embedded into an actual exoskeleton interface.

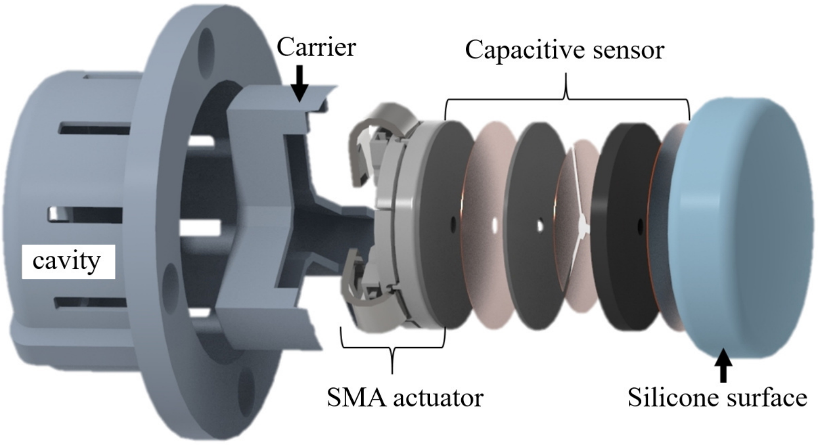

Figure 8.2.: CASU disassembled with interface cavity, carrier, actuator and in-silicone embedded force sensor. The presented components weight $30\,\mathrm{g}$. [8] © IEEE 2023.

8.2.3. Shape Memory Alloy Actuation

The actuator consists of three NiTi strips ($22\,\mathrm{mm} \times 5.5\,\mathrm{mm} \times 0.5\,\mathrm{mm}$ each) with an austenite finish temperature $\mathrm{A_f} = 40\,^\circ\mathrm{C}$, chosen to be above but close to body temperature (Figure 8.3a). This choice limits the heat transfer from actuator to body and minimizes the power demand due to a small temperature difference between body surface ($33.5\,^\circ\mathrm{C}$ to $36.9\,^\circ\mathrm{C}$ [217]) and $\mathrm{A_f}$, where shape change commences. Each strip starts in its original straight shape and is then cold-formed to an arch of up to 180° to form a compliant, spring-like flexure bearing with the shape memory effect as inherent actuation mechanism, one DOF for each strip (Figure 8.3 a–c). The three bent strips are then joined together in a circular shaped shell, additively manufactured by stereo-lithography (Form3, Durable Resin, Formlabs GmbH, Germany). The strips then form a triangular parallel-kinematic structure with a total of three DOF. When the temperature of the strips exceed $\mathrm{A_f}$, the strips start to re-obtain a straight shape and thus behave similar to a revolute joint (Figure 8.3d). Combined with the carrier element, this movement pushes the actuator against the body (Figure 8.3e). The carrier also restricts the axial rotation of the actuator by guiding the strips within their boundaries in the plane and constrains flexion angles between 90° and 180° throughout utilization to prevent the strips from loosing their characteristic compliance and becoming irreversibly deformed.

Each strip is actuated individually using heating wire wrapped around each strip's joint center point ($58.4\,\Omega\mathrm{m}^{-1}$, Ø $0.15\,\mathrm{mm}$, $500\,\mathrm{mm}$). This approach limits driving cur-

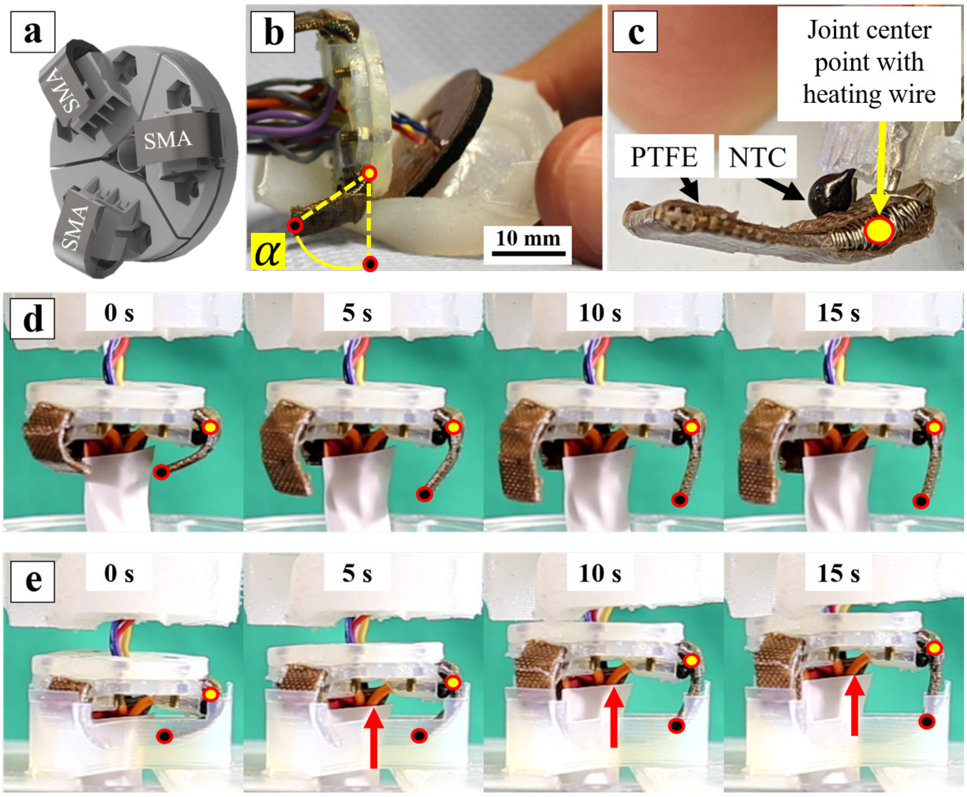

Figure 8.3.: Actuator design with a configuration of three parallel NiTi strips clamped in an additively manufactured shell, cold-formed to flexure bearings (a+b) and equipped with heating wire and temperature sensor (c). Driving mechanism demonstrated ($I < 1.2\,\mathrm{A}$ per strip) for the free actuator part (d) and combined with the carrier, constraining flexion angles to $90^\circ < \alpha < 180^\circ$, creating an upwards movement and leading to a normal force (e). [8] © IEEE 2023.

rents to maximum 1.2 A and leads to an exclusive heat conduction from the wire to the strip at the exact location where the shape memory effect creates a relevant shape change. The remaining strip surface temperature does not follow a steep ramp and can instead, provide the cooling surface for heat convection to the ambiance. This way, no additional active cooling is required. The strip is then covered with adhesive heat-resistant polytetrafluoroethylene (PTFE) film. A temperature sensor with negative temperature coefficient (NTC) and a measuring range of −55 °C to 125 °C is mounted to each strip in proximity to the heating wire. The sensors allow an estimate of the strips' temperatures and therefore aid individual control, preventing the entire actuator from overheating. It is worth mentioning, that this design does not require an antagonistic element to re-bend the strips after actuation has ended, since the on-body application serves as such.

8.2.4. Capacitive Force Sensing

To measure the interaction force between the actuation unit and the human body, a capacitive sensor with three measuring points is utilized. Figure 8.4 shows the multi-layer sensor (right) consisting of three conductive layers (top-down: ground, sensing, and shield) which are electrically isolated from each other. The ground and sensing layers comprise a plate capacitor with a capacitance

$$C \propto \epsilon(d_0 - d)^a \tag{8.1}$$

where ϵ is a constant related to the material between the electrodes i.e., the permittivity, d_0 is the initial distance between those two layers, i.e., the thickness of the foam in between them, and d the compression due to the interaction force. a is an experimentally determined constant describing the nonlinearity. It is set to be $[-1, -2]$. The shield layer protects the measurement against electrical interference from below.

The compressible layer is electricity isolating and made of elastic foam comprising elastomeric ethylene-propylene-diene monomer (EPDM) (Shore A 30) and acts as a pressure transducer. The other isolating layers are non-compressible. The relation between the acting pressure and the resulting compression for soft foams can be roughly described

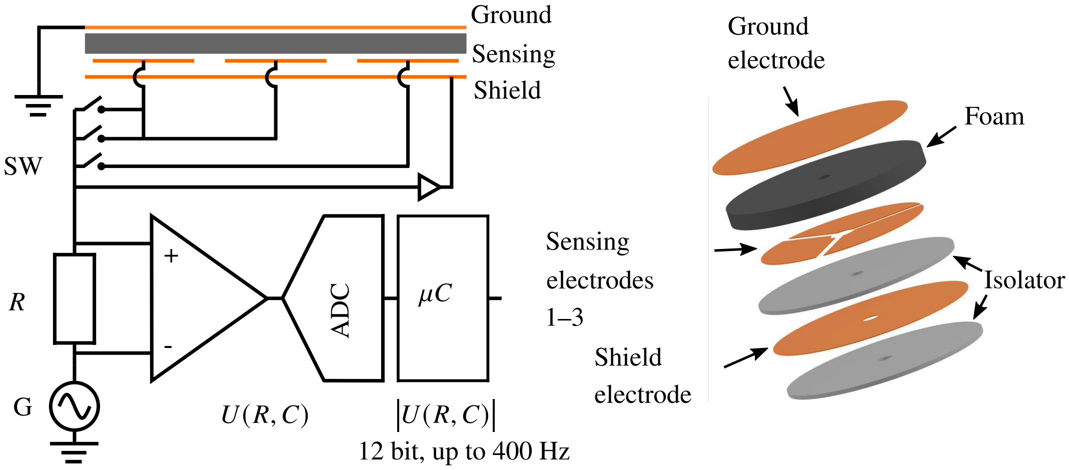

Figure 8.4.: Schematic of the capacitive measurement circuit (left). The resulting capacitance between the sensing electrodes and the ground is captured for each single or joint sensing electrodes. The force sensor (right) consists of three conductive layers, where the second layer is divided into three sensing electrodes. [8] © IEEE 2023.

by $P \propto d^b$, where d is the compression due to the interaction force, and b is experimentally determined as 2. The measured force F, which acts on the sensor area A_sens and corresponds to the pressure $P = F/A_\text{sens}$, is reported as $F \propto d^b A_\text{sens}$. During force measurement, the relation $\Delta F(\Delta C)$ is approximately linear since $\Delta F/\Delta d$, $\Delta C/\Delta d$ are conversely nonlinear, such that their nonlinearities cancel each other out. Figure 8.4 illustrates a simplified measurement circuit (left). The three sensing electrodes are driven by an analog switch (SW) capable of joining multiple electrodes to increase sensitivity. In total, a seven-electrode arrangement can be configured. The alternating current through a shunt resistor R is measured, digitized, and its amplitude sampled with up to 400 Hz. The sensor values are provided over an inter-integrated circuit (I2C) to universal serial bus (USB) adapter to the host computer at 200 Hz. A corresponding ROS node reads out the sensor and applies data preprocessing, such as offsetting and filtering.

8.3. Experimental Evaluation of the Compliant Actuator-Sensor Unit

The experimental setup for the systematic evaluation of the CASU is shown in Figure 8.5a. The CASU was placed into a customized scaffold that constrains rotation around z. The scaffold was then mounted onto a Stewart Platform (M-850, Physik Instrumente GmbH, Germany) to move the CASU against an opposing 3-axis FTS (Section 8.2.1). The FTS surface simulated an idealized flat body surface and provided reference force data. A proportional-integral (PI) controller was implemented to control the normal force (measured by the FTS), allowing to simulate the initial donning force F_don. This force is applied to the body when attaching the device, while F_hold is the holding force of the CASU when worn (Figure 8.5b). A preselected minimum force level $F_\text{hold-min}$ could be sustained with an on-off controller, while $F_\text{hold-max}$ was determined as the maximum applicable force after a given actuation time, revealing $F_\text{offset} = F_\text{hold-max} - F_\text{hold-min}$ (Figure 8.6a). All controllers were implemented in Python 3.96. Furthermore, a thermal imaging camera (FLIR E60, Teledyne FLIR LLC, USA) measured the temperature on the outer surface of the CASU. The data of the platform's pose, FTS, capacitive sensor, inner temperature sensors, and power supply were acquired using ROS.

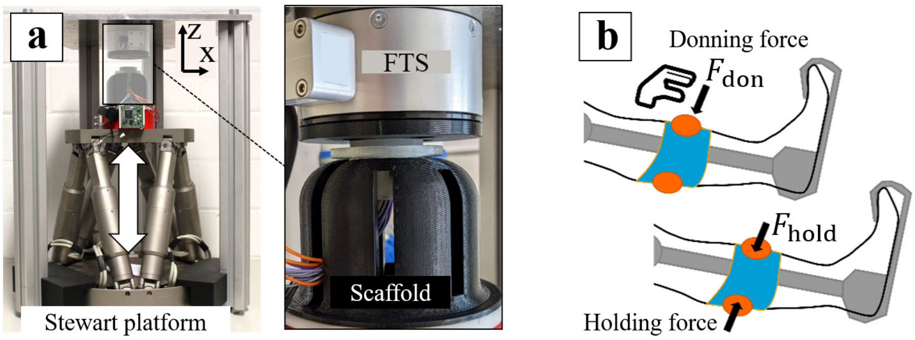

Figure 8.5.: Experimental setup including a Stewart Platform for controlled displacement of the CASU in z and against a 3-axis force-torque sensor (FTS) (a). This setup allowed for calibration, as well as to simulate actuation and sensing behavior under various configurations of donning force F_don during attachment and the actively applied holding force F_hold (b). [8] © IEEE 2023.

8.3.1. Characterization of the Shape Memory Alloy Actuator

An initial study with a series of power configurations was conducted to seek a suitable power range, resulting in a trade-off between high applicable F_{offset}, excessive temperature rise, and limitation of mobile power supplies. For all succeeding experiments, all NiTi strips were actuated simultaneously and within that given power range. To identify an appropriate control current for each strip, the temperature development and cooling time were analyzed with the configuration of $F_{\text{don}} = 30\,\text{N}$ and $F_{\text{hold-min}} = 20\,\text{N}$ for control currents ranging from $0.5\,\text{A}$ (mean $0.4\,\text{W}$) up to $2.0\,\text{A}$ (mean $4.1\,\text{W}$) per strip (Figure 8.6). Actuation periods of $30\,\text{s}$ created F_{offset} up to $16\,\text{N}$ for $2\,\text{A}$ at the cost of increasing the inner temperature to almost $120\,°\text{C}$ and a passive cooling time of over $400\,\text{s}$ afterward. Thus, for all succeeding experiments, a current limit of maximum $1.2\,\text{A}$, $1.0\,\text{A}$ and $1.05\,\text{A}$ were set for the three strips, respectively. The different currents were chosen to achieve a visible synchronous flexion of the strips without load.

Various Load Conditions

Then, the operability under various loads, i.e., combinations of donning (F_{don}) and holding ($F_{\text{hold-min}}$), was investigated, considering the aforementioned load range below $50\,\text{N}$. Thereby, maximum inner temperature T_{max} and passive cooling time t_{cool} (i.e., time after actuation to re-obtain body surface temperature of $34\,°\text{C}$) were measured. Figure 8.7 shows the results for one single actuation cycle with varying force configurations for (a) constant $F_{\text{don}} = 50\,\text{N}$ and (c) constant $F_{\text{hold-min}} = 10\,\text{N}$ with respective F_{offset} between $7.2\,\text{N}$ and $13.7\,\text{N}$, requiring a maximum power demand of $3.1\,\text{W}$ per NiTi strip. The highest F_{offset} was found for the configurations with $F_{\text{don}} = 50\,\text{N}$ (Figure 8.7b). The maximum inner temperature T_{max} remained for all configurations below $86\,°\text{C}$. F_{offset} increases with F_{don} (Figure 8.7d), contradicting the expectation that the actuation performance would drop as F_{don} increases. Instead, higher initial forces during fastening allowed the actuator to perform better, making it an ideal component of an interface actuator. It is hypothesized that higher F_{don} compressed the compliant CASU more effectively, bringing the NiTi strips into a stronger bending shape. This increased the possible mechanical displacement of the strips during phase transition from martensite to austenite.

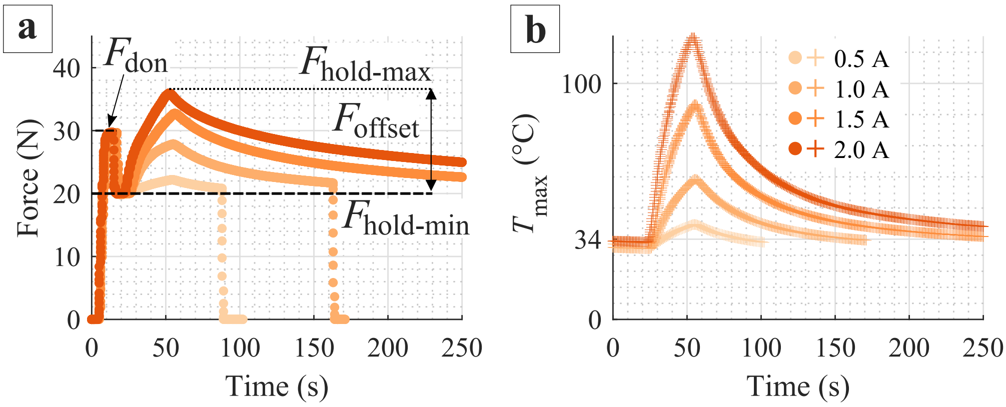

Figure 8.6.: Investigation results of the force range (a) and temperature behavior (b) for control currents of $0.5\,\text{A}$ (mean $0.4\,\text{W}$) up to $2.0\,\text{A}$ (mean $4.1\,\text{W}$) per strip. Configuration featured $F_{\text{don}} = 30\,\text{N}$ and $F_{\text{hold-min}} = 20\,\text{N}$ with F_{offset} of up to $16\,\text{N}$ and maximum inner temperatures T_{max} of $120\,°\text{C}$. Force drops to zero indicate that T_{max} has reached body surface temperature of $34\,°\text{C}$. [8] © IEEE 2023.

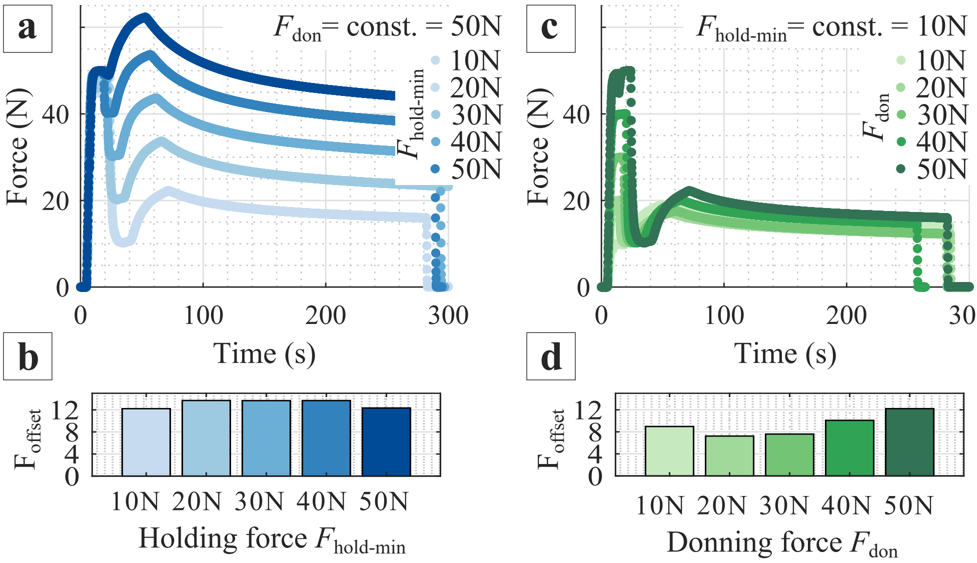

Figure 8.7.: Actuator performance at control currents of maximum 1.2 A for (a, b) constant $F_{\text{hold-min}} = 10\,\text{N}$ and (c, d) constant $F_{\text{don}} = 50\,\text{N}$ in the operation range of 0 N to 50 N, revealing a maximum F_{offset} of 13.7 N. Higher F_{don} lead to higher F_{offset} (d). [8] © IEEE 2023.

Force Control Mode

In addition, the actuator was evaluated during force control mode to sustain a given $F_{\text{hold-min}}$ using the FTS. Figure 8.8 shows the results for the control experiment with the initial configuration of $F_{\text{don}} = 30\,\text{N}$ and $F_{\text{hold-min}} = 20\,\text{N}$, using the FTS measurement as control input. The robotic Stewart Platform was programmed to lower $F_{\text{hold-min}}$ by 2 N each 15 s. The SMA actuator had to use that time to re-obtain and hold the setpoint force of 20 N. The actuator could withstand for four entire cycles (i.e., approx. 8 N) before it failed to reach the setpoint. This performance for consecutive cycles is consistent with the observations during aforementioned single-cycle operation and the F_{offset} limitation. The behavior is intelligible, since the displacement of the actuator strips was limited due to their small size. When their maximum bending angle was reached, further retraction of the Stewart Platform could not be compensated for.

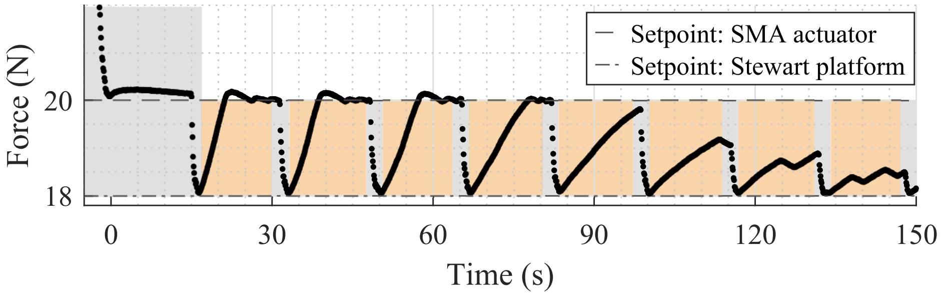

Figure 8.8.: Testing the SMA actuator control and using FTS data as idealized force input for the configuration $F_{\text{don}} = 30\,\text{N}$ and $F_{\text{hold-min}} = 20\,\text{N}$. Every 15 s, the Stewart platform moved away from the CASU to simulate a force drop of 2 N (grey). The SMA actuator aimed to re-obtain $F_{\text{hold-min}}$ (orange). After four cycles, the SMA actuator became unable to follow the setpoint since the NiTi strips were maximally bent. [8] © IEEE 2023.

8.3.2. Characterization of the Capacitive Sensor

To calibrate the capacitive force sensor and develop a sensor model to render force values, the experiment setup was utilized to iteratively load the CASU within $64\,\mathrm{s}$ and unload it in $63\,\mathrm{s}$. Since the SMA actuator generates heat, it was crucial to investigate the temperature influence on the capacitive force measurement. To this end, the unloaded actuators were operated five times for $30\,\mathrm{s}$, initially starting from room temperature. Capacitive sensor values, the actuator's inner temperature, and the unit's outer temperature were recorded.

Results, illustrated in Figure 8.9, show the relation between the capacitive sensor values and the applied normal force to be nearly linear, as reasoned in Section 8.2.4. The maximum hysteresis is $4\,\mathrm{N}$, which results in a relative hysteresis error of 8%. There is also an observable drift in the sensor values along the experiment iteration due to the creep behavior of the foam. Also related, the results show a small jump in the $0\,\mathrm{N}$ position. Presumably, after the first load interaction, the foam retained residual compression resulting in higher initial electrical capacitance. This might also be traced back to displacements in the CASU after the first load.

The results were further used to develop a linear model, which renders forces from capacitive sensor values, and applied for the on-body proof of concept. Conceding an ideal donning force and no displacement or slipping at the exoskeleton interface, the capacitive sensor provided reliable force sensing.

The investigation of the heat impact on the capacitive force measurement revealed a direct correlation between the actuator temperature inside the CASU and the capacitive force values, as shown in Figure 8.10. Variation in the capacitive measurement value was related to the temperature of the multi-layer sensor and especially to the heat absorbed by the foam. The foam acts as dielectric material with temperature-dependent permittivity $\epsilon(T)$, which contributes to the resulting capacitance

$$C \propto \epsilon(T)\frac{1}{d_0 - d} \tag{8.2}$$

where T is the temperature of the foam, d_0 the thickness of the unloaded sensor, and d the compression. However, as the temperature inside the CASU was being recorded, a model could be developed to compensate for temperature influences. The violet line in

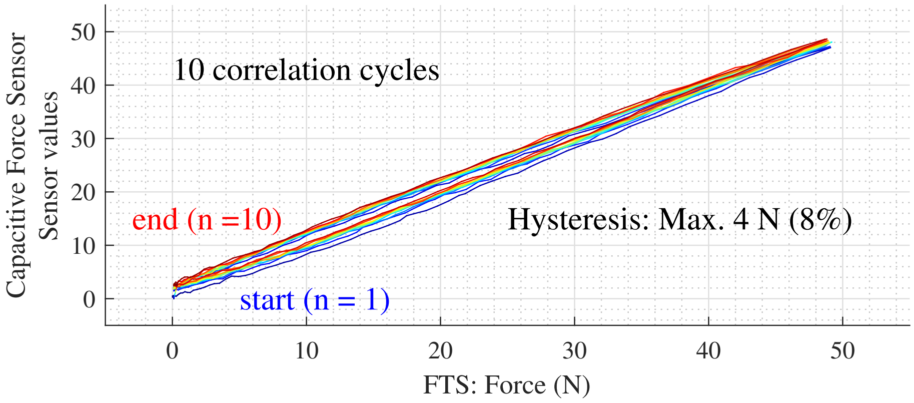

Figure 8.9.: Correlation of capacitive sensor values and the reference normal force after ten iterations ($n = 10$) loading the CASU between $0\,\mathrm{N}$ to $50\,\mathrm{N}$. [8] © IEEE 2023.

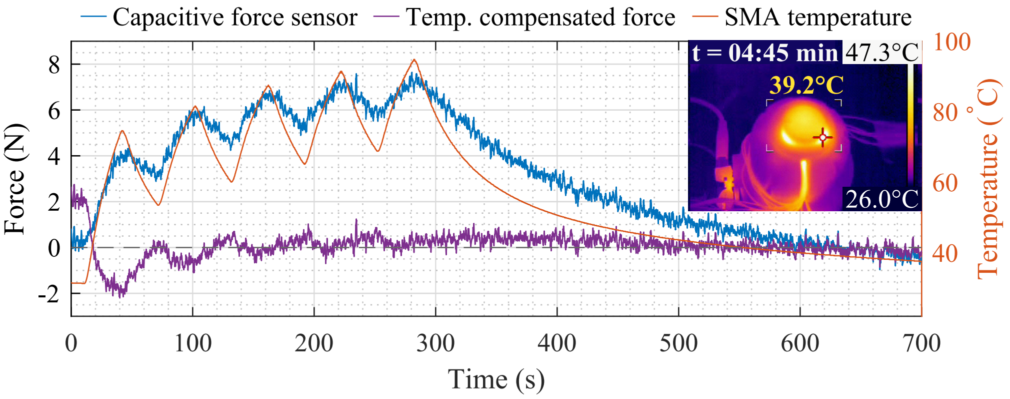

Figure 8.10.: Correlation of inner temperature of NiTi strips (red) and capacitive force sensing (blue) for five consecutive heating cycles without load. A model driven from the correlation was applied to compensate the temperature dependency of the force measurement (purple). The surface temperature of the CASU did not exceed 39.2 °C (thermal image). [8] © IEEE 2023.

Figure 8.10 shows the temperature-compensated capacitive force measurement. In a final actuator test, five consecutive unloaded actuation cycles were conducted to investigate heat transmission to the body to rule out potential heat damage to the skin. Each actuation cycle included heating for 30 s followed by passive cooling for 30 s. It is noteworthy, that the temperature on the silicone surface towards the human body only reached a maximum temperature of 39.2 °C (thermal image), which can be considered an acceptable temperature for long-term use [200].

8.3.3. On-Body Testing

In a first attempt to demonstrate the approach qualitatively on a human body, the CASU was attached onto the aforementioned subject to maintain comparability (Figure 8.11a). Sensing and controlled actuation were tested for a single sequence of the aforementioned movements (1)–(4) (Figure 8.11b), using capacitive sensor data as control input and an exemplary setpoint force $F_{\text{hold-min}} = 20\,\text{N}$. Consequently, the CASU was supposed to actively compensate for interaction forces below that setpoint and passively monitor the interaction forces above.

The results are shown in Figure 8.12 and depict that the desired setpoint was successfully reached before body movement begins, and re-obtained between (2) and (3) and after (4). In between (1) and (2), no control intervention was required. Characteristic patterns of the interaction force between the subject's muscles and the interface are visible for each movement modality, which rise from a predefined (i.e., known) plateau of $F_{\text{hold-min}} = 20\,\text{N}$, potentially enhancing post-processing steps such as motion recognition.

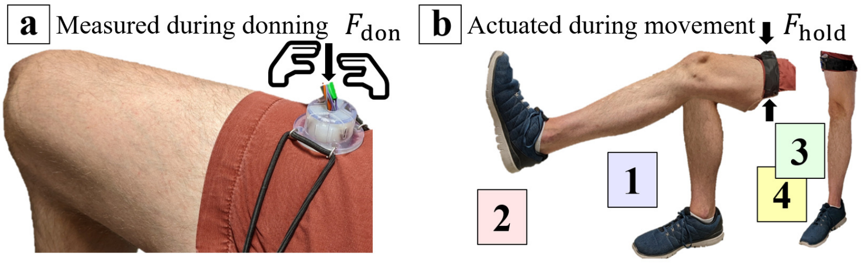

Figure 8.11.: a: Experimental setup for investigating leg activity when the CASU was attached onto the right thigh. b: The sequence consisted of non-dynamic muscle contraction (1), knee stretching and flexing (2), standing-up (3) and sitting-down (4). [8] © IEEE 2023.

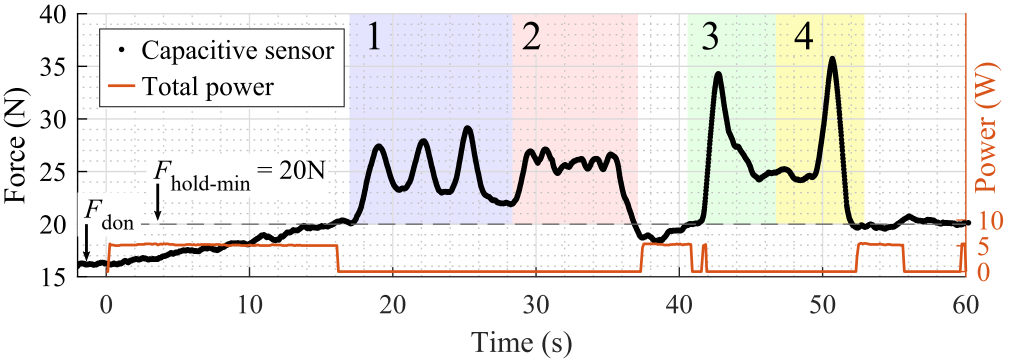

Figure 8.12.: Interaction forces between user and interface, measured by the active CASU during one single sequence of four different movements scenarios including 3× muscle contraction (1), 3× knee stretching and flexing (2), 1× standing up (3), and 1× sitting down (4). Starting from $F_{\text{don}} = 16\,\text{N}$, a contact force $F_{\text{hold-min}}$ of 20 N was sustained during the measurement. [8] © IEEE 2023.

8.4. Towards Integrated Exoskeleton Interfaces

In this chapter, a novel design and technical characterization of a SMA-driven, compact, and compliant actuator-sensor unit was presented, that can be comfortably worn over clothing without jeopardizing performance or heat hazard. The results show that the presented design can effectively sustain a defined interface fit with the human body, and thus, compensate for unintended interface displacements. Consequently, this can increase the measurement quality of interaction forces between body and exoskeleton for efficient motion recognition. This work thus contributes to the overall research objective of this dissertation of achieving compliance, miniaturization, and practicability in the realm of healthcare robotics by means of a SMA.

Yet, the deployed SMA actuation generally comes with relatively low energy efficiency, which must be critically discussed in the context of a mobile exoskeleton. To this end, the results show a power demand for the SMA actuator below $5.5\,\text{W}$, required for only a short time span during different consecutive lower limb movements. For safety, the actuator and its electric currents below $1.2\,\text{A}$ are electrically shielded through grounding and separated from the body by non-conductive resin material layers and a silicone surface protection. The CASU is thus assumed to be suitable for a mobile and safe exoskeleton interface. Furthermore, and in regard to the experiments, manually obtaining a specific donning scenario and replicating identical movement cycles without specialized equipment for human movement studies can be arduous and lacks the level of repeatability achieved with the experimental setup. Additionally, enrolling only a single participant, does not yield statistically significant insights, yet. Nevertheless, it serves as an initial demonstration of the viability of the presented approach.

Future work should turn CASU into a stand-alone module and integrate it into an exoskeleton interface. Furthermore, an extensive user study with multiple subjects is required, featuring the movement sequence presented in this work and also activities of daily living, to investigate both, technical performance and practical usability.

Part IV.

Smart Material Systems for Healthcare Applications

9. Critical Discussion

The research presented in this dissertation, while pioneering in many respects of application-driven development and implementation of selected smart materials, also uncovers several critical challenges and opportunities for future improvements in the field of healthcare technology.

This chapter contains a discussion for each of the featured materials. It should be noted, that the previous Chapters 4–8 contain a more detailed application-specific discussion, combined with a comparison to the related work in each respective field. To avoid redundancy in this dissertation, the ferromagnetic and piezoresistive polymer applications are combined and briefly addressed. Then, the three SMA applications in this dissertation are discussed in further detail. This includes the limitations and challenges, as well as a best-practice guideline for handling this smart material. It is meant to extend the Chapters 4, 5, and 8, by providing a concise, and generalizing view on the research contribution of this dissertation in regard to SMAs.

Ferromagnetic and Piezoresistive Sensing

Smart material sensing in this dissertation included the integration of ferromagnetic and piezoresistive polymer materials. In the context of this dissertation, the focus was narrowed to one work for ferromagnetic sensing (i.e., Compliant Sensor Array for Passive Magnetic Instrument Tracking, Chapter 6) and one for piezoresistive sensing (i.e., Sensorized Training Platform for Endovascular Surgery, Chapter 7). This limited the breadth of discussion and conclusions, especially when contrasted with the broader scope of SMA contributions.

The compliance and flexibility of the materials used was a crucial factor. Piezoresistive polymer films, by their nature, are compliant, lending themselves well to applications requiring compliance and flexibility. Ferromagnetic materials, particularly permanent magnetic components, are primarily rigid. However, in the case of ferromagnetic sensing, the compliant element was the sensor array. This adaptability was crucial for wearability and conformity to the wearer's body. In this work, the instrument was simulated with a permanent magnet. In the future, the ferromagnetic material is intended for attachment to endovascular instruments like guidewires and guidewires, possibly as a coating to preserve the instrument's inherent flexibility and compliance.

Safety considerations regarding piezoresistive polymer films in this study were minimal. They were not being used on-, or inside the human body, but instead only in a vascular phantom. Similarly, the safety of the magnetic sensor array was not a major concern, as it involved no creation or manipulation of magnetic fields, which could become hazardous in the operating room. It is worth noting that when magnetized instruments are used in procedures like endovascular interventions, they should be kept away from strong magnetic fields, such as those generated by MRI machines, to mitigate safety concerns.

The works presented in this dissertation prioritized efficient prototyping and simplicity, facilitating replication and modification by other research groups. The materials used, including piezoresistive and ferromagnetic materials, were off-the-shelf and cost-effective. This included commercially available items like Velostat, electric circuit components, and microcontrollers. As a result, the technical and performance potentials of these materials were not maximized. This approach led to the expectation of limited durability, an aspect that remained unexplored in this dissertation.

Shape Memory Alloy – Actuation and Sensing

Commercially available medical devices made from SMAs are almost exclusively deploying the aspect of superelasticity (Section 3.1.3). Furthermore, these devices are usually designed for single-use procedures, such as implants, and guidewires for endovascular surgery. Beyond these superelastic devices in healthcare, a strong focus lies on 1D SMA-based linear actuators (i.e., wire actuators) and sensors [155–158], allowing for compact contraction when stimulated by heat, as presented in Section 5.2.1.

In contrast, and as an important further development to these endeavors, this dissertation has experimentally demonstrated the following aspects with respect to robotic systems with integrated SMAs:

- Highly compact extendable tendon-driven **continuum robots** with state-of-the-art workspace and reach can provide multiple extension and retraction cycles during one or multiple operations (i.e., **multiple-use**), due to a novel self-assembly design and their **superelastic** SMA backbone from NiTi.
- Flexible **surgical instrument**s can perform complex antagonistic **2D shape-change** while estimating their current shape via **self-sensing**, due to the NiTiCu-based wires that provide structural integrity, inherent actuation, and sensing.
- CASUs in exoskeleton interfaces can automatically regulate the force with which they conform and hold to the human body, due to embedded NiTi actuator strips in a spring-like configuration (not superelastic). They deploy directly the shape memory of the material for a **2D expanding motion**.

Table 9.1 provides an overview over the presented robotic and sensor systems, which will be helpful to discuss the challenges and limitations of SMAs for healthcare technology.

9.1. Challenges and Limitations of SMAs

SMAs, in particular in the form of NiTi or NiTiCu, are widely commercially available in various forms of raw material, including wires, strips, rods, tubes, and plates. It is important to highlight that these alloys come with certain drawbacks, including higher cost in comparison with other conventional and shape memory materials, and further technical challenges.

9.1.1. Material Processing

The conventional machining (i.e., milling, turning, cutting) of SMAs is usually difficult due to the material's hardness, as well as the effects of strain hardening, and fatigue

Table 9.1.: Overview over the stimulus-related technical specification of the SMA-based applications developed in this dissertation. "–" indicates the absence of measurements.

	Continuum Robot Chapter 4, [1]	**Flexible Instrument** Chapter 5, [2,4]	**CASU** Chapter 8, [8]
SMA	NiTi	NiTiCu	NiTi
Austenite finish temperature	−10 °C	65 °C	40 °C
Geometry	wire	wire	strips
Dimensions	Ø 1.0 mm	Ø 0.7 mm	3 × (5.5 mm × 0.5 mm)
Length	> 240 mm	230 mm	3 × 22 mm
U-shape	no	yes	yes
Load (maximum)	–	90 mN	50 N + 13.7 N
Heating	–	intrinsic	extrinsic
Current (maximum)	–	3 A	3 × 1.2 A
Voltage (maximum)	–	2.6 V	2.6 V
Additional actuation	motors	–	–
Bending (maximum)	–	19 mm	–
Response time	–	< 15 s	< 15 s
Temperature (maximum)	–	< 80 °C	< 86 °C
– on tissue	–	–	< 39.2 °C
Use case	MIS	MIS	Exoskeleton

hardening, increasing the tool wear. Furthermore, in case of superelastic NiTi, its elastic deformation under external load, makes machining also challenging [218].

Raw SMA material can be obtained and joined via welding [219], or cut and tailored by means of laser processing [220, 221]. Laser processing in particular is thereby usually limited to 2D sheets. However, with both welding and laser processing, the heat transmission to the material must be strictly controlled. High temperatures in the SMA may influence the crystalline structure and thus alter the transition temperatures or the shape memory locally and in uncontrolled manner. This may lead to stress within the material and an unintended shape memory behavior. An alternative method employed in smart material fabrication is additive manufacturing, such as laser powder bed fusion [222, 223]. This technique, which involves material accumulation as opposed to material separation, theoretically offers a greater degree of design freedom for smart material objects. However, it is important to note that the material properties of the final product may not always meet the requirements for the intended application, particularly in terms of accuracy, void defects, and surface roughness [224, 225].

For the scope of this dissertation with a special focus on health care robotics, NiTi in the form of wires and strips was utilized. Rather than creating custom components, this dissertation focused on the skillful integration of off-the-shelf NiTi parts. This approach revealed that the cylindrical cross-section of the wire is advantageous for use as a superelastic backbone in continuum robots (Chapter 4, [1]). Additionally, it facilitates the implementation of intricate 2D shape morphing, and potentially, complex 3D shape transformations in flexible instruments (Chapter 5, [2]). However, the strip geometry with its rectangular cross-section proved more practical compared to the wire geometry. Its flat surface was not only easier to clamp, providing mechanical fixation, but also facilitated the attachment of power supply electrodes. Furthermore, the large flat surfaces of the strip facilitate heat transfer to and from the strip, allowing for faster material response compared to wires.

9.1.2. Shape Setting of Shape Memory Alloys

Commercially available raw SMA material comes with a predefined shape memory. Usually, for wires this is the straight orientation, for sheets and strips it is the straight flat orientation. One can design an actuation system in such a way, that deploys this initial shape memory. Alternatively, a new shape memory can be forced on the material. In order to do so, the material has to be cold-formed into the desired shape and then fixated firmly in a rack. The material must then undergo a heat treatment with subsequent quenching, as shown in Section 5.1.2.

Heat Treatment of Shape Memory Alloys

There are various heating options to exceed the required material temperatures of $> 425\,^\circ\mathrm{C}$ [149, 150]. Two were tested within this dissertation:

- **Convection** and **conduction heating** in a furnace.
- **Joule heating** connected to a power-supply.

Professional furnaces for industrial or laboratory usage are relatively slow but provide the most accurately controlled temperature courses while also guaranteeing a homogeneous heat distribution in the material. Alternatively, it was found that power supplies ($I > 33\,\mathrm{A}$) can heat up wire diameters of maximal Ø $2.0\,\mathrm{mm}$ to $500\,^\circ\mathrm{C}$ in less than $1\,\mathrm{min}$ by Joule heating. Yet, the temperature control of this method is challenging, since the highest temperatures usually occur where the electrodes are in contact with the smart material. The distribution will therefore be more heterogeneous compared to the furnace environment. Furthermore, caution is advised against employing simplified variants of the Joule heating approach, especially those replacing the laboratory power supply with mobile $12\,\mathrm{V}$ batteries, as outlined in [226]. The risk lies in the potential for uncontrolled battery discharge, leading to current peaks that may rapidly oxidize the shape memory material.

Fixation for Shape-Setting

Despite employing diverse heat treatment methods, shaping smart materials to desired forms remains challenging. This is particularly true for intricate geometries like the S-shape, necessitating sophisticated rack designs, as shown in Section 5.1.2, [2]. Materials selected for these racks must exhibit high temperature resistance. Two were tested within this work:

- **Fiber boards**, medium density to high density [226] for 2D shapes.
- **Metal**, (e.g., Al) for 2D, and potentially 3D shapes.

Al (melting temperature: $660\,^\circ\mathrm{C}$ [227]) has been found to be still suitable for heat treatment of the SMA with temperatures $< 500\,^\circ\mathrm{C}$. By means of computer numerical control (CNC) machining technology, the fabrication of complex shapes in 2D, and even 3D are feasible. Yet, Al is recommended solely for furnace-based methods, due to its relatively high conductivity for heat, and electric current [227].

In contrast, when using Joule heating, the rack material should be non-conductive to prevent the deflection and grounding of electric currents through the rack, rather than through the SMA. Besides, the rack material should not act as a heat sinks (i.e., cooling).

Consequently, fire-resistant high density fiber boards have been tested. However, although easy to process by laser-cutting, the susceptibility of fiber board racks to damage from heat and the forces, exerted by smart materials returning to their pre-programmed shapes, remains a concern.

In the context of healthcare robotics, a proper preparation of the smart material is key to secure a reliable functionality when integrated in the robotic system. For both tested materials, the repeatability of these processes was challenging, as also backed up by [228]. While temperature control in a furnace is manageable, the precise positioning within the clamping racks remains a potential source of variability in outcomes for both rack material options and both heating methods.

Furthermore, it is also important to recognize that the raw materials supplied by manufacturers are subject to fluctuations in characteristics such as transition temperatures, material compositions, and heat treatments. Therefore, when envisioning medical instruments and devices, each batch must be subjected to rigorous material testing to ensure uniformity in the starting material.

9.1.3. Material Integration and Configuration

Many SMA actuation systems employ the one-way shape memory effect, effectively eliminating the need for extensive material training associated with two-way memory behavior. This one-way approach, however, doesn’t naturally provide reversible actuation. To overcome this, reversible actuation is achieved through antagonistic setups. A **mechanical spring** can act as an antagonist, offering simplicity and reducing smart material usage. When inactive, it returns the instrument to its original shape.

Another method involves an antagonistic **dual-SMA** setup using an additional SMA component, ensuring stability and maintaining intermediate shapes when not activated. In healthcare robotics, these antagonistic approaches have distinct implications. The dual antagonistic approach stands out for its independence and safety, particularly under energy loss, maintaining the instrument’s equilibrium state, i.e., deformation. In contrast, the mechanical spring option, while simple, risks hazardous back-deformation in the case of an energy fallout (e.g., flexible surgical instruments, Chapter 5, [2]).

A third option is the **application-specific** antagonistic configuration, optimized for particular use cases. In these configurations, the specific application itself, actively resets the SMA actuator (e.g., compliant actuator-sensor units embedded in physical exoskeleton interfaces, Chapter 8, [8]). While this method is efficient (i.e., less hardware components), it requires detailed knowledge of the specific application. It is ideally suited for on-body applications but requires careful consideration of potential malfunctions and may have limitations in its applicability across a broader range of uses.

9.1.4. Stimulus and Material Response

Table 9.1 also provides an overview over the stimulus-related specifications, revealing the performance of the shape memory effect, investigated in this dissertation. It is important to recognize that the three applications and their quantitative results cannot be directly compared due to discrepancies in the materials used and differences in implementation, including configuration and heating approach. Yet, the systematic listing canalizes the main findings of this dissertation.

In this section, the stimulus and material response of only the non-superelastic applications, namely the flexible instrument and CASU, are discussed.

Application and Ambient Temperature Conditions

When the SMA is deployed directly on the skin or in direct tissue contact within the body, heat flux from the body towards the material will influence the smart material's temperature. It can heat or cool the smart material, depending on the temperature difference. The body temperature T_{body} (on-, or within the body) of the targeted application site, and the ambient temperature T_{amb} both effect this heat flux. They are thus important quantities for the design of an appropriate material stimulation. For most cases of intracorporeal applications in MIS, one can define $T_{\mathrm{amb}} = T_{\mathrm{body}}$. On the other hand, for most cases of on-body applications, one should make a case distinction. The higher of both temperatures T_{amb}, and T_{body} should be considered the dominant influence. This approach of prioritizing the highest temperature is recommended, since only the heating flux from the body/environment to the SMA is relevant, which increases its temperature and thus contributing to its actuation. In comparison, lower body and environmental temperatures would naturally cool the material only, which is a preferred system characteristic.

Consequently, the application site is pivotal in selecting the appropriate material, specifically concerning the transformation temperature A_{f}. It can be stated, that choosing transformation temperatures close to the expected steady-state ambient temperature, makes the actuation more effective (i.e., faster response time), and more efficient (i.e., requiring less heating energy). However, it is also more likely, that the material is actuated inadvertently or the control over the material stimulation is lost due to overheating.

The core body temperature of healthy humans is regulated within a relatively consistent and narrow range across various body sites (rectal, tympanic, urine, oral, and axillary), typically ranging from $35.69\,^{\circ}\mathrm{C}$ to $37.45\,^{\circ}\mathrm{C}$. The normal body temperature is commonly considered to be $36.8\,^{\circ}\mathrm{C}$ [229], with a median temperature of approximately $36.7\,^{\circ}\mathrm{C}$ [230]. Therefore, in such a context, the design of smart material actuators can be tailored under the assumption of a consistent ambient temperature (T_{amb} = constant). However, in intracorporeal applications, inadvertent actuation may occur, particularly in instances where the patient experiences a condition such as fever (pyrexia) or hyperthermia, resulting in an increased body temperature. To address this challenge, flexible instruments for MIS can also be constructed using SMAs with an austenite finish temperature $A_{\mathrm{f}} \approx 60\,^{\circ}\mathrm{C}$ (Chapter 5, [2]), thus enabling their use even in patients with elevated body temperatures. However, since protein denaturation can begin at temperatures as low as $40\,^{\circ}\mathrm{C}$ [231], a shielding insulation is mandatory to protect the human tissue from severe heat damage and cell death.

In contrast to the inner body temperature, the outer skin temperature may vary more strongly in the range from $30.7\,^{\circ}\mathrm{C}$ to $38.6\,^{\circ}\mathrm{C}$ [232]. It depends on various factors, including the body part of interest, the physical activity of the person [232], and the exposure to external heat sources (e.g., sunlight, radiators). When SMA actuators are worn on clothing (Chapter 8, [8]), the dependency on the skin temperature becomes less relevant. Against external heat sources, an additional shielding housing around the actuator can improve the heat resistances. Yet, this will also reduce the passive cooling capability (negative heat exchange) from the actuator. As with in-body applications, SMA with $A_\mathrm{f} \approx 60\,^\circ\mathrm{C}$ might be the better choice. It is worth mentioning that unlike intracorporeal applications, higher temperatures are less critical when occurring outside the body.

Temperature Management

As a thermo-responsive smart material, SMAs remember their original shape above the austenite finish temperature A_f. In order to increase the material's temperature independently of the ambient temperature T_amb, two methods were presented:

- **Intrinsic** heating via Joule heating through the SMA material.
- **Extrinsic** (secondary) heating via heating elements (e.g., high-resistance wire).

The temperature distribution in the smart material is essential. For a quick actuation response, a fast temperature change is required at those surfaces, underneath which the largest deformation is expected, and desired. In the same way, heat transfer and subsequent cooling in the absence of an active heat source allows for a quick drop in the material stress, decreasing of applicable forces. The faster the temperature can be regulated both ways, the faster is the controllable material response at the largest displacement. In contrast, other parts of the material component can warm up slower or, preferably, even remain cold if there is no deformation to be expected.

Intrinsic heating (Joule heating) is a simple approach where an electric current is sent through the shape memory material itself, without further components required. In comparison to the presented shape setting in Section 9.1.2, the currents used are much lower for the shape memory actuation. This was investigated in Chapter 5, [2], where $0.7\,\mathrm{mm}$ wires were activated by $3\,\mathrm{A}$ $(2.6\,\mathrm{V})$. Experiments revealed a considerately high current for intracorporeal applications due to the relatively low resistance of the wire. Yet, the high current allowed for a maximum bending of up to $19\,\mathrm{mm}$ over an instrument length of $115\,\mathrm{mm}$ in under $15\,\mathrm{s}$ and a maximum blocking force of $90\,\mathrm{mN}$. It is noteworthy, that the flexible instrument featured two SMA wires in an antagonistic configuration. Hence, the instrument is inherently stiffer when compared with the stand-alone material wire, since the shape memory effect of one wire must deform both the antagonistic wire and itself.

For intrinsic Joule heating, however, the effective temperature change depends on the electrical resistance of the smart material component and its electrical connections. Wherever the resistance is high, heat energy is transferred to the material and heats it up locally. In the linear smart material component, such as a wire or strip, one can anticipate a consistent and relatively low resistance along its length. However, a comparatively higher resistance typically arises at the points where the electrodes make contact with the smart material, as noted in [233]. This relatively high contact resistance leads to temperature peaks at the electrodes (usually located at the rear end of a continuum robot, and flexible instrument, respectively), rather than close to the area of large deformation. Hence, Joule heating not only favors an unintended homogeneous temperature rise in the entire smart material, but also temperature peaks at the electrodes, where inappropriate.

It is noteworthy, that for all kind of robotic systems applied close to, or even within the human body, heat from the material towards human tissue should be minimized at all times.

To overcome the unfavorable temperature distribution, extrinsic heating is a promising alternative and was investigated in Chapter 8, [8]. Extrinsic heating sources, such as high-resistance heating wires, also apply the Joule heating principle. They can be placed in close contact to the surface of interest. Therefore, heat is immediately transferred to where it is needed most, i.e., where the material should perform the largest displacements. In comparison with the intrinsic method of Joule heating within the smart material, extrinsic heating requires additional components and wiring. Yet, the heat transfer is more efficient and the required currents are lower, allowing for smaller conductors, and making it less hazardous in the case of malfunction. To substantiate the difference from the Joule heating approach deployed for the flexible instrument, a similar current was distributed to three separate heating wires at a similar power input ($\approx 10\,\mathrm{W}$). This configuration, as shown in Chapter 8 [8], was able to provide effective force offsets of $13.7\,\mathrm{N}$ within a force range of up to $62\,\mathrm{N}$.

It is noteworthy, that this dissertation investigated setups without active cooling, i.e., only passive-cooling (convection) was exploited. On the other hand, adding active cooling (e.g., air fan, cooling liquids) could be an additional feature, increasing the material response frequencies. Yet, additional cooling elements decrease the overall efficiency further. Thus, the necessity of an additional active cooling feature should be assessed carefully.

Control

Both, intrinsic, and extrinsic heating stimuli, were successfully implemented by means of off-the-shelf microcontrollers with heuristically tuned PID controllers. The feedback loop regulated the displacement (flexible instrument), and force (CASU), respectively. This approach was sufficient to drive each of the robotic systems. Based on the experimental evaluation, a data-driven model was not required for actuation, but investigated for the self-sensing of the displacement of the flexible instrument. However, it should be noted, that in order to implement a closed feedback-loop for the flexible instrument, marker tracking using external visual imaging devices was necessary. In a real MIS application, visually supported servoing of the instrument (e.g., based on endoscopic imaging) may be subject to more influencing factors and disturbances. Further research in this matter is necessary, as the control of SMAs constitutes a distinct research domain beyond the scope of this work. Yet, a short overview and outlook is given in the following.

In order to advance from PID, and also fuzzy-PID [234], approaches towards more complex control regimes, a bigger focus lies on handling the nonlinear and hysteretic characteristics of SMAs. It should be noted, that the specific “history” of each SMA specimen influences the nonlinear characteristics. The nonlinearity is hence considered time-variant, which becomes less impactful after extensive training, i.e., thermo-mechanical loading cycles [77]. Thus, a standard amount of training cycles, and the subsequent specimen characterization could be key measures for accurate control beyond any heuristic control strategy. To address the nonlinear characteristics, the PID control can be extended by a neural network modeling the hysteretic behavior, as in [235]. Furthermore, and leaving the conventional PID controllers with its constant parameters aside, regimes develop to become more dynamic, by using for example a Variable Structure Control with gain switches [236]. A similar approach is the discontinuous Sliding-Mode Control, that can be model-based [237], or data-driven [238], aiming for robustness against disturbances and model-uncertainties. Furthermore, so continuous Adaptive Control strategies adapt their parameters in real-time based on the observed performance of the system [239].

In contrast to data-driven strategies, model-based regimes build on a profound understanding of the material response and the particular specimen. Ideally, the specimen must be firstly characterized [240], providing data for the subsequent model parametrization. Material modeling still remains a challenging task, exceeding the scope of this work. For further details on modeling SMAs, refer to [241–243]. Recent robotic-related research directions in SMA modeling, address for example superelastic modeling for continuum robots [244], and thermodynamic plastic deformation mechanisms [245].

9.1.5. Hazards

The application of SMAs in health care robotics is not without challenges, specific to the medical field. A critical examination reveals shortcoming and even hazards that must be taken into account when choosing SMAs for a robotic component.

Mechanical Integrity

Although mechanically superior to polymer-based materials [96] and highly elastic compared to stainless steel [95], the endurance of NiTi is still subject to ongoing research. Critical aspects include the structural integrity [246], and thermo-mechanical fatigue [93], especially for long-term utilization as implant materials or multiple-use biomedical actuators. However, for robotic components designed as single-use actuators, the long-term risks are limited.

Biocompatibility

Biocompatibility is a crucial consideration for implants and instruments used within the human body. While Ni can exhibit inflammatory and genotoxic effects [247], NiTi is generally recognized as biocompatible in body fluids [248, 249]. The reason for this enhancement is, that NiTi forms a protective titan oxide (TiO2) surface layer, preventing the toxic Ni ions from being released to the human body. In this sense, NiTi is even more biocompatible than stainless steel alloys, e.g., AISI 316 LVM, with a high anti-corrosive content of chromium (Cr) and Ni [250]. However, for a robust and sustainable biocompatibility, NiTi requires surface treatments such as mechanical polishing, electropolishing, and etching [251]. Moreover, additional coatings can increase the biocompatibility further [252–254]. It should be noted that the NiTi materials utilized in this dissertation cannot be used in a biomedical application without one or multiple of the aforementioned surface treatments.

Thermal and Electrical Hazards

The potential thermal damage caused by the temperature-induced actuation of SMAs, when in contact with human tissue, is another significant concern. Tolerable temperatures, critical for preventing cell damage, must be thoroughly considered. Research indicates that temperatures above $45\,^{\circ}\mathrm{C}$ can be detrimental to cells [255,256]. Specific studies have shown irreversible changes in brain tissue at $44\,^{\circ}\mathrm{C}$ for extended periods [257] and thigh muscle tissue damage at temperatures exceeding $50.4\,^{\circ}\mathrm{C}$ [258]. It is worth mentioning, that despite the different austenite finish temperatures A_f for the flexible instrument ($60\,^{\circ}\mathrm{C}$) and the CASU ($40\,^{\circ}\mathrm{C}$), a similar power input would evidently still lead to a similar maximum temperature of $80\,^{\circ}\mathrm{C}$, and $86\,^{\circ}\mathrm{C}$, respectively (Table 9.1). Compared to the acceptable temperature range for body tissue, this temperature presents an obvious hazard. Yet, the experimental results of the CASU show, that despite this high temperature within the actuation components, a technical shielding or encapsulation is a valid protection measure. This way, the silicone layer in direct contact with the skin only exhibited an appropriate maximum temperature of $39.2\,^{\circ}\mathrm{C}$. A similarly effective shielding approach is also required for any SMA-based flexible instrument. Fortunately, the same shielding then also functions as an electrically insulating barrier, and a sterile cover as recommended for extendable continuum robots in Section 4.4, [1].

Ferromagnetic Interference

Finally, the ferromagnetic properties of NiTi are a notable consideration, especially in clinical settings with strong electromagnetic fields, like hybrid operating rooms equipped with MRI machines. Although NiTi is primarily considered paramagnetic [259], specific thermal conditions, and tensile deformation can induce ferromagnetic properties [260]. Furthermore, particular heat treatments can lead to strongly ferromagnetic Ni oxide layers [259]. Therefore, understanding and managing these magnetic properties are crucial for safe and effective use of SMA-based actuators in clinical environments.

9.2. Best-Practice for Shape Memory Alloys

Based on the findings and challenges regarding SMAs presented in this dissertation, the following best-practice design workflow is recommended for SMA-based actuators in the realm of robotic applications in healthcare:

1. **Ambient conditions:** The expected ambient temperature range in-, on- or beyond the human body should be defined as

   $$T_{\mathrm{amb}} = [\min(T_{\mathrm{amb}}), \max(T_{\mathrm{amb}})] \tag{9.1}$$

   for the targeted application. Furthermore, a tolerance offset T_{offset}[1] should be considered.
2. **Material choice:** For most robotic applications, the commercially available compositions of NiTi should be sufficient. The specific variant, e.g., ratio of Ni and Ti, and Cu content allows for the fine-tuning, such as the hysteretic characteristic. More importantly, the austenite finish temperature A_{f} should be chosen so that

   $$A_{\mathrm{f}} > \max(T_{\mathrm{amb}}) + T_{\mathrm{offset}}. \tag{9.2}$$

3. **Material integration:** Strips with rectangular cross-sections should be preferred over circular cross-sections, due to advantages regarding assembly and heat exchange.
4. **Material processing:** Shape-setting beyond the original austenite shape, provided by the manufacturer, should be avoided. Preferably, the SMA components can be cold-formed before assembly, and then actuated to deform back into the original, usually straight shape.
5. **Temperature management:** Intrinsic actuation (Joule heating) requires less hardware effort, but comes at a cost of higher electric currents and a disadvantageous temperature distribution. In contrast, extrinsic actuation is more effective at lower currents, and thus, recommended if the robotic setup allows. To reduce space demand, an active cooling strategy should be avoided. Instead, natural convection should be considered, especially for on-body applications. For intracorporeal applications, the heat transfer to human tissue can act as a passive cooling mechanism, if the austenite finish temperature A_{f} is chosen wisely. However, it must be emphasized that high required temperatures for the smart material may cause the human tissue to overheat, potentially leading to irreversible damage.
6. **Control:** It is recommended to start off with a heuristically (model-free) tuned PID controller. If an experimental setup is available, which allows for the characterization of the SMA material specimen, data-driven and model-driven strategies can be applied, to address the nonlinearities more effectively.
7. **Safety measures:** To minimize the risks of thermal and electrical hazards, as well as toxic and non-sterile contamination, SMA actuators necessitate a meticulously prepared and intact surface. Ideally, they should also have an additional protective layer or a robotic cover.

---

[1] Examples for heuristic tolerance offsets: SMA-driven Laryngoscope, used intracorporeally: 3 °C; SMA-driven exoskeleton interface, used as a wearable: 6 °C.

9.3. Towards SMA-Driven Healthcare Robotics

Despite the presented limitations and challenges, SMAs and their capacity as superelastic components, and material-driven actuators, make them a fascinating material for biomedical environments in healthcare robotics.

Surgical Instruments

SMAs are already preferably used in the operating room due to their superelastic characteristic, e.g., as endovascular implants, guidewires, and also as elastic backbones for continuum robots. However, the consequent utilization of the inherent material-actuation in practice is still scarce. In contrast, this dissertation presented various performant SMA applications for healthcare robotics.

For future endeavors, the current boundaries should be pushed, from 1D SMA-wire actuators towards flexible instruments with complex 2D- or even 3D-shape changes for surgical devices, and ultra-compact, self-assembling continuum robots. Ideally, the exploitation of SMAs can lead towards light-weight, hand-held robotic devices. The applications, presented in this work, have been solely tested under laboratory conditions. In order to transfer this technology then to the operating room, the aspects of shielding and sterilization must be targeted firstly. Then, the aforementioned performance advantages of the shape memory material, and its potential hazards should be studied, and evaluated in cadaver studies, preclinical studies using live animals, and finally aiming for human clinical trials. The future vision calls for the creation of highly adaptable and customizable devices capable of modification during preoperative or even intraoperative clinical workflows. For such an innovative development, however, clinics must be enabled to handle SMA materials and alter the material's shapes on-site, and in accordance with medical imaging technology. This approach would allow operative interventions, such as those in endovascular, laparoscopic, and neurosurgery, to leverage advanced path planning alongside optimized surgical instruments for precise execution of the surgical plan [59].

Exoskeleton Interfaces

In exoskeleton applications, SMAs offer a valuable actuation modality, which is already employed in diverse ways. Unlike in surgical settings, where thermal stimulation and effective temperature management without active cooling features pose greater risks, the hazards associated with SMAs are comparatively lower. Additionally, while lightweight design is crucial for wearables, the spatial requirements are less critical compared to surgical instruments and medical robots designed for intracorporeal operations. This explains the extensive body of research beyond the scope of this dissertation, exploring the use of SMAs in wearable applications and exoskeletons. In this dissertation, the concept of a CASU has been introduced. The future perspective encompasses to design exoskeleton interfaces with multiple CASUs at optimized positions on the human body. Then, large user studies should target the evaluation of the efficiency and effectiveness to control the attachment of the exoskeleton to the user. The vision extends to the development of physical interfaces capable of material-induced deformation to accommodate individual users. In this scenario, the embedded CASUs would focus solely on real-time force control, ensuring consistent fit throughout the duration of wear.

10. Overall Conclusion

This dissertation presented a series of meaningful advancements in the fields of robotics and surgical technology in order to address the initially posed research question and the central thesis as possible response:

How can smart materials be applied for robotic and sensing applications in healthcare?

Shape memory alloys, ferromagnetic materials, and piezoresistive polymers can be applied in the realms of minimally invasive surgery and exoskeletons to improve compliance, flexibility, miniaturization, and practicability of robotic and sensing systems in healthcare.

The presented research stands out as it intends to validate this thesis statement with its exploration into practical deployment of those materials in the domain of healthcare robotics. It features three innovative SMA-based designs for actuation and sensing, as well as two sensor systems, deploying a ferromagnetic material, and a piezoresistive polymer, respectively. The achievements of this dissertation are briefly summarized in the following, confirming the thesis.

Extendable Continuum Robots using SMA for Gastroendoscopy

This dissertation introduced a novel design of a self-assembling, tendon-driven continuum robotic structure. Due to its superelastic, **compliant** robotic backbone from a SMA, the components can be stored efficiently within the actuation unit, before the continuum robotic structure is assembled during the extension procedure (**miniaturization**). Furthermore, the proposed design allows for a dynamical adjustment of the section and segment lengths during the extension process (**practicability**). The presented approach is scalable, and demonstrated state-of-the-art dexterity and workspace range, highlighting its significant potential in enhancing existing and future tendon-driven robotic systems for MIS in the operating room, for example in the context of transoral gastroendoscopy.

Flexible Surgical Instruments using SMA for Laparoscopy

Another pivotal area of this dissertation is the application of a SMA for inherent actuation, and self-sensing in the development of **flexible** surgical instruments. Their innovative design compactly incorporates SMA wire loops in active-antagonist arrangements, effectively utilizing these components to realize geometries ranging from simple bends to complex S-shapes. This approach significantly streamlines the setup, **miniaturizing** it to its fullest extent. Additionally, a data-driven polynomial model has been developed to predict the deflection of the 2D bending instrument using its electrical resistance. The model requires force sensing augmentation for handling unknown load scenarios and is tailored to the specific geometry of the tested actuator. Due to the deployment of a SMA, the proposed instrument design, with its bending, and straightening capabilities, shows the potential of combining structural integrity, actuation, and sensing within a single material component (**practicability**). Consequently, the design may prove highly beneficial, enhancing the dexterity of otherwise static and rigid surgical tools employed in MIS, such as in laparoscopic applications.

Compliant Sensor Array Tracking Magnets for Endovascular Surgery

The dissertation also explores the realm of magnetic sensing and -tracking in surgical technology by introducing a novel **compliant** sensor array designed for inherent shape estimation and subsequent tracking of surgical instruments made from ferromagnetic materials. Characterized by its self-sensing ability and minimal spatial footprint (**miniaturization**), the wearable array utilizes a tracking algorithm based on a permanent magnet model and least squares optimization. Results revealed that although stronger bending radii were associated with larger shape estimation errors, overall tracking accuracy improved, leading to a reduction in Euclidean distance error. The presented solution not only enhances instrument tracking precision, a critical aspect of surgical procedures for ensuring patient safety during endovascular interventions (**practicability**). It also holds promise for reducing the spatial footprint of magnetic tracking systems and thereby improving the surgical workflow for the clinicians in the field of endovascular surgery.

Training Platform with Piezoresistive Polymers for Endovascular Surgery

Furthermore, a sensorized training platform was presented, marking an important leap in medical training, particularly for endovascular interventions. This platform was designed to meet the critical need for intense practice in catheter and guidewire handling dexterity, a key skill in this field. It features a modular design with additively manufactured vessel phantoms that replicate patient-specific anatomy, enhancing the realism of the training experience. The integration of **compliant** and configurable piezoresistive polymer sensors into the elastic vessel walls (**miniaturization**) to measure impact forces, provides invaluable feedback to trainees, allowing them to refine their skills effectively (**practicability**). The presented training platform points to its vast potential for the domain of endovascular surgery, preparing novices for the operating room, and providing a patient-specific experimental training ground for experienced professionals.

Compliant SMA-based Actuator-Sensor Unit for Exoskeleton Interfaces

This dissertation also investigated the incorporation of active CASUs into exoskeleton interfaces for precise measurements and optimal fit. A CASU features highly **miniaturized** SMA strip actuators in a **compliant** parallel layout, and offers controllable actuation crucial for accurate adjustments of the holding force. Its integrated capacitive force sensor, capable of sensing through clothing, allows subsequently to identify limb movement patterns, underscores its sensing reliability. Emphasizing **practicability**, especially in counteracting interface displacements during everyday activities, this work substantiates the CASU's proficiency in adaptive settings. Such validation augments its applicability in humanoid robotics and assistive technologies, offering substantial benefits to individuals with physical impairments.

Should Smart Materials be Utilized in Health Care Robotics?

In conclusion, this dissertation has presented a detailed exploration of the selected smart materials, emphasizing their remarkable potential in the field of healthcare technology. It has been demonstrated that these materials can provide substantial improvements in actuation and sensing capabilities regarding increased compliance, flexibility, space efficiency, and practicability compared to conventional methodologies. This is achieved through the innovative design of integrated actuator and sensor systems, which simultaneously contribute to the structural integrity of the devices.

Given the limited scope of this research, the focus was primarily on a selected trio of materials, providing a punctual yet insightful exploration into their capabilities and applications. Each of the developed prototypes serves as a proof-of-concept. The experimental evaluation conducted have shown promising results, establishing the technical feasibility of handling, and effectively applying these different materials. Despite these advances, it is acknowledged that transitioning from experimental demonstrations to real-world technical solutions remains a significant challenge.

This dissertation should, however, serve as a foundation for future research, encouraging a more open-minded approach towards the development of enhanced materials. The application of these materials in healthcare is particularly challenging due to the high safety standards required in the field of healthcare technology. Nevertheless, the potential innovations that these smart materials promise could really push the boundaries in the field, leading to compact, efficient devices. These devices may soon become as integral to medical professionals as current medical instruments and implants made from superelastic NiTi.

To produce innovation in healthcare technology leveraging smart materials, it is essential to prioritize not only technical material advancement but also cultivate collaborative partnerships between innovation-driven clinicians focused on patient welfare and technical experts in material science and robotic engineering. The successful transition from laboratory prototypes to clinically approved devices is pivotal for scalability, involving not only overcoming technical hurdles but also navigating regulatory, ethical, and practical considerations. Paramount among these concerns are ensuring patient safety, meeting stringent regulatory standards, and achieving cost-effectiveness for clinical viability. In summary, this dissertation underscores the vast potential of smart materials and emphasizes the imperative of interdisciplinary collaboration for their seamless integration into healthcare technology, paving the way for significant advancements in the field.

Part V.

Appendix

AI Utilization Statement

Various institutions are involved in formulating guidelines for the utilization of generative artifical intelligence (AI) tools in copyright and scientific writing. As of the composition of this dissertation, a universal consensus or widely embraced standard regarding the usage of generative AI remains elusive. Consequently, the following section provides an overview of which generative AI tools were utilized in the writing of this dissertation and how they were employed, ensuring full transparency.

Which generative AI tools were used?

The primarily utilized generative AI tools in this dissertation were ChatGPT-3.5 and ChatGPT-4.0 (OpenAI, USA). Additionally, GPTs (Generative Pre-trained Transformers), which are extensions based on ChatGPT but specialized and augmented for specific tasks or domains, were employed. The utilized GPTs included:

- Consensus, Scholar GPT.
- Scientific Writing Assistant, Research Assistant.
- Translate GPT, Translate any Language.
- Grammar and Spelling Optimizer, Proofread Pro.

How was generative AI used?

The following list outlines how the aforementioned tools were utilized in the writing of this dissertation:

- Conducted language translation tasks (English-German, German-English).
- Enhanced the literature review using AI-based search engines.
- Generated text blocks based on prestructured content.
- Summarized and paraphrased own content and clearly referenced content from other research works, respectively.
- Improved text quality, conciseness, flow, and clarity.
- Employed for grammar and spelling checks.

All content, whether generated or altered by an AI tool, underwent meticulous review and revision to ensure the accuracy of the communicated information.

Acronyms

1D one-dimensional. 48, 56, 106, 116

2D two-dimensional. 48, 56, 59, 61, 62, 65, 68, 70, 106–108, 116, 117, 133, 138

3D three-dimensional. 48, 56, 65, 68, 93, 107, 108, 116

AI artifical intelligence. 123

Al aluminum. 31, 49, 50, 108, 137

ANOVA analysis of variance. 82

at atomic percentage. 23

CAD computer-aided design. 80, 139

CASU compliant actuator-sensor unit. 92–94, 97–102, 106, 107, 110, 112, 114, 116, 118, 119, 139–141

CAT computed axial tomography. 3

CI confidence interval. 42

CMD coordinate measuring device. 71–74, 131, 139

CNC computer numerical control. 108

Co cobalt. 26

Cr chromium. 113

CT computed tomography. 3, 24

CTA computed tomography angiography. 67, 77, 79, 80

Cu copper. 18, 31, 115

DC direct current. 39

DOF degrees-of-freedom. 12, 13, 35, 42, 44, 47, 48, 54, 67, 68, 77, 82, 95

EMG electromyography. 93

EPDM elastomeric ethylene-propylene-diene monomer. 96

FDM fused deposition modelling. 37

Fe iron. 26

FTS force-torque sensor. 93, 97, 99, 140

GI gastrointestinal. 10

I2C inter-integrated circuit. 97

IMU inertial measurement unit. 68, 93

MIS minimally invasive surgery. 4, 5, 7, 9, 10, 14, 15, 46, 48, 64, 77, 110, 112, 117, 118
MITK The Medical Imaging Interaction Toolkit. 80
MRI magnetic resonance imaging. 3, 24, 25, 105, 114

Nd neodymium. 26
Ni nickel. 21, 23, 26, 113–115
NiTi nickel-titanium. 23, 36, 37, 54, 56, 95, 98, 99, 101, 106, 107, 113–115, 119, 140
NiTiCu nickel-titanium-copper. 23, 48, 57, 106, 107, 137
NTC negative temperature coefficient. 96

Pb lead. 18
PCB printed circuit board. 68–70
PI proportional-integral. 97
PID proportional-integral-derivative. 39, 50, 51, 112, 115, 137
Pr praseodymium. 26
PTFE polytetrafluoroethylene. 96
PWM pulse-width-modulation. 39, 51

ROS Robot Operating System. 81, 97

SLA stereolithography. 37
Sm samarium. 26
SMA shape memory alloy. 5, 7, 17–23, 31, 36–38, 40, 44, 46–51, 53–58, 64, 65, 77, 92–94, 99, 100, 102, 105–118, 133, 135–137, 140

Ti titanium. 21, 23, 115

UI user interface. 12, 13
USB universal serial bus. 97

VR virtual reality. 78

List of Variables

This list contains all variables declared and utilized within this dissertation. To enhance readability, the list is organized according to the chapters of this document. The first subgroup ("General Variables") includes variables used multiple times across different chapters. Following this, chapter-specific variable listings are provided. It's important to note that all variables are presented in *italic* characters. However, subscripts are italicized only if they represent variables themselves; otherwise, they are in normal font. Additionally, vectors are highlighted in ***bold*** font.

General Variables

Δ	change, difference
∇	nabla operator
A	cross-sectional area
C	electric capacitance
$\boldsymbol{F}$	force
I	electric current
l	length
n	number of samples, sample size
O	origin in Cartesian space
P	point in Cartesian space
$\boldsymbol{p}$	position vector
$\bar{\boldsymbol{p}}$	mean position vector
R	electric resistance
R_0	electric resistance reference
T	temperature
T_0	temperature reference
T_{amb}	ambient temperature
T_{body}	temperature on-, or within the body
T_{max}	maximum temperature

T_{offset}	temperature offset (recommended)
t	time
U	electric voltage
U_{max}	electric voltage at maximum
V	volume
w	width
x	Cartesian coordinate
y	Cartesian coordinate
z	Cartesian coordinate

Shape Memory Alloys – Section 3.1

α_T	temperature coefficient
ε	uniaxial strain
$\varepsilon_{\mathrm{trans}}$	transformation strain
ξ_{M}	crystalline fraction of martensite phase
ξ_{R}	crystalline fraction of R-phase (rhombohedral)
σ	uniaxial stress
σ_{f}	uniaxial stress at finishing level
σ_{s}	uniaxial stress at starting level
υ	Poisson’s ratio
ρ	electric resistivity
ρ_0	electric resistivity reference
ρ_{A}	electric resistivity of austenite phase
ρ_{M}	electric resistivity of martensite phase
ρ_{R}	electric resistivity of R-phase (rhombohedral)
A_{f}	temperature, austenite finish
A_{s}	temperature, austenite start
M_{f}	temperature, martensite finish
M_{s}	temperature, martensite start

Magnetic Materials – Section 3.2

ϵ_0	permittivity in vacuum
μ_0	permeability in vacuum
ρ_m	magnetic charge density
ρ_s	magnetic charge density on a surface
ρ_v	magnetic charge density within a volume
ϱ	electric charge density
$\boldsymbol{B}$	magnetic field, -flux density, -induction
$\mathrm{d}\boldsymbol{m}$	time-averaged magnetic moment
$\mathrm{d}V$	mesoscopic volume
$\boldsymbol{E}$	electric field (flux)
$\boldsymbol{e}_\mathrm{n}$	unit normal vector
$\boldsymbol{F}_\mathbf{E}$	electric force
$\boldsymbol{F}_\mathbf{L}$	Lorentz force
$\boldsymbol{F}_\mathbf{M}$	magnetic force
$\boldsymbol{H}$	magnetic field intensity, -strength; auxiliary field; magnetizing field
H_c	coercivity
$\boldsymbol{J}$	electric current density
$\boldsymbol{j}_\mathbf{m}$	electric current density distribution
$\boldsymbol{M}$	magnetization
$\boldsymbol{M}_\mathbf{mes}$	mesoscopic average magnetization
M_r	residual magnetization, remanence
M_sat	saturation magnetization
$\boldsymbol{m}$	magnetic moment (individual atom or a magnetic dipole)
q_e	electric charge, e.g., electron
q_m	magnetic charge
U_H	Hall voltage, Hall potential
$\boldsymbol{v}_\mathrm{d}$	drifting velocity

Piezoresistive Polymers – Section 3.3

π_l	piezoresistive coefficient, longitudinal

π_t	piezoresistive coefficient, transverse
ρ_pol	electric resistivity of a piezoresistive polymer
σ_l	piezoresistive stress, longitudinal
σ_t	piezoresistive stress, transverse

Self-Assembly of Continuum Robots with Shape Memory Alloys – Chapter 4

e_bend	bending error
e_disk	disk positioning error
$\bar{e}_\mathrm{disk}$	mean disk positioning error over all runs and sections
n_p	number of samples of the position vector $\boldsymbol{p}$

Shaping Surgical Instruments with Shape Memory Alloys – Chapter 5

φ	bending angle
φ_error	steady-state error of bending angle
φ_set	bending angle setpoint
e	estimation error
$\bar{e}$	mean estimation error over all evaluation trials N_trial
e_k	estimation error for a measurement point k
$\bar{e}_k$	mean estimation error over all measurement points N_data
e_max	estimation error at maximum
i	index variable for the polynomial of R
j	index variable for the polynomial of F_z
k	index variable for measurement points
K_D	derivative gain
K_I	integral gain
K_P	proportional gain
N_data	number of measurement points during data acquisition
N_R	maximum polynomial degree of R
N_F	maximum polynomial degree of F_z
p_{ij}	polynomial coefficients
Q_RMS	root-mean-square error

s	deflection at distal tip
$\hat{s}$	estimated deflection at distal tip
s_{eval}	deflection at distal tip (recorded for evaluation)
T_{wire}	temperature at wire surface
tr	index variable for evaluation trials

Compliant Sensor Array for Passive Magnetic Instrument Tracking – Chapter 6

λ	bending angle of the sensor array
$\hat{\lambda}$	bending angle of the sensor array (estimated)
λ_{cmd}	bending angle of the evaluation frame, measured using a CMD
$\hat{\lambda}_{\mathrm{error}}$	bending shape estimation error (angular)
μ_{r}	relative permeability
Φ	loss function
$\boldsymbol{B}_u$	magnetic flux density as measured
$\hat{\boldsymbol{B}}_u$	magnetic flux density as estimated
e_{array}	Euclidean distance error of target tracking
h_{ws}	height of the cylindrical workspace
Q_{LS}	cost function for least squares approach
q	inner term of cost function
r	radius of the circular shaped sensor array
r_{ws}	radius of the cylindrical workspace
u	index variable for sensors in the sensor array

Sensorized Training Platform for Endovascular Surgery – Chapter 7

χ	impact-runtime score
$\bar{F}$	mean impact force
N_{P}	total number of participants
n_{P}	number of participants in a subgroup
t_{run}	runtime
$\bar{t}_{\mathrm{run}}$	mean runtime

Compliant Actuator-Sensor Unit – Chapter 8

α	flexion angle
ϵ	permittivity
A_{sens}	sensor surface area
a	capacity constant describing nonlinearity
b	compression constant
d	thickness of foam compression
d_0	foam thickness of unloaded sensor
F_{don}	donning force (initial force configuration)
F_{hold}	holding force
$F_{\text{hold-max}}$	maximum applicable force
$F_{\text{hold-min}}$	minimum force level
F_{offset}	force offset
P	pressure (compression)

List of Tables

5.1. Coefficients for the 2D polynomial model. [4] 🅭🅯 4.0. 61

5.2. Results of the model evaluation. Absolute mean and maximum estimation errors for nine load-heat scenarios. Color-coded from the lowest error (green) to the highest error (red). [4] 🅭🅯 4.0. 63

9.1. Overview over the stimulus-related technical specification of the SMA-based applications developed in this dissertation. “–” indicates the absence of measurements. 107

List of Figures

1.1. Visual abstract of this dissertation, delineating the organizational structure of this document by the sequential order of chapters through numerical labels. The contributions include three robotic systems deploying SMA-based actuation (top row), as well as three material-based sensor systems utilizing ferromagnetic materials, shape memory alloys, and piezoresistive materials (bottom row). Adapted from [1–8], 🅭🅯 4.0. and © IEEE 2023. 7

2.1. Schematic of selected robotic types for healthcare: articulated robots (left), continuum robots (middle), and exoskeletons (right). 11

3.1. A typical stress-strain-temperature behavior illustrating the shape memory effect for a typical SMA. The different crystalline structures of austenite and martensite are schematically indicated. Adapted from [77]. 19

3.2. Typical hysteresis response of SMA. The crystalline composition exhibits nonlinear changes with temperature. 19

3.3. Schematic of a typical transformation cycle of a simple SMA wire with an original bent shape in the austenite, hot temperature phase (left), and a targeted straight shape for the martensite phase (right). The one-way shape memory effect (SME) is indicated with black arrows, while the two-way shape memory effect is shown in pink. The two-way shape memory effect does not require external cold-forming. 20

3.4. Typical pseudoelastic behavior of a SMA when deformed under external stress above austenite finish temperature A_f. The material undergoes stress-induced phase changes at a constant temperature. Adapted from [77]. 21

3.5. Typical hysteresis loop of a ferromagnetic material. The ferromagnetic object is exposed to an external magnetic field $\boldsymbol{H}$ until it reaches saturation magnetization M_sat. Upon removal of the external field, the magnetization decreases but retains a residual magnetization M_r. H_c denotes the reverse field needed to cancel magnetization (coercivity). Adapted from [103]. . . 27

3.6. Coulombian magnetic model to calculate $\boldsymbol{H(p)}$ at a point P from the origin O. The field derives from a magnetic charge q_m on the outer surface of the magnet, defined by $\boldsymbol{p'}$ and the surface defined by the unit normal vector $\boldsymbol{e}_\mathrm{n}$. Adapted from [103]. 28

3.7. Schematic of the Hall effect. Adapted from [112]. 29

4.1. The extendable tendon-driven continuum robot, featuring extension, retraction and omnidirectional bending of two segments. The robotic structure is assembled by clamping the disks onto the superelastic SMA backbone during the extension process and disassembled by loosening for retraction. [1] © IEEE 2023. 37

4.2. The proposed robotic system including the actuation in cross-section with feed and storage for disks and backbone, (a) and a scheme of the superelastic SMA backbone and tendons routing through the entire disk storage for a two segment continuum robot (b). [1] © IEEE 2023. 38

4.3. Mechanism of the self-assembling procedure with disk hub and lever (a) without tendons. For extending the robot, a disk is released from the disk storage and pulled forward (b). Due to the sweeping groove in the channel wall, the lever is rotated during the forward movement, shrinking its inner diameter, and joining the disk with the backbone (c). The procedure is reversible, allowing also for retraction. Adapted from [1] © IEEE 2023. . 39

4.4. Investigating the repeatability of disk positioning during the self-assembling procedure. For a reference section length of $31\,\mathrm{mm}$ all disks were assembled (n = 5). The measured section length revealed that the disk positioning error e_{disk} remains < $1.9\,\mathrm{mm}$ ($0.8\,\%$ relative to maximum extension). Adapted from [1] © IEEE 2023. 40

4.5. Investigating friction forces on backbone routing through released (a) and clamped disks with symmetrical (b) and asymmetrical (c) load. [1] © IEEE 2023. 41

4.6. Experimental workspace exploration using both segments with extended length of $90\,\mathrm{mm}$ (a) and $240\,\mathrm{mm}$ (b), demonstrating the usual dexterity from conventional tendon-driven continuum robots. The workspace volume increases with extension length. [1] © IEEE 2023. 42

4.7. Evaluation setup with a magnetic field generator to measure the sensor pose at the distal tip of the robotic structure. In order to minimize the influence of the sensor's weight, its connection cable is suspended from above the setup. [1] © IEEE 2023. 42

4.8. Investigated configurations to determine repeatability performance of distal (1–3), proximal (4–6) and both segments combined (7–10). [1] © IEEE 2023. 43

4.9. Repeatability errors e_{bend} for the bending of configurations 1–10 for distal, proximal and both segments combined (n = 10). Error bars indicate the confidence interval (CI) of the measurement system. Adapted from [1] © IEEE 2023. 43

4.10. Comparing extendable length and robotic outer diameter of this work to related work. High extendable length and small diameter size are desired. Wang *et al.* [131] are excluded since they move their entire actuation units instead of extending the robotic structure. Adapted from [1] © IEEE 2023. 44

4.11. Testing the continuum robot demonstrator in a medical phantom, mimicking a transoral endoscopy of the esophagus as a proof of concept. The entire extendable length was used to traverse the esophagus and reach the stomach (red marker). Tip additionally indicated due to partially translucent resin material. [1] © IEEE 2023. 45

5.1. Concept of the compact flexible actuator for minimally invasive instruments featuring two shape memory alloy (SMA) wire loops with preset shape memory for shape changing (orange), reset into straight shape (green) and central supply channel, e.g., for a gripping tool. The desired shapes are bent (I) and S-shape (II). [2] 🅭🅯 4.0. 49

5.2. Fabrication steps: Cold-forming wire loops (1), followed by heat treatment with customized racks from Al at $425\,^{\circ}\mathrm{C}$ (2). All wire loops are straightened by cold-forming (3) and inserted in the additively manufactured monolithic backbone, followed by the final curing of the instrument (4). [2] 🅭🅯 4.0. 50

5.3. Closed-loop control setup including marker tracking, angle computation (Python 3.9) and a PID-Controller running on a microcontroller. [2] 🅭🅯 4.0. 51

5.4. Results of the workspace characterization for configuration I and II, showing initial pose (translucent) and maximum deflection (a+c). Shape was estimated using mean and standard deviation of marker positions at specific time steps over $n = 10$ experiment runs (b+d). The obtained shape change (orange) was reversed by the subsequent straightening (green). Dashed plots indicate the observed recoils after actuation has ended. [2] 🅭🅯 4.0. 52

5.5. Bending angle φ for configuration I controlled in closed-loop for setpoints φ_{set} (a). In contrast, bending angle φ for configuration I during characterization, with actuation phases for bending (orange) and setback (green) in open-loop control (b). [2] 🅭🅯 4.0. 52

5.6. Schematic of a minimally invasive surgery (MIS) with a flexible instrument made of a shape memory alloy (SMA). Augmenting the video endoscopy with information about deflection s and interaction forces $\boldsymbol{F}$. [4] 🅭🅯 4.0. 55

5.7. Simplified instrument design with a flat U-shaped wire from NiTiCu (a). Schematic of the shape changes between martensite (blue) and austenite states at $A_{\mathrm{f}} = 65\,^{\circ}\mathrm{C}$ (red). Known parameters include power supply voltage U, ambient temperature T_{amb}, and load. Current I, force components F_x and F_z, deflection s, and wire temperature T_{wire} were measured during the experiments. [4] 🅭🅯 4.0. 57

5.8. Experimental setup for data acquisition of the SMA actuator. Two load cells (red) record reaction forces F_x and F_z at the clamping. Tracking ArUco markers at the clamping and the distal tip (yellow) allow measuring the deflection s. [4] 🅭🅯 4.0. 57

5.9. Actuator bending shape at $0\,\mathrm{s}$, $4.5\,\mathrm{s}$ and $12\,\mathrm{s}$. A visible deflection of the distal tip over an actuation period of $0\,\mathrm{s}$ to $12\,\mathrm{s}$ can be observed. [4] 🅭🅯 4.0. 59

5.10. Actuator surface temperature during an actuation cycle, captured with a thermal imaging camera. Heating period was set to $12\,\mathrm{s}$, followed by a (passive) cooling phase for the remaining $228\,\mathrm{s}$ of data recording. Every trial started at $T_{\mathrm{wire}} < 27\,^{\circ}\mathrm{C}$. [4] 🅭🅯 4.0. 59

5.11. Schematic of the polynomial model with the input variables of resistance R, force F_z, and heat status. The output is a deflection estimate $\hat{s}$. [4] 🅭🅯 4.0. 60

5.12. Measured resistance R and deflection s for no load of a full actuation cycle of the actuator, including heating (red) and cooling phase (blue). Colored arrows indicate the chronicle order of subsets 1–4, subdividing the actuation cycle into four polynomial submodels, based on whether the resistance R increases or decreases. Semi-transparent circles denote the transitions between subsets. [4] 🅭🅯 4.0. 60

5.13. Load-heat scenarios for model evaluation with no load (a), 20 g (b) weight, and blocked at 50% (c). [4] 🅭🅯 4.0. 61

5.14. Schematic of the evaluation of the polynomial model. Measured deflection data s_{eval} is collected for nine scenario-heating cases and compared to the estimated deflection of the model $\hat{s}$ to find the estimation error e. [4] 🅭🅯 4.0. 62

5.15. 2D polynomial model for subsets 1–4 correlating resistance R and force F_z in order to find the deflection s. Comparing the model's estimation $\hat{s}$ and measured deflection s_{eval} for 12 s heating time and without load. [4] 🅭🅯 4.0. 62

5.16. Evaluation results of the polynomial model for nine exemplary load-heat scenarios. Comparing mean estimated deflection $\hat{s}$ to mean measured deflection s_{eval} for three different load cases and heating cases for 12 s (a–c), 4.5 s (d–f) and 4.5 s, and 6 s (g–i). [4] 🅭🅯 4.0. 63

6.1. Tracking a magnetic target (e.g., ferromagnetically enhanced surgical instrument) with a wearable compliant 4×4 Hall-effect array. Bottom: The sensor system is donned onto the human body and bent. A circular bending shape is determined through self-sensing, facilitated by a removable reference magnet. Then the magnetic target can be tracked within the body. Adapted from [5] © IEEE 2023. 69

6.2. Model of the array's circular bending shape, e.g., for $\lambda = 0°$ (yellow) and $\lambda = 135°$ (orange). [5] © IEEE 2023. 71

6.3. Experimental evaluation setup. The sensor array was attached to an evaluation frame (here: 90°) and bending shape estimation was performed using a reference magnet (a, purple) which had been removed from the scene prior to tracking. The magnetic target (red) was then moved by a Stewart platform beneath the sensor array and its path (b) was tracked. [5] © IEEE 2023. 72

6.4. Left: Evaluation frames for different bending angles λ to maintain known bending poses during evaluation. Right: Results of the estimated bending angle $\hat{\lambda}$ and the corresponding error $\hat{\lambda}_{\text{error}}$. [5] © IEEE 2023. 73

6.5. Path deviation between target tracking (green) and robotic reference path (black) for the smallest and largest bending angles. Sensor locations measured with CMD are indicated by spheres (blue), estimated locations by squares (red). The tracking accuracy visibly improves when comparing the flat sensor array ($\lambda = 0°$) to the maximum bent array ($\lambda = 225°$). [5] © IEEE 2023. 74

6.6. Euclidean distance error e_{array} of target tracking with trend indication (dashed) for different bending angles λ, estimated bending angles $\hat{\lambda}$, and measured bending angles λ_{cmd}. The median Euclidean distance error decreases consistently from $3.38\,\text{mm}$ for $\lambda = 0°$ to $1.31\,\text{mm}$ for $\lambda = 225°$ [5] © IEEE 2023. 75

7.1. The modular endovascular training platform during the experimental evaluation at Heidelberg University Hospital. Top-left: Schematic of a module box with an additively manufactured, patient-specific vessel phantom and an integrated impact force sensor made from piezoresistive polymers. Adapted from [7] 🅭🅯 4.0. 79

7.2. Render of the three modules of the training platform in a CAD model. Each module comprises the respective section of the individualized vessel phantom, as well as hardware for sensing and processing. [7] 🅭🅯 4.0. . . 80

7.3. The modular sensorized training platform as used for the participant study. Indicated positions of “START” and “TARGET” between a total of three module boxes, as well as the three sensor locations per box (orange). Bottom: Medical experts during the participant study. [7] 🅭🅯 4.0. 83

7.4. Mean values over five runs and all sensors for runtime $\bar{t}_{\text{run}}$ (a, d), impact force $\bar{F}$ (b, e), and impact-runtime score χ (c, f) for each participant. Analysis of participant groups based on their expertise (top row) and experience (bottom row) with the mean values for each group (dashed line). [7] 🅭🅯 4.0. 84

7.5. Analysis of variance for the participant study. Displayed are estimated means and comparison intervals for runtime $\bar{t}_{\text{run}}$ (a, d), impact force $\bar{F}$ (b, e), and impact-runtime score χ (c, f), for groups of expertise (top) and experience (bottom). [7] 🅭🅯 4.0. 85

7.6. Runtime of all medical participants (P1–P10) and non-medical participants (P11–P20) for all runs. Color-code indicates mean impact force $\bar{F}$ over all sensors, normalized for $0.2\,\text{N}$. [7] 🅭🅯 4.0. 86

8.1. The schematic (right) shows a lightweight robotic exoskeleton and its physical human-robot interfaces (blue) on the lower limbs. It incorporates the innovative Compliant Actuator-Sensor Units (left), which are positioned within specific cavities (orange). [8] © IEEE 2023. 92

8.2. CASU disassembled with interface cavity, carrier, actuator and in-silicone embedded force sensor. The presented components weight $30\,\text{g}$. [8] © IEEE 2023. 94

8.3. Actuator design with a configuration of three parallel NiTi strips clamped in an additively manufactured shell, cold-formed to flexure bearings (a+b) and equipped with heating wire and temperature sensor (c). Driving mechanism demonstrated ($I < 1.2\,\mathrm{A}$ per strip) for the free actuator part (d) and combined with the carrier, constraining flexion angles to $90° < \alpha < 180°$, creating an upwards movement and leading to a normal force (e). [8] © IEEE 2023. 95

8.4. Schematic of the capacitive measurement circuit (left). The resulting capacitance between the sensing electrodes and the ground is captured for each single or joint sensing electrodes. The force sensor (right) consists of three conductive layers, where the second layer is divided into three sensing electrodes. [8] © IEEE 2023. 96

8.5. Experimental setup including a Stewart Platform for controlled displacement of the CASU in z and against a 3-axis force-torque sensor (FTS) (a). This setup allowed for calibration, as well as to simulate actuation and sensing behavior under various configurations of donning force F_{don} during attachment and the actively applied holding force F_{hold} (b). [8] © IEEE 2023. 97

8.6. Investigation results of the force range (a) and temperature behavior (b) for control currents of $0.5\,\mathrm{A}$ (mean $0.4\,\mathrm{W}$) up to $2.0\,\mathrm{A}$ (mean $4.1\,\mathrm{W}$) per strip. Configuration featured $F_{\text{don}} = 30\,\mathrm{N}$ and $F_{\text{hold-min}} = 20\,\mathrm{N}$ with F_{offset} of up to $16\,\mathrm{N}$ and maximum inner temperatures $T_{\max}$ of $120\,°\mathrm{C}$. Force drops to zero indicate that $T_{\max}$ has reached body surface temperature of $34\,°\mathrm{C}$. [8] © IEEE 2023. 98

8.7. Actuator performance at control currents of maximum $1.2\,\mathrm{A}$ for (a, b) constant $F_{\text{hold-min}} = 10\,\mathrm{N}$ and (c, d) constant $F_{\text{don}} = 50\,\mathrm{N}$ in the operation range of $0\,\mathrm{N}$ to $50\,\mathrm{N}$, revealing a maximum F_{offset} of $13.7\,\mathrm{N}$. Higher F_{don} lead to higher F_{offset} (d). [8] © IEEE 2023. 99

8.8. Testing the SMA actuator control and using FTS data as idealized force input for the configuration $F_{\text{don}} = 30\,\mathrm{N}$ and $F_{\text{hold-min}} = 20\,\mathrm{N}$. Every $15\,\mathrm{s}$, the Stewart platform moved away from the CASU to simulate a force drop of $2\,\mathrm{N}$ (grey). The SMA actuator aimed to re-obtain $F_{\text{hold-min}}$ (orange). After four cycles, the SMA actuator became unable to follow the setpoint since the NiTi strips were maximally bent. [8] © IEEE 2023. 99

8.9. Correlation of capacitive sensor values and the reference normal force after ten iterations ($n = 10$) loading the CASU between $0\,\mathrm{N}$ to $50\,\mathrm{N}$. [8] © IEEE 2023. 100

8.10. Correlation of inner temperature of NiTi strips (red) and capacitive force sensing (blue) for five consecutive heating cycles without load. A model driven from the correlation was applied to compensate the temperature dependency of the force measurement (purple). The surface temperature of the CASU did not exceed $39.2\,°\mathrm{C}$ (thermal image). [8] © IEEE 2023. . 101

8.11. a: Experimental setup for investigating leg activity when the CASU was attached onto the right thigh. b: The sequence consisted of non-dynamic muscle contraction (1), knee stretching and flexing (2), standing-up (3) and sitting-down (4). [8] © IEEE 2023. 101

8.12. Interaction forces between user and interface, measured by the active CASU during one single sequence of four different movements scenarios including 3× muscle contraction (1), 3× knee stretching and flexing (2), 1× standing up (3), and 1× sitting down (4). Starting from $F_{\text{don}} = 16\,\text{N}$, a contact force $F_{\text{hold-min}}$ of $20\,\text{N}$ was sustained during the measurement. [8] © IEEE 2023. 102

Bibliography

[1] **Nikola Fischer**, M. Becher, L. Höltge, and F. Mathis-Ullrich, "A self-assembling extendable tendon-driven continuum robot with variable length," *IEEE Robotics and Automation Letters*, vol. 8, no. 12, pp. 8518–8524, 2023. [Online]. Available: https://doi.org/10.1109/LRA.2023.3325781

[2] **Nikola Fischer** and F. Mathis-Ullrich, "Compact flexible actuator based on a shape memory alloy for shaping surgical instruments," *at - Automatisierungstechnik*, vol. 71, no. 7, pp. 547–553, 2023. [Online]. Available: https://doi.org/10.1515/auto-2023-0049

[3] **Nikola Fischer**, P. Ho, C. Marzi, P. Schuler, and F. Mathis-Ullrich, "A Laryngoscope with Shape Memory Actuation," *Current Directions in Biomedical Engineering*, 2024, accepted for publication.

[4] **Nikola Fischer**, J. Knapp, and F. Mathis-Ullrich, "Shape-sensing by self-sensing of shape memory alloy instruments for minimal invasive surgery," *at - Automatisierungstechnik*, vol. 71, no. 7, pp. 554–561, 2023. [Online]. Available: https://doi.org/10.1515/auto-2023-0058

[5] **Nikola Fischer**, J. Kriechbaum, D. Berwanger, and F. Mathis-Ullrich, "Compliant hall-effect sensor array for passive magnetic instrument tracking," *IEEE Sensors Letters*, vol. 7, no. 3, pp. 1–4, 2023. [Online]. Available: https://doi.org/10.1109/LSENS.2023.3250971

[6] **Nikola Fischer**, P. Scheikl, C. Marzi, B. Galindo-Blanco, A. Kisilenko, B. Müller-Stich, M. Wagner, and F. Mathis-Ullrich, "Flexible Facile Tactile Sensor for Smart Vessel Phantoms," *Current Directions in Biomedical Engineering*, vol. 7, no. 1, pp. 7–11, 2021. [Online]. Available: https://doi.org/10.1515/cdbme-2021-1019

[7] **Nikola Fischer**, C. Marzi, K. Meisenbacher, A. Kisilenko, T. Davitashvili, M. Wagner, and F. Mathis-Ullrich, "A sensorized modular training platform to reduce vascular damage in endovascular surgery," *International Journal of Computer Assisted Radiology and Surgery*, 2023. [Online]. Available: https://doi.org/10.1007/s11548-023-02935-w

[8] **Nikola Fischer**, H. Alagi, B. Hein, M. Beigl, and F. Mathis-Ullrich, "A compliant actuator-sensor unit using a shape memory alloy and capacitive force sensing for active exoskeleton interfaces," in *2023 IEEE-RAS 22nd International Conference on Humanoid Robots (Humanoids)*, 2023, pp. 1–7. [Online]. Available: https://doi.org/10.1109/Humanoids57100.2023.10375226

[9] F. Götmark, P. Cafaro, and J. O'Sullivan, "Aging Human Populations: Good for Us, Good for the Earth," *Trends in Ecology & Evolution*, vol. 33, no. 11, pp. 851–862, nov 2018. [Online]. Available: https://doi.org/10.1016/j.tree.2018.08.015

[10] S. A. Ward, S. Parikh, and B. Workman, "Health perspectives: International epidemiology of ageing," *Best Practice & Research Clinical Anaesthesiology*,

vol. 25, no. 3, pp. 305–317, 2011, perioperative Morbidity and Mortality in the Elderly. [Online]. Available: https://www.sciencedirect.com/science/article/pii/S1521689611000474

[11] World Heart Federation, *World Heart Report 2023: Confronting the World's Number One Killer*. Geneva, Switzerland: World Heart Federation, 2023.

[12] K. Kaur, N. Kumar, J. V. Singh, P. M. S. Bedi, and H. Singh, *Recent Development of Quinoline Derivatives as Anticancer Agents: 2015–2022*. Cham: Springer Nature Switzerland, 2023, p. 218. [Online]. Available: https://doi.org/10.1007/16833_2023_125

[13] V. M. Merabishvili, "Age-Related Cancer Risks (Analytical Indicators of Registration and Early Diagnosis)," *Advances in Gerontology*, vol. 8, no. 2, pp. 104–110, 2018. [Online]. Available: https://doi.org/10.1134/S2079057018020091

[14] P. van Heemskerken, H. Broekhuizen, J. Gajewski, R. Brugha, and L. Bijlmakers, "Barriers to surgery performed by non-physician clinicians in sub-Saharan Africa—a scoping review," *Human Resources for Health*, vol. 18, no. 1, p. 51, 2020. [Online]. Available: https://doi.org/10.1186/s12960-020-00490-y

[15] M. Boniol, T. Kunjumen, T. S. Nair, A. Siyam, J. Campbell, and K. Diallo, "The global health workforce stock and distribution in 2020 and 2030: a threat to equity and 'universal' health coverage?" *BMJ global health*, vol. 7, no. 6, jun 2022.

[16] E. Nikoleishvili, "Factors affecting nurses' shortage – literature review," *American Journal of Biomedical Science & Research*, 2021.

[17] C. M. Ranucci, Q. Lai, S. Quaresima, A. M. Paganini, S. Celani, M. Rossi, G. D. Tebala, and S. Di Saverio, *New Trends in Laparoscopic Procedures in the Emergency Abdominal Surgery*. Cham: Springer International Publishing, 2023, pp. 269–278. [Online]. Available: https://doi.org/10.1007/978-3-031-17273-1_23

[18] F. Khan, B. Amatya, W. de Groote, M. Owolabi, I. M. Syed, A. Hajjoui, M. Babur, T. Sayed, Y. Frizzell, A. S. Naicker, M. Fourtassi, A. Elmalik, and M. Galea, "Capacity-building in clinical skills of rehabilitation workforce in low- and middle-income countries." *Journal of rehabilitation medicine*, vol. 50 5, pp. 472–479, 2018.

[19] R. Ghosh, V. Palanivelu, E. Tebbutt, and S. Deepak, "Training of mid-level rehabilitation workers for community-based rehabilitation programmes," *Disability, CBR & Inclusive Development*, 2021.

[20] O. Jansen, D. Grasmücke, R. Meindl, M. Tegenthoff, P. Schwenkreis, M. Sczesny-Kaiser, M. Wessling, T. Schildhauer, C. Fisahn, and M. Aach, "Hybrid assistive limb exoskeleton hal in the rehabilitation of chronic spinal cord injury: Proof of concept; the results in 21 patients." *World neurosurgery*, vol. 110, pp. e73–e78, 2017.

[21] L. Awad, J. Bae, K. O'Donnell, S. D. D. Rossi, K. Hendron, L. Sloot, P. Kudzia, S. P. Allen, K. Holt, T. Ellis, and C. Walsh, "A soft robotic exosuit improves walking in patients after stroke," *Science Translational Medicine*, vol. 9, 2017.

[22] M. Baklouti, P. Guyot, E. Monacelli, and S. Couvet, "Force controlled upper-limb powered exoskeleton for rehabilitation," *2008 IEEE/RSJ International Conference on Intelligent Robots and Systems*, pp. 4202–4202, 2008.

[23] E. Delgado, C. Cumplido, J. Ramos, E. Garces, G. Puyuelo, A. Plaza, M. Hernandez, A. Gutiérrez, T. Taverner, M. Destarac, M. Martínez, and E. García, "Atlas2030 pediatric gait exoskeleton: Changes on range of motion, strength and spasticity in children with cerebral palsy. a case series study," *Frontiers in Pediatrics*, vol. 9, 2021.

[24] S. Galle, W. Derave, F. M. Bossuyt, P. Calders, P. Malcolm, P. Malcolm, and D. D. Clercq, "Exoskeleton plantarflexion assistance for elderly." *Gait & posture*, vol. 52, pp. 183–188, 2017.

[25] A. Kapsalyamov, P. Jamwal, S. Hussain, and M. Ghayesh, "State of the art lower limb robotic exoskeletons for elderly assistance," *IEEE Access*, vol. 7, pp. 95 075–95 086, 2019.

[26] S. Upasani, R. Franco, K. Niewolny, and D. Srinivasan, "The potential for exoskeletons to improve health and safety in agriculture—perspectives from service providers," *IISE Transactions on Occupational Ergonomics and Human Factors*, vol. 7, pp. 222 – 229, 2019.

[27] K. Imaizumi, S. Homma, Y. Miyaoka, H. Matsui, N. Ichikawa, T. Yoshida, N. Takahashi, and A. Taketomi, "Exploration of the advantages of minimally invasive surgery for clinical T4 colorectal cancer compared with open surgery: A matched-pair analysis," *Medicine*, vol. 101, no. 32, 2022.

[28] M. E. Rentschler, J. Dumpert, S. R. Platt, S. M. Farritor, and D. Oleynikov, "Natural orifice surgery with an endoluminal mobile robot," *Surgical Endoscopy*, vol. 21, no. 7, pp. 1212–1215, 2007. [Online]. Available: https://doi.org/10.1007/s00464-007-9400-z

[29] M. Schwab, Ed., *Laparoscopy*. Berlin, Heidelberg: Springer Berlin Heidelberg, 2009, pp. 1629–1629. [Online]. Available: https://doi.org/10.1007/978-3-540-47648-1_3276

[30] S. Balzora. (2018, September) Upper gi endoscopy (egd). American College of Gastroenterology. Accessed February 8, 2023. [Online]. Available: https://gi.org/topics/upper-gi-endoscopy-egd

[31] M. Katoh and B. Luther, *Endovaskuläre und chirurgische Standardausrüstung und -methodik*. Berlin, Heidelberg: Springer Berlin Heidelberg, 2021, pp. 45–74. [Online]. Available: https://doi.org/10.1007/978-3-662-61476-1_3

[32] R. Bogdanova, P. Boulanger, and B. Zheng, "Depth perception of surgeons in minimally invasive surgery," *Surgical Innovation*, vol. 23, pp. 515 – 524, 2016.

[33] O. S. Bholat, R. S. Haluck, R. H. Kutz, P. J. Gorman, and T. M. Krummel, "Defining the role of haptic feedback in minimally invasive surgery," *Studies in Health Technology and Informatics*, vol. 62, pp. 62–66, 1999.

[34] C. G. L. Cao, C. L. MacKenzie, and S. Payandeh, "Task and motion analyses in endoscopic surgery," *Dynamic Systems and Control*, 1996.

[35] J. A. Jordan, A. Gallagher, J. McGuigan, and N. McClure, "Virtual reality training leads to faster adaptation to the novel psychomotor restrictions encountered by laparoscopic surgeons," *Surgical Endoscopy*, vol. 15, pp. 1080–1084, 2001.

[36] A. Spiers, S. Baillie, T. Pipe, and G. Asimakopolous, "Negating the fulcrum effect in manual laparoscopic surgery: Investigating skill acquisition with a haptic

simulator," *The International Journal of Medical Robotics and Computer Assisted Surgery*, vol. 13, 2017.

[37] V. Vitiello, S.-L. Lee, T. Cundy, and G.-Z. Yang, "Emerging robotic platforms for minimally invasive surgery," *IEEE Reviews in Biomedical Engineering*, vol. 6, pp. 111–126, 2013.

[38] B. Siciliano and O. Khatib, *Springer handbook of robotics*, 2016.

[39] S. W. Wong, Z. H. Ang, P. F. Yang, and P. Crowe, "Robotic colorectal surgery and ergonomics," *Journal of Robotic Surgery*, vol. 16, no. 2, pp. 241–246, 2022. [Online]. Available: https://doi.org/10.1007/s11701-021-01240-5

[40] Y. Rivero-Moreno, S. Echevarria, C. Vidal-Valderrama, L. Pianetti, J. Cordova-Guilarte, J. Navarro-Gonzalez, J. Acevedo-Rodríguez, G. Dorado-Avila, L. Osorio-Romero, C. Chavez-Campos, and K. Acero-Alvarracín, "Robotic surgery: A comprehensive review of the literature and current trends," *Cureus*, vol. 15, 2023.

[41] D. Koh, W. S. Jang, J. W. Park, W. Ham, W. Han, K. Rha, and Y. Choi, "Efficacy and safety of robotic procedures performed using the da vinci robotic surgical system at a single institute in korea: Experience with 10000 cases," *Yonsei Medical Journal*, vol. 59, pp. 975 – 981, 2018.

[42] H. W. Richards, A. Kulaylat, J. N. Cooper, D. McLeod, K. Diefenbach, and M. Michalsky, "Trends in robotic surgery utilization across tertiary children's hospitals in the united states," *Surgical Endoscopy*, vol. 35, pp. 6066 – 6072, 2020.

[43] C. Vásquez-Lastra, C. Decanini-Terán, A. Maffuz-Aziz, J. Alfaro-Alfaro, J. A. Huante-Pérez, E. Wolpert-Barraza, L. F. Sánchez-Marle, and A. Gutiérrez-Hernández, "Robotic surgery at ABC Medical Center: first 500 procedures experience." *Gaceta medica de Mexico*, vol. 157, no. 2, pp. 181–186, 2021.

[44] A. Smith, L. Picheca, and Q. Mahood, "Robotic surgical systems for orthopedics," *Canadian Journal of Health Technologies*, 2022.

[45] J. Rahman, K. Al-Tawil, and W. Khan, "Use of robotic-assisted surgery in orthopedics," *General Principles of Orthopedics and Trauma*, 2019.

[46] F. Böhm, J. Greve, R. Riepl, T. Hoffmann, and P. Schuler, "Robotics in otorhinolaryngology, head and neck surgery," *HNO*, 2021.

[47] S. Swain, "Robotic surgery in otorhinolaryngology and head-and-neck oncology," *Indian Journal of Health Sciences and Biomedical Research (KLEU)*, vol. 16, pp. 336 – 341, 2023.

[48] V. Stumpo, V. Staartjes, A. Klukowska, A. Golahmadi, P. Gadjradj, M. Schröder, A. Veeravagu, M. Stienen, C. Serra, and L. Regli, "Global adoption of robotic technology into neurosurgical practice and research," *Neurosurgical Review*, vol. 44, pp. 2675–2687, 2020.

[49] O. Khanna, R. A. Beasley, D. Franco, and S. DiMaio, "The path to surgical robotics in neurosurgery," *Operative Neurosurgery*, vol. 20, pp. 514–520, 2021.

[50] A. Jonsson and A. D. Patel, *The Background of Robotic Surgery*. Cham: Springer International Publishing, 2018, pp. 191–193. [Online]. Available: https://doi.org/10.1007/978-3-319-51362-1_14

[51] J. Cornejo, J. P. Perales-Villarroel, R. Sebastian, and J. A. Cornejo-Aguilar, “Conceptual design of space biosurgeon for robotic surgery and aerospace medicine,” *2020 IEEE ANDESCON*, pp. 1–6, 2020.

[52] J. Yang, J. Shi, and H. Xie, “Research on SMA actuated tendon driven hand exoskeleton with bidirectional finger joint motion coupling for rehabilitation usage,” *2015 IEEE International Conference on Cyber Technology in Automation, Control and Intelligent Systems, IEEE-CYBER 2015*, pp. 336–340, 2015.

[53] H. Muaddi, R. Chow, K. K. W. Chan, S. Singh, S. Rask, L. Venkat Raghavan, and E. Chow, “Clinical outcomes of robotic surgery compared to conventional surgical approaches,” *Surgical Endoscopy*, vol. 34, no. 12, pp. 5533–5541, 2020.

[54] A. Karategos, J. Farquharson, B. Liu, and N. Yassin, “Ep-458 robotic surgery improves outcomes for patients with benign and malignant colorectal conditions,” *British Journal of Surgery*, 2022.

[55] S. Erkoç, C. Guclu, G. Ergin, B. Safak, B. Meço, and A. Yılmaz, “Anesthesia management and patient outcomes in robotic assisted laparoscopic surgery,” *Medicine Science | International Medical Journal*, vol. 41, pp. 1024–1033, 2022.

[56] R. V. Patel, S. F. Atashzar, and M. Tavakoli, “Haptic feedback and force-based teleoperation in surgical robotics,” *Proceedings of the IEEE*, vol. 110, pp. 1012–1027, 2022.

[57] ——, “Haptic feedback and force-based teleoperation in surgical robotics,” *Proceedings of the IEEE*, vol. 110, no. 7, pp. 1012–1027, 2022.

[58] G. Chirikjian and J. Burdick, “A modal approach to hyper-redundant manipulator kinematics,” *IEEE Transactions on Robotics and Automation*, vol. 10, no. 3, pp. 343–354, 1994.

[59] S. Peikert, C. Kunz, **Fischer, Nikola**, M. Hlaváč, A. Pala, M. Schneider, and F. Mathis-Ullrich, “Automated linear and non-linear path planning for neurosurgical interventions,” in *2022 International Conference on Robotics and Automation (ICRA)*, 2022, pp. 7731–7737.

[60] C. J. Payne and G.-Z. Yang, “Hand-Held Medical Robots,” *Annals of Biomedical Engineering*, vol. 42, no. 8, pp. 1594–1605, 2014. [Online]. Available: https://doi.org/10.1007/s10439-014-1042-4

[61] O. Omisore, S. Han, J. Xiong, H. Li, Z. Li, and L. Wang, “A review on flexible robotic systems for minimally invasive surgery,” *IEEE Transactions on Systems, Man, and Cybernetics: Systems*, vol. 52, pp. 631–644, 2022.

[62] J. Burgner-Kahrs, D. C. Rucker, and H. Choset, “Continuum Robots for Medical Applications: A Survey,” *IEEE Transactions on Robotics*, vol. 31, no. 6, pp. 1261–1280, 2015.

[63] S. H. Collins, M. B. Wiggin, and G. S. Sawicki, “Reducing the energy cost of human walking using an unpowered exoskeleton,” *Nature*, vol. 522, no. 7555, pp. 212–215, 2015. [Online]. Available: https://doi.org/10.1038/nature14288

[64] R. Chin, E. T. Hsiao-Wecksler, E. Loth, G. Kogler, S. D. Manwaring, S. N. Tyson, K. A. Shorter, and J. N. Gilmer, “A pneumatic power harvesting ankle-foot orthosis to prevent foot-drop,” *Journal of NeuroEngineering and Rehabilitation*, vol. 6, no. 1, p. 19, 2009. [Online]. Available: https://doi.org/10.1186/1743-0003-6-19

[65] P. Maurice, J. Čamernik, D. Gorjan, B. Schirrmeister, J. Bornmann, L. Tagliapietra, C. Latella, D. Pucci, L. Fritzsche, S. Ivaldi, and J. Babič, "Objective and subjective effects of a passive exoskeleton on overhead work," *IEEE Transactions on Neural Systems and Rehabilitation Engineering*, vol. 28, no. 1, pp. 152–164, 2020.

[66] B. Kalita, J. Narayan, and S. K. Dwivedy, "Development of Active Lower Limb Robotic-Based Orthosis and Exoskeleton Devices: A Systematic Review," *International Journal of Social Robotics*, vol. 13, no. 4, pp. 775–793, 2021.

[67] Z. Guo, H. Yu, and Y. H. Yin, "Developing a Mobile Lower Limb Robotic Exoskeleton for Gait Rehabilitation," *Journal of Medical Devices*, vol. 8, no. 4, p. 044503, 08 2014. [Online]. Available: https://doi.org/10.1115/1.4026900

[68] H. Munawar, M. Yalcin, and V. Patoglu, "Assiston-gait: An overground gait trainer with an active pelvis-hip exoskeleton," in *2015 IEEE International Conference on Rehabilitation Robotics (ICORR)*, 2015, pp. 594–599.

[69] J. C. Maldonado-Mejía, M. Múnera, C. A. R. Diaz, H. Wurdemann, M. Moazen, M. J. Pontes, M. E. Vieira Segatto, M. E. Monteiro, and C. A. Cifuentes, "A fabric-based soft hand exoskeleton for assistance: the ExHand Exoskeleton." *Frontiers in neurorobotics*, vol. 17, p. 1091827, 2023.

[70] T. Bagneschi, D. Chiaradia, G. Righi, G. D. Popolo, A. Frisoli, and D. Leonardis, "A soft hand exoskeleton with a novel tendon layout to improve stable wearing in grasping assistance," *IEEE Transactions on Haptics*, vol. 16, no. 2, pp. 311–321, 2023.

[71] N. Kladovasilakis, I. Kostavelis, P. Sideridis, E. Koltzi, K. Piliounis, D. Tzetzis, and D. Tzovaras, "A novel soft robotic exoskeleton system for hand rehabilitation and assistance purposes," *Applied Sciences*, vol. 13, no. 1, 2023. [Online]. Available: https://www.mdpi.com/2076-3417/13/1/553

[72] S. Christensen, S. Rafique, and S. Bai, "Design of a powered full-body exoskeleton for physical assistance of elderly people," *International Journal of Advanced Robotic Systems*, vol. 18, no. 6, p. 17298814211053534, 2021. [Online]. Available: https://doi.org/10.1177/17298814211053534

[73] S. Bai, M. Islam, V. Power, and L. OŚullivan, "User-centered development and performance assessment of a modular full-body exoskeleton (axo-(suit)," *Biomimetic Intelligence and Robotics*, vol. 2, no. 2, p. 100032, 2022. [Online]. Available: https://www.sciencedirect.com/science/article/pii/S2667379721000322

[74] M. Fontana, R. Vertechy, S. Marcheschi, F. Salsedo, and M. Bergamasco, "The body extender: A full-body exoskeleton for the transport and handling of heavy loads," *IEEE Robotics & Automation Magazine*, vol. 21, no. 4, pp. 34–44, 2014.

[75] S. Kim, D. Srinivasan, M. A. Nussbaum, and A. Leonessa, "Human gait during level walking with an occupational whole-body powered exoskeleton: Not yet a walk in the park," *IEEE Access*, vol. 9, pp. 47 901–47 911, 2021.

[76] S. V. Sarkisian, M. K. Ishmael, and T. Lenzi, "Self-aligning mechanism improves comfort and performance with a powered knee exoskeleton," *IEEE Transactions on Neural Systems and Rehabilitation Engineering*, vol. 29, pp. 629–640, 2021.

[77] P. Kumar and D. Lagoudas, *Introduction to Shape Memory Alloys*. Boston, MA: Springer US, 2008, pp. 1–51. [Online]. Available: https://doi.org/10.1007/978-0-387-47685-8_1

[78] C. D. Near, "Piezoelectric actuator technology," in *Smart Structures and Materials 1996: Smart Structures and Integrated Systems*, I. Chopra, Ed., vol. 2717, International Society for Optics and Photonics. SPIE, 1996, pp. 246 – 258. [Online]. Available: https://doi.org/10.1117/12.239027

[79] V. Sharapov, *General Information About Piezoelectric Sensors*. Berlin, Heidelberg: Springer Berlin Heidelberg, 2011, pp. 1–69. [Online]. Available: https://doi.org/10.1007/978-3-642-15311-2_1

[80] K. K. Sappati and S. Bhadra, "Piezoelectric polymer and paper substrates: A review," *Sensors*, vol. 18, no. 11, 2018. [Online]. Available: https://www.mdpi.com/1424-8220/18/11/3605

[81] J. Bautista-Quijano, F. Avilés, J. Aguilar, and A. Tapia, "Strain sensing capabilities of a piezoresistive mwcnt-polysulfone film," *Sensors and Actuators A: Physical*, vol. 159, no. 2, pp. 135–140, 2010. [Online]. Available: https://www.sciencedirect.com/science/article/pii/S0924424710001081

[82] R. Samatham, K. J. Kim, D. Dogruer, H. R. Choi, M. Konyo, J. D. Madden, Y. Nakabo, J. D. Nam, J. Su, S. Tadokoro, W. Yim, and M. Yamakita, *Active Polymers: An Overview*. London: Springer London, 2007, pp. 1–36. [Online]. Available: https://doi.org/10.1007/978-1-84628-372-7_1

[83] Y. Xia, Y. He, F. Zhang, Y. Liu, and J. Leng, "A review of shape memory polymers and composites: Mechanisms, materials, and applications," *Advanced Materials*, vol. 33, no. 6, p. 2000713, 2021. [Online]. Available: https://onlinelibrary.wiley.com/doi/abs/10.1002/adma.202000713

[84] H.-J. Bargel, *Grundlagen der Metall- und Legierungskunde*. Berlin, Heidelberg: Springer Berlin Heidelberg, 2022, pp. 1–89. [Online]. Available: https://doi.org/10.1007/978-3-662-63961-0_1

[85] A. Bekker and L. Brinson, "Phase diagram based description of the hysteresis behavior of shape memory alloys," *Acta Materialia*, vol. 46, no. 10, pp. 3649–3665, 1998. [Online]. Available: https://www.sciencedirect.com/science/article/pii/S1359645497004904

[86] P. Rodriguez and G. Guénin, "Stability of the two way memory effect during thermal cycling of a high ms temperature cu-al-ni alloy," in *Martensitic Transformations*, ser. Materials Science Forum, vol. 56. Trans Tech Publications Ltd, 1 1990, pp. 541–546.

[87] T. Baxevanis, Y. Chemisky, and D. C. Lagoudas, "Finite element analysis of the plane strain crack-tip mechanical fields in pseudoelastic shape memory alloys," *Smart Materials and Structures*, vol. 21, no. 9, p. 094012, aug 2012. [Online]. Available: https://dx.doi.org/10.1088/0964-1726/21/9/094012

[88] C. Müller and O. Bruhns, "A thermodynamic finite-strain model for pseudoelastic shape memory alloys," *International Journal of Plasticity*, vol. 22, no. 9, pp. 1658–1682, 2006. [Online]. Available: https://www.sciencedirect.com/science/article/pii/S0749641906000179

[89] K. Otsuka and T. Kakeshita, "Science and technology of shape-memory alloys: New developments," *MRS Bulletin*, vol. 27, no. 2, p. 91–100, 2002.

[90] B. Lynch, X.-X. Jiang, A. Ellery, and F. Nitzsche, "Characterization, modeling, and control of ni-ti shape memory alloy based on electrical resistance feedback,"

Journal of Intelligent Material Systems and Structures, vol. 27, no. 18, pp. 2489–2507, 2016. [Online]. Available: https://doi.org/10.1177/1045389X16633764

[91] W.-T. Park, *Piezoresistivity*. Dordrecht: Springer Netherlands, 2016, pp. 3246–3252. [Online]. Available: https://doi.org/10.1007/978-94-017-9780-1_222

[92] S. J. Furst, J. H. Crews, and S. Seelecke, "Stress, strain, and resistance behavior of two opposing shape memory alloy actuator wires for resistance-based self-sensing applications," *Journal of Intelligent Material Systems and Structures*, vol. 24, no. 16, pp. 1951–1968, 2013.

[93] D. C. Lagoudas, D. A. Miller, L. Rong, and P. K. Kumar, "Thermomechanical fatigue of shape memory alloys," *Smart Materials and Structures*, vol. 18, no. 8, p. 085021, jul 2009. [Online]. Available: https://dx.doi.org/10.1088/0964-1726/18/8/085021

[94] A. Cragg, G. Lund, J. Rysavy, F. Castañeda*, W. Castañeda-Zúñiga, and K. Amplatz*, "Nonsurgical placement of arterial endoprostheses: a new technique using nitinol wire." *Radiology*, vol. 147 1, pp. 261–3, 1983.

[95] C.-P. O. Yang, C.-P. Hsu, W.-Y. Chen, I. Chen, C. Weng, C.-K. Chen, and C. Shih, "Aortic remodeling after endovascular repair with stainless steel-based stent graft in acute and chronic type b aortic dissection." *Journal of vascular surgery*, vol. 55 6, pp. 1600–10, 2012.

[96] O. Teebken and A. Haverich, "Tissue engineering of small diameter vascular grafts." *European journal of vascular and endovascular surgery : the official journal of the European Society for Vascular Surgery*, vol. 23 6, pp. 475–85, 2002.

[97] S. A. Shabalovskaya, "Surface, corrosion and biocompatibility aspects of Nitinol as an implant material." *Bio-medical materials and engineering*, vol. 12, no. 1, pp. 69–109, 2002.

[98] Y. Tanaka, Y. Himuro, R. Kainuma, Y. Sutou, T. Omori, and K. Ishida, "Ferrous polycrystalline shape-memory alloy showing huge superelasticity," *Science*, vol. 327, no. 5972, pp. 1488–1490, 2010.

[99] R. S. Kotha, R. K. Alla, M. Shammas, and R. K. Ravi, "An overview of orthodontic wires," *Trends Biomater Artif Organs*, vol. 28, no. 1, pp. 32–36, 2014.

[100] V. D. Sars, S. Haliyo, and J. Szewczyk, "A practical approach to the design and control of active endoscopes," *Mechatronics*, vol. 20, no. 2, pp. 251–264, 2010.

[101] S. Kumar, P. Shivashankar, and S. Gopalakrishnan, "A half a decade timeline of shape memory alloys in modeling and applications," *ISSS Journal of Micro and Smart Systems*, vol. 9, no. 1, pp. 1–32, 2020.

[102] Z. Shang, J. Ma, Z. You, and S. Wang, "A braided skeleton surgical manipulator with tunable diameter," in *2020 8th IEEE RAS/EMBS International Conference for Biomedical Robotics and Biomechatronics (BioRob)*, 2020, pp. 223–228.

[103] J. M. D. Coey, *Magnetism and Magnetic Materials*. Cambridge, UK: Cambridge University Press, 2010.

[104] J. C. Maxwell, "A dynamical theory of the electromagnetic field," *Philosophical Transactions of the Royal Society of London*, vol. 155, pp. 459–512, 1865.

[105] D. J. Griffiths, *Introduction to Electrodynamics*, 4th ed. Cambridge, UK: Cambridge University Press, 2017.

[106] P. A. Tipler and G. Mosca, *Quellen des Magnetfelds*. Berlin, Heidelberg: Springer Berlin Heidelberg, 2009, pp. 1045–1089. [Online]. Available: https://doi.org/10.1007/978-3-642-54166-7_24

[107] S. Roth and A. Stahl, *Kraft und Feld*. Berlin, Heidelberg: Springer Berlin Heidelberg, 2018, pp. 25–89. [Online]. Available: https://doi.org/10.1007/978-3-662-54445-7_2

[108] W. Demtröder, *Static Magnetic Fields*. Cham: Springer International Publishing, 2019, pp. 81–118. [Online]. Available: https://doi.org/10.1007/978-3-030-02291-4_3

[109] J. Lucas, P. Lucas, T. Le Mercier, A. Rollat, and W. Davenport, “Chapter 13 - permanent magnets based on rare earths: Fundamentals,” in *Rare Earths*, J. Lucas, P. Lucas, T. Le Mercier, A. Rollat, and W. Davenport, Eds. Amsterdam: Elsevier, 2015, pp. 213–230. [Online]. Available: https://www.sciencedirect.com/science/article/pii/B9780444627353000139

[110] A. Inoue and F. Kong, “Soft magnetic materials,” *Reference Module in Materials Science and Materials Engineering*, 2020.

[111] A. J. Petruska and J. J. Abbott, “Optimal permanent-magnet geometries for dipole field approximation,” *IEEE Transactions on Magnetics*, vol. 49, no. 2, pp. 811–819, 2013.

[112] A. Giuliani, “Order, disorder and phase transitions in quantum many body systems,” *Istituto Lombardo - Accademia di Scienze e Lettere - Rendiconti di Scienze*, 11 2017.

[113] C. Tong, *Conductive Materials for Printed Flexible Electronics*. Cham: Springer International Publishing, 2022, pp. 119–157. [Online]. Available: https://doi.org/10.1007/978-3-030-79804-8_3

[114] Y. Zhang and L. Li, “Modelling and design of mems piezoresistive out-of-plane shear and normal stress sensors,” *Sensors*, vol. 18, no. 11, 2018. [Online]. Available: https://www.mdpi.com/1424-8220/18/11/3737

[115] D. Toker, D. Azulay, N. Shimoni, I. Balberg, and O. Millo, “Tunneling and percolation in metal-insulator composite materials,” *Phys. Rev. B*, vol. 68, p. 041403, Jul 2003. [Online]. Available: https://link.aps.org/doi/10.1103/PhysRevB.68.041403

[116] A. Dzedzickis, E. Sutinys, V. Bucinskas, U. Samukaite-Bubniene, B. Jakstys, A. Ramanavicius, and I. Morkvenaite-Vilkonciene, “Polyethylene-carbon composite (velostat®) based tactile sensor,” *Polymers*, vol. 12, no. 12, 2020. [Online]. Available: https://www.mdpi.com/2073-4360/12/12/2905

[117] D. Giovanelli and E. Farella, “Force Sensing Resistor and Evaluation of Technology for Wearable Body Pressure Sensing,” *Journal of Sensors*, vol. 2016, p. 9391850, 2016. [Online]. Available: https://doi.org/10.1155/2016/9391850

[118] J. Martínez-Cesteros, C. Medrano-Sánchez, J. Castellanos-Ramos, J. A. Sánchez-Durán, and I. Plaza-García, “Creep and hysteresis compensation in pressure-sensitive mats for improving center-of-pressure measurements,” *IEEE Sensors Journal*, vol. 23, pp. 29 585–29 593, 2023. [Online]. Available: https://api.semanticscholar.org/CorpusID:264372237

[119] D. A. Valle-Lopera, A. F. Castaño-Franco, J. Gallego-Londoño, and A. M. Hernández-Valdivieso, “Test and fabrication of piezoresistive sensors for contact pressure measurement,” *Revista Facultad de Ingenieria*, vol. 2017, no. 82, pp. 47–52, 2017.

[120] A. Fatema, S. Chauhan, M. Datta, and A. M. Hussain, “Investigation of the long-term reliability of a velostat-based flexible pressure sensor array for 210 days,” *IEEE Transactions on Device and Materials Reliability*, pp. 1–1, 2023.

[121] E. Jeong, J. Lee, and D. E. Kim, “Finger-gesture recognition glove using velostat (ICCAS 2011),” *International Conference on Control, Automation and Systems*, no. Iccas, pp. 206–210, 2011.

[122] P. Junjie, H. Jincheng, S. Yixiao, M. Hailiang, and B. Guanjun, “Fingertip tactile sensor based on velostat piezoresistive material,” in *2023 IEEE International Conference on Robotics and Biomimetics (ROBIO)*, 2023, pp. 1–5.

[123] M. Carrozzino, G. Avveduto, F. Tecchia, P. Gurevich, and B. Cohen, “Navigating immersive virtual environments through a foot controller,” *Proceedings of the ACM Symposium on Virtual Reality Software and Technology, VRST*, pp. 23–26, 2014.

[124] B. W. Lee and H. Shin, “Feasibility Study of Sitting Posture Monitoring Based on Piezoresistive Conductive Film-Based Flexible Force Sensor,” *IEEE Sensors Journal*, vol. 16, no. 1, pp. 15–16, 2016.

[125] M. Hopkins, R. Vaidyanathan, and A. H. McGregor, “Examination of the Performance Characteristics of Velostat as an In-Socket Pressure Sensor,” *IEEE Sensors Journal*, vol. 20, no. 13, pp. 6992–7000, 2020.

[126] M. Russo, S. M. H. Sadati, X. Dong, A. Mohammad, I. D. Walker, C. Bergeles, K. Xu, and D. A. Axinte, “Continuum robots: An overview,” *Advanced Intelligent Systems*, vol. 5, no. 5, p. 2200367, 2023.

[127] R. J. Webster, J. M. Romano, and N. J. Cowan, “Mechanics of precurved-tube continuum robots,” *IEEE Transactions on Robotics*, vol. 25, no. 1, pp. 67–78, 2009.

[128] D. C. Rucker and R. J. Webster III, “Statics and dynamics of continuum robots with general tendon routing and external loading,” *IEEE Transactions on Robotics*, vol. 27, no. 6, pp. 1033–1044, 2011.

[129] I. Robert J. Webster and B. A. Jones, “Design and kinematic modeling of constant curvature continuum robots: A review,” *The International Journal of Robotics Research*, vol. 29, no. 13, pp. 1661–1683, 2010.

[130] J. Starke, E. Amanov, M. T. Chikhaoui, and J. Burgner-Kahrs, “On the merits of helical tendon routing in continuum robots,” in *2017 IEEE/RSJ International Conference on Intelligent Robots and Systems (IROS)*, 2017, pp. 6470–6476.

[131] M. Wang, X. Dong, W. Ba, A. Mohammad, D. Axinte, and A. Norton, “Design, modelling and validation of a novel extra slender continuum robot for in-situ inspection and repair in aeroengine,” *Robotics and Computer-Integrated Manufacturing*, vol. 67, no. August 2020, 2021.

[132] X. Dong, D. Axinte, D. Palmer, S. Cobos, M. Raffles, A. Rabani, and J. Kell, “Development of a slender continuum robotic system for on-wing inspection/repair of gas turbine engines,” *Robotics and Computer-Integrated Manufacturing*, vol. 44, no. April, pp. 218–229, 2017.

[133] B. Kang, R. Kojcev, and E. Sinibaldi, "The first interlaced continuum robot, devised to intrinsically follow the leader," *PLoS ONE*, vol. 11, no. 2, pp. 0–16, 2016.

[134] Y. Liu and P. Ben-Tzvi, "A new extensible continuum manipulator using flexible parallel mechanism and rigid motion transmission," *Journal of Mechanisms and Robotics*, vol. 13, no. 3, pp. 1–7, 2021.

[135] A. Kanada and T. Mashimo, "Mobile Continuum Robot with Unlimited Extensible Sections," *IEEE International Conference on Intelligent Robots and Systems*, no. October 2018, pp. 7117–7122, 2018.

[136] D. Matsuura, R. Shioya, H. H. Asada, and Y. Takeda, "An extendable continuum robot arm using a flexible screw as a backbone to propel inside a confined space with discontinuous contact area," *Proceedings of the Institution of Mechanical Engineers, Part C: Journal of Mechanical Engineering Science*, p. 095440622210800, 2022.

[137] E. Amanov, T. D. Nguyen, and J. Burgner-Kahrs, "Tendon-driven continuum robots with extensible sections—A model-based evaluation of path-following motions," *International Journal of Robotics Research*, vol. 40, no. 1, pp. 7–23, 2021.

[138] T.-D. Nguyen and J. Burgner-Kahrs, "A tendon-driven continuum robot with extensible sections," in *2015 IEEE/RSJ International Conference on Intelligent Robots and Systems (IROS)*, 2015, pp. 2130–2135.

[139] B. Kuo and D. Urma, "Esophagus - anatomy and development," *GI Motility online*, 05 2006.

[140] B. Ouyang, Y. Liu, and D. Sun, "Design of a three-segment continuum robot for minimally invasive surgery," *Robotics and Biomimetics*, vol. 3, no. 1, p. 2, 2016.

[141] G. Palli and S. Pirozzi, "A miniaturized optical force sensor for tendon-driven mechatronic systems: Design and experimental evaluation," *Mechatronics*, vol. 22, no. 8, pp. 1097–1111, 2012.

[142] M. R. Abdul Kadir, D. E. O. Dewi, M. N. Jamaludin, M. Nafea, and M. S. Mohamed Ali, "A multi-segmented shape memory alloy-based actuator system for endoscopic applications," *Sensors and Actuators, A: Physical*, vol. 296, pp. 92–100, 2019.

[143] E. Allen and J. Swensen, "Design of a highly-maneuverable pneumatic soft actuator driven by intrinsic SMA coils (PneuSMA actuator)," in *IEEE/RSJ International Conference on Intelligent Robots and Systems (IROS)*, 2020, pp. 8667–8672.

[144] J. H. Lee, Y. S. Chung, and H. Rodrigue, "Long shape memory Alloy tendon-based soft Robotic actuators and implementation as a soft gripper," *Scientific reports*, vol. 9, no. 1, p. 11251, 2019.

[145] W. Wang, Y. Tang, and C. Li, "Controlling bending deformation of a shape memory alloy-based soft planar gripper to grip deformable objects," *International Journal of Mechanical Sciences*, vol. 193, p. 106181, 2021.

[146] D. Reynaerts, J. Peirs, and H. Van Brussel, "Shape memory micro-actuation for a gastro-intestinal intervention system," *Sensors and Actuators, A: Physical*, vol. 77, no. 2, pp. 157–166, 1999.

[147] B. Konh, P. Berkelman, and S. Karimi, "Needle tip manipulation and control of a 3d steerable sma-activated flexible needle," in *2020 8th IEEE RAS/EMBS Interna-*

tional Conference for Biomedical Robotics and Biomechatronics (BioRob), 2020, pp. 903–909.

[148] Z. Ren, M. Zarepoor, X. Huang, A. P. Sabelhaus, and C. Majidi, "Shape memory alloy (SMA) actuator with embedded liquid metal curvature sensor for closed-loop control," *Frontiers in Robotics and AI*, vol. 8, no. March, pp. 1–12, 2021.

[149] C. Haberland and M. H. Elahinia, "Fabricating NiTi SMA components," *Shape Memory Alloy Actuators: Design, Fabrication and Experimental Evaluation*, pp. 191–238, 2015.

[150] A. Rao, A. R. Srinivasa, and J. N. Reddy, *Design of shape memory alloy (SMA) actuators*. Springer, 2015, vol. 3.

[151] A. K. Golahmadi, D. Z. Khan, G. P. Mylonas, and H. J. Marcus, "Tool-tissue forces in surgery: A systematic review," *Annals of Medicine and Surgery*, vol. 65, p. 102268, 2021.

[152] A. Syed, Z. T. H. Agasbal, T. Melligeri, and B. Gudur, "Flex Sensor Based Robotic Arm Controller Using Micro Controller," *Journal of Software Engineering and Applications*, vol. 05, no. 05, pp. 364–366, 2012. [Online]. Available: http://www.scirp.org/journal/doi.aspx?DOI=10.4236/jsea.2012.55042

[153] V. Mishra, N. Singh, U. Tiwari, and P. Kapur, "Fiber grating sensors in medicine: Current and emerging applications," *Sensors and Actuators A: Physical*, vol. 167, no. 2, pp. 279–290, June 2011. [Online]. Available: https://linkinghub.elsevier.com/retrieve/pii/S092442471100118X

[154] B. Han, S. Ding, and X. Yu, "Intrinsic self-sensing concrete and structures: A review," *Measurement*, vol. 59, pp. 110–128, Jan. 2015. [Online]. Available: https://www.sciencedirect.com/science/article/pii/S026322411400428X

[155] K. Ikuta, "Micro/miniature shape memory alloy actuator," in *, IEEE International Conference on Robotics and Automation Proceedings*, May 1990, pp. 2156–2161 vol.3.

[156] *Self-Sensing Control of Antagonistic SMA Actuators Based on Resistance-Displacement Hysteresis Compensation*, ser. Smart Materials, Adaptive Structures and Intelligent Systems, vol. ASME 2020 Conference on Smart Materials, Adaptive Structures and Intelligent Systems, 09 2020. [Online]. Available: https://doi.org/10.1115/SMASIS2020-2224

[157] M. Kaiser, N. Neblung, and M. Gurka, "Implementation and Investigation of a Compact, Powerful System for Diagnosis and Control of Shape Memory Alloys in Technical Applications," in *ASME 2019 Conference on Smart Materials, Adaptive Structures and Intelligent Systems*. Louisville, Kentucky, USA: American Society of Mechanical Engineers, Sept. 2019, p. V001T04A004. [Online]. Available: https://asmedigitalcollection.asme.org/SMASIS/proceedings/SMASIS2019/59131/Louisville,%20Kentucky,%20USA/1071395

[158] N. Ma, G. Song, and H.-J. Lee, "Position control of shape memory alloy actuators with internal electrical resistance feedback using neural networks," *Smart Materials and Structures*, vol. 13, no. 4, pp. 777–783, Aug. 2004. [Online]. Available: https://iopscience.iop.org/article/10.1088/0964-1726/13/4/015

[159] C.-C. Lan and C.-H. Fan, "An accurate self-sensing method for the control of shape memory alloy actuated flexures," *Sensors and Actuators A: Physical*,

vol. 163, no. 1, pp. 323–332, Sept. 2010. [Online]. Available: https://www.sciencedirect.com/science/article/pii/S0924424710003511

[160] C.-C. Lan, C.-M. Lin, and C.-H. Fan, “A Self-Sensing Microgripper Module With Wide Handling Ranges,” *IEEE/ASME Transactions on Mechatronics*, vol. 16, no. 1, pp. 141–150, Feb. 2011.

[161] D. Tarniță, D. Tarniță, N. G. Bîzdoaca, I. Mîndrilă, and M. Vasilescu, “Properties and medical applications of shape memory alloys.” *Romanian journal of morphology and embryology*, vol. 50 1, pp. 15–21, 2009.

[162] H. Scherngell and A. Kneissl, “Training and stability of the intrinsic two-way shape memory effect in ni-ti alloys,” *Scripta Materialia*, vol. 39, no. 2, pp. 205–212, 1998. [Online]. Available: https://www.sciencedirect.com/science/article/pii/S1359646298001559

[163] D. K. Soother, J. Daudpoto, and B. S. Chowdhry, “Challenges for practical applications of shape memory alloy actuators,” *Materials Research Express*, vol. 7, no. 7, p. 073001, jul 2020. [Online]. Available: https://dx.doi.org/10.1088/2053-1591/aba403

[164] A. M. Franz, T. Haidegger, W. Birkfellner, K. Cleary, T. M. Peters, and L. Maier-Hein, “Electromagnetic tracking in medicine–a review of technology, validation, and applications,” *IEEE transactions on medical imaging*, vol. 33, no. 8, pp. 1702–1725, 2014.

[165] Z. Yaniv, E. Wilson, D. Lindisch, and K. Cleary, “Electromagnetic tracking in the clinical environment,” *Medical physics*, vol. 36, no. 3, pp. 876–892, 2009.

[166] S. Su, W. Yang, H. Dai, X. Xia, M. Lin, B. Sun, and C. Hu, “Investigation of the relationship between tracking accuracy and tracking distance of a novel magnetic tracking system,” *IEEE Sensors Journal*, vol. 17, no. 15, pp. 4928–4937, 2017.

[167] L. Maréchal, S. Foong, S. Ding, K. L. Wood, V. Patil, and R. Gupta, “Design optimization of a magnetic field-based localization device for enhanced ventriculostomy,” *Journal of Medical Devices*, vol. 10, no. 1, 2016.

[168] I. S. M. Khalil, A. Adel, D. Mahdy, M. M. Micheal, M. Mansour, N. Hamdi, and S. Misra, “Magnetic localization and control of helical robots for clearing superficial blood clots,” *APL bioengineering*, vol. 3, no. 2, p. 026104, 2019.

[169] D. Son, S. Yim, and M. Sitti, “A 5-d localization method for a magnetically manipulated untethered robot using a 2-d array of hall-effect sensors,” *IEEE/ASME Transactions on Mechatronics*, vol. 21, no. 2, pp. 708–716, 2016.

[170] C. Hu, M. Li, S. Song, W. Yang, R. Zhang, and M. Q.-H. Meng, “A cubic 3-axis magnetic sensor array for wirelessly tracking magnet position and orientation,” *IEEE Sensors Journal*, vol. 10, no. 5, pp. 903–913, 2010.

[171] C. Hu, Y. Ren, X. You, W. Yang, S. Song, S. Xiang, X. He, Z. Zhang, and M. Q.-H. Meng, “Locating intra-body capsule object by three-magnet sensing system,” *IEEE Sensors Journal*, vol. 16, no. 13, pp. 5167–5176, 2016.

[172] Y. Fu and Y.-X. Guo, “Wearable permanent magnet tracking system for wireless capsule endoscope,” *IEEE Sensors Journal*, vol. 22, no. 8, pp. 8113–8122, 2022.

[173] Z. Sun, S. Foong, L. Maréchal, T. H. Teo, U.-X. Tan, and A. Shabbir, “Using heterogeneous sensory measurements in a compliant magnetic localization system

for medical intervention," in *2015 IEEE International Conference on Advanced Intelligent Mechatronics (AIM)*, 2015, pp. 133–138.

[174] Z. Sun, K. C. T. Soh, S. Udomsawaengsup, A. Shabbir, and S. Foong, "Modular design of a real-time passive magnetic localization system for enhanced safety in nasogastric intubation," in *2016 6th IEEE International Conference on Biomedical Robotics and Biomechatronics (BioRob)*, 2016, pp. 329–334.

[175] B. D. Cullity and C. D. Graham, *Introduction to magnetic materials*, 2nd ed. Hoboken, N.J: IEEE/Wiley, 2009.

[176] B. Triggs, P. F. McLauchlan, R. I. Hartley, and A. W. Fitzgibbon, "Bundle adjustment — a modern synthesis," in *Vision Algorithms: Theory and Practice*, B. Triggs, A. Zisserman, and R. Szeliski, Eds. Berlin, Heidelberg: Springer Berlin Heidelberg, 2000, pp. 298–372.

[177] K. See, K. Chui, W. Chan, K. Wong, and Y. Chan, "Evidence for endovascular simulation training: A systematic review," *European Journal of Vascular and Endovascular Surgery*, vol. 51, no. 3, pp. 441–451, 2016. [Online]. Available: https://www.sciencedirect.com/science/article/pii/S1078588415007601

[178] D. E. Kendrick, A. F. Gosling, A. Nagavalli, V. S. Kashyap, and J. C. Wang, "Endovascular Simulation Leads to Efficiency and Competence in Thoracic Endovascular Aortic Repair Procedures," *Journal of Surgical Education*, vol. 72, no. 6, pp. 1158–1164, 2015. [Online]. Available: http://dx.doi.org/10.1016/j.jsurg.2015.05.010

[179] E. B. Mazomenos, P.-L. Chang, A. Rolls, D. J. Hawkes, C. D. Bicknell, E. V. Poorten, C. V. Riga, A. Desjardins, and D. Stoyanov, "A Survey on the Current Status and Future Challenges Towards Objective Skills Assessment in Endovascular Surgery," *Journal of Medical Robotics Research*, vol. 01, no. 03, p. 1640010, 2016.

[180] S. Aggarwal, E. Choudhury, S. Ladha, P. Kapoor, and U. Kiran, "Simulation in cardiac catheterization laboratory: Need of the hour to improve the clinical skills," *Annals of Cardiac Anaesthesia*, vol. 19, no. 3, pp. 521–526, 2016.

[181] K. Ahmed, A. N. Keeling, M. Fakhry, H. Ashrafian, R. Aggarwal, P. A. Naughton, A. Darzi, N. Cheshire, T. Athanasiou, and M. Hamady, "Role of virtual reality simulation in teaching and assessing technical skills in endovascular intervention," *Journal of Vascular and Interventional Radiology*, vol. 21, no. 1, pp. 55–66, 2010. [Online]. Available: https://www.sciencedirect.com/science/article/pii/S1051044309009610

[182] B. A. Eslahpazir, J. Goldstone, M. T. Allemang, J. C. Wang, and V. S. Kashyap, "Principal considerations for the contemporary high-fidelity endovascular simulator design used in training and evaluation," *Journal of Vascular Surgery*, vol. 59, no. 4, pp. 1154–1162, 2014. [Online]. Available: http://dx.doi.org/10.1016/j.jvs.2013.11.074

[183] I. Torres and N. De Luccia, "Artificial vascular models for endovascular training (3D printing)," *Innovative Surgical Sciences*, vol. 3, no. 3, pp. 225–234, 2020.

[184] D. Y. Kim, X. Tan, M. Jeong, D. Li, A. Miernik, and T. Qiu, "A high-fidelity artificial urological system for the quantitative assessment of endoscopic skills," *Journal of Functional Biomaterials*, vol. 13, no. 4, 2022. [Online]. Available: https://www.mdpi.com/2079-4983/13/4/301

[185] M. Kaschwich, A. Dell, F. Matysiak, J. Bouchagiar, A. Bayer, M. Scharfschwerdt, F. Ernst, M. Kleemann, and M. Horn, "Development of an ultrasound-capable phantom with patient-specific 3d-printed vascular anatomy to simulate peripheral endovascular interventions," *Annals of Anatomy - Anatomischer Anzeiger*, vol. 232, p. 151563, 2020. [Online]. Available: https://www.sciencedirect.com/science/article/pii/S0940960220301072

[186] C. J. Payne, H. Rafii-Tari, and G. Z. Yang, "A force feedback system for endovascular catheterisation," *IEEE International Conference on Intelligent Robots and Systems*, pp. 1298–1304, 2012.

[187] W. Chi, H. Rafii-Tari, C. J. Payne, J. Liu, C. Riga, C. Bicknell, and G. Z. Yang, "A learning based training and skill assessment platform with haptic guidance for endovascular catheterization," *Proceedings - IEEE International Conference on Robotics and Automation*, pp. 2357–2363, 2017.

[188] H. Rafii-Tari, C. J. Payne, J. Liu, C. Riga, C. Bicknell, and G. Z. Yang, "Towards automated surgical skill evaluation of endovascular catheterization tasks based on force and motion signatures," *Proceedings - IEEE International Conference on Robotics and Automation*, pp. 1789–1794, 2015.

[189] M. F. Fillinger, R. K. Greenberg, J. F. McKinsey, and E. L. Chaikof, "Reporting standards for thoracic endovascular aortic repair (tevar)," *Journal of vascular surgery*, vol. 52, no. 4, pp. 1022–1033, 2010.

[190] A. S. Gorgey, "Robotic exoskeletons: The current pros and cons," *World Journal of Orthopedics*, vol. 9, no. 9, pp. 112–119, 2018.

[191] J. Beil, G. Perner, and T. Asfour, "Design and control of the lower limb exoskeleton KIT-EXO-1," *IEEE International Conference on Rehabilitation Robotics*, vol. 2015-September, pp. 119–124, 2015.

[192] X. Jin, Y. Cai, A. Prado, and S. K. Agrawal, "Effects of exoskeleton weight and inertia on human walking," *Proceedings - IEEE International Conference on Robotics and Automation*, pp. 1772–1777, 2017.

[193] J. Masood, J. Ortiz, J. Fernández, L. A. Mateos, and D. G. Caldwell, "Mechanical design and analysis of light weight hip joint parallel elastic actuator for industrial exoskeleton," in *2016 6th IEEE International Conference on Biomedical Robotics and Biomechatronics (BioRob)*, 2016, pp. 631–636.

[194] K. Langlois, D. Rodriguez-Cianca, B. Serrien, J. De Winter, T. Verstraten, C. Rodriguez-Guerrero, B. Vanderborght, and D. Lefeber, "Investigating the Effects of Strapping Pressure on Human-Robot Interface Dynamics Using a Soft Robotic Cuff," *IEEE Transactions on Medical Robotics and Bionics*, vol. 3, no. 1, pp. 146–155, 2021.

[195] A. A. Manorama, S. Baek, J. Vorro, A. Sikorskii, and T. R. Bush, "Blood perfusion and transcutaneous oxygen level characterizations in human skin with changes in normal and shear loads - Implications for pressure ulcer formation," *Clinical Biomechanics*, vol. 25, no. 8, pp. 823–828, 2010.

[196] C. Bach Baunsgaard, U. Vig Nissen, A. Katrin Brust, A. Frotzler, C. Ribeill, Y. B. Kalke, N. León, B. Gómez, K. Samuelsson, W. Antepohl, U. Holmström, N. Marklund, T. Glott, A. Opheim, J. Benito, N. Murillo, J. Nachtegaal, W. Faber, and F. Biering-Sørensen, "Gait training after spinal cord injury: Safety, feasibility and

gait function following 8 weeks of training with the exoskeletons from ekso bionics article," *Spinal Cord*, vol. 56, no. 2, pp. 106–116, 2018.

[197] M. Wilcox, A. Rathore, D. Z. M. Ramirez, R. C. Loureiro, and T. Carlson, "Muscular activity and physical interaction forces during lower limb exoskeleton use," *Healthcare Technology Letters*, vol. 3, no. 4, pp. 273–279, 2016.

[198] D. Copaci, F. Martin, L. Moreno, and D. Blanco, "SMA Based Elbow Exoskeleton for Rehabilitation Therapy and Patient Evaluation," *IEEE Access*, vol. 7, pp. 31 473–31 484, 2019.

[199] S. J. Park and C. H. Park, "Suit-type Wearable Robot Powered by Shape-memory-alloy-based Fabric Muscle," *Scientific Reports*, vol. 9, no. 1, pp. 1–8, 2019.

[200] K. Hyeon, J. Jeong, C. Chung, M. Cho, S. Hussain, and K.-u. Kyung, "Design of a wearable mechanism With shape memory alloy (SMA)-based artificial muscle for assisting with shoulder abduction," *IEEE Robotics and Automation Letters*, vol. 7, no. 4, pp. 10 635–10 642, 2022.

[201] N. Moslemi, S. Gohari, F. Mozafari, and M. Gol, "A novel smart assistive knee brace incorporated with shape memory alloy wire actuator," *Journal of Intelligent Material Systems and Structures*, vol. 31, no. 13, pp. 1543–1556, 2020.

[202] A. Alminnawi, Y. Kobayashi, T. Otani, and M. Tanaka, "Shape memory alloy actuated ankle foot orthosis for reduction of locomotion force," in *World Automation Congress Proceedings*. TSI Enterprises, August 2021, pp. 271–276.

[203] H. Moein and C. Menon, "An active compression bandage based on shape memory alloys: A preliminary investigation," *BioMedical Engineering Online*, vol. 13, no. 1, pp. 1–13, 2014.

[204] Y. He, D. Eguren, T. P. Luu, and J. L. Contreras-Vidal, "Risk management and regulations for lower limb medical exoskeletons: a review," *Medical Devices (Auckland, N.Z.)*, vol. 10, pp. 89–107, 2017.

[205] A. M. Georgarakis, R. Stampfli, P. Wolf, R. Riener, and J. E. Duartc, "A Method for Quantifying Interaction Forces in Wearable Robots," *Proceedings of the IEEE RAS and EMBS International Conference on Biomedical Robotics and Biomechatronics*, vol. 2018-August, pp. 789–794, 2018.

[206] S. Wang, B. Zhang, Z. Yu, and Y. Yan, "Differential soft sensor-based measurement of interactive force and assistive torque for a robotic hip exoskeleton," *Sensors*, vol. 21, no. 19, 2021.

[207] C. Marquardt, P. Weiner, M. Dežman, and T. Asfour, "Embedded barometric pressure sensor unit for force myography in exoskeletons," in *2022 IEEE-RAS 21st International Conference on Humanoid Robots (Humanoids)*, 2022, pp. 67–73.

[208] N. Hoffmann, S. Ersoysal, G. Prokop, M. Hoefer, and R. Weidner, "Low-cost force sensors embedded in physical human&ndash;machine interfaces: Concept, exemplary realization on upper-body exoskeleton, and validation," *Sensors*, vol. 22, no. 2, 2022.

[209] N. Hoffmann, S. Ersoysal, and R. Weidner, "Towards embedded force sensors in exoskeletons for evaluating interaction forces in interfaces," in *Annals of Scientific Society for Assembly, Handling and Industrial Robotics*, T. Schüppstuhl, K. Tracht, and D. Henrich, Eds. Berlin, Heidelberg: Springer Berlin Heidelberg, 2020, pp. 69–79.

[210] K. Langlois, E. Roels, G. Van De Velde, C. Espadinha, C. Van Vlerken, T. Verstraten, B. Vanderborght, and D. Lefeber, “Integration of 3d printed flexible pressure sensors into physical interfaces for wearable robots,” *Sensors*, vol. 21, no. 6, pp. 1–17, 2021.

[211] S. Jiang, Q. Gao, H. Liu, and P. B. Shull, “A novel, co-located emg-fmg-sensing wearable armband for hand gesture recognition,” *Sensors and Actuators A: Physical*, vol. 301, p. 111738, 2020.

[212] J. Bessler, L. Schaake, R. Kelder, J. H. Buurke, and G. B. Prange-Lasonder, “Prototype Measuring Device for Assessing Interaction Forces between Human Limbs and Rehabilitation Robots - A Proof of Concept Study,” in *2019 IEEE 16th International Conference on Rehabilitation Robotics (ICORR)*, 2019, pp. 1109–1114.

[213] T. Graven-Nielsen, H. B. Vaegter, S. Finocchietti, G. Handberg, and L. Arendt-Nielsen, “Assessment of musculoskeletal pain sensitivity and temporal summation by cuff pressure algometry: A reliability study,” *Pain*, vol. 156, no. 11, pp. 2193–2202, 2015.

[214] C. Giuglea, S. Marinescu, I. P. Florescu, and C. Jecan, “Pressure sores–a constant problem for plegic patients and a permanent challenge for plastic surgery.” *Journal of medicine and life*, vol. 3, no. 2, pp. 149–153, 2010.

[215] K. Ullakko, J. Huang, V. Kokorin, and R. O’Handley, “Magnetically controlled shape memory effect in ni2mnga intermetallics,” *Scripta Materialia*, vol. 36, no. 10, pp. 1133–1138, 1997. [Online]. Available: https://www.sciencedirect.com/science/article/pii/S1359646296004836

[216] J. Qiu, J. Tani, D. Osanai, and Y. Urushiyama, “High-speed actuation of shape memory alloy,” in *Smart Structures and Devices*, D. K. Sood, R. A. Lawes, and V. V. Varadan, Eds., vol. 4235, International Society for Optics and Photonics. SPIE, 2001, pp. 188 – 197. [Online]. Available: https://doi.org/10.1117/12.420858

[217] W. Bierman, “The temperature of the skin surface,” *Journal of the American Medical Association*, vol. 106, no. 14, pp. 1158–1162, 04 1936.

[218] C. Velmurugan, V. Senthilkumar, S. Dinesh, and D. Arulkirubakaran, “Machining of niti-shape memory alloys-a review,” *Machining Science and Technology*, vol. 22, pp. 355 – 401, 2018.

[219] Z. Zeng, M. Yang, J. P. Oliveira, D. Song, and B. Peng, “Laser welding of NiTi shape memory alloy wires and tubes for multi-functional design applications,” *Smart Materials and Structures*, vol. 25, no. 8, 2016.

[220] B. V. Krishna, S. Bose, and A. Bandyopadhyay, “Laser processing of net-shape NiTi shape memory alloy,” *Metallurgical and Materials Transactions A: Physical Metallurgy and Materials Science*, vol. 38, no. 5, pp. 1096–1103, 2007.

[221] A. Pequegnat, M. Daly, J. Wang, Y. Zhou, and M. I. Khan, “Dynamic actuation of a novel laser-processed NiTi linear actuator,” *Smart Materials and Structures*, vol. 21, no. 9, 2012.

[222] I. McCue, C. Peitsch, T. Montalbano, A. Lennon, J. Sopcisak, M. Trexler, and S. Storck, “Scalable laser powder bed fusion processing of nitinol shape memory alloy,” *MRS Communications*, vol. 9, pp. 1214–1220, 2019.

[223] K. Safaei, M. Nematollahi, P. Bayati, and H. Dabbaghi, “Torsional behavior and microstructure characterization of additively manufactured NiTi shape memory

alloy tubes," *Engineering Structures*, vol. 226, p. 111383, 2024. [Online]. Available: https://doi.org/10.1016/j.engstruct.2020.111383

[224] M. Matthews, G. Guss, S. Khairallah, A. Rubenchik, P. J. DePond, and W. King, "Denudation of metal powder layers in laser powder bed fusion processes," *Acta Materialia*, vol. 114, pp. 33–42, 2016.

[225] F. Calignano, "Investigation of the accuracy and roughness in the laser powder bed fusion process," *Virtual and Physical Prototyping*, vol. 13, pp. 104 – 97, 2018.

[226] H. B. Gilbert and R. J. Webster, "Rapid, reliable shape setting of superelastic nitinol for prototyping robots," *IEEE Robotics and Automation Letters*, vol. 1, no. 1, pp. 98–105, 2016.

[227] E. Roos, K. Maile, and M. Seidenfuß, *Nichteisenmetalle*. Berlin, Heidelberg: Springer Berlin Heidelberg, 2017, pp. 235–280. [Online]. Available: https://doi.org/10.1007/978-3-662-49532-2_7

[228] M. Elahinia, M. Hashemi, M. Tabesh, and S. Bhaduri, "Manufacturing and processing of niti implants: A review," *Progress in Materials Science*, vol. 57, pp. 911–946, 2012.

[229] I. I. Geneva, B. Cuzzo, T. Fazili, and W. Javaid, "Normal body temperature: A systematic review," *Open Forum Infectious Diseases*, vol. 6, 2019.

[230] A. Werner and H.-C. Gunga, *Monitoring of Core Body Temperature in Humans*. Cham: Springer International Publishing, 2020, pp. 477–498. [Online]. Available: https://doi.org/10.1007/978-3-030-16996-1_26

[231] J. R. Lepock and K. Ritchie, "Protein denaturation in intact hepatocytes and isolated cellular organelles during heat shock," *The Journal of Cell Biology*, vol. 122, pp. 1267 – 1276, 1993.

[232] P. Mehnert, J. Malchaire, B. Kampmann, A. Piette, B. Griefahn, and H. Gebhardt, "Prediction of the average skin temperature in warm and hot environments," *European Journal of Applied Physiology*, vol. 82, pp. 52–60, 2000.

[233] M. Andrusca, M. Adam, R. Burlica, A. Munteanu, and A. Dragomir, "Considerations regarding the influence of contact resistance on the contacts of low voltage electrical equipment," *2016 International Conference and Exposition on Electrical and Power Engineering (EPE)*, pp. 123–128, 2016.

[234] D. J. S. Ruth, J.-W. Sohn, K. Dhanalakshmi, and S.-B. Choi, "Control aspects of shape memory alloys in robotics applications: A review over the last decade," *Sensors*, vol. 22, no. 13, 2022. [Online]. Available: https://www.mdpi.com/1424-8220/22/13/4860

[235] M. Zhou and Q. Zhang, "Hysteresis model of magnetically controlled shape memory alloy based on a pid neural network," *IEEE Transactions on Magnetics*, vol. 51, pp. 1–4, 2015.

[236] M. Elahinia and H. Ashrafiuon, "Nonlinear control of a shape memory alloy actuated manipulator," *Journal of Vibration and Acoustics*, vol. 124, pp. 566–575, 2002.

[237] H. Ashrafiuon and V. R. Jala, "Sliding Mode Control of Mechanical Systems Actuated by Shape Memory Alloy," *Journal of Dynamic Systems, Measurement, and Control*, vol. 131, no. 1, 12 2008. [Online]. Available: https://doi.org/10.1115/1.3023121

[238] M. Liu, Z. Zhao, and L. Hao, "Data-driven sliding mode control of shape memory alloy actuators with prescribed performance," *Smart Materials and Structures*, vol. 30, 2021.

[239] B. Kada, K. Juhany, I. Al-Qadi, and M. Bourchak, "Design of an advanced distributed adaptive control for multi-sma actuators," *International Journal of Advanced Computer Science and Applications*, 2023.

[240] R. Dutta, L. Chen, D. Renshaw, and D. Liang, "Artificial intelligence automates the characterization of reversibly actuating planar-flow-casted niti shape memory alloy foil," *PLoS ONE*, vol. 17, 2022.

[241] D. C. Lagoudas, *Shape memory alloys - modeling and engineering applications*, D. C. Lagoudas, Ed. Springer, 2006.

[242] D. Lagoudas, D. Hartl, Y. Chemisky, L. MacHado, and P. Popov, "Constitutive model for the numerical analysis of phase transformation in polycrystalline shape memory alloys," *International Journal of Plasticity*, vol. 32-33, pp. 155–183, 2012.

[243] C. Cisse, W. Zaki, and T. Ben Zineb, "A review of constitutive models and modeling techniques for shape memory alloys," *International Journal of Plasticity*, vol. 76, pp. 244–284, 2016. [Online]. Available: https://www.sciencedirect.com/science/article/pii/S0749641915001436

[244] H. Shi, Y. Liu, P. Chen, Y. Luo, and Y. Chen, "Fractional-order dynamics modeling for continuum robots," *2023 International Conference on Fractional Differentiation and Its Applications (ICFDA)*, pp. 1–5, 2023.

[245] *Thermodynamical Model of NiTi SMA Including Plastic Deformation Mechanisms*, ser. Shape Memory Proceedings, vol. SMST 2022: Extended Abstracts from the International Conference on Shape Memory and Superelastic Technologies, 05 2022. [Online]. Available: https://doi.org/10.31399/asm.cp.smst2022p0065

[246] M. M. Hasan and T. Baxevanis, "Structural fatigue and fracture of shape memory alloy actuators: Current status and perspectives," *Journal of Intelligent Material Systems and Structures*, vol. 33, no. 12, pp. 1475–1486, 2022. [Online]. Available: https://doi.org/10.1177/1045389X211057216

[247] L. Capasso, M. Camatini, and M. Gualtieri, "Nickel oxide nanoparticles induce inflammation and genotoxic effect in lung epithelial cells." *Toxicology letters*, vol. 226 1, pp. 28–34, 2014.

[248] J. Putters, D. M. K. Sukul, G. R. de Zeeuw, A. Bijma, and P. Besselink, "Comparative cell culture effects of shape memory metal (nitinol), nickel and titanium: a biocompatibility estimation." *European surgical research. Europaische chirurgische Forschung. Recherches chirurgicales europeennes*, vol. 24 6, pp. 378–82, 1992.

[249] S. Nagaraja and A. Pelton, "Corrosion resistance of a nitinol ocular microstent: Implications on biocompatibility." *Journal of biomedical materials research. Part B, Applied biomaterials*, 2020.

[250] D. Wever, A. Veldhuizen, J. D. Vries, H. Busscher, D. Uges, and J. R. Horn, "Electrochemical and surface characterization of a nickel-titanium alloy." *Biomaterials*, vol. 19 7-9, pp. 761–9, 1998.

[251] S. Rosenbloom, P. K. Kumar, and C. C. Lasley, "The role of surface oxide thickness and structure on the corrosion and nickel elution behavior of nitinol biomedical

implants." *Journal of biomedical materials research. Part B, Applied biomaterials*, 2021.

[252] C. Liu, D. Hu, J. Xu, D. Yang, and M. Qi, "In vitro electrochemical corrosion behavior of functionally graded diamond-like carbon coatings on biomedical nitinol alloy," *Thin Solid Films*, vol. 496, pp. 457–462, 2006.

[253] R. Hang, M. Zhang, S. Ma, and P. Chu, "Biological response of endothelial cells to diamond-like carbon-coated niti alloy." *Journal of biomedical materials research. Part A*, vol. 100 2, pp. 496–506, 2012.

[254] R. Zhang, G. Cui, X. Su, X.-X. Yu, and Z. Li, "A novel functionally graded ni-graphene coating and its corrosion resistance," *Journal of Alloys and Compounds*, vol. 829, p. 154495, 2020.

[255] R. O. Rawson, J. D. Hardy, and K. A. Vasko, "Visceral tissue vascularization: An adaptive response to high temperature," *Science*, vol. 158, pp. 1203 – 1204, 1967.

[256] E. Warmt, T. Kießling, R. Stange, A. Fritsch, M. Zink, and J. Käs, "Thermal instability of cell nuclei," *New Journal of Physics*, vol. 16, 2014.

[257] N. Matsumi, K. Matsumoto, N. Mishima, E. Moriyama, T. Furuta, A. Nishimoto, and K. Taguchi, "Thermal damage threshold of brain tissue–histological study of heated normal monkey brains," *Neurologia medico-chirurgica*, vol. 34, no. 4, pp. 209–215, 1994.

[258] N. McDannold, R. King, F. Jolesz, and K. Hynynen, "Usefulness of mr imaging-derived thermometry and dosimetry in determining the threshold for tissue damage induced by thermal surgery in rabbits," *Radiology*, vol. 216, no. 2, pp. 517–523, 2000.

[259] J. W. Combs, E. Levin, C. Cheng, S. Daly, S. Yeralan, and T. Duerig, "Effects of heat treatment on the magnetic properties of nitinol devices," *Shape Memory and Superelasticity*, vol. 5, pp. 429 – 435, 2019.

[260] L. Kveglis, F. M. Noskov, M. Volochaev, A. Nyavro, and A. Filarowski, "Magnetic properties of nickel-titanium alloy during martensitic transformations under plastic and elastic deformation," *Symmetry*, vol. 13, p. 665, 2021.